Flux profiles of superconductors in high magnetic fields

Ramsbottom, Henry David

Flux Profiles Of Superconductors In High Magnetic Fields

Henry David RAMSBOTTOM
University of Durham

A thesis submitted in partial fulfilment of the requirements for the degree of Doctor of Philosophy

Department of Physics, University of Durham
1996

Abstract

A probe has been designed and built for measuring the magnetisation critical current density $J_C(B,T)$ and magnetic field profiles inside superconducting samples. This is the first flux penetration probe capable of making measurements as a function of temperature, in the range 2-30 K (accurate to 100 mK), which combines high ac. fields of up to 100 mT (at 19.7 Hz) with very large dc. fields of up to 17 T.

A critical state model has been used to calculate the magnetic response of a superconductor to low frequency, high amplitude ac. fields. The analysis has been performed for both a cylindrical and slab geometry and calculated up to the 10^{th} harmonic. The overshoot commonly observed in magnetic field profiles is found to be an artifact of the analysis and is not indicative of sample granularity.

Flux penetration measurements have been made on commercial, multifilamentary NbTi wire from 4.2 K up to T_C in magnetic fields up to 10 T. The $J_C(B,T)$ is in good agreement with transport data on the same wire and the functional form of the volume pinning force obeys the Fietz-Webb scaling law of the form $F_P \propto h(1-h)$, where h is the reduced field. The spatial variation of $J_C(B,T)$ is small and the harmonic response in a transverse field is consistent with the analysis for a non-granular sample. This is expected for a bulk pinning, homogeneous superconductor such as NbTi.

Measurements have also been made on high quality, bulk $PbMo_6S_8$ (PMS). After hot isostatic pressing the $J_C(B,T)$ increased by a factor of 20. Doping PMS with gadolinium provides a rare opportunity to study the coexistence of superconductivity and magnetism. Although T_C increases, both $J_C(B,T)$ and $H_{irr}(T)$ decrease dramatically. For all of the PMS samples, $F_P \propto h^{1/2}(1-h)^2$ which suggests that $J_C(B,T)$ is limited by grain boundary pinning.

Copyright

H. D. Ramsbottom
January 1996.

Acknowledgements

My thanks go to the following:-

The Engineering and Physical Sciences Research Council for providing financial support, Prof. A. D. Martin, Prof. D. Bloor and Prof. B. K. Tanner for allowing me the use of the Department of Physics facilities and my supervisor, Dr. D. P. Hampshire for his advice, encouragement and enthusiasm.

The non-academic staff at the Department of Physics. P. Armstrong, M. Greener, P. Luke and G. Teasdale, (mechanical workshop). T. Jackson and C. Mullaney, (electronics workshop). D. Stockdale, (computing). V. Greener, M. Lee, and P. A. Russell, (audio-visual). W. Dobby, C. Doolan, J. Dobson, P. Foley and N. Thompson, (technical support). Miss. J. Bell, Mrs. N. Bingham, Mrs. C. Bones, Miss. P. A. Carse, Miss. C. Hedley, Miss. R. Lumpkin and Mrs. L. A. Wilkinson, (secretarial staff).

Many others who have assisted at various stages. A. Crum (Engineered Pressure Systems, National Forge Europe) for use of the HIP, Dr. K. Durose (Department of Physics, University of Durham) for his help with the SEM, Dr. R. Richards (IRC in Polymer Science, University. of Durham) and Dr. C. W. Lehman (Department of Chemistry, University of Durham) for use of the XRD facilities, T. Willis (Applied Superconductivity Centre, University of Wisconsin-Madison, USA) and R. Barter (IRC in Superconductivity, University of Cambridge) for the ac. susceptibility measurements on PMS. R. Hart, G. Haswell (Department of Chemistry, University of Durham) for making the Nb_3Sn magnet former. H. Jones, A. Hickman, G. Sheratt (The Clarendon Laboratory, University of Oxford) for help with the construction of the Nb_3Sn magnet. Dr. L. Le Lay (BICC Superconductors, UK) and Dr. D. Evans (Department of Physics, University of Durham) for very useful discussions and valuable suggestions.

Some very good friends. Doctors Christopher Friend, Christopher Gregory, John Hudson, Jon Makar, Toni Rogers, Dirk Rose, Stephen Westwood and Dong-Ning Zheng, together with Salamat Ali, Paul Barker, Ian Daniel, Hamidi Hamid, Thomas Hase, Alton Horsfall, Christopher Leighton, Robert Luscombe, Caroline Moore and Ian Pape.

Contents

1 Introduction **1**

1.1 Motivation 1

1.2 Summary of chapters 2

2 Introduction to Superconductivity **3**

2.1 Introduction 3

2.2 Magnetism 3

2.2.1 Origin of magnetic moments 3

2.2.2 Properties of magnetic materials 4

2.3 Superconductivity 5

2.3.1 A historic discovery 5

2.3.2 Zero resistance and the Meissner effect 6

2.3.3 Type I and type II superconductors 7

2.4 The phenomenological theory 8

2.4.1 The London model 8

2.4.2 The Ginzburg-Landau theory 9

2.5 The microscopic theory (BCS) 12

2.5.1 The electron-phonon interaction 12

2.5.2 The important predictions of BCS theory 13

2.6 Superconducting materials 15

3 Review of Flux Penetration **20**

3.1 Introduction 20

3.2 The critical state 20

3.2.1 Irreversibility, flux pinning and scaling laws 20

3.2.2 The critical state model 22

3.2.3 Bean's analysis 24

3.3 Extension for ac. fields 27

3.3.1 Lock-in amplifiers 27

3.3.2 Measurement technique 28

3.3.3 Ac. susceptibility 30
3.3.4 Bean - harmonic analysis 30
3.4 Magnetic field profiles 32
3.4.1 Campbell's analysis 32
3.4.2 Harmonic analysis 33
3.5 Alternative techniques 35
3.5.1 Decoration experiments 35
3.5.2 Hall probe investigations 36
3.5.3 Magneto-optical imaging 37
3.5.4 Scanning tunnelling microscopy (STM) 38

4 The Harmonic Response of a Superconductor to Low Frequency, High Amplitude AC. Fields 44
4.1 Introduction 44
4.2 Low ac. fields 44
4.2.1 Calculating the voltage waveform 44
4.2.2 Fourier analysis 49
4.3 High ac. fields ($b_m > 2b_p$) 50
4.3.1 Calculating the voltage waveform 50
4.3.2 Fourier analysis 53
4.4 Magnetic field profiles / Discussion 59
4.5 Conclusion 62

5 A Probe for Measuring Flux Profiles of Superconductors from 4.2 K to T_C in High Magnetic Fields 65
5.1 Introduction 65
5.2 System description 66
5.2.1 External circuitry 66
5.2.2 Top end of probe 67
5.2.3 Bottom end of probe 67
5.2.4 Thermometry 72
5.2.5 General design considerations 73
5.3 System operation 73

5.4 Results and discussion 75
5.5 The Nb_3Sn coil 78
5.5.1 Coil fabrication 78
5.5.2 High field measurements 81
5.5.3 High field performance 81
5.6 Conclusion 83

6 Critical Current Densities, Scaling Relations and Flux Pinning in NbTi as Determined by Flux Penetration Measurements 86
6.1 Introduction 86
6.2 Experimental 87
6.2.1 Experimental procedure 87
6.2.2 Experimental results 87
6.3 Analysis of results 89
6.3.1 Magnetic field profiles 89
6.3.2 Critical current density 91
6.3.3 Scaling relations and flux pinning 92
6.4 Harmonic analysis 93
6.5 Discussion 96
6.6 Conclusion 97

7 Flux Penetration Measurements on unHIP'ed and HIP'ed Samples of the Chevrel Phase Superconductor $PbMo_6S_8$ . . 99
7.1 Introduction 99
7.2 Experimental 100
7.2.1 Sample preparation and quality 100
7.2.2 Experimental results 102
7.3 Analysis of results 106
7.3.1 Magnetic field profiles 106
7.3.2 Critical current density 106
7.3.3 Scaling relations and flux pinning 107

7.4 Discussion 107
7.5 Conclusion 115

8 Flux Penetration Measurements and Harmonic Response of a HIP'ed Sample of Gd Doped $PbMo_6S_8$ 119
8.1 Introduction 119
8.2 Experimental 120
8.2.1 Sample preparation and quality 120
8.2.2 Experimental procedure 122
8.2.3 Experimental results 122
8.3 Analysis of results 123
8.3.1 Magnetic field profiles 123
8.3.2 Critical current density 129
8.3.3 Scaling relations and flux pinning 129
8.4 Harmonic analysis 133
8.5 Discussion 136
8.6 Conclusion 137

9 Conclusion 140
9.1 Introduction 140
9.2 Summary 140
9.3 Future work 143

Appendices 144
Appendix 1 Published work 144
Appendix 2 Courses and conferences 145
Appendix 3 Computer programs 146

Variables

A	vector potential of the magnetic field
A	cross-sectional area
A_0	constant in field dependent J_C
a_n	coefficient in loss component of the induced voltage
α_n^*	coefficient in loss component of the induced voltage (Bean)
$\alpha\ddagger$	constant in GL expression for the free energy of a Cooper pair
α	microstructural constant
B	net external field
B_0	constant in field dependent J_C
B_{int}	internal field
B_{ext}	external field
B_C	thermodynamic critical field
B_{C1}	lower critical field
B_{C2}	upper critical field
B_{C3}	the 3rd critical field
b	reduced magnetic field
b	net internal field
b_P	field required to fully penetrate the sample
b_m	magnitude of the applied ac. field
b_{min}	field at which V_{min} occurs
b_n	coefficient in lossless component of the induced voltage
β_n^*	coefficient in lossless component of the induced voltage (Bean)
$\beta\ddagger$	constant in GL expression for the free energy of a Cooper pair
C_P	specific heat
c	constant associated with fact that V_{min} does not occur at b_P
$c_{1,2,3}$	coefficients of the voltage waveform
χ	susceptibility
Δ	energy gap

δ	depth to which the magnetic field penetrates
E	electric field strength
E_F	Fermi energy
e	charge on an electron
ξ_{GL}	Ginzburg-Landau coherence length
ξ_0	BCS coherence length
F_P	volume pinning force
F_{PMAX}	maximum volume pinning force
f_n	free energy of normal state
f_s	free energy of superconducting state
γ	Sommerfeld constant
$\mu_0 H$	applied dc. field
$\mu_0 h$	applied ac. field
h	reduced magnetic field
h	Planck's constant
$\hbar$	Planck's constant / 2π
I	current
J	angular momentum
J	current density
J_C	critical current density
j_s	supercurrent
k	constant determined by the coil geometry
k^l	electron wave vector
k_B	Boltzman's constant
κ_{GL}	Ginzburg-Landau parameter

L	length of sample
λ_L	London penetration depth
m	magnetic moment
m_e	mass of electron
M	magnetisation
M	atomic mass
μ	magnetic dipole moment
μ_0	permeability of free space
μ_B	Bohr magneton
$N(E)$	density of states
n	index for temperature dependence of pinning
n_s	fraction of super-electrons
ω	angular frequency
ω_D	Debye frequency
ρ	electric charge density
ϕ	flux
ϕ_0	the flux quantum
ϕ_T	total flux
$\psi(r)$	Ginzburg-Landau order parameter
q	wave vector of virtual phonon
r	radius
r_m	radius of sample
S	surface integral
T	temperature
T_C	critical temperature

t	reduced temperature
t	time
t_r	time taken to fully reverse the ac. field
θ	phase angle
θ_R	rotation angle
V	voltage
V_t	Verdet constant
V_{ep}	electron-phonon coupling constant
V_{min}	minimum of the induced harmonic voltage
v_s	velocity of super-electrons
v_F	Fermi velocity
z	width of the slab sample

Chapter 1
Introduction.

1.1 Motivation.

Superconductivity is one of the most exciting areas of modern physics. With properties such as zero resistance and perfect diamagnetism, superconductors offer the possibility of studying a new state of matter that has important technological applications. The critical current density (J_C) of superconductors is a key parameter in establishing their use for these applications. Flux penetration measurements can be used to determine the magnetic field and temperature dependence of J_C. As a contactless technique, it is possible to measure bulk samples that have very high J_C, without the problems of sample heating associated with transport current measurements. Flux penetration measurements also provide crucial information on scaling relations and for identifying flux pinning mechanisms. However, unlike more traditional methods such as transport critical current density and dc. magnetisation, they can uniquely obtain the spatial variation of the magnetic field inside a superconductor. These 'flux profiles' can be analysed to give the spatial distribution of J_C, together with information on the material properties of a sample such as granularity and homogeneity.

Data is required over a large range of magnetic field and temperatures so that the theories for various pinning mechanisms can be considered. The variable temperature analysis is also important in the development of new materials for applications. Results have been obtained on two low temperature superconductors (LTS). NbTi was chosen because it is probably the most extensively studied and industrially useful superconductor. Hence these measurements serve as a standard for assessing conductors being developed for high field applications. The other material was the Chevrel phase superconductor $PbMo_6S_8$ (PMS). With an upper critical field above 54 T at 4.2 K, Chevrel phase superconductors are of great interest both as a potential material for high field applications and for fundamental studies of superconductivity.

1.2 Summary of chapters.

Chapter 2 highlights the fundamental aspects of superconductivity. After a brief historical introduction both phenomenological and microscopic theories are discussed. Chapter 3 reviews flux penetration. It begins by examining the relevant theory, from the critical state model to more complex ac. phenomenon. The ideas covered in this section are used in the analysis of the experimental results in later chapters. This chapter also gives a review of the alternative techniques for measuring magnetic field profiles inside superconducting samples. Chapter 4 presents a new model for describing the harmonic response of superconductors to low frequency, high amplitude ac. fields. The analysis is crucial to the understanding of magnetic field profiles produced by flux penetration measurements.

Chapter 5 describes the design, construction and use of a probe for making flux penetration measurements and measuring the harmonic response of a superconductor from 2-30 K in magnetic fields up to 15 T. This includes the recent development of an ac. superconducting Nb_3Sn coil which will enable measurements to be made on bulk superconducting samples with high J_C in dc. fields up to 17 T. The results are used to calculate the critical current density, scaling relations and magnetic field profiles. This provides crucial information for identifying the mechanisms limiting J_C.

The next three chapters present and analyse the results of flux penetration measurements on three different superconducting samples. In Chapter 6 a commercial multifilamentary NbTi wire is used. Measurements are made with the applied field both parallel to the filaments (axial b) and perpendicular to the filaments (transverse b). Chapter 7 presents data on the Chevrel phase superconductor $PbMo_6S_8$ (PMS). In this chapter, the effect of hot isostatic pressing (HIP'ing) on various superconducting properties is examined. In chapter 8, results are presented on a Gadolinium doped sample of PMS $(Pb_{0.7}Gd_{0.3})Mo_6S_8$ (Gd-PMS). The sample offers the possibility of studying the coexistence of superconductivity and magnetism.

Finally, chapter 9 summarises the main conclusions and makes suggestions for further work.

Chapter 2

Introduction to Superconductivity.

2.1 Introduction.

Superconductivity, the disappearance of the dc. electrical resistivity of certain materials at low temperatures, is one of the most unusual phenomena in solid state physics. This chapter gives an introduction to the superconducting state and presents the fundamental theories that have been proposed to describe it.

Section 2.2 describes the origins of the magnetic dipole moment and the magnetic properties of normal materials. This includes a description of diamagnetism, paramagnetism and ferromagnetism. Section 2.3 gives a brief introduction to superconductivity. This begins with the historic discovery which is followed by a description of the two characteristic properties of a superconductor, ie. zero resistance and the Meissner effect. The section ends with a summary of the magnetic properties of type I and type II superconductors.

In section 2.4 the phenomenological theories of the London brothers and Ginzburg-Landau (GL) are presented. The London model is based on the two fluid model. It considers a superconductor consisting of both normal-electrons and super-electrons and introduces the idea of a penetration depth. Ginzburg-Landau theory describes superconductivity more generally in terms of an order parameter. The GL equations were solved by Abrikosov to predict the structure of the flux line lattice. The more recent microscopic theory of superconductivity is shown section 2.5. The electron-phonon interaction and the important predictions of BCS theory are discussed. Section 2.6 lists a few superconducting materials together with their fundamental parameters.

2.2 Magnetism.

2.2.1 Origin of magnetic moments.

Moving electric charges have magnetic fields associated with them. The quantisation

of the angular momentum of the electron gives rise to the fundamental unit of magnetic dipole moment, the Bohr magneton, μ_B. The dipole moment associated with a loop of current, I, is IA, where A is the area of the loop. If the current consists of an electron of charge, e, and mass, m_e, rotating in a circular orbit of radius, r, at angular frequency, ω, then the magnetic dipole moment, m, is

$$m = IA = -e(\omega/2\pi)\pi r^2 = -\tfrac{1}{2} e\omega r^2 \qquad (2.1)$$

The angular momentum $J = m_e\omega r^2$ and so

$$m = -(e/2m_e)J \qquad (2.2)$$

The angular momentum is quantised in units of $\hbar$, ie. $h/2\pi$, where h is Planck's constant. The lowest non-zero value for m is the Bohr magneton $\mu_B = eh/4\pi m_e$, ie. 9.2741×10^{-24} $J.T^{-1}$. The susceptibility of gadolinium above its Curie temperature is 10^5 compared with a value of -1 for a superconductor in the Meissner state. Susceptibility, $\chi = M/H$.

2.2.2 Properties of magnetic materials.

a. Diamagnetism.

In these materials $\chi \approx -10^{-5}$. The magnetic response opposes the applied magnetic field. Metals such as copper, silver and gold are diamagnetic. Superconductors are known as perfect diamagnets because $\chi = -1$.

b. Paramagnetism.

In these materials $\chi \approx 10^{-3}$-10^{-5}. The magnetisation is preferentially aligned parallel to the applied field. Metals such as aluminium and most ionic solids are paramagnetic.

c. Ferromagnetism.

Spontaneous magnetisation occurs, ie. M is finite in zero applied field and is not proportional to H. $\chi = \lim_{B\to0} dM/dH$. Ferromagnets are characterised by the hysteresis in their magnetisation (M-H) loops. In ferromagnets, nearest neighbour magnetic moments are aligned parallel to each other whereas in antiferromagnets they are antiparallel. Iron, cobalt and nickel together with a few rare earth metals such as gadolinium are ferromagnetic.

2.3 Superconductivity.

2.3.1 A historic discovery.

In 1908 Heike Kammerlingh-Onnes succeeded in liquifying helium. It became possible to study physical phenomena below 10 K. He began by investigating how the resistance of metals changed as the temperature approached absolute zero. Mercury was chosen as the first metal to be studied since it could be obtained in a very pure state. In 1911 Onnes discovered that at about 4 K the resistance of the sample fell abruptly to zero [1]. He named this new state of matter, the superconducting state [2]. Since then a large number of substances have been found to be superconducting below a certain critical temperature, T_C. In 1986 a new family of high temperature superconductors (HTS) were discovered with a T_C greater than the economically important barrier of 77 K. Indeed, recently there have been reports of superconductivity at 250 K [3-5].

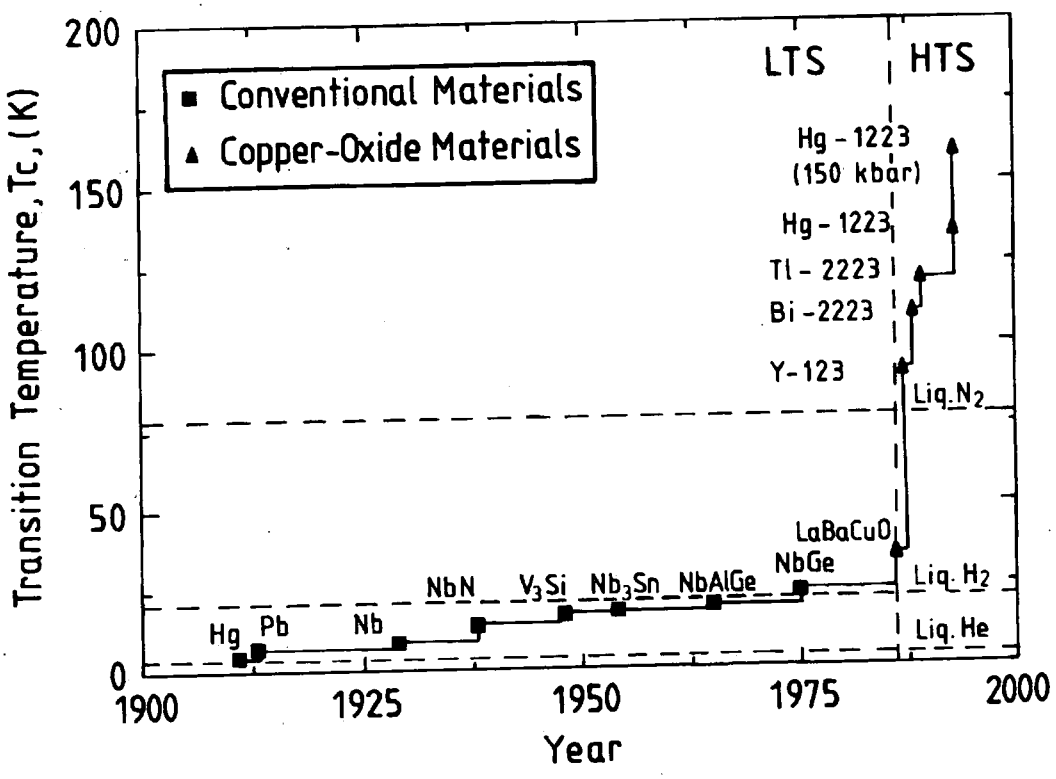

Figure 2.1 Evolution of the superconducting transition temperature T_C. Note the dramatic increase in 1986 on the discovery of the new high temperature superconductors. HTS data from [6-10].

2.3.2 Zero resistance and the Meissner effect.

The most amazing property of a superconductor is the complete disappearance of the electrical resistivity below T_C. Indeed, persistent currents with no measurable decay have been shown to flow in a superconductor for over two and a half years [11]. This corresponds to a resistivity which is 18 orders of magnitude smaller than that of copper at room temperature.

The second fundamental property of a superconductor is that when it is cooled down from the normal state to below T_C in the presence of a small magnetic field, the flux inside the sample is expelled. This was discovered in 1933 and is known as the Meissner effect [12]. Alternatively, the superconducting sample will become normal if a magnetic field is applied that is greater than a certain critical field, B_C. This is not a result of infinite conductivity but is another intrinsic property of a superconductor. Taking Maxwell's equation, $\nabla \times E = \nabla \times (\rho J) = -dB/dt$, zero resistivity would imply $dB/dt=0$. The Meissner effect however always occurs, whether the sample is cooled in a magnetic field or if the field is applied after cooling below T_C. Hence the superconducting state is in thermodynamic equilibrium exhibiting perfect diamagnetism.

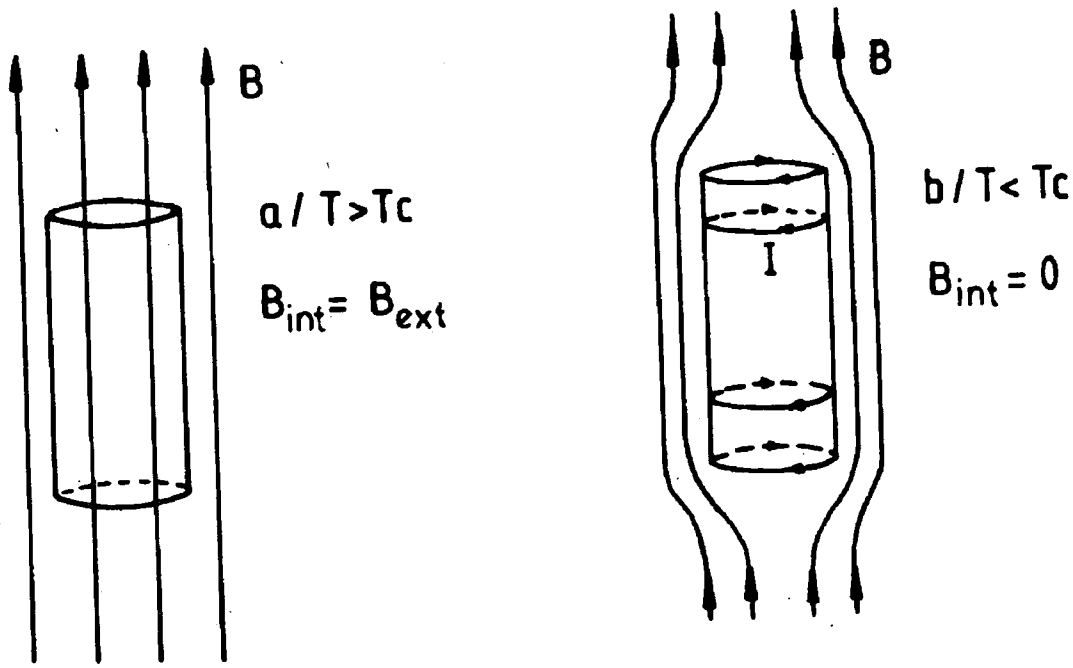

Figure 2.2 The Meissner effect showing flux exclusion below T_C.

Associated with an electric current is a magnetic field. Thus if a superconductor carries a current such that the field it produces is equal to B_C, then the resistance of the sample returns. The current density at which this occurs is called the critical current density, J_C.

2.3.3 Type I and type II superconductors.

Superconductors may be divided into two classes depending on the way in which the transition from the superconducting to the normal state proceeds. Consider a superconducting sample cooled in zero applied field. On applying a magnetic field, a type I superconductor excludes the flux up to the thermodynamic critical field B_C. Above B_C, the entire sample enters the normal state, the resistance returns and the magnetic moment becomes zero. ie. The internal field, B_{int} is equal to the applied field, B_{ext}. For a type II superconductor, the flux is completely excluded only up to the lower critical field B_{C1}, at which point it penetrates in quantised flux lines. The superconductivity is only destroyed when the applied field is greater than the upper critical field, B_{C2}.

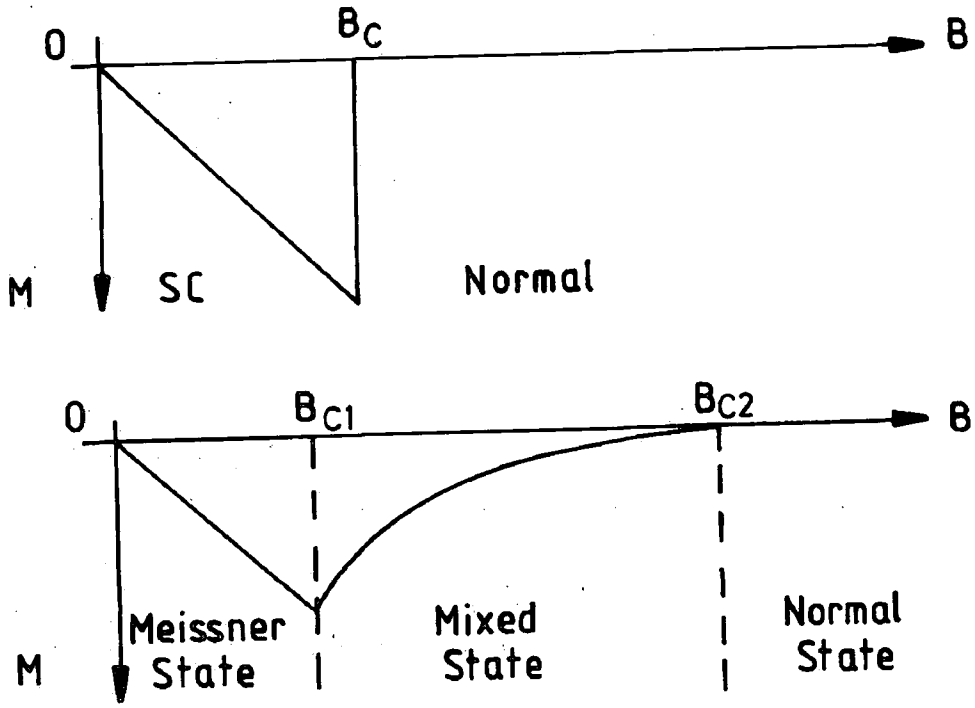

Figure 2.3 Magnetisation curves for a type I and a type II superconductor.

2.4 The phenomenological theory.

2.4.1 The London model.

The Meissner effect and field penetration cannot be deduced from Maxwell's equations alone. The London brothers showed that in order to account for the magnetic properties, it was necessary to introduce two additional equations [13]. In the two fluid model of superconductivity [14], only a temperature dependent fraction n_s, of the total number of electrons, n, are superconducting. The London model assumes that the supercurrent is always determined by the local magnetic field. Thus the equation for the supercurrent is $j_s = n_s e v_s$ and $m_e(dv_s/dt) = eE$. This leads to,

$$\frac{dj_s}{dt} = \frac{n_s e^2}{m_e} E \qquad (2.3)$$

where, m_e is the electron mass, v_s is the velocity of the super-electrons and E is the electric field strength. Combining equation 2.3 with Maxwell's equation $\nabla \times E = -dB/dt$ and integrating they obtained,

$$\nabla \times j_s = - \frac{n_s e^2}{m_e} B \qquad (2.4)$$

Equations 2.3 and 2.4 are the two London equations. The first one describes a conductor with zero resistance and the second one describes the Meissner effect. Applying Maxwell's equation $\nabla \times B = \mu_0 j_s$ to equation 2.4 and solving for a simple one-dimensional case gives a characteristic length called the London penetration depth, λ_L.

$$\lambda_L = \left(\frac{m_e}{\mu_0 n_s e^2} \right)^{\frac{1}{2}} \qquad (2.5)$$

The London penetration depth describes the range over which the field extends inside the superconductor. Combining the second London equation with the Maxwell equation $\nabla \times B = \mu_0 j_s$ gives $\nabla^2 B = B/\lambda_L^2$. If this is solved for fields parallel to the surface, then

$$B(x) = B_0 e^{\frac{-x}{\lambda_L}} \qquad (2.6)$$

ie. the field decays exponentially in the sample within the London penetration depth.

2.4.2 The Ginzburg-Landau theory.

A completely new approach to considering a superconductor in an external magnetic field and the effect of field penetration was proposed by Ginzburg and Landau in 1950 [15]. Their theory is based on the idea of long range order. They introduced a pseudo-wavefunction ψ as an order parameter for the superconducting electrons. $\psi(r,\phi)=\psi(r)e^{i\phi}$, where ϕ is the phase. GL theory represents a generalisation of London's theory to allow for spatial variations in n_S, (with magnetic fields, currents etc.). The order parameter ψ is defined to be zero in a normal region and is related to the density of paired super-electrons in a fully superconducting region by,

$$n_s(r) = |\psi(r)|^2 \tag{2.7}$$

The GL treatment of superconductivity is based on the theory of second order phase transitions. They formulated an expression for the superconducting free energy of a Cooper-pair in a magnetic field. This included an expressions for the intrinsic condensation energy and the kinetic energy. The expression for the free energy can be expanded in a series of $|\psi|^2$ of the form,

$$f_s = f_n + \alpha^{\ddagger}|\psi|^2 + \frac{1}{2}\beta^{\ddagger}|\psi|^4 + \frac{1}{2m_e}|(-i\hbar\nabla - 2eA)\psi|^2 + \frac{B^2}{2\mu_0} \tag{2.8}$$

where f_n is the free energy in the normal state and $\alpha^{\ddagger}$ and $\beta^{\ddagger}$ are coefficients. The first three terms come from Landau's theory of 2nd order phase transitions [16]. Minimising the free energy with respect to ψ gives,

$$\left[\alpha^{\ddagger} + \beta^{\ddagger}|\psi|^2 + \frac{1}{2m_e}(i\hbar\nabla - 2eA)^2\right]\psi = 0 \tag{2.9}$$

where A is the vector potential of the magnetic field. Minimising the free energy with respect to A gives an equation for the supercurrent.

$$j_S = -\frac{ie\hbar}{m_e}(\psi^*\nabla\psi - \psi\nabla\psi^*) - \frac{4e^2}{m_e}\psi^*\psi A \tag{2.10}$$

These are the two Ginzburg-Landau equations, with the boundary condition,

$$(-i\hbar\nabla - 2eA_n)\psi = 0 \tag{2.11}$$

ie. the current flowing through the surface of the sample is zero.

A characteristic length emerges from Ginzburg-Landau theory. The coherence length, ξ_{GL}, is the distance over which the order parameter decays at a superconducting-normal interface. Empirically, the temperature dependence at near T_C is,

$$\xi_{GL} \propto (1-t)^{-1/2} \tag{2.12}$$

where t is the reduced temperature, T/T_C. The GL penetration depth varies in the same way as λ_L and ξ_{GL} close to T_C. At T_C both λ_{GL} and ξ_{GL} become infinite, the normal vortex cores expand to fill the entire material and flux penetration is complete.

The GL theory can be formulated in terms of the Ginzburg-Landau parameter

$$\kappa_{GL} = \frac{\lambda_{GL}}{\xi_{GL}} \tag{2.13}$$

Ginzburg and Landau showed that at a superconducting-normal boundary the condition $\kappa_{GL} = 1/\sqrt{2}$ describes the point at which the surface energy goes from positive to negative. Type I superconductors are characterised by $\kappa_{GL} < 1/\sqrt{2}$ which corresponds to a positive surface energy and type II superconductors are characterised by $\kappa_{GL} > 1/\sqrt{2}$ which corresponds to a negative surface energy.

In 1957 Abrikosov solved the GL equations for a type II superconductor in the mixed state [17]. He showed that a magnetic field penetrates a superconductor as tubes of flux (fluxons), each containing one flux quantum ϕ_0,

$$\phi_0 = \frac{h}{2e} = 2.07\times10^{-15}\ Wb \tag{2.14}$$

where h is Planck's constant and e is the charge on an electron. Flux quantisation was confirmed experimentally by two groups in 1962 [18,19]. Each flux line consists of magnetic flux surrounded by a vortex of super-electrons at a distance λ_L, see figure 2.4. The core is in the normal state. When the fluxons enter a superconductor they attempt to organise in such a way as to minimise their free energy. This array of fluxons is known as the flux line lattice (FLL). In a homogeneous superconductor, Abrikosov calculated that the fluxons would arrange themselves in a square lattice. Kleiner et al [20] corrected the calculation to arrive at the hexagonal (or triangular) configuration, as shown in figure 2.5.

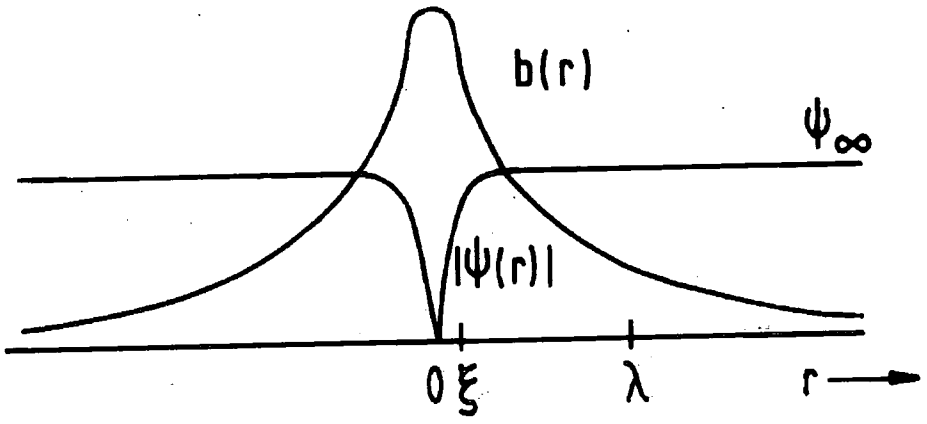

Figure 2.4 The structure of an isolated Abrikosov flux vortex. The value of b(r) is approximately $2B_{C1}$.

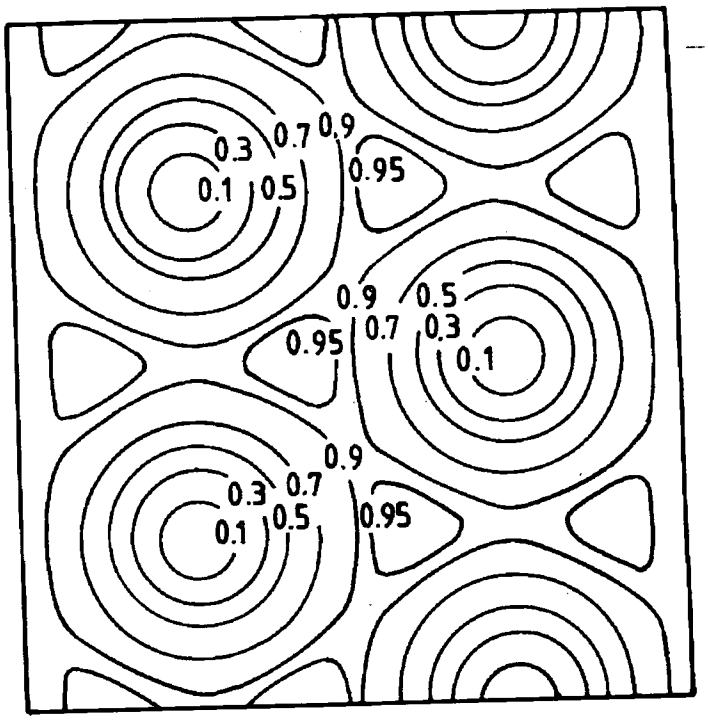

Figure 2.5 The spatial variation of $|\psi|^2$ in a type II superconductor showing the hexagonal flux line lattice.

The two critical fields can then be derived as,

$$B_{C2} = \frac{\phi_0}{2\pi\xi_{GL}^2} = \sqrt{2}\kappa_{GL}B_C \tag{2.15}$$

$$B_{C1} \approx \frac{\phi_0}{4\pi\lambda_{GL}^2}\ln\kappa_{GL} \approx \frac{B_C}{\sqrt{2}\kappa_{GL}}\ln\kappa_{GL} \tag{2.16}$$

If a field is applied parallel to the surface of sample, a superconducting region can exist at the surface for fields greater than B_{C2}, up to a field given by,

$$B_{C3} = 1.695 B_{C2} \tag{2.17}$$

As the angle of the applied field is changed, B_{C3} reduces to B_{C2} when the field is perpendicular to the surface.

2.5 The microscopic theory (BCS).

2.5.1 The electron-phonon interaction.

The fundamental idea underlying the modern theory of superconductivity is that the electrons pair up with one another due to a special type of attractive interaction. In 1957 Cooper showed that if two electrons are attracted to each other, then the lowest energy state is one in which the electrons bind to form Cooper-pairs [21].

The pairing interaction between electrons occurs because the motion of one electron modifies the vibration of an ion in the lattice of the superconductor. This in turn interacts with a second electron. The total effect is a net attractive force between the electrons. The distance over which this pair is correlated is the BCS coherence length ξ_0. The electron pairs can be considered to be interacting by the exchange of a virtual phonon. The two electron quantisation of the charge on a superconductor has been shown experimentally [22].

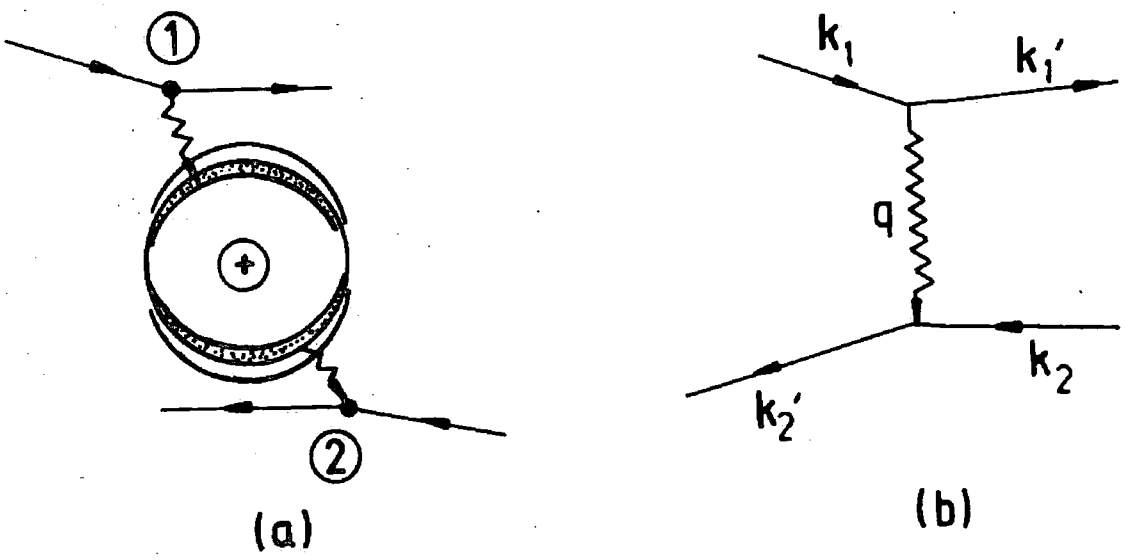

Figure 2.6 The pinning interaction between 2 electrons considered as
a. Transfer of momentum through a lattice vibration.
b. Via the exchange of a virtual phonon of wave vector q.
(k and k' are the wave vectors before and after the interaction.)

2.5.2 The important predictions of BCS theory.

The development of this pairing hypothesis culminated in the theory proposed by Bardeen, Cooper and Schrieffer in 1957 [23] which is the basis of our current understanding of superconductivity. BCS theory considers pairs of electrons with opposite momentum and spin (or wave vectors k↑ and -k↓). The distance over which these Cooper-pairs interact is the BCS coherence length, ξ_0,

$$\xi_0 = 0.18\frac{\hbar v_F}{k_B T_C} \qquad (2.18)$$

where v_F is the Fermi velocity. BCS theory predicts the zero temperature values and temperature dependencies of several superconducting parameters, including :-

a. The critical temperature.

BCS theory predicts that the superconducting transition temperature in zero applied magnetic field is,

$$T_C = 1.13 \frac{\hbar \omega_D}{k_B} \exp\left(-\frac{1}{N(E_F)\, V_{ep}}\right) \qquad (2.19)$$

where ω_D is the Debye frequency, k_B is Boltzmann's constant, $N(E_F)$ is the density of states at the Fermi surface and V_{ep} is an electron phonon coupling constant.

b. The isotope effect.

If V_{ep} is constant then $\omega_D \propto 1/\sqrt{M}$ and thus,

$$T_C \propto M^{-1/2} \qquad (2.20)$$

where M is the atomic mass of the isotope. This is known as the isotope effect and had been observed some years before BCS theory [24,25].

c. Thermodynamic critical field.

For all temperatures up to T_C, BCS theory predicts that the temperature dependence of the thermodynamic critical field is,

$$B_C(t) = B_C(0)(1-t^2) \qquad (2.21)$$

This prediction has been confirmed experimentally for lead and aluminium [26].

d. Low temperature specific heat.

Another successful prediction by BCS was the temperature dependence of the specific heat. As the temperature approaches zero,

$$C_P \propto \gamma \exp\left(\frac{\Delta(0)}{k_B T}\right) \qquad (2.22)$$

where γ is the Sommerfeld constant and $\Delta(0)$ is the energy gap at 0 K. This dependence has been confirmed for tin and vanadium [27].

e. The energy gap.

In the normal state, single unpaired electrons occupy all states up to the Fermi surface.

In the superconducting state, the net attractive interaction these pairs causes a Bose condensation into a ground state. The energy gap between a paired state and two single electron states is denoted by 2Δ. BCS theory gives the energy gap at zero temperature,

$$2\Delta(0) = 3.52 k_B T_C \tag{2.23}$$

and near to T_C as

$$\frac{\Delta(t)}{\Delta(0)} = 1.74(1-t)^{1/2} \tag{2.24}$$

To break up a Cooper pair requires an energy of greater than 2Δ. Therefore above T=0 both Cooper pairs and single electrons exist. The BCS predictions for the energy gap have been confirmed experimentally by infra-red absorption [28], ultrasound attenuation [29], and tunnelling experiments [30].

2.6 Superconducting materials.

Since 1911 hundreds of superconducting materials have been discovered. Table 2.1 lists the important properties of a variety of materials. These include elemental, conventional low-T_C (LTS), new high-T_C (HTS) and Chevrel phase (CPS) superconductors.

Material	T_C **(K)**	$B_{C2}(0)$ **(T)**	$B_{C1}(0)$ **(mT)**	κ_{GL}	ξ_{GL} **(nm)**	λ_{GL} **(nm)**
Pb	7.2	0.08	80	0.46	65	30
NbTi	9.8	12	60	18	5	90
Nb_3Sn	18.6	23	17	50	4	200
Y-123 (// ab-plane)	92	670	85	100	1	100
Y-123 (// c-axis)	92	120	25	87.5	2	175
Bi-2223 (// ab-plane)	110	1200	2	1560	0.5	780
Bi-2223 (// c-axis)	110	40	0.2	783	3.0	2350
$PbMo_6S_8$	14	56	6.4	144	2.5	360

Table 2.1 The important parameters for various superconducting materials. T_C, B_{C1} and B_{C2} are experimental data [31-35] and the other parameters have been calculated using the Ginzburg-Landau relations.

With B_{c2}'s greater than 50 T at 4.2 K, Chevrel phase superconductors are a promising candidate for technological applications. Figure 2.7 highlights their attractive high field performance and compares it to other superconductors. A comparison is also made with an anisotropic HTS, with the magnetic field applied both parallel and perpendicular to the c-axis. (The shaded areas correspond to uncertainties related to the definition of B_{c2}.) Figure 2.8 shows the general crystal structure of a Chevrel phase superconductor, which can be approximated by a cubic structure.

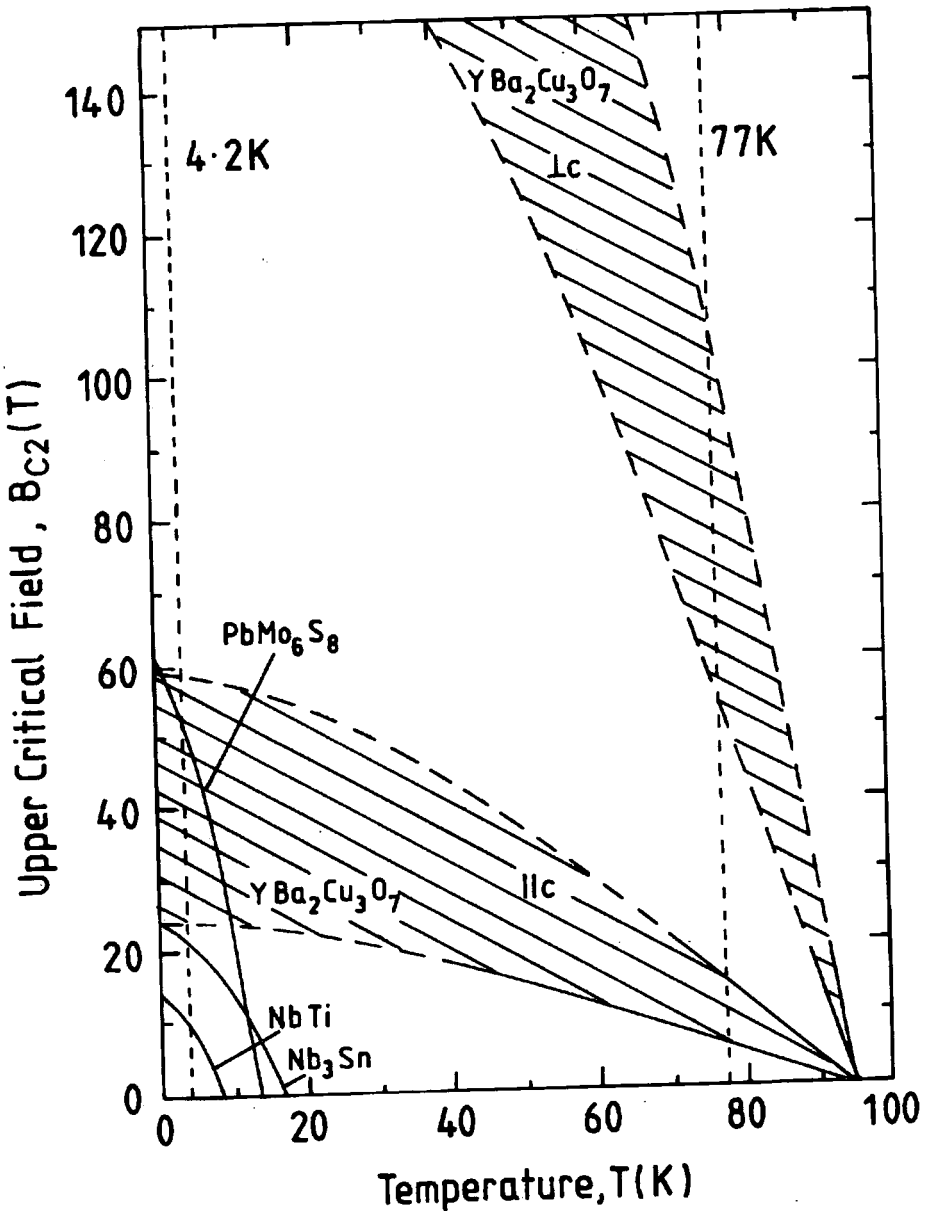

Figure 2.7 The temperature dependence of the upper critical field of $PbMo_6S_8$ compared with both LTS and HTS [36].

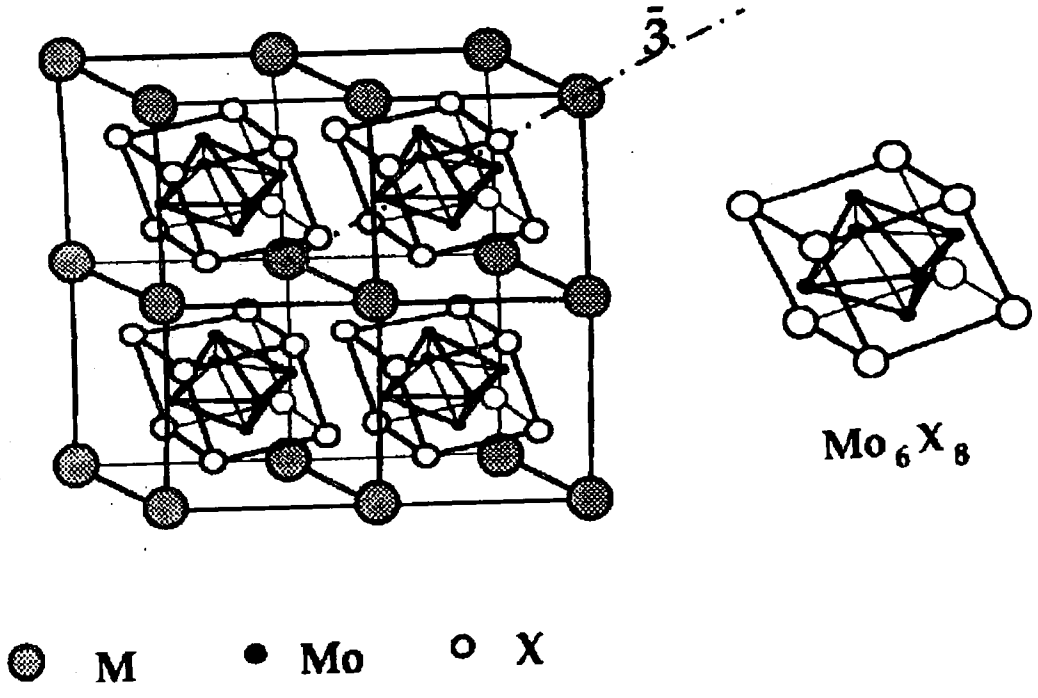

Figure 2.8 The crystal structure of the Chevrel phase superconductors [37]. (Where for $PbMo_6S_8$, M = lead, Mo = molybdenum and X = sulphur.)

References.

[1] Onnes H K *Comm. Leiden* **120b** (1911).

[2] Onnes H K *Comm. Leiden Suppl. Nr.* **34** (1913).

[3] Laguës M, Xie X M, Tebbji H, Xu X Z, Mairet V, Hatterer C, Beuran C F and Deville-Cavellin *Science* **262** 1850 (1993).

[4] Tholence J L, Souletie B, Laborde O, Capponi L L, Challout C and Marezio M *Phys. Lett. A* **184** 215 (1994).

[5] Levi B G *Phys. Today* **Feb.** 17 (1994).

[6] Bednorz J G and Müller K A *Z. Phys. B* **64** 189 (1986).

[7] Wu M K, Ashburn J R, Torng C J, Hor P H, Meng R L, Gao L, Huang Z J, Wang Y Q and Chu C W *Phys. Rev. Lett.* **58** (9) 908 (1987).

[8] Maeda H, Tanaka Y, Fukutomi M and Asano T *Japan. J. Appl. Phys.* 27 (2) 4209 (1988).

[9] Schilling A, Cantoni M, Guo J D and Ott H R *Nature* **363** 56 (1993).

[10] Chu C W, Gao L, Chen F, Huang Z J, Meng R L and Xue Y Y *Nature* **365** 323 (1993).

[11] Quinn D J and Ittner W B *J. Appl. Phys.* **33** 748 (1962).

[12] Meissner W and Ochsenfeld R *Naturwissenschaften* **21** 787 (1933).

[13] London F and London H *Proc. Royal Soc. (London)* **A149** 71 (1935).

[14] Gorter C J and Casimir H B G *Physica* **1** 305 (1934).

[15] Ginzburg V L and Landau L D *Zh. Eksp. Teor. Fiz.* **20** 1064 (1950)

[16] Landau L D and Lifshitz E M *Course of Theoretical Physics* **5** 430 Permagon Press (1957)

[17] Abrikosov A A *Sov. Phys. JETP* **5** 1174 (1957). [Translation of *Zh. Eksp. Teor. Fiz.* **32** 1442 (1957)].

[18] Deaver B S and Fairbank W M *Phys. Rev. Lett.* **7** 43 (1961).

[19] Doll R and Näbauer M *Phys. Rev. Lett.* **7** 51 (1961).

[20] Kleiner W H Roth L M and Autler S H *Phys. Rev.* **133** A1266 (1964).

[21] Cooper L N *Phys. Rev.* **104** 1189 (1956)

[22] Lafarge P, Joyez P, Esteve D, Urbina C and Devoret M H *Nature* **365** 423 (1993).

[23] Bardeen J Cooper L N and Schrieffer J R *Phys. Rev.* **108** (5) 1175 (1957)

[24] Serin B, Reynolds C A and Lohman C *Phys. Rev.* **86** 162 (1952).

[25] Maxwell E *Phys. Rev.* **86** 235 (1952).

[26] Swihart J C, Scalapino D J and Wada Y *Phys. Rev. Lett.* **14** 106 (1965).

[27] Biondi M A, Forrester A T, Garfunkel M P and Satterthwaite C B *Rev. Mod. Phys.* **30** 1109 (1958).

[28] Richards P L and Tinkham M *Phys. Rev.* **119** 575 (1960).

[29] Morse R W and Bohm H V *Phys. Rev.* **108** 1094 (1957).

[30] Giaever I and Megerle K *Phys. Rev.* **122** 1101 (1961).

[31] *CRC handbook of physics and chemistry 69th Ed.* ed. Weast R C (CRC Press Inc, Florida) (1988).

[32] *Applied superconductivity : Metallurgy and physics of Titanium alloys* ed. Collings E W (Plenum Press, New York) (1986).

[33] Burns G *High temperature superconductivity : An introduction* (Academic Press, UK) (1992).

[34] Matsubara I, Tanigawa H, Ogura T, Yamashita H and Kinoshita M *Phys. Rev. B* **45** (13) 7414 (1992).

[35] Zheng D N, Ramsbottom H D and Hampshire D P *Phys. Rev. B* **52** (17) 12931 (1995).

[36] Powell R L and Clark A F *Cryogenics* **17** 697 (1977).

[37] Chevrel R, Sergent M, Le Lay L, Padiou J, Pena O, Dubots P, Genevey P, Couach M and Vallier J C *Rev. Phys. Appl.* **23** 1777 (1988).

Chapter 3

Review of Flux Penetration.

3.1 Introduction.

This chapter is a review of flux penetration into superconductors. Section 3.2 highlights the ideas which are crucial for understanding the magnetic response of a superconductor. It begins with a discussion of irreversible magnetic measurements, flux pinning and scaling relations. This is followed by a description of Bean's critical state model.

Section 3.3 describes the effect of ac. fields. It explains how the magnetisation of a superconductor can be measured in response to an applied magnetic field. Low field phenomenon such as ac. susceptibility and the harmonic response of a superconductor to ac. fields are discussed. Section 3.4 describes Campbell's extension to Bean's work for high ac. fields, and explains how to experimentally determine magnetic field profiles of superconducting samples. The technique is non-destructive and provides some of the clearest evidence for the granular nature of superconducting samples. Flux penetration measurements are the focus of this thesis.

Section 3.5 reviews some of the alternative techniques for measuring magnetic field profiles of superconductors. These include decoration experiments, Hall probe investigations, magneto-optic imaging and scanning tunnelling microscopy.

3.2 The critical state.

3.2.1 Irreversibility, flux pinning and scaling laws.

When flux lines enter a superconducting sample they arrange themselves in a hexagonal Abrikosov lattice in order to minimise their free energy [1]. If a current flows then the flux lines experience a force, they move and a voltage is produced. Thus an ideal superconductor will have zero J_C. However in a real superconductor there are always some inhomogeneities which can pin the flux lines. These include defects, grain boundaries, impurity phases and non-superconducting precipitates. Pinning centres

restrain the movement of flux lines which can result in gradients in the internal field. Screening currents can flow which either trap field within the sample or exclude field from it. The process leads to the irreversible magnetic properties of type II superconductors, as seen for example in dc. magnetisation curves. The strength with which the flux lines are pinned is known as the volume pinning force, F_P, [2].

$$F_P = J_C \times B \tag{3.1}$$

Measurements by Fietz and Webb lead to the discovery that this pinning force could be represented by a single universal curve at all temperatures [3]. This universal scaling can be represented by,

$$F_P = \alpha [B_{C2}(T)]^n f(b) \tag{3.2}$$

where b is the reduced field B/B_{C2}, α is a constant depending on sample microstructure and the index n is a constant which determines the temperature dependence of the pinning. Various models have been proposed to define the function F_P, ie. to account for the field and temperature dependence of J_C. Kramer [4], suggested,

$$F_P = \alpha B_{C2}^n b^{1/2}(1-b)^2 \tag{3.3}$$

This functional form describes the pinning in materials such as Nb_3Sn and $PbMo_6S_8$. However, the pinning in NbTi is more accurately described by a relationship discovered by Hampshire and Taylor [5].

$$F_P = \alpha B_{C2}^n b(1-b) \tag{3.4}$$

Flux pinning is addressed in a more general manner by Freyhardt [6] and Dew-Hughes [7] who consider many types of geometrical pinning sites and their interactions with flux lines. They summarised the form of the scaling law for many materials. Thus the dominant pinning mechanism in a material may be deduced from pinning force data.

The pinning of flux lines creates two regions in the superconducting section of the B-T phase diagram which are separated by the so called irreversibility line, as shown in figure 3.1. In the reversible region flux lines can move, and thus the sample has a negligible or zero J_C. In the irreversible region the flux lines are pinned.

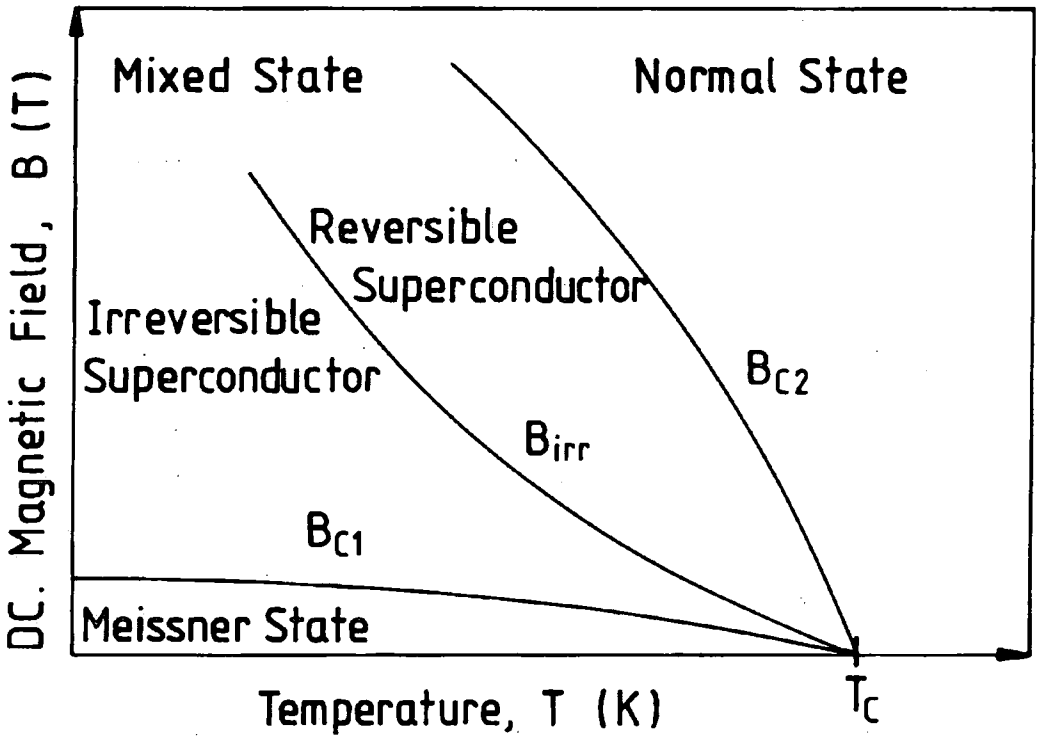

Figure 3.1 Schematic B-T phase diagram for a HTS.
For a conventional LTS $B_{irr}(T)$ is very close to $B_{C2}(T)$.

3.2.2 The critical state model.

In 1964 Bean proposed a model to explain the irreversible behaviour of type II superconductors [8]. This is known as the critical state model. The theory relates the magnetic moment induced in a superconductor to the critical current density flowing. Figure 3.2 shows the magnetic field and current profiles inside a superconducting sample after applying a dc. field ($\mu_0 H$). In agreement with Lenz's law, lossless supercurrents flow to a depth δ to expel the field. The critical state model assumes that the current density flowing must be either equal to the critical current density ($\pm J_C$) or zero. The applied field can be increased until it is equal to the field required to fully penetrate the sample (B_P), ie. the depth to which the field penetrates (δ) is equal to the sample radius (r_m). At this point, a current density equal to J_C flows throughout the entire sample. This can be related to the magnetisation (M) by $J_C = M/a$, where 'a' is a characteristic dimension of the sample. A more complex analysis to extract the field dependence of J_C, which considers the effect of the self-field, is discussed by Johansen et al [9,10].

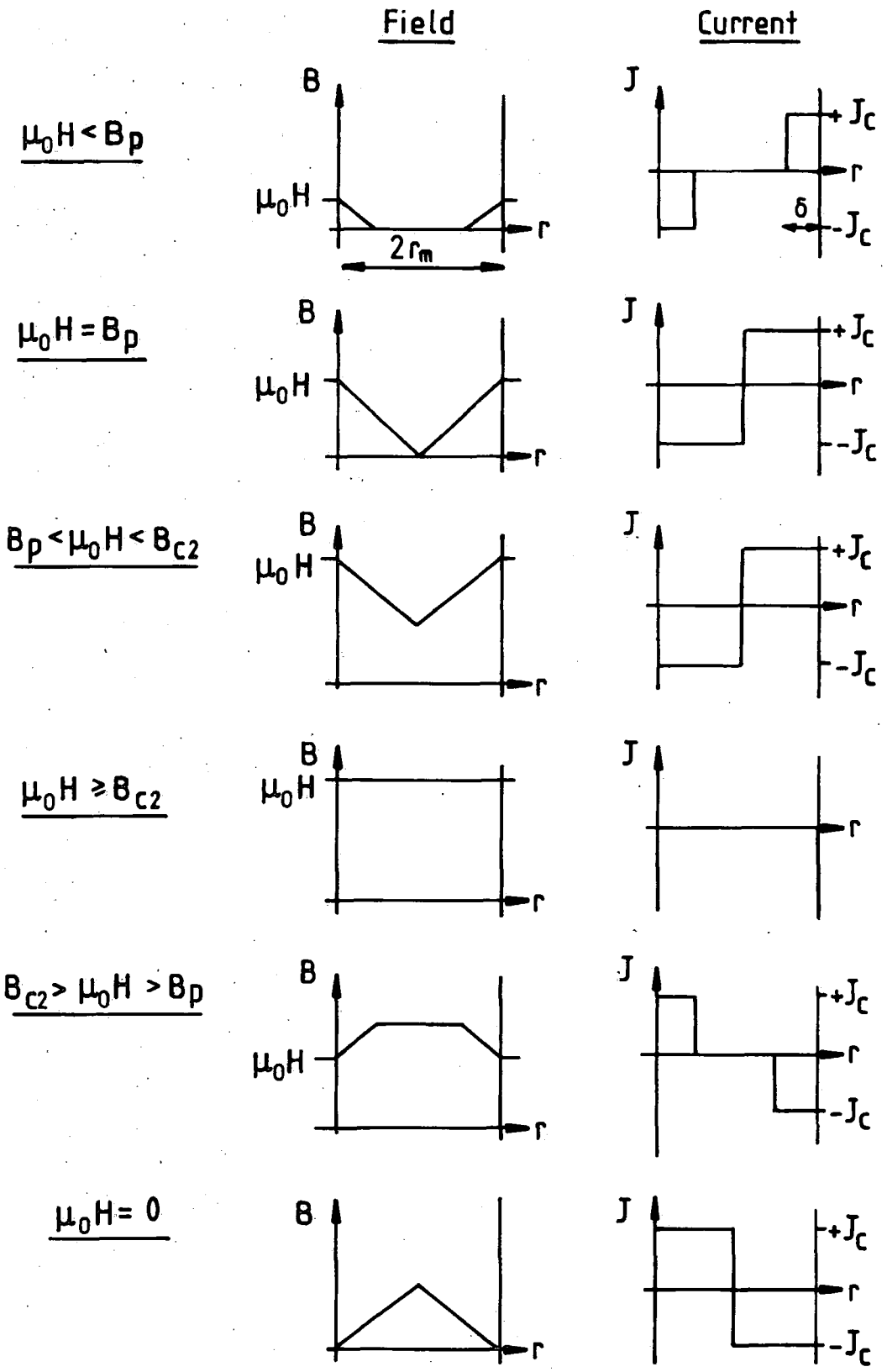

Figure 3.2 The magnetic field and critical current profiles inside a cylindrical superconducting sample after applying then removing a dc. magnetic field ($\mu_0 H$).

3.2.3 Bean's analysis.

Bean's original work derives expressions for the net internal field, b and the average magnetisation, M. This section outlines these calculations and presents the formalism required for the following chapter. The analysis has been completed for a superconducting sample of both a cylindrical and slab geometry, as shown in figure 3.3. The analysis is considered for low ac. fields, ie. those less than that required to fully penetrate the sample.

Figure 3.4 shows the possible magnetic field profiles which can arise on decreasing the field from its maximum value b_m. It is possible to write an expression for the magnetic field as a function of radius, ie. b(r). In Bean's model it is assumed that J_C does not change significantly over the field range b_m. In the flux penetration measurements described in this thesis, b_m is smaller (≈100 mT) than the much larger applied dc. field (≈10 T).

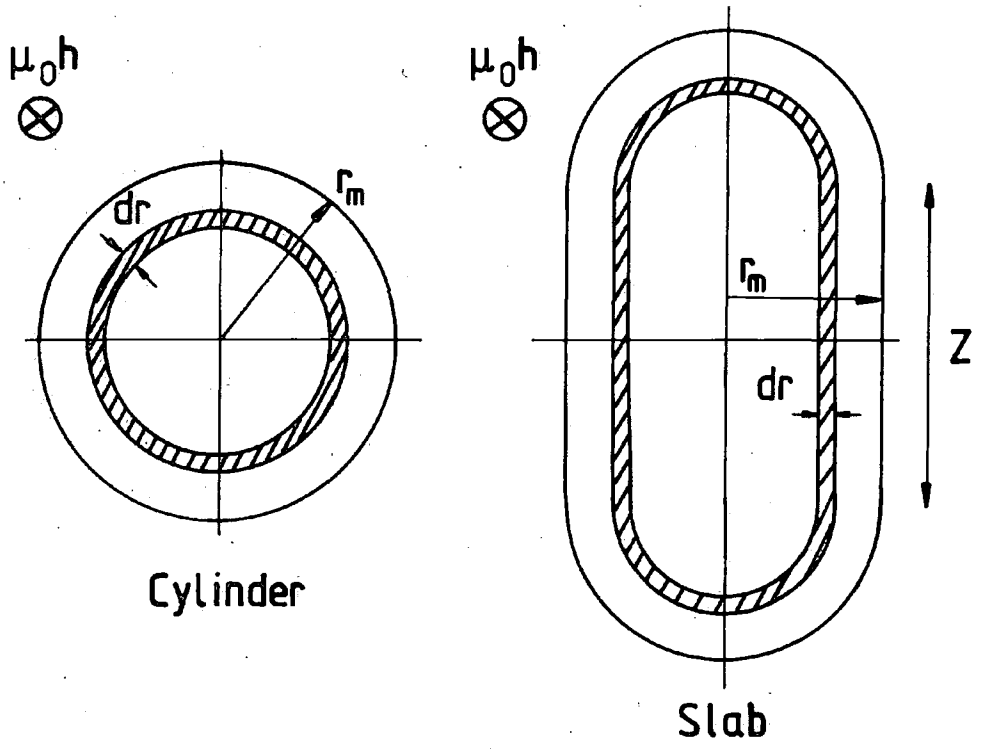

Figure 3.3 The analysis is performed for a superconducting sample of both a cylindrical and slab geometry. The shaded regions show the elemental current loops. For the slab $z >> r_m$, so end effects can be ignored. ($\mu_0 h$ is the applied ac. field.)

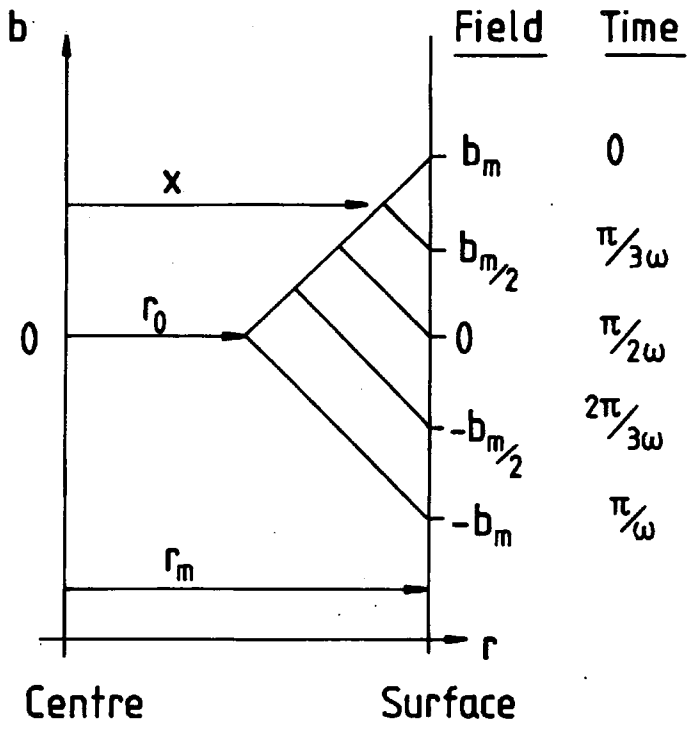

Figure 3.4 Possible magnetic field profiles inside a superconducting sample as a result of a low decreasing magnetic field.

From figure 3.4 it can be seen that,

$$0 \leq r < r_0 \qquad b(r) = 0 \tag{3.5}$$

$$r_0 \leq r < x \qquad b(r) = + b_m - \left|\frac{db}{dx}\right|(r_m - r) \tag{3.6}$$

$$x \leq r \leq r_m \qquad b(r) = + b + \left|\frac{db}{dx}\right|(r_m - r) \tag{3.7}$$

where,

$$x = r_m - \left(\frac{b_m - b}{2\mu_0 J_C}\right) \tag{3.8}$$

and,

$$r_0 = r_m - \left(\frac{b_m}{\mu_0 J_C}\right) \tag{3.9}$$

where b_m is the magnitude of the ac. field at t = 0.

From Bean's critical state model, the gradient of the magnetic field is equal to the critical current density,

$$\left|\frac{db}{dx}\right| = \mu_0 J_C \tag{3.10}$$

The total flux, ϕ_T, within the sample is obtained by integrating over the cross-sectional area of the sample, A.

$$\phi_T = \int_0^A d\phi \tag{3.11}$$

For the cylindrical sample of radius r_m lying parallel to the magnetic field, (axial b),

$$\phi_T = \int_0^{r_m} 2\pi r\, b(r)\, dr \tag{3.12}$$

and a slab of width z.

$$\phi_T = \int_0^{r_m} z\, b(r)\, dr \tag{3.13}$$

Given,

$$\mu_0 M = b - \mu_0 h = \frac{\phi_T}{A} - \mu_0 h \tag{3.14}$$

where A is the cross-sectional area of the sample and $\mu_0 h$ is the applied ac. field. Using equations 3.5-3.9 in equations 3.12 and 3.14, in a decreasing field applied parallel to the long axis of the sample, (axial b), for an infinite cylinder radius r_m.

$$\mu_0 M = -b + \frac{1}{2b_p}\left(b_m^2 + 2b.b_m - b^2\right) - \frac{1}{4b_p^2}\left(b_m^3 + b.b_m^2 - b^2.b_m + \frac{1}{3}b^3\right) \tag{3.15}$$

Similarly, using equations 3.5-3.9 in equations 3.13 and 3.14, for an infinite slab, thickness $2r_m$,

$$\mu_0 M = -b + \frac{1}{4b_p}\left(b_m^2 + 2b.b_m - b^2\right) \tag{3.16}$$

where b_m is the magnitude of the ac. field and b_p is the field required to fully penetrate the sample [11].

The case for an infinite cylinder, with the field applied perpendicular to the axis of the sample, (transverse b), has been solved analytically. Zenkevitch et al [12] have outlined the method which gives reasonable approximations for the magnetisation over the full field range. At low magnetic fields, the internal region gets screened by the induced

supercurrents which flow primarily in the peripheral portions of the superconducting cylinder. The sample is assumed to be in the critical state and the problem reduces to that of describing the position of the front boundary of the field penetration and hence the distribution of the screening currents over the cylinder cross-section. (A polar coordinate system is used.) The resulting differential equations can be solved analytically to obtain an expression for the local magnetic moment, from which the magnetisation can be calculated. For this geometry, the local value of the magnetic moment changes in the direction of the applied field and so it makes no sense to define a local value of M. In contrast, for a sample in an axial field, the net field along the axis of the cylinder is constant and the magnetisation can be considered as simply the difference between the internal and external fields [13]. Zenkevitch finds that for an infinite cylinder with the field applied perpendicular to the axis of the sample, (transverse b).

$$\mu_0 M = \frac{4 b_P}{3}\left(1 + \frac{(b_m - b - 2b_p)^3}{(2b_p)^3}\right) - \frac{2 b_P}{3}\left(1 + \frac{(b_m - b_p)^3}{b_p^3}\right) \qquad \textbf{(3.17)}$$

Expressions for ascending field are obtained by replacing M by -M and b by -b.

3.3 Extension for ac. fields.

3.3.1 Lock-in amplifiers.

In flux penetration measurements a lock-in amplifier (LIA) is used to measure the response of a superconducting sample to an applied ac. magnetic field. There are three main types :-

a. Analogue LIA (square wave reference).

Early analogue LIAs used a square wave as a reference signal. The polarity of the input signal is reversed in synchronism with the reference signal and the result is time averaged. The LIA performs a convolution of the input signal with the square wave reference. Thus the output will contain contributions not only from the reference frequency but also from higher order odd harmonics (which fall off in magnitude as 1/n,

cf. the Fourier components for a square wave). Such LIAs may have filters centred at the reference frequency to reduce the magnitude of these higher order harmonics.

b. Analogue LIA (sine wave reference).

The more modern analogue LIAs use a sine wave as the reference signal. Thus when the LIA performs a convolution with a sine wave input signal, the resulting output consists only of the fundamental Fourier component (1st harmonic) at the reference frequency. A drawback of these analogue LIAs is that they suffer from zero drift, output offsets and gain errors associated with the fact that the reference sine wave may vary in amplitude.

c. Digital LIA (sine wave reference).

Recently digital LIAs have been developed. These multiply the digitised input voltage (16 bit A/D at 256 kHz) with a digitally computerised sine wave reference. ie. Every 4 μs, the input signal is sampled and the result is multiplied by the reference sine wave. The reference sine wave is computed to 20 bits of accuracy and thus has very low harmonic content, (at the -120 dB level). Since only the signal at this single reference frequency is detected, a digital LIA is completely insensitive to signals at harmonics of the reference. Digital LIAs eliminate many problems associated with analogue LIAs.

3.3.2 Measurement technique.

Flux penetration measurements are made by superimposing an ac. field ($\mu_0 h$) onto a large dc. field ($\mu_0 H$), as shown in figure 3.5. The shading shows the region of flux motion. The technique involves using a primary coil to generate an ac. field and a set of oppositely wound secondary coils to measure the magnetisation of the sample. If the two secondary coils, 1 and 2, are of similar geometry but wound in opposite sense and the sample is placed in coil 1, the voltage across the secondary coils (V) can be related to the rate of change of flux ($d\phi/dt$).

$$V = -\frac{d\phi}{dt} \qquad \textbf{(3.18)}$$

For a cylindrical sample in an axial field (and a slab sample), $B=\mu_0(H+M)$ and so it is possible to write an expression relating the induced voltage to the magnetisation of the

sample.

$$V = -kL\frac{d}{dt}\left(\mu_0\int^2(H+h).dS - \mu_0\int^1(H+h+M).dS\right) \qquad \textbf{(3.19)}$$

where k is a constant determined by the coil geometry, L is the length of the sample, M is the induced magnetisation of the sample and S is a surface integral. This voltage is measured using a lock-in amplifier. (For a cylindrical sample in a transverse field, the change in symmetry means that the magnetisation can be calculated analytically by summing the contributions of the elementary current loops to find the total magnetic moment and then dividing by the volume [13].)

When the coils are balanced,

$$V = kLA\,\mu_0\frac{dM}{dt} \qquad \textbf{(3.20)}$$

where A is the cross-sectional area of the sample area of the sample. The sign convention used in chapters 3 and 4 ensures that when the lock-in amplifier is phased on the current in the primary coil, paramagnetic materials give a positive lossless voltage and superconducting materials a negative one.

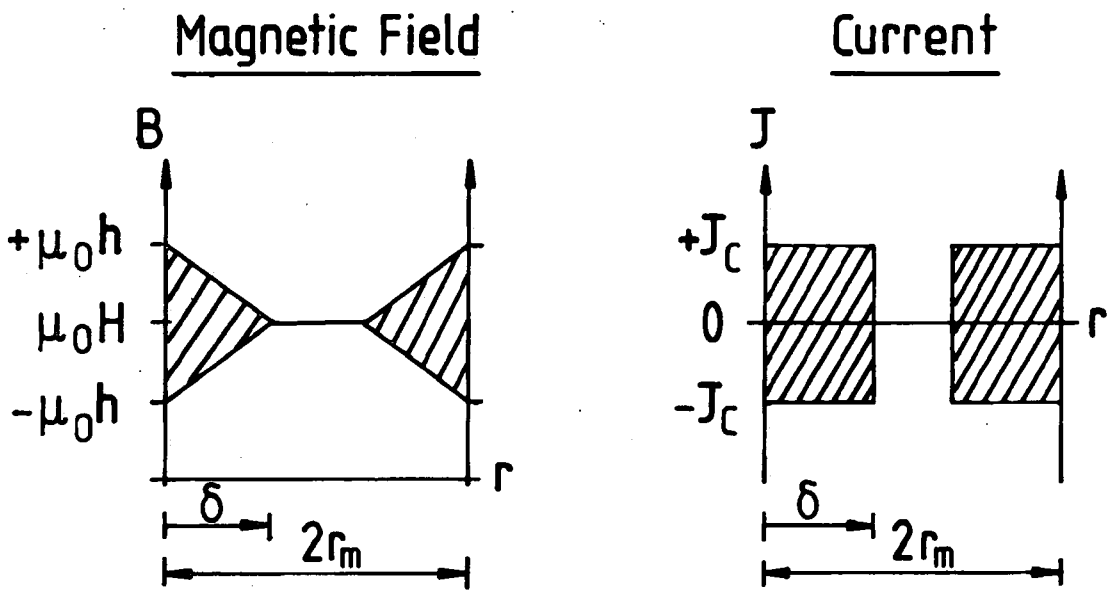

Figure 3.5 The response of a superconducting sample to an ac. field ($\mu_0 h$) superimposed onto a dc. field ($\mu_0 H$).

3.3.3 Ac. susceptibility.

Ac. susceptibility is widely used to characterise the basic properties of superconducting samples. Measurements are made with a coaxial, mutual inductance coil system consisting of a primary (excitation) coil and two oppositely wound secondary (pick-up) coils [14-18] . The sample is in one of the secondary coils. In ac. susceptibility measurements, components of the induced voltage both in-phase and out-of-phase with the ac. field, represent the loss and lossless components of the susceptibility, χ'' and χ'. Ac. susceptibility can be used to measure T_C [19-22] and B_{C1} [23]. It also gives information on phase purity [24-27] and granularity [28-34]. Most controversially, it has been used to experimentally determine the irreversibility line [35-39].

3.3.4 Bean - harmonic analysis.

Bean also considered the response of a superconductor to ac. magnetic fields, by measuring the voltage in a coil of wire surrounding the sample. Following his analysis for a cylinder in a two coil system, in the limit b << b_p, equation 3.16 becomes,

$$\mu_0 M = -b + \frac{1}{2b_p}\left(\pm b_m^2 + 2b.b_m \mp b^2 \right) \tag{3.21}$$

where the upper signs are for decreasing fields and the lower signs are for increasing fields. If the ac. field is of the form,

$$b = b_m \cos(\omega t) \tag{3.22}$$

then,

$$\mu_0 M = -b_m \cos(\omega t) + \left(\frac{b_m^2}{b_p} \right) \cos(\omega t) \pm \left(\frac{b_m^2}{b_p^2} \right) \left(1 - \cos^2(\omega t) \right) \tag{3.23}$$

This can be written as a Fourier series.

$$\mu_0 M = \sum_{n=1}^{\infty} \left(\alpha_n^* \sin(n\omega t) + \beta_n^* \cos(n\omega t) \right) \tag{3.24}$$

Using equation 3.20 and differentiating equation 3.24 gives,

$$V = K b_m \omega \sum_{n=1}^{\infty} \left(\alpha_n^* n \cos(n\omega t) - \beta_n^* n \sin(n\omega t) \right) \tag{3.25}$$

where K = kLA and the α_n^*'s and β_n^*'s are the loss and lossless components of the induced voltage.

He predicted that in very low fields ($b_m^3 \to 0$), the α_n^*'s, the odd harmonics are,

$$\alpha_n^* = -\left(\frac{1}{\pi}\right)\left(\frac{b_m}{b_p}\right)\left(\frac{2}{(n+2)(n-2)}\right) \tag{3.26}$$

and that all of the even harmonics are zero.

$$\alpha_n^* = 0 \tag{3.27}$$

Equation 3.26 differs from Bean's original work by a factor of 2. (This has also been found by Ji et al [40].) For the β_n^*'s, the first harmonic is,

$$\beta_1^* = 1 - \frac{b_m}{b_p} \tag{3.28}$$

and all others are zero.

$$\beta_n = 0 \tag{3.29}$$

From this harmonic analysis, the minimum of the first harmonic voltage across the secondary coils (V_{min}), which occurs approximately when the field fully penetrates the sample, can be related to the critical current (J_C) density by,

$$V_{min} = -cKb_p\omega J_C \tag{3.30}$$

where $c \approx 1$ due to the fact that V_{min} does not occur at b_p, (see chapter 4). In high ac. fields, good agreement is found with J_C values obtained from transport data [41-43]. In low dc. fields, where J_C is a strong function of field, Bean's harmonic analysis which assumes a field independent J_C, breaks down. Anderson and Kim [44,45] suggested a field dependent J_C of the form,

$$J_C = \frac{A_0}{B_0 + b} \tag{3.31}$$

where A_0 and B_0 are constants. Calculations of the harmonic signal as a function of dc. field have been completed by Müller et al [46,47] and Ji et al [40]. Complementary measurements of ac. susceptibility, which give harmonics as a function of temperature, confirm non-zero even harmonics when the critical current density is a strong function of field. These results have also been demonstrated by other authors [48-51].

3.4 Magnetic field profiles.

3.4.1 Campbell's analysis.

Using the critical state model, Campbell considered the magnetic response of a superconductor to an ac. field superimposed on a dc. field and demonstrated that it can be used to measure the magnetic field profile within the sample [52]. Campbell showed that in low ac. fields, it is possible to calculate the depth to which the field has penetrated from the differential of the total voltage (V) across the secondary coils with respect to the field (b_m) through the primary coils (dV/db_m). (Assuming that $J_C(B)$ is constant over the amplitude of the ac. field and that the critical state is cylindrically symmetric in a cylindrical sample.) He considered the total flux within the sample. If the amplitude of the ac. field is increased by db_m, the extra flux which enters the sample is given by

$$d\phi = [\pi r_m^2 - \pi(r_m - \delta)^2]\, db_m \tag{3.32}$$

where r_m is the radius of the sample and δ is the depth to which the field penetrates. Thus,

$$\frac{d\phi}{db_m} = \pi\delta(2r_m - \delta) \tag{3.33}$$

The lossless voltage can be related to the total flux within the sample by,

$$V = 2k\phi \tag{3.34}$$

where k is a constant determined by the sample geometry. Differentiating with respect to the applied field gives,

$$\frac{dV}{db_m} = 2k\frac{d\phi}{db_m} \tag{3.35}$$

When the sample is fully penetrated, $\delta = r_m$, $b_m = b_p$ and $V = V_{min}$. Integrating equation 3.35 gives,

$$V_{min} = 2kr_m^2 b_p \tag{3.36}$$

Therefore, the minimum voltage across the secondary coils per unit ac. field is,

$$(V_{min}/b_p) = 2kr_m^2 \tag{3.37}$$

Using equation 3.33 and 3.37, rearranging and solving for small δ gives,

$$\delta = \frac{r_m}{2(V_{\min}/b_p)}\left(\frac{dV}{db_m}\right) \tag{3.38}$$

The depth to which the field has penetrated, δ, can now be calculated from the gradient of a graph of V against b_m. Thus at small amplitudes, a graph of b_m versus δ is a direct plot of the flux profile within the sample.

3.4.2 Harmonic analysis.

Campbell's technique considers the total voltage (ie. all harmonics) across the secondary coils. In contrast, the flux profiles in this thesis are calculated from the lossless component of the 1st harmonic, (measured using a digital LIA). From the coefficient of the first harmonic for a cylinder with axial b, (equation 3.28),

$$V = -Kb_m\omega\left(1 - \frac{b_m}{b_p}\right) \tag{3.39}$$

when differentiated with respect to the applied field this becomes,

$$\frac{dV}{db_m} = -K\omega\left(1 - \frac{2\delta}{r_m}\right) \tag{3.40}$$

where from figure 3.5, $\delta = b_m/\mu_0 J_C$ and $r_m = b_p/\mu_0 J_C$.
Thus, the depth to which the field penetrates is,

$$\delta = \frac{r_m}{2}\left(1 + \left(\frac{1}{K\omega}\right)\left(\frac{dV}{db_m}\right)\right) \tag{3.41}$$

This can be written as,

$$\delta = \frac{r_m}{2}\left(1 - \frac{|dV/db_m|}{|dV/db_m|_{MAX}}\right) \tag{3.42}$$

where $|dV/db_m|_{MAX}$ is the value of $|dV/db_m|$ at $\delta=0$. r_m is calculated using $|dV/db_m|_{MAX} = K\omega$, $K = kLA$ and $A = \pi r_m^2$, ie,

$$r_m = \left(\frac{1}{\pi k L \omega}\left|\frac{dV}{db_m}\right|_{MAX}\right)^{\frac{1}{2}} \tag{3.43}$$

Equations of the form of 3.42 have been used by many authors to plot flux profiles [53-57].

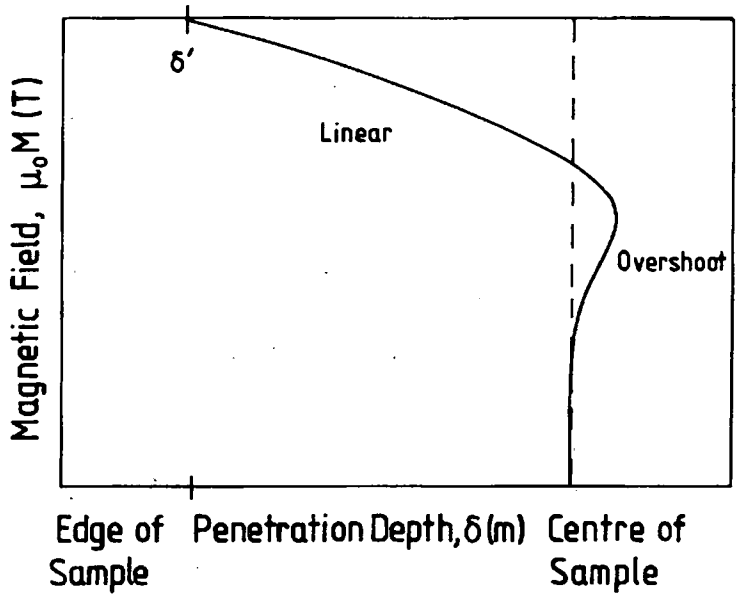

Figure 3.6 A graph to show a typical flux profile highlighting the important features.

A typical flux profile is shown in figure 3.6. There are three main features:-

i. A large apparent penetration of the sample at very small applied field, [58,59]. This is attributed to the motion of flux bundles inside pinning wells [13,60]. Analysis through force-displacement curves allows the nature of the pinning and the interaction distance between flux lines and pinning centres to be studied [61].

ii. A linear range which indicates a region of constant J_C, generally the bulk of the sample. Using Maxwell's equations, the spatial variation of J_C is given by,

$$J_C(\delta) = \left| \frac{dM(\delta)}{d\delta} \right| \qquad \textbf{(3.44)}$$

Küpfer has used this approach to determine both inter and intragranular J_C [62].

iii. A region of overshoot at the highest penetration depth values which suggests a non-physical result, ie. penetration into the sample decreasing with increasing ac. field. A number of authors [62-64] have suggested that this overshoot is the result of a strong field dependence of J_C, which at low fields can be attributed to sample granularity. However measurements in this thesis show an overshoot for very high dc. fields which are not explained by granularity or a field dependent J_C. The next chapter addresses the origin of the overshoot in detail.

3.5 Alternative techniques.

Flux profile measurements enable the determination of the spatial distribution of the critical current density and thus are crucial for understanding the pinning mechanisms involved in superconducting materials. These measurements are direct and very local, in contrast to more traditional methods such as muon spin rotation (μSR) [65-69] or small angle neutron diffraction (SAND) [70-75]. These evaluate the average field distribution using assumptions of a vortex lattice and a homogeneous sample. Various techniques have been developed.

3.5.1 Decoration experiments.

These experiments use small ferromagnetic particles which "decorate" regions on the surface of the superconductor where there is a magnetic field [76-78]. The particles must be much smaller than the vortex size (ie. 5-10 nm) and have low kinetic energy. These requirements are met by evaporating a ferromagnetic material (Fe, Ni or Co) close to the sample. The resultant "Bitter" pattern produced at the surface gives a picture of the vortex structure at the time of decoration. Unfortunately, this technique is restricted to low fields, $B<B_{C1}$, so that the magnetic field of neighbouring vortices do not overlap. Decoration experiments only give an image of the FLL as it leaves the sample.

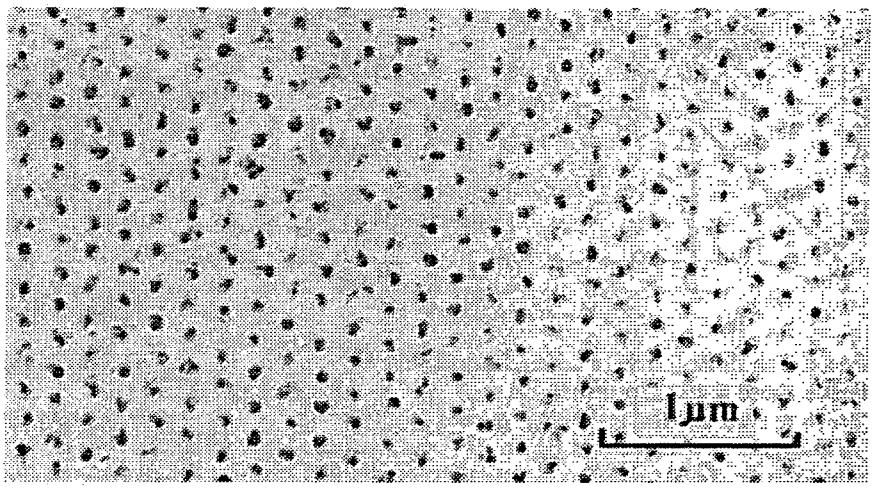

Figure 3.7 A Bitter pattern showing the hexagonal flux line lattice structure of the mixed state in a type II superconductor.

3.5.2 Hall probe investigations.

There are two possible configurations, stationary or scanning. A stationary Hall probe measures the local magnetic field at the surface of the sample and is used to record the magnetization as a function of field and temperature [79-83]. Typically the Hall sensor is 100 μm^2 in size. A scanning Hall probe allows detailed spatial resolution of critical state profiles to be measured [84-89]. The smallest probes have an active area of <1 μm^2 and scan a region of approximately 1 mm^2. As with decoration experiments, both stationary and scanning Hall probes are only able to measure the magnetic field at the surface of a sample. Direct measurements of the field inside a superconductor can be made by moving a Hall probe in a thin slot in the material [90-92]. However, this is not an accurate measurement due to the size of the probe and distortions caused by the slot. Figure 3.8 shows the field profile across a sample for various external fields.

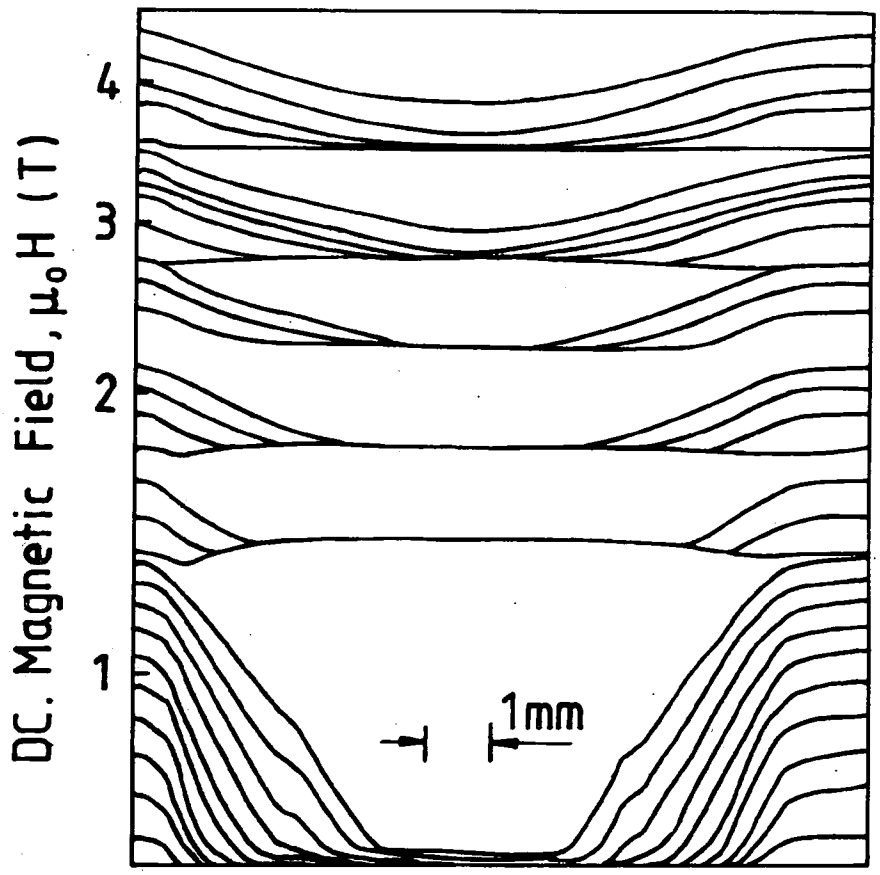

Figure 3.8 The field distribution in a NbTi sample in increasing field as measured by driving a Hall probe through a fine gap in the sample [90].

3.5.3 Magneto-optical imaging.

Magneto-optical techniques [93-100] offer the unique possibility to observe dynamic flux motion with a relatively high resolution. All magneto-optical techniques for flux visualisation are based on the Faraday effect [101]. This states that a magneto-optically active material, such as EuSe [102], will rotate linearly polarised light through an angle, θ_R, proportional to the local magnetic field. ie $\theta_R = V_T t H$. Where t is the thickness and V_T is the Verdet constant of the magneto-optically active material. The magnetic field distribution is imaged by detecting the rotation of the polarisation plane of linearly polarised light within a magneto-optically active layer which is placed immediately above the superconductor. The best spatial resolution of this technique is $\approx$ 0.5 μm, intermediate between the decoration technique and Hall probe measurements. However the technique is limited to low temperatures (< 20 K) as the Verdet constant decreases dramatically with increasing temperature.

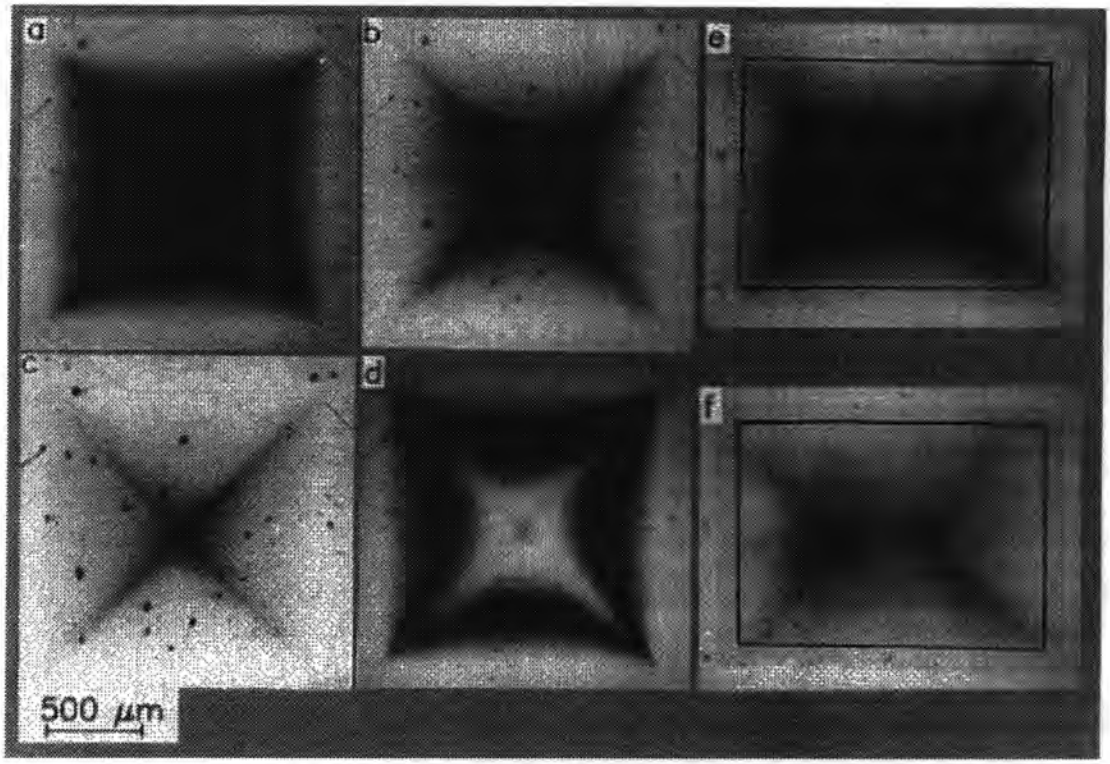

Figure 3.9 The magnetic field distribution in YBCO-123 visualised by a magneto-optical technique [103].

3.5.4 Scanning tunnelling microscopy (STM).

Using scanning tunnelling microscopy (STM) it is also possible to image the FLL [104,105]. The vortices are imaged by tunnelling with a tip-sample bias voltage set just above the energy gap, (≈1.1 meV) and recording the differential conductance on the surface. STM can also be used as a local spectroscopic tool to observe the variation in the density of states both in and around a single flux line. (The differential conductance is directly proportional to the density of states.) With STM it is possible to study a sample over the whole range of magnetic fields. However, scans are limited to a region 5 μm^2, take 1 hour to complete and are only able to image the FLL at the surface of the sample.

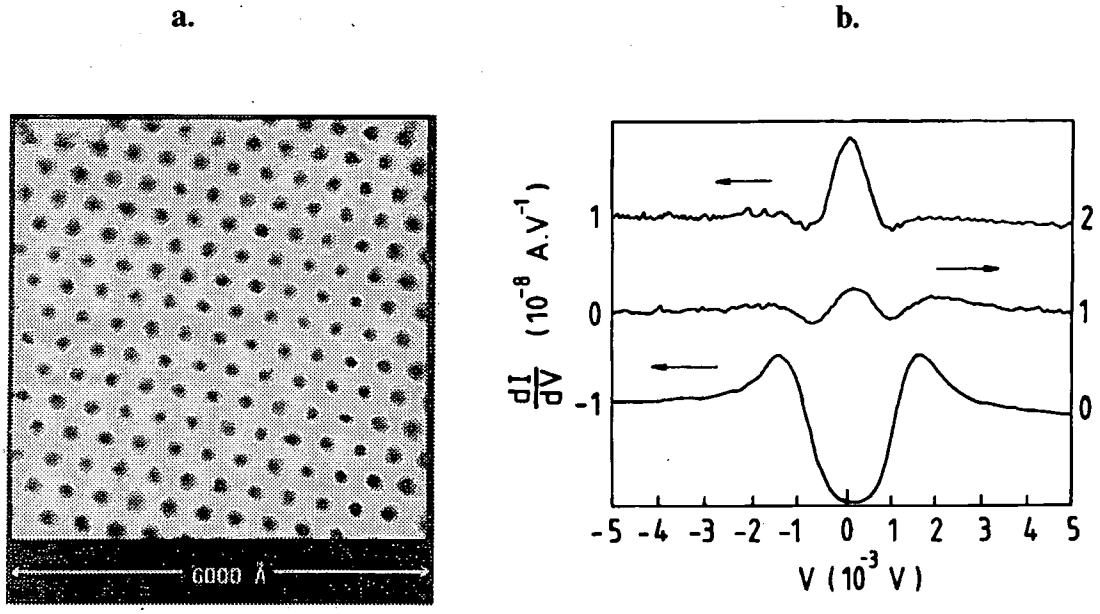

Figure 3.10 a. An STM image of the FLL.

b. The differential conductance on a vortex, 7.5 nm from a vortex and 200 nm from a vortex.

References.

[1] Abrikosov A A *Sov. Phys. JETP* **5** 1174 (1957).

[2] Evetts J E, Campbell A M and Dew-Hughes D *J. Phys. C* **1** 715 (1968).

[3] Fietz W A and Webb W W *Phys. Rev.* **178** 657 (1969).

[4] Kramer E J *J. Appl. Phys.* **44** (3) 1360 (1973).

[5] Hampshire R G and Taylor M T *J. Phys. F* **2** 89 (1972).

[6] Freyhardt H C *IEEE Trans. on Mag.* **MAG-19** (3) 545 (1983).

[7] Dew-Hughes D *Philos. Mag.* **30** 293 (1974).

[8] Bean C P *Rev. Mod. Phys.* **36** 31 (1964).

[9] Johansen T H and Bratsberg H *J. Appl. Phys.* **76** (12) 8001 (1994).

[10] Johansen T H and Bratsberg H *J. Appl. Phys.* **77** (8) 3945 (1995).

[11] Goldfarb R B, Lelental M and Thompson C A *Magnetic Susceptibility of Superconductors and other Spin Systems* ed. Hein R A et al 49 (Plenum Press, New York) (1992).

[12] Zenkevitch V B, Romanyuk A S and Zheltov V V *Cryogenics* 20 703 (1980).

[13] Campbell A M *Magnetic Susceptibility of Superconductors and other Spin Systems* ed. Hein R A et al 129 (Plenum Press, New York) (1992).

[14] Maxwell E *Rev. Sci. Instrum.* **36** 553 (1965).

[15] Whitmore S C, Ryan S R and Sanders T M *Rev. Sci. Instrum.* **49** (11) 1579 (1978).

[16] Owers-Bradley J R, Zhou W S and Halperin W P *Rev. Sci. Instrum.* **52** (7) 1106 (1981).

[17] Deutz A F, Hulstman R and Kranenburg F J *Rev. Sci. Instrum.* **60** (1) 113 (1989)

[18] Fabbricatore P, Farinon S, Gemme G, Musenich R, Parodi R and Zhang B *Cryogenics* **33** (12) 1170 (1993).

[19] Larbalestier D C, Daeumling M ,Cai X, Seuntjens J, McKinnell J, Hampshire D, Lee P, Meingast C, Willis T, Muller H, Ray R D, Dillenburg R G, Hellstrom E E and Joynt R *J. Appl. Phys.* **62** (8) 3308 (1987).

[20] Li Y Q, Noh D and Gallois B *J. Appl. Phys.* **68** (7) 3775 (1990).

[21] Bonney L A, Willis T C and Larbalestier D C *IEEE Trans. on Appl. Supercond.* **3** (1) 1582 (1993).

[22] Karkut M G, Heill L K, Vinokur V M, Slaski M, Sagdahl L T, Tuset E D and

Fossheil K *Cryogenics* **33** (1) 60 (1993).

[23] Loughran R J and Goldfarb R B *Physica C* **181** 138 (1991).

[24] Mazaki H, Takano M, Kanno R and Takeda Y *Jap. J. of Appl. Phys.* **26** (5) L780 (1987).

[25] Goldfarb R B, Clark A F, Braginski A I and Panson A J *Cryogenics* **27** 475 (1987).

[26] Ishida T and Mazaki H Jap. *J. of Appl. Phys.* **26** (8) L1296 (1987).

[27] Couach M, Khoder A F, Monnier F, Sergent M, Chevrel R, Le Lay L and Dubots P *Physica C* **153-155** 463 (1988).

[28] Hautanen K E, Oussena M and Cave J R *Cryogenics* **33** (3) 329 (1993).

[29] Dhingra I and Das B K *Supercond. Sci. Technol.* **6** 765 (1993).

[30] Flippen R B, Askew T R and Osofsky M S *Physica C* **201** 391 (1992).

[31] Pena O, Perrin C and Sergent M *Supercond. Sci. Technol.* **6** 183 (1993).

[32] Suryanarayanan R, Paulus W, Rao M S R, Gorochov O, Ouhammou L and Heger G *Supercond. Sci. Technol.* **5** 82 (1992).

[33] Mazaki H, Takano M, Takada J, Oda K, Kitaguchi H, Miura Y, Ikeda Y, Tomii Y and Kubozoe T *Jap. J. of Appl. Phys.* **27** (9) L1639 (1988).

[34] Gomis V, Catalán I, Pérez F, Martinez B, Fontcuberta J, Fuertes A and Obradors X *Cryogenics* **33** (1) 39 (1993).

[35] Gömöry F and Takács S *Physica C* **217** 297 (1993).

[36] Suryanarayanan R, Leelaprute S and Niarchos D *Physica C* **214** 277 (1993).

[37] Takács S and Gömöry F *Cryogenics* **33** (1) 133 (1993).

[38] Loegel B, Mehdaoui A, Bolmont D, Danesi P, Bourgault D and Tournier R *Physica C* **210** 432 (1993).

[39] Frischherz M C, Sauerzopf F M, Weber H W, Murakami M and Emel'chenko G A *Supercond. Sci. Technol.* **8** 485 (1995).

[40] Ji L, Sohn R H, Spalding G C, Lobb C J and Tinkham M *Phys. Rev. B* **40** (16) 10936 (1989).

[41] Hampshire D P and Larbalestier D C *IEEE Trans. on Mag.* **25** (2) 1956 (1989).

[42] Hampshire D P and Larbalestier D C *IEEE Trans. on Mag.* **25** (2) 2382 (1989).

[43] Ramsbottom H D and Hampshire D P *Inst. Phys. Conf. Series No* **148** *EUCAS'95* 259 (1995).

[44] Kim Y B, Hempstead C F and Strnad A R *Phys. Rev.* **129** (2) 528 (1963).

[45] Anderson P W and Kim Y B *Rev. Mod. Phys.* **36** 39 (1964)

[46] Müller K H, MacFarlane J C and Driver R *Physica C* **158** 366 (1989).

[47] Müller K H *Physica C* **159** 717 (1989).

[48] Ishida T and Goldfarb R B *Phys. Rev. B* **41** (13) 8937 (1990).

[49] Lam Q H, Kim Y and Jeffries C D *Phys. Rev. B* **42** (7) 4846 (1990).

[50] Müller K H, MacFarlane J C and Driver R *Physica C* **158** 69 (1989).

[51] Luzyanin I D, Ginzburg S L, Khavronin V P and Logvinova G Y *Phys. Lett A* **141** (1,2) 85 (1989).

[52] Campbell A M *J. Phys. C* **2** 1492 (1969).

[53] Dang A, Godelaine P A and Ausloos M *Cryogenics* **34** ICEC Suppl. 829 (1994).

[54] Godelaine P A and Ausloos M *Solid State Comms.* **73** (11) 759 (1990).

[55] Godelaine P A and Ausloos M *Solid State Comms.* **76** (6) 785 (1990).

[56] Daeumling M, Seuntjens J and Larbalestier D C *Appl. Phys. Lett.* **52** (7) 590 (1988).

[57] Kawamura H, Figiyoshi T and Miyahara K *Supercond. Sci Technol.* **8** 806 (1995).

[58] Kresse R, Küpfer H, Meier-Hirmer R, Matsushita T and Kimura K *Applied Superconductivity Vol. 1 Proc. European Conf. on Appl. Supercond.* 337 (1993).

[59] Ni B, Munakata T, Matsushita T, Iwakuma M, Funaki K, Takeo M and Yamafuji K *Jap. J. of Appl. Phys.* **27** (9) 1658 (1988).

[60] Campbell A M *Cryogenics* **30** (S) 809 (1990).

[61] Campbell A M *J. Phys. C* **4** 3186 (1971).

[62] Küpfer H, Apfelstedt I, Flükiger R, Keller C, Meier-Hirmer R, Runtsch B, Turowski A, Wiech U and Wolf T *Cryogenics* **28** 650 (1988).

[63] Campbell A M and Blunt F J *Physica C* **172** (3-4) 253 (1990).

[64] Gömöry F, Takács S, Lobotka P, Frölich K and Plecháček V *Physica C* **160** 1 (1989).

[65] Uemura Y J *J. Appl. Phys.* **64** (10) 6087 (1988).

[66] Uemura Y J, Le L P, Luke G M, Sternlieb B J, Brewer J H, Kadono R, Kiefl R F, Kreitzman S R and Riseman T M *Physica C* **162-164** 857 (1989).

[67] Uemura Y J, Keren A, Le L P, Luke G M, Sternlieb B J, Wu W D, Brewer J H, Wetten R L, Huang S M, Lin S, Kaner R B, Diederich F, Donovan S, Grüner G and Holczer K *Nature* **352** 605 (1991).

[68] Aeppli G and Harshman D R *High Temperature Superconductivity* ed. Ashkenazi J et al 621 (Plenum Press, New York) (1991).

[69] Lee S L, Zimmermann P, Keller H, Warden M, Savić I M, Schauweker R, Zech D, Cubitt R, Forgan E M, Kes P H, Li T W, Menovsky A A and Tarnawski Z *Phys. Rev. Lett.* **71** (23) 3862 (1993).

[70] Christen D K, Kerchner H R, Sekula S T and Thorel P *Phys. Rev. B* **21** (1) 102 (1980).

[71] Forgan E M, Paul D M, Mook H A, Timmins P A, Keller H, Sutton S and Abell J S *Nature* **343** 735 (1990).

[72] Forgan E M *Physica B* **169** 107 (1991).

[73] Bishop D J *Nature* **365** 394 (1993).

[74] Cubitt R, Forgan E M, Yang G, Lee S L, Paul D M, Mook H A, Yethiraj M, Kes P H, Li T W, Menovsky A A, Tarnawski Z and Mortensen K *Nature* **365** 407 (1993).

[75] Gammel P L, Huse D A, Kleinman R N, Batlogg B, Oglesby C S, Bucher E, Bishop D J, Mason T E and Mortensen K *Phys. Rev. Lett.* **72** (2) 278 (1994).

[76] Grigorieva I V *Supercond. Sci. Tech.* **7** 161 (1994).

[77] Bishop D J, Gammel P L, Murray C A, Mitzi D B and Kapitulnik A *Physica B* **169** 72 (1991).

[78] Bishop D J *Nature* **371** 746 (1994).

[79] Konczykowski M, Holtzberg F and Lejay P *Supercond. Sci. Tech.* **4** S331 (1991).

[80] Zhang J, Sheldon P and Ahrenkiel R K *Rev. Sci. Instrum.* **63** (4) 2259 (1992).

[81] Koziol Z, Tarnawski Z and Franse J J M *Solid State Comms.* **85** (12) 991 (1993).

[82] Brawner D A, Schilling A, Ott H R, Haung R J, Ploog K and von Klitzing K *Phys. Rev. Lett.* **71** (5) 785 (1993).

[83] Konczykowski M, Wolfus Y, Yeshurun Y and Holtzberg F *Physica A* **200** 305 (1993).

[84] Brawner D A and Ong N P *J. Appl Phys.* **73** (8) 3890 (1993).

[85] Chang A M, Hallen H D, Hess H F, Kao H L, Kwo J, Sudbø A and Chang T Y *Europhys. Lett.* **20** (7) 6456 (1992).

[86] Xing W, Heinrich B, Zhou H, Fife A A and Crag A R *J. Appl. Phys.* **76** (7) 4244 (1994).

[87] Johnson M D, Everett J, Dhallé M, Grasso G, Flükiger R, Yang M, Grovenor

C R M and Caplin A D *Inst. of Phys. Conf. Series No.* **148** *EUCAS'95* 415 (1995).

[**88**] Mohamed M A K and Jung J *Phys. Rev. B* **44** (9) 4512 (1991).

[**89**] Paasi, J Polá M, Lahtinen M, Plecháček V and Söderlund L *Cryogenics* **32** (11) 1076 (1992).

[**90**] Coffey H T *Cryogenics* **7** 73 (1967).

[**91**] Voigt H *Z. Phys.* **213** 119 (1968).

[**92**] Sikora A, Makiej B and Trojnar E *Phys. Lett.* **27A** (3) 175 (1968).

[**93**] Koblischka M R and Wijngaarden R J *Supercond. Sci. Tech.* **8** 199 (1995).

[**94**] Koblischka M R *Inst. Phys. Conf. Series No* **148** *EUCAS'95* 579 (1995).

[**95**] Allers P B *Phys. Rev.* **105** (1) 104 (1957).

[**96**] DeSorbo W *Phys. Rev. Lett.* **4** (8) 406 (1960).

[**97**] Kirchner H *Phys. Lett.* **30A** (8) 437 (1969).

[**98**] Huebener R P, Kampwirth R T and Clem J R *J. Low T. Phys.* **6** (3/4) 275 (1972).

[**99**] Theuss H, Forkl A and Kronmüller H *Physica C* **190** 345 (1992).

[**100**] Yokoyama Y, Suzuki Y, Hasami Y, Obara H, Yosimi T, Kita Y, Kosaka S and Yoshida S *Jap. J. of Appl. Phys.* **30** (11A) L1864 (1991).

[**101**] Faraday M *Philos. Trans.* **136** 1 (1846).

[**102**] Schuster T, Koblischa M R, Ludescher B, Moser N and Kronmüller H *Cryogenics* **31** 811 (1991).

[**103**] Brandt E H *Preprint : Reports on Progress in Physics* (1995).

[**104**] Hess H F, Robinson R B, Dynes R C, Valles Jr. J M and Waszczak J V *Phys. Rev. Lett.* **62** (2) 214 (1989).

[**105**] Hess H F, Murray C A, Waszczak J V *Phys. Rev. Lett.* **69** (14) 2138 (1992).

Chapter 4

The Harmonic Response of a Superconductor to Low Frequency, High Amplitude AC Fields.

4.1 Introduction.

Flux penetration measurements provide a unique opportunity to study the spatial variation of J_C. Unfortunately the approach remains controversial in many aspects of data interpretation [1]. To infer sample properties such as granularity, spatial variation of J_C and possible pinning mechanisms it is important to fully understand the analysis.

In this chapter, the response of a superconducting sample to low frequency, high amplitude ac. fields is calculated. Section 4.2 contains the solution for low ac. fields, ie. for fields less than those required to fully penetrate the sample. Bean's original work is extended to other geometries. A Fourier analysis is then used to generate the harmonic response of both the loss and lossless components. This is evaluated for the first 10 harmonics, ie. from 1F to 10F.

Section 4.3 contains the solution for large ac. fields, ie. for fields greater than those required to fully penetrate the sample. The solution is given for both a cylindrical and slab geometry and the results plotted graphically. In section 4.4 there is a discussion of the analysis. The chapter concludes with a summary of the most important findings.

4.2 Low ac. fields.

4.2.1 Calculating the voltage waveform.

The analysis is considered for ac. fields less than those required to fully penetrate the sample. Figure 4.1 shows the magnetic field profiles which can arise [2]. Following the formalism outlined in chapter 3, it is possible to write expressions for the magnetic field as a function of radius, ie. b(r).

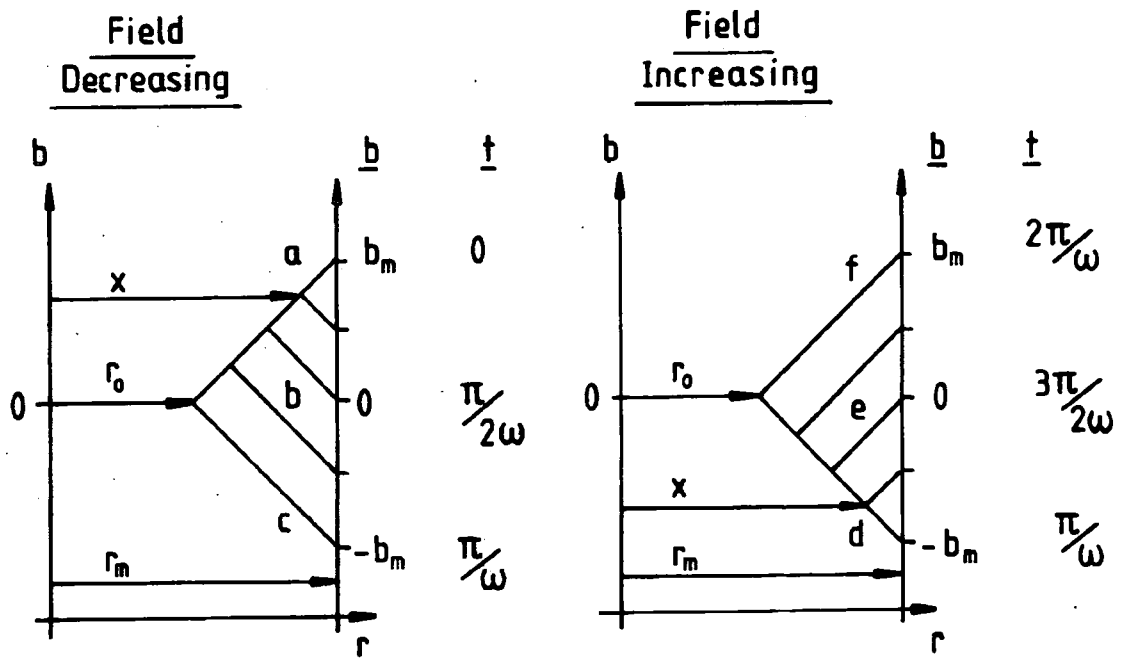

Figure 4.1 Possible magnetic field profiles inside a superconducting sample as a result of a low ac. field. (a,b,c-field decreasing, d,e,f-field increasing)

The flux profiles can be considered in two parts. In section I (a-c), the field decreases from its maximum value, b_m and t=0 until the profile is fully reversed, at b=-b_m and t=π/ω. In section II (d-f), the field increases from its minimum value until the the original profile is returned, at b=+b_m and t=$2\pi/\omega$.

Section I $0 \le t < \pi/\omega$

$$r_0 \le r < x \qquad b(r) = + b_m - \left|\frac{db}{dx}\right|(r_m - r) \tag{4.1}$$

$$x \le r \le r_m \qquad b(r) = + b + \left|\frac{db}{dx}\right|(r_m - r) \tag{4.2}$$

Section II $\pi/\omega \le t < 2\pi/\omega$

$$r_0 \le r < x \qquad b(r) = - b_m + \left|\frac{db}{dx}\right|(r_m - r) \tag{4.3}$$

$$x \le r \le r_m \qquad b(r) = + b - \left|\frac{db}{dx}\right|(r_m - r) \tag{4.4}$$

The total flux, ϕ_T, within the sample is obtained by integrating over the cross-sectional area of the sample, A.

$$\phi_T = \int_0^A d\phi \tag{4.5}$$

For a cylinder of radius r_m lying parallel to the magnetic field (axial b) then,

$$\phi_T = \int_0^{r_m} 2\pi r b(r)\, dr \tag{4.6}$$

The magnetisation of the sample is measured using a set of two secondary coils, coils 1 and 2. If these are of similar geometry, wound in opposite sense and the sample is placed in coil 1, then the voltage induced across both coils (V), is proportional to the rate of change of flux in the sample.

$$V = - kL \frac{d\phi_T}{dt} \tag{4.7}$$

Where k is a constant determined by the coil geometry and L is the length of the sample. Using the chain rule,

$$V = - kL \frac{d\phi_T}{dx} \cdot \frac{dx}{dt} \tag{4.8}$$

From figure 4.1 it can be seen that,

$$x = r_m - \left(\frac{b_m \pm b}{2\mu_0 J_C} \right) \tag{4.9}$$

where the ± is for increasing/decreasing field. Combining equations 4.8 and 4.9 gives,

$$V = - \frac{kL}{2\mu_0 J_C} \cdot \frac{d\phi_T}{dx} \cdot \frac{db}{dt} \tag{4.10}$$

In the coil which contains the superconducting sample,

$$b(r) = b_m \cos(\omega t) \tag{4.11}$$

and without the superconducting sample.

$$b(r) = b_m \tag{4.12}$$

It is now possible to calculate individually the voltage induced across both coils from the magnetisation of the sample in response to both sections of the ac. magnetic field.

The voltage in coil 1, (with the superconducting sample) is,

$$V_1 = kL(\pi r_m^2) b_m \omega \begin{bmatrix} + \left(\frac{b_m}{b_p} - \frac{5b_m^2}{16 b_p^2}\right).\sin(\omega t) \\ \mp \left(\frac{b_m}{2 b_p} - \frac{b_m^2}{4 b_p^2}\right).\sin(2\omega t) \\ + \left(-\frac{b_m^2}{16 b_p^2}\right).\sin(3\omega t) \end{bmatrix} \quad \textbf{(4.13)}$$

where from figure 4.1, $b_p=\mu_0 J_C r_m$ and $\mp$ is for decreasing/increasing field. The prefactor ensures that subsequent terms are dimensionless and so can be considered as a differential susceptibility.

The voltage in coil 2, (without the superconducting sample) is,

$$V_2 = kL(\pi r_m^2) b_m \omega .\sin(\omega t) \quad \textbf{(4.14)}$$

for both increasing and decreasing field.

Following equation 3.19, the total voltage induced across both secondary coils is,

$$V = V_2 - V_1 \quad \textbf{(4.15)}$$

So the total waveform is,

$$V(t) = K b_m \omega \begin{bmatrix} [c_1.\sin(\omega t) + c_2.\sin(2\omega t) + c_3.\sin(3\omega t)]_0^{\pi/\omega} + \\ [c_1.\sin(\omega t) - c_2.\sin(2\omega t) + c_3.\sin(3\omega t)]_{\pi/\omega}^{2\pi/\omega} \end{bmatrix} \quad \textbf{(4.16)}$$

where,

$$K = kL(\pi r_m^2)$$

$$c_1 = \left(1 - \frac{b_m}{b_p} + \frac{5b_m^2}{16b_p^2}\right)$$

$$c_2 = \left(\frac{b_m}{2b_p} - \frac{b_m^2}{4b_p^2}\right) \qquad \textbf{(4.17)}$$

$$c_3 = \left(\frac{b_m^2}{16b_p^2}\right)$$

$$b_P = \mu_0 J_C r_m$$

Alternatively, the values of $c_{1,2,3}$ can be obtained directly from equations 3.15 and 3.16 by differentiating with respect to b. Repeating the analysis for a slab where z is the thickness of the sample and r_m is the half-width gives,

$$K = kL(2r_m z)$$

$$c_1 = \frac{1}{2}\left(1 - \frac{b_m}{2b_p}\right)$$

$$c_2 = \frac{1}{2}\left(\frac{b_m}{4b_p}\right) \qquad \textbf{(4.18)}$$

$$c_3 = 0$$

$$b_P = \mu_0 J_C r_m$$

For a cylinder, radius r_m, with the field applied perpendicular to the long axis (transverse b), Goldfarb et al [3] find that $c_{1,2,3}$ are twice those when in an axial field. (Using methods as outlined by Zenkevitch et al [4], cf. section 3.2.3)

$$K = kL(\pi r_m^2)$$

$$c_1 = \left(2 - \frac{2b_m}{b_p} + \frac{5b_m^2}{8b_p^2}\right)$$

$$c_2 = \left(\frac{b_m}{b_p} - \frac{b_m^2}{2b_p^2}\right) \qquad \textbf{(4.19)}$$

$$c_3 = \left(\frac{b_m^2}{8b_p^2}\right)$$

$$b_P = \left(\frac{2}{\pi}\right)\mu_0 J_C r_m$$

4.2.2 Fourier analysis.

This voltage can be expressed as a Fourier series of the form,

$$V(t) = K b_m \omega \sum_{n=1}^{\infty} \left(a_n \cos(n\omega t) + b_n \sin(n\omega t) \right) \tag{4.20}$$

where the dimensionless a_n's and b_n's are given by,

$$a_n = \left(\frac{1}{K b_m \omega}\right)\left(\frac{\omega}{\pi}\right) \int_0^{2\pi/\omega} V(t)\cos(n\omega t)\, dt \tag{4.21}$$

and,

$$b_n = \left(\frac{1}{K b_m \omega}\right)\left(\frac{\omega}{\pi}\right) \int_0^{2\pi/\omega} V(t)\sin(n\omega t)\, dt \tag{4.22}$$

In the complete solution, the a_n's are,

$$a_1 = \left(\frac{8}{3\pi}\right) c_2 \tag{4.23}$$

and,

$$a_3 = -\left(\frac{8}{5\pi}\right) c_2 \tag{4.24}$$

and all other odd a_n's are,

$$a_n = -\left(\frac{4n}{\pi(n+2)(n-2)}\right) c_2 \tag{4.25}$$

where values of K and $c_{1,2,3}$ are from equations 4.17 - 4.19. All even a_n's are zero. The a_n's represent the loss component of the induced voltage, where a_1 is the magnitude of the 1st harmonic. Similarly for the for b_n's,

$$b_1 = c_1 \tag{4.26}$$

and

$$b_3 = c_3 \tag{4.27}$$

and all other b_n's are zero. The b_n's represent the lossless component of the induced voltage, where b_1 is the magnitude of the 1st harmonic. These results are consistent with Bean's results for very small ac. fields, comparing equations 4.23-4.27 with equations 3.26-3.29, (where $\alpha_n^* = a_n/n$ and $\beta_n^* = b_n/n$). However, the results above are valid over a larger field range, ie. $b_m < b_P$, and can be used for both cylindrical and slab geometries with appropriate values of $c_{1,2,3}$ and b_P, (equations 4.17-4.19).

4.3 High ac. fields. ($b_m > 2\ b_p$)

4.3.1 Calculating the voltage waveform.

The analysis can be performed for ac. fields greater than those required to fully penetrate the sample. Figure 4.2 shows the magnetic field profiles which can arise.

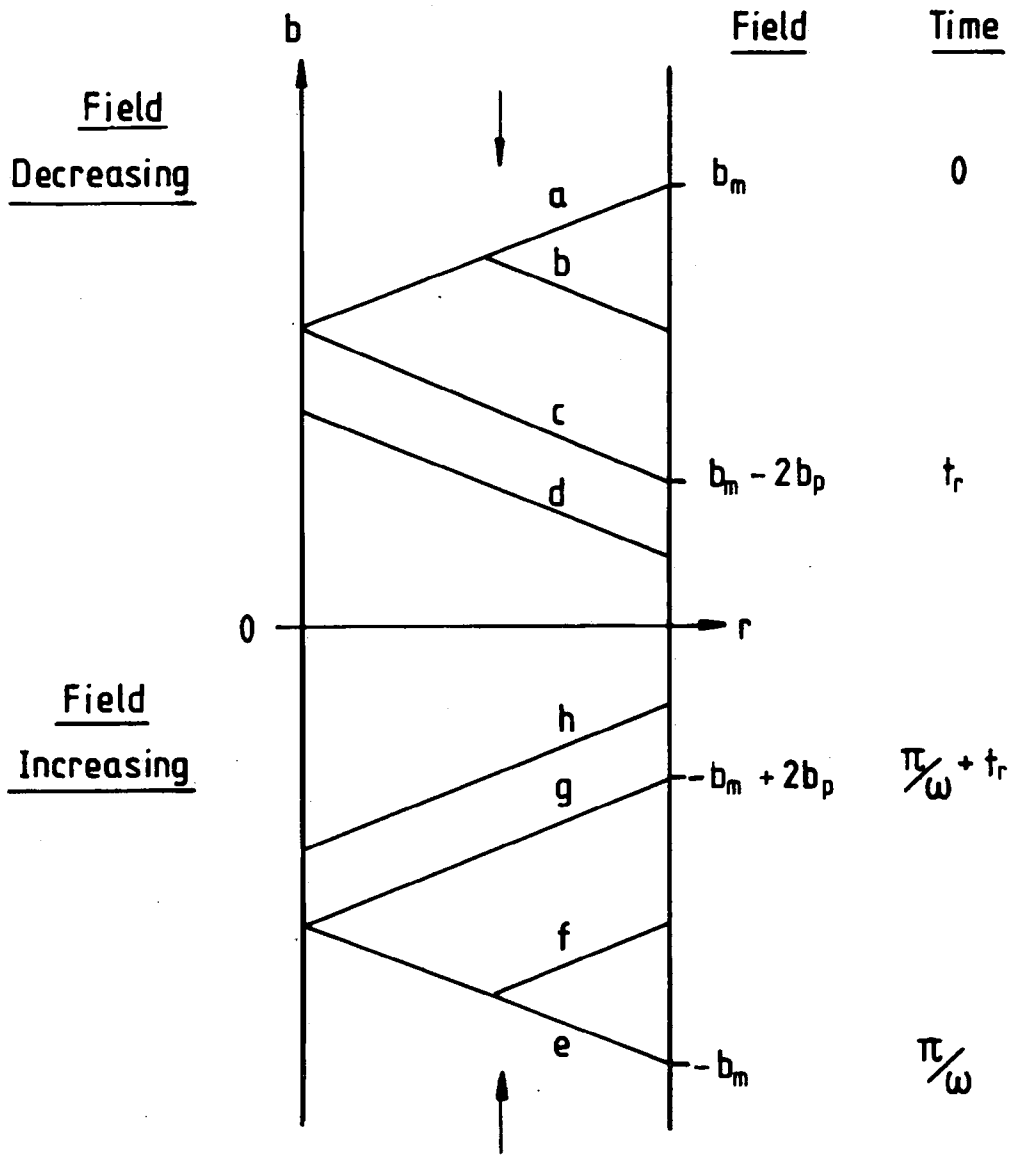

Figure 4.2 Possible magnetic field profiles inside a superconductor for high ac. fields. b_p is the field required to fully penetrate the sample and t_r is the time taken to reverse the ac. field.
(a→d→e - field decreasing, e→h→a - field increasing)

The flux profiles can be considered in four parts. In section I (a→c), the ac. field decreases from its maximum value b_m at t=0, until the profile is fully reversed at $b=b_m-2b_p$ and $t=t_r$ and in section II (c→e), the ac. field decreases to its minimum value $-b_m$ while the gradient of the field is constant. In section III (e→g), the ac. field increases from its minimum value until the field profile is fully reversed at $b=-b_m+2b_p$ and $t=\pi/\omega+t_r$ and in section IV (g→a), the ac. field increases to its maximum value and the gradient of the field is constant. As before, in each of these four sections it is possible to write an expression for the magnetic field as a function of radius, ie. b(r).

Section I. $0 \le t < t_r$

$$0 \le r < x \qquad b(r) = + b_m - \left|\frac{db}{dx}\right|(r_m - r) \tag{4.28}$$

$$x \le r \le r_m \qquad b(r) = + b + \left|\frac{db}{dx}\right|(r_m - r) \tag{4.29}$$

Section II. $t_r \le t < (\pi/\omega)$

$$0 \le r \le r_m \qquad b(r) = + b + \left|\frac{db}{dx}\right|(r_m - r) \tag{4.30}$$

Section III. $(\pi/\omega) \le t < (t_r + \pi/\omega)$

$$0 \le r < x \qquad b(r) = - b_m + \left|\frac{db}{dx}\right|(r_m - r) \tag{4.31}$$

$$x \le r \le r_m \qquad b(r) = + b - \left|\frac{db}{dx}\right|(r_m - r) \tag{4.32}$$

Section IV. $(t_r + \pi/\omega) \le t < (2\pi/\omega)$

$$0 \le r \le r_m \qquad b(r) = + b - \left|\frac{db}{dx}\right|(r_m - r) \tag{4.33}$$

where t_r is the time taken to fully reverse the ac. field.

$$t_r = \frac{1}{\omega}.\cos^{-1}\left[1 - \left(\frac{2\mu_0 J_C r_m}{b_m}\right)\right] \tag{4.34}$$

The induced voltage is,

$$V(t) = K b_m \omega \left[\begin{array}{l} [\, c_1.\sin(\omega t) + c_2.\sin(2\omega t) + c_3.\sin(3\omega t)\,]_0^{t_r} + \\ [\, c_1.\sin(\omega t) - c_2.\sin(2\omega t) + c_3.\sin(3\omega t)\,]_{\pi/\omega}^{t_r+\pi/\omega} \end{array} \right] \tag{4.35}$$

where $c_{1,2,3}$ are given by equations 4.17 - 4.19.

Figure 4.3 shows the induced voltage as a function of time. It is possible to experimentally record such voltage waveforms using a digital storage scope or computerised signal analysis techniques [5-9].

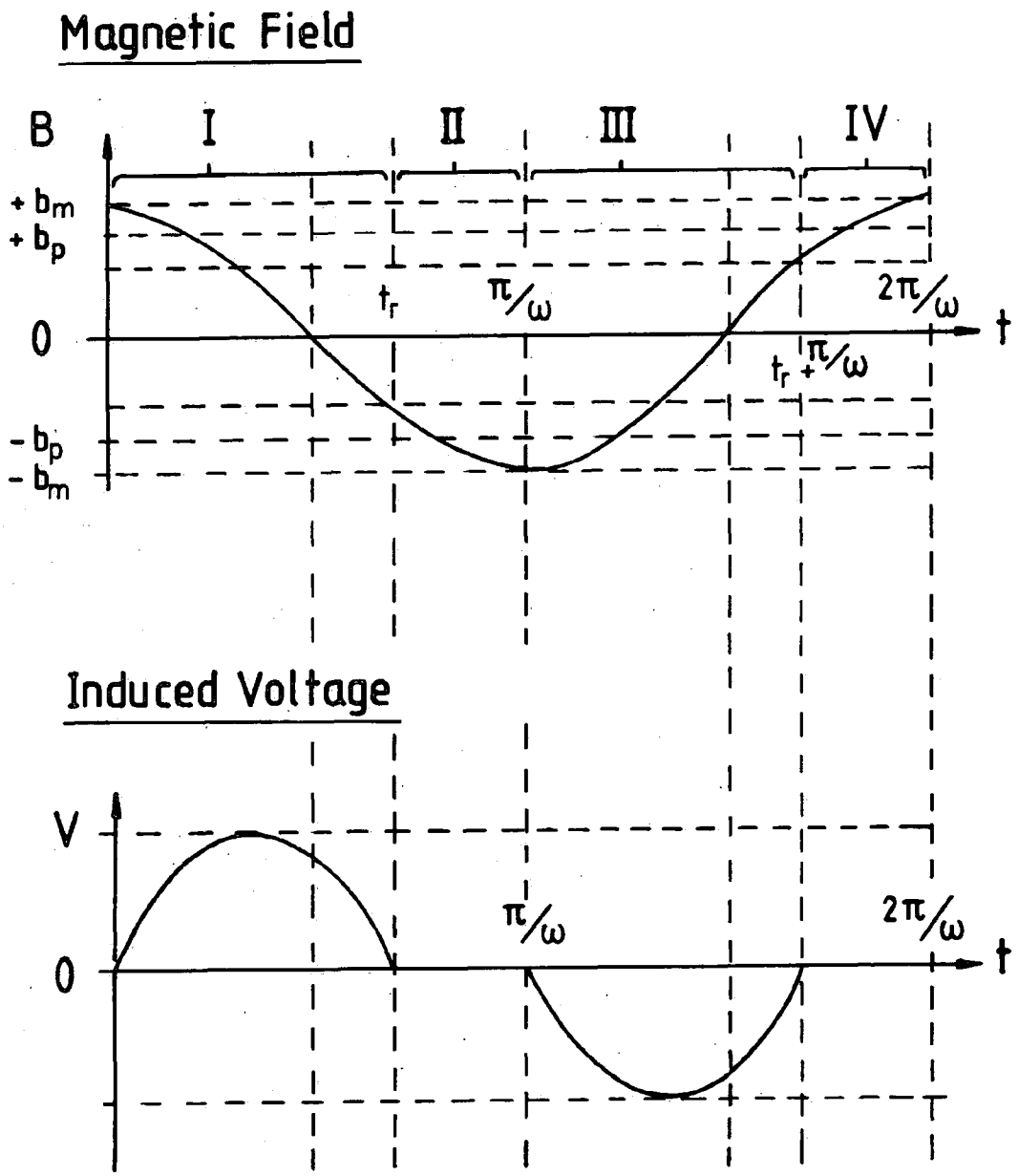

Figure 4.3 The applied ac. magnetic field and resulting induced voltage shown as a function of time.

4.3.2 Fourier analysis.

This voltage can be expressed as a Fourier series in the form of equation 4.20.

$$V(t) = K b_m \omega \sum_{n=1}^{\infty} \left(a_n \cos(n\omega t) + b_n \sin(n\omega t) \right) \qquad \textbf{(4.36)}$$

For the complete solution, the odd a_n's are,

$$a_n = \left(\frac{1}{\pi}\right)\left[\sum_{i=1}^{3}\left(\frac{c_i}{n+i}\right)[1-\cos((n+i)\omega t_r)] - \sum_{j}\left(\frac{c_j}{n-j}\right)[1-\cos((n-j)\omega t_r)]\right] \qquad \textbf{(4.37)}$$

For n=1 j=2,3, for n=3 j=1,2 and for n≥5 j=1,2,3. All of the even a_n's are zero. The a_n's represent the loss component of the induced voltage. Figures 4.4 and 4.5 show the solution up to the 10th harmonic for a cylinder, (axial b).

Similarly the odd b_n's are,

$$b_n = -\left(\frac{1}{\pi}\right)\left[\sum_{i=1}^{3}\left(\frac{c_i}{n+i}\right).\sin((n+i)\omega t_r) - \sum_{j}\left(\frac{c_j}{n-j}\right).\sin((n-j)\omega t_r) - c_k \omega t_r\right] \qquad \textbf{(4.38)}$$

For n=1 k=1 j=2,3, for n=3 k=0 j=1,2 and for n≥5 k=0 j=1,2,3. All of the even b_n's are zero. The b_n's represent the lossless component of the induced voltage. Figures 4.6 and 4.7 show the induced voltages generated up to the 10th harmonic for a cylindrical sample, (axial b).

For the loss component, the harmonic voltages measured by the lock-in amplifier are simply the coefficients of cos(nωt), ie. $V_n = Kb_m\omega a_n$. The lossless voltage lags the applied field, since $\sin(\omega t)=\cos(\omega t-\pi/2)$. So for the lossless components, $V_n = -Kb_m\omega b_n$. The solutions have been calculated using the mathematical package MATHCAD v.6.

As before, the equivalent equations for a slab (axial b) and cylinder (transverse b) can be obtained by substituting the appropriate values for K, $c_{1,2,3}$ and b_p, (ie. equations 4.18, 4.19). The solutions for a slab are shown graphically in figures 4.8-4.11.

For both geometries, the 1st harmonic of the loss voltage increases as $b_m \to \infty$. For all other odd harmonics, the loss voltage first decreases to a minimum and then increases

monotonically as $b_m \to \infty$, (cf. figures 4.5, 4.9). For the higher harmonics (5F-9F), oscillations can be seen in the induced voltage. In contrast, the 1st and 3rd harmonics of the lossless voltage decrease to a negative value and then increase monotonically to zero as $b_m \to \infty$. For all other odd harmonics, the lossless voltage oscillates, then decreases to a negative value before rising to zero as $b_m \to \infty$, (cf. figures 4.7, 4.11). Again, for the higher harmonics (5F-9F), several oscillations can be seen in the induced voltage. For both geometries, the minimum value of the lossless voltage is of similar magnitude for all odd harmonics, (cf. figures 4.7, 4.11).

For a cylinder, the initial gradient (dV/db_m) for all odd harmonics of both the loss and lossless induced voltages, is twice as large for transverse b than for axial b and the field required to fully penetrate the sample (b_P) is a factor of $2/\pi$ lower, (cf. equations 4.17, 4.19). Thus the minimum value of the induced voltage is a factor of $4/\pi \approx 1.27$ higher for transverse b than for axial b. Table 4.1 shows the minimum values of the loss and lossless induced voltage (V_{min}) and the fields at which they occur (b_{min}) for both the cylinder and slab (axial b).

Geometry	Harmonic	Loss		Lossless	
		V_{min} ($-Kb_m\omega$)	b_{min} (b_P)	V_{min} ($-Kb_m\omega$)	b_{min} (b_P)
Cylinder	1 F	0.00	0.00	0.32	0.80
(axial b)	3 F	0.15	1.35	0.34	4.60
	5 F	0.16	3.30	0.34	12.39
	7 F	0.17	6.28	0.34	24.64
	9 F	0.17	10.25	0.34	39.68
Slab	1 F	0.00	0.00	0.25	1.00
(axial b)	3 F	0.13	1.75	0.26	6.00
	5 F	0.14	4.38	0.26	16.22
	7 F	0.14	8.33	0.26	31.57
	9 F	0.15	13.62	0.26	52.04

Table 4.1 Values of V_{min} and b_{min} in the loss and lossless induced voltage for both the cylinder and slab sample (axial b).

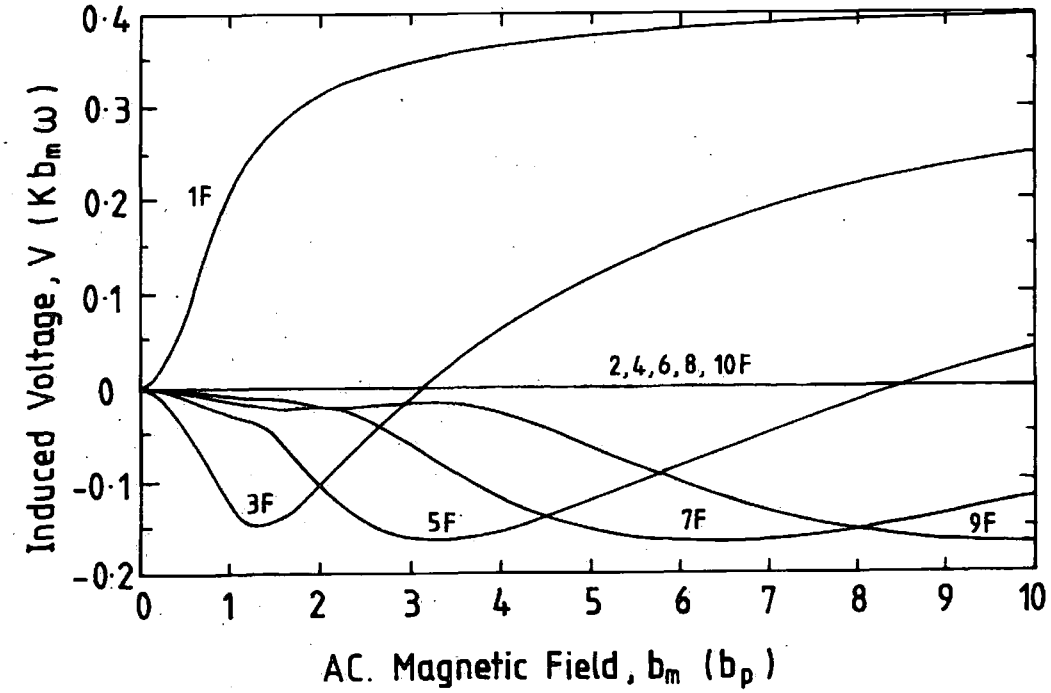

Figure 4.4 The loss component of the induced harmonic voltage for a cylinder (axial b) where the maximum ac. field is 10 × that required to fully penetrate the sample. Note that all of the even harmonics are zero.

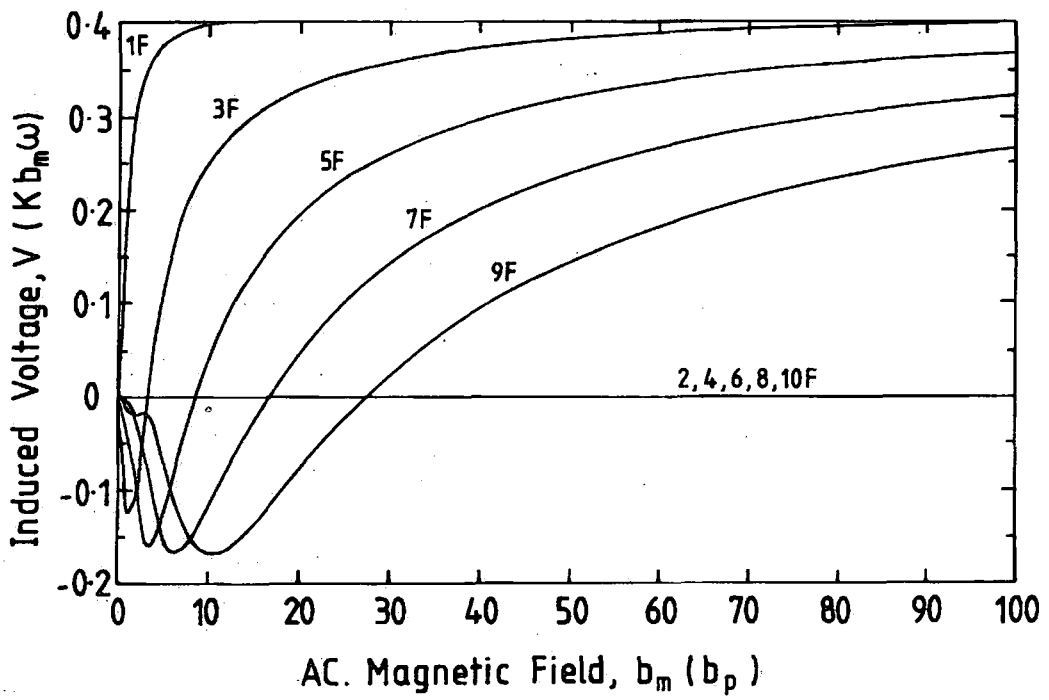

Figure 4.5 The loss component of the induced harmonic voltage for a cylinder (axial b), where the maximum ac. field is 100 × that required to fully penetrate the sample. Note that all of the even harmonics are zero.

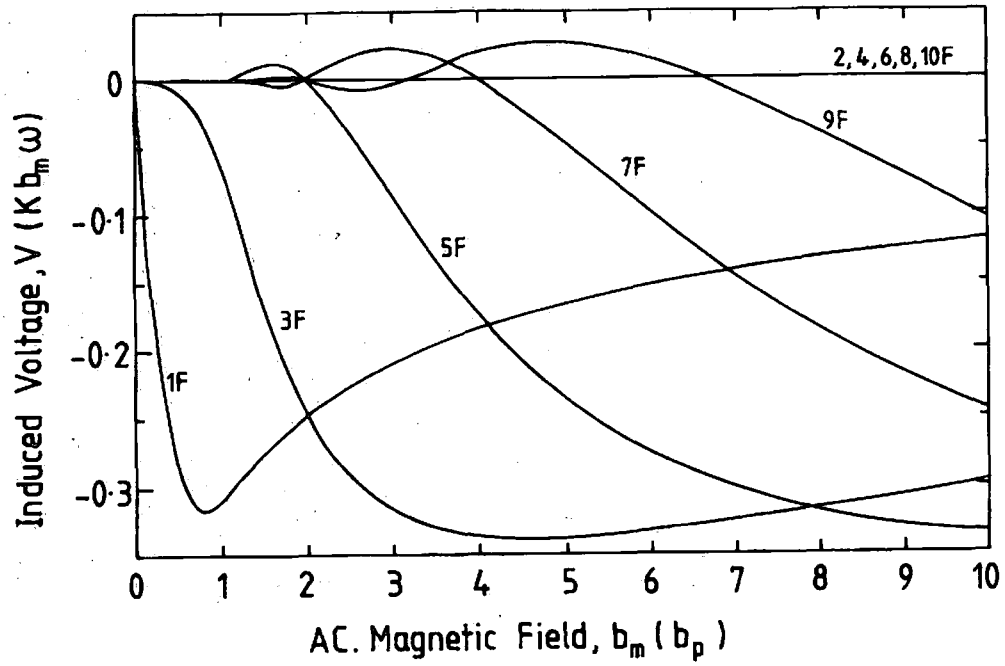

Figure 4.6 The lossless component of the induced harmonic voltage for a cylinder (axial b), where the maximum ac. field is 10 × that required to fully penetrate the sample.

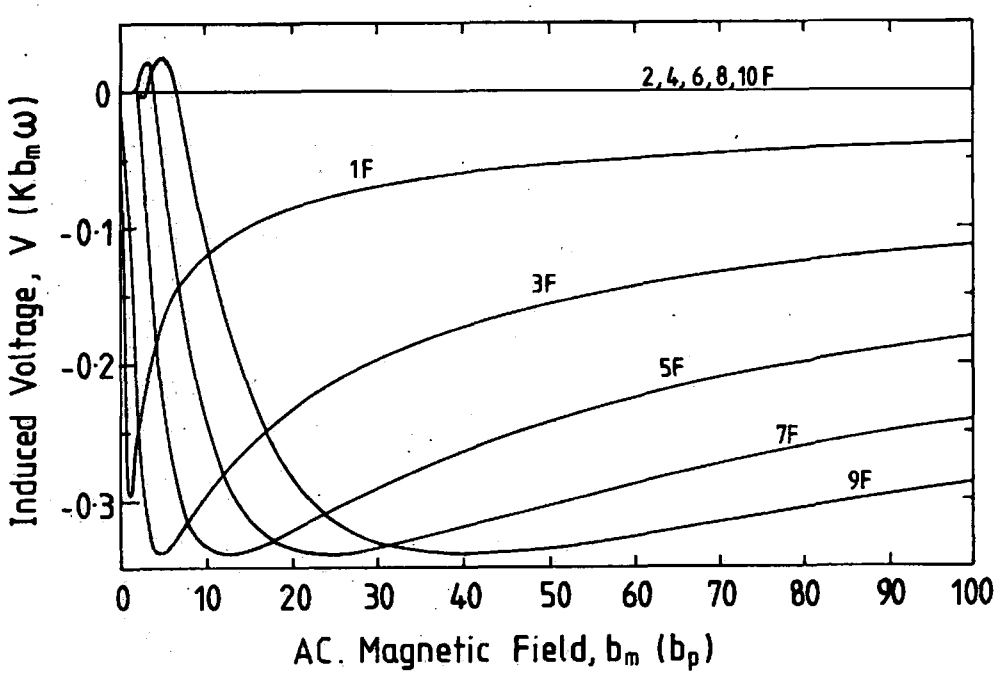

Figure 4.7 The lossless component of the induced harmonic voltage for a cylinder (axial b), where the maximum ac. field is 100 × that required to fully penetrate the sample.

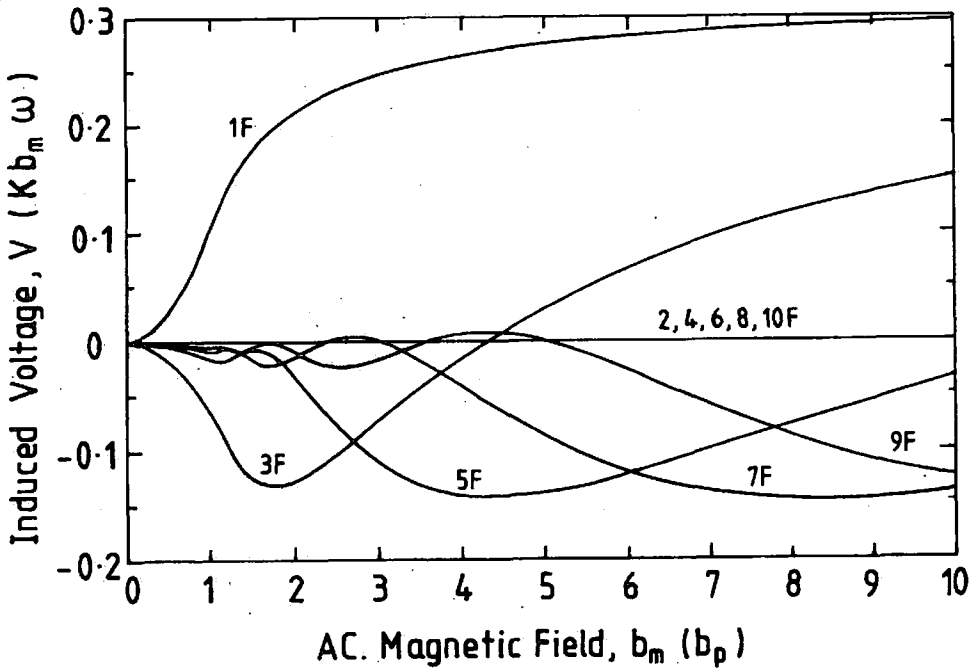

Figure 4.8 The loss component of the induced harmonic voltage for a slab (axial b), where the maximum ac. field is 10 × that required to fully penetrate the sample.

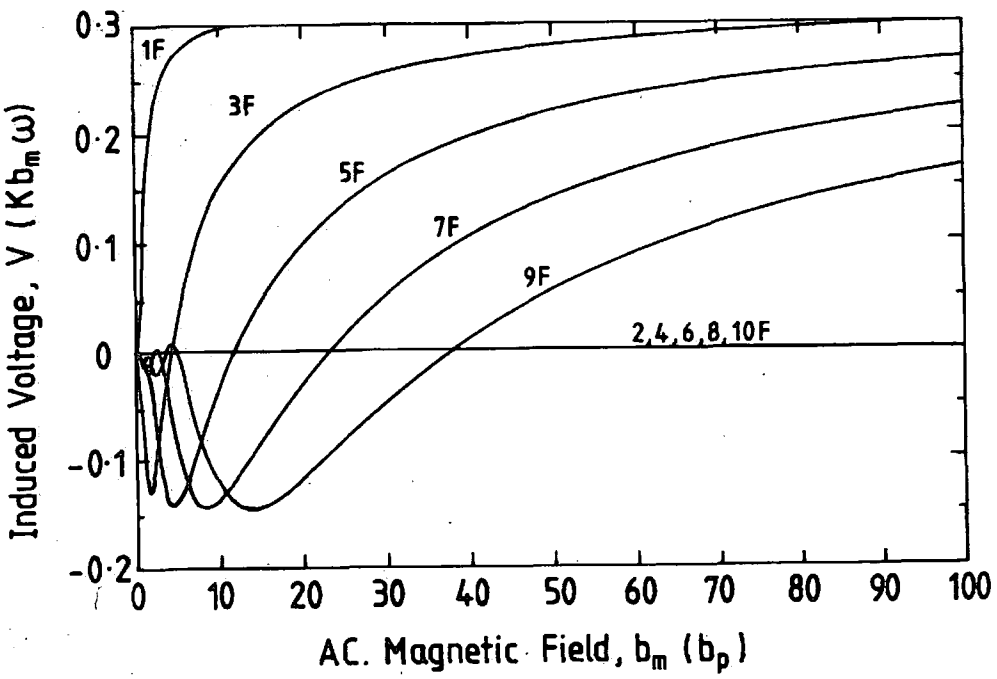

Figure 4.9 The loss component of the induced harmonic voltage for a slab (axial b), where the maximum ac. field is 100 × that required to fully penetrate the sample.

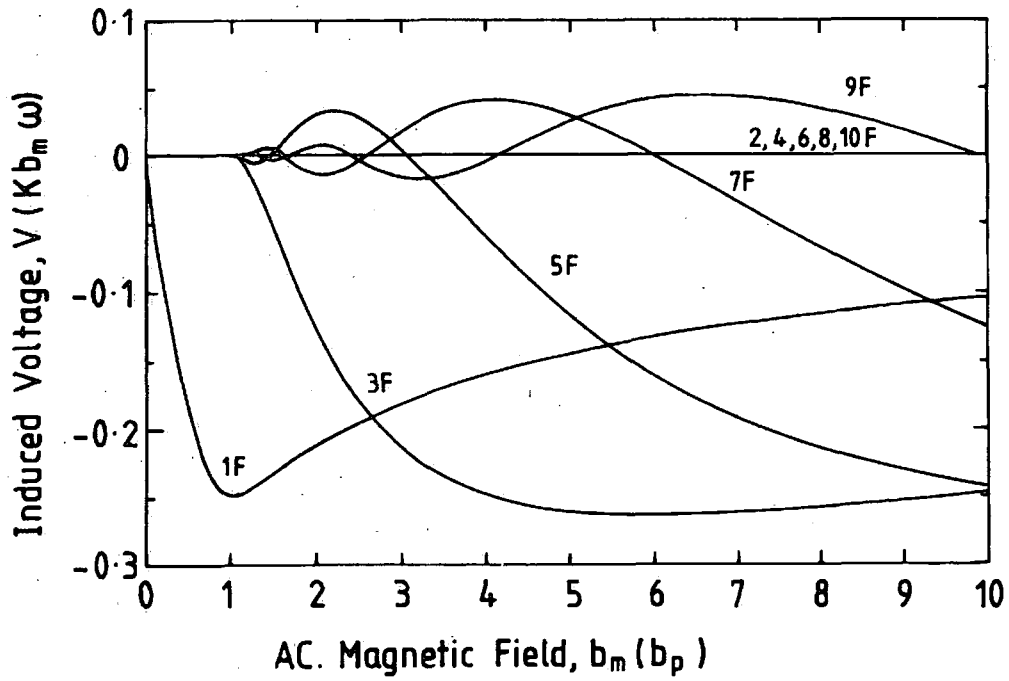

Figure 4.10 The lossless component of the induced harmonic voltage for a slab (axial b) where the maximum ac. field is 10 × that required to fully penetrate the sample.

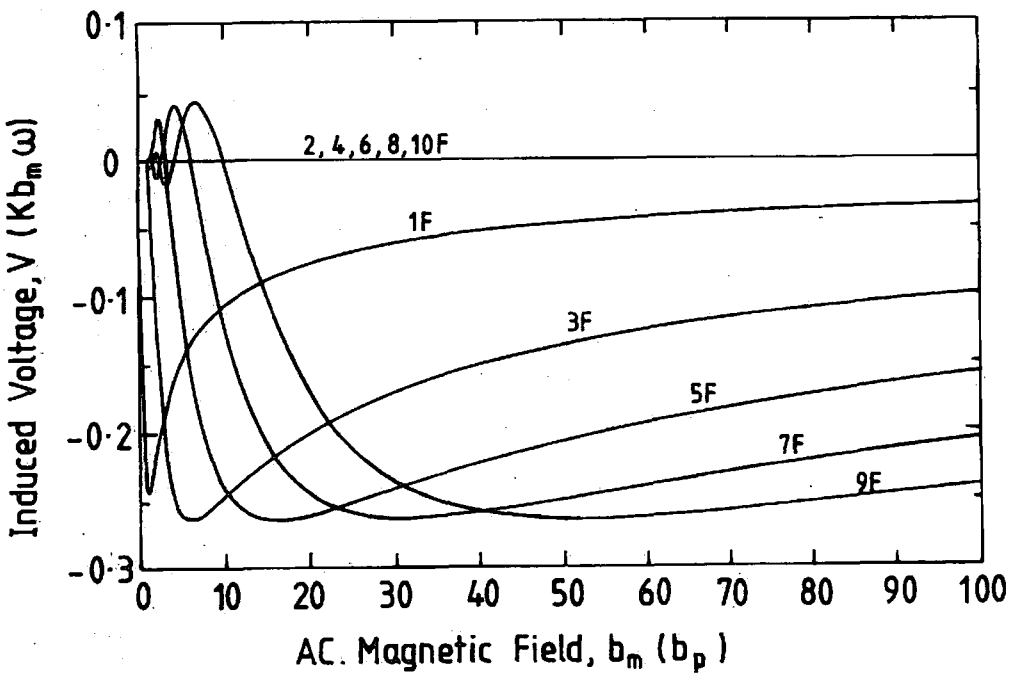

Figure 4.11 The lossless component of the induced harmonic voltage for a slab (axial b), where the maximum ac. field is 100 × that required to fully penetrate the sample.

4.4 Magnetic field profiles / Discussion.

The harmonic flux profile analysis can be completed by differentiating the first (fundamental) harmonic of the lossless voltage with respect to the field, b_m.

For the cylinder (axial b), with $b_m < b_P$.

$$V = -K b_m \omega c_1 \tag{4.39}$$

Substituting in for c_1 gives,

$$V = -K b_m \omega \left[1 - \frac{b_m}{b_P} + \frac{5 b_m^2}{16 b_P^2} \right] \tag{4.40}$$

and differentiating with respect to the ac. field, b_m.

$$\frac{dV}{db_m} = -K\omega \left[1 - \frac{2 b_m}{b_P} + \frac{15 b_m^2}{16 b_P^2} \right] \tag{4.41}$$

Following equation 3.40, this can be rewritten as,

$$\frac{|dV/db_m|}{|dV/db_m|_{MAX}} = 1 - 2\left(\frac{\delta}{r_m}\right) + \frac{15}{16}\left(\frac{\delta}{r_m}\right)^2 \tag{4.42}$$

Solving this quadratic and taking only the physically meaningful solution gives,

$$\frac{\delta}{r_m} = \frac{16}{15}\left[1 - \left(1 - \frac{15}{16}\left(1 - \frac{|dV/db_m|}{|dV/db_m|_{MAX}} \right) \right)^{\frac{1}{2}} \right] \tag{4.43}$$

For small ac. fields, ie. $b_m << b_P$,

$$\delta = \frac{r_m}{2}\left(1 - \frac{|dV/db_m|}{|dV/db_m|_{MAX}} \right) \tag{4.44}$$

where from equation 4.17,

$$r_m = \left(\frac{1}{kL\pi\omega} \left| \frac{dV}{db_m} \right|_{MAX} \right)^{\frac{1}{2}} \tag{4.45}$$

which is in agreement with equations 3.42 and 3.43.

For a cylindrical sample (transverse b), equation 4.44 is correct, where from equation 4.19,

$$r_m = \left(\frac{1}{2kL\pi\omega} \left| \frac{dV}{db_m} \right|_{MAX} \right)^{\frac{1}{2}} \tag{4.46}$$

but δ has no simple physical interpretation, since in this orientation the dimension of the sample perpendicular to the applied field is not constant. Repeating the analysis for the slab gives,

$$\delta = r_m \left(1 - \frac{|dV|\, db_m|}{|dV|\, db_m|_{MAX}} \right) \tag{4.47}$$

where from equation 4.18,

$$r_m = \frac{1}{2kLz\omega} \left| \frac{dV}{db_m} \right|_{MAX} \tag{4.48}$$

This equation provides a simple solution for all fields less than those required to fully penetrate the sample, ie. $b_m \leq b_P$, and is used throughout this thesis.

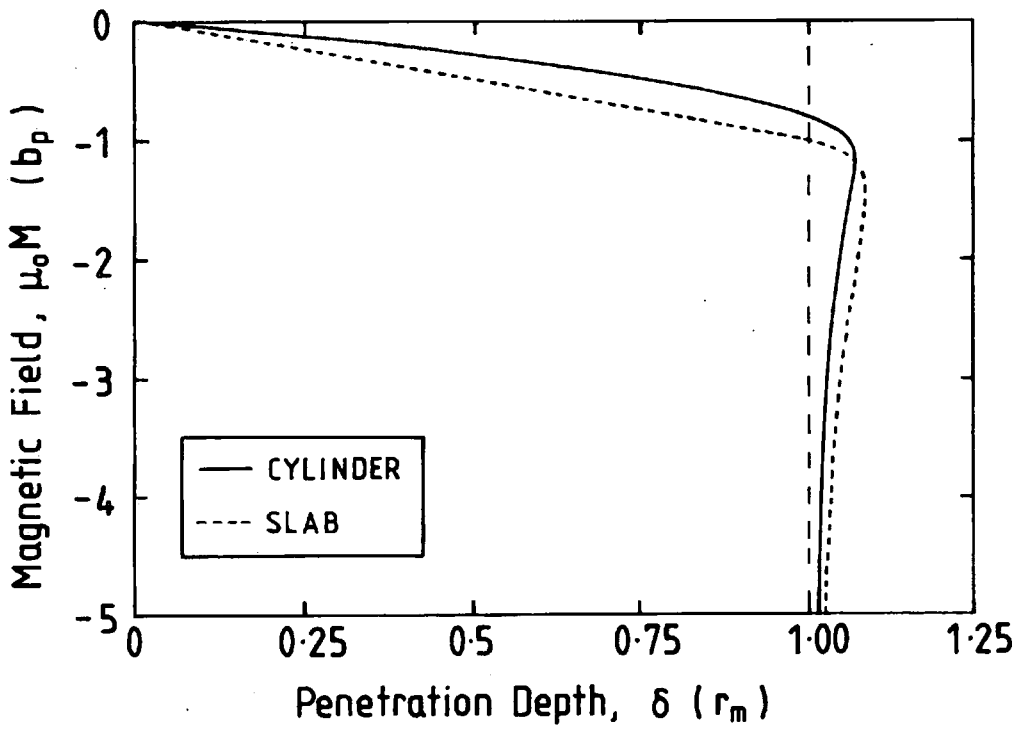

Figure 4.12 Flux profiles for a slab and cylinder.

V_{min} and δ for the slab have been scaled to those for the cylinder.

Figure 4.12 shows the standard flux profile analysis for a slab and cylinder, (axial b). The graph shows the essential features characteristic of a homogeneous sample. ie. The maximum value of the penetration depth δ (determined from $| dV/db_m |_{MAX}$) is equal to the macroscopic dimension of the sample, the gradient in the magnetic field is approximately constant throughout the sample and a region of overshoot in the flux profile is expected. The analysis demonstrates that the overshoot found for the lossless 1st harmonic is also to be expected if an analogue, square wave reference LIA is used, (which includes higher order harmonics). The magnitude of these higher order harmonics reduce at least as fast as 1/n, (depending on the filters used). By adding to the signal at the reference frequency, components of the higher order harmonics, figures 4.6, 4.7, 4.10 or 4.11 show that the total voltage will eventually increase beyond its minimum value and back to zero. Thus an overshoot will still be seen in the flux profile of a homogeneous, non-granular superconductor with a single, field independent J_C. Such contributions from higher harmonics will cause the overshoot to broaden and occur at higher ac. fields.

The flux profile of a granular superconductor can be generated by considering the superposition of the two flux profiles produced by the intra and intergranular J_C. Figure 4.13 shows such a flux profile where the characteristic dimension of the grains is ⅓ that of the sample but their J_C is a factor of 10 higher. For $\delta < r_m$, the figure shows two gradients in the magnetic field, ie. two values for $dM/d\delta$, consistent with two distinct values of J_C.

This is a simplified description of a granular system since in practice no magnetic moment will be produced by the inner grains of a granular system at low ac. fields. (Currents circulating in the outer grains will effectively screen the inner grains.) Equally, the two gradients shown in figure 4.13 cannot be associated with any specific spatial variation in J_C [10]. Nevertheless, comparing figures 4.12 and 4.13 shows that even when the cylindrical symmetry of the sample (axial b) and the critical state are not present, information can still be obtained on the spatial variation of J_C. A more detailed analysis of flux penetration measurements on samples with both an inter and intragranular J_C has been performed by Müller et al [11].

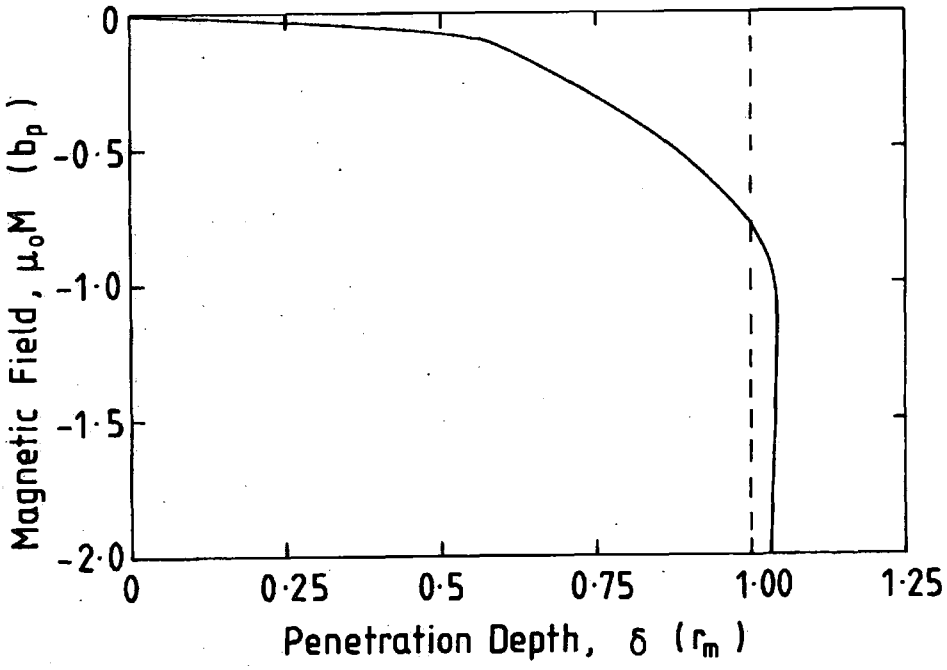

Figure 4.13 The flux profile of a granular superconductor. The two gradients are a result of the sample having both an inter and intragranular J_C.

A number of authors [12-15] have suggested that the overshoot in the flux profiles are due to the large field dependence of J_C, which at low fields can be attributed to sample granularity. Thus chapter presents an additional mechanism to explain the overshoot. In our analysis of a homogeneous sample with a single field independent J_C, a minimum is still seen in the first harmonic of the lossless component of the induced voltage. This results in an overshoot in the flux profile, (see figure 4.12). The presence of two distinct gradients and not the overshoot provides evidence for granularity, (see figure 4.13)

4.5 Conclusion.

A critical state model has been used to calculate the magnitude and the functional form of the magnetic response of a superconducting sample in an applied ac. magnetic field. The analysis has been performed for both a cylinder and slab geometry and evaluated up to the 10^{th} harmonic.

In flux penetration measurements the first harmonic of the lossless component of the induced voltage is recorded. As can be seen in figure 4.6, there is a sharp fall in this voltage to a minimum value. After this the voltage slowly increases, as the ac. field increases beyond that required for full penetration. This result does not depend on the microstructural properties of the sample.

It has been shown that the presence of an overshoot in the flux profile is an artifact of the analysis and cannot be used as direct evidence for granularity. In the following chapters, experimental confirmation of the overshoot in non-granular superconducting materials is provided.

References.

[1] Chen Q Y *Magnetic susceptibilities of superconductors and other spin systems* ed. Hein R A et al 81 (Plenum Press, New York) (1991).

[2] Bean C P *Rev. Mod. Phys.* **36** 31 (1964).

[3] Goldfarb R B, Lelental M and Thompson C A *Magnetic Susceptibility of Superconductors and other Spin Systems* ed. Hein R A et al 49 (Plenum Press, New York) (1992).

[4] Zenkevitch V B, Romanyuk A S and Zheltov V V *Cryogenics* **20** 703 (1980).

[5] Cave J *Ph.D. Thesis University of Cambridge UK* (1978).

[6] Ullamaier H A *Phys. Stat. Solid* **17** 631 (1966).

[7] Fabbricatore P, Gemme G, Musenich R, Occhetto M and Parodi R *Cryogenics* **32** (6) 559 (1992).

[8] Ghatak S K, Mitra A and Sen A *Phys. Rev. B* **45** (2) 951 (1992).

[9] Rollins R W and Silcox J *Solid State Comms.* **4** 323 (1966).

[10] Küpfer H, Apfelstedt I, Flükiger R, Keller C, Meier-Hirmer R, Runtsch B, Turowski A, Wiech U and Wolf T *Cryogenics* **29** 268 (1989).

[11] Müller K H, MacFarlane J C and Driver R *Physica C* **158** 366 (1989)

[12] Campbell A M *Cryogenics* **30** (S) 809 (1990).

[13] Campbell A M *Magnetic Susceptibility of Superconductors and other Spin Systems* ed. Hein R A et al 129 (Plenum Press, New York) (1992).

[14] Campbell A M and Blunt F J *Physica C* **172** 253 (1990).

[15] Gömöry, F Takács S, Lobotka P, Fröhlich K and Plecháček V *Physica C* **160** 1 (1989).

Chapter 5

A Probe for Measuring Magnetic Field Profiles Inside Superconductors from 4.2 K to T_C in High Magnetic Fields.

5.1 Introduction.

Recent developments in cryocooler technology have created the possibility of superconducting applications such as high field magnets, power cables and SMES [1] operating in a cryogen free environment at temperatures from 4.2 K up to 30 K [2]. Variable temperature analysis is becoming increasingly important in the development of new materials for these applications.

Flux penetration measurements of the radial distribution of the critical current density in a bulk superconductor were first described by Campbell [3] and later by Rollins et al [4]. In this chapter, a new probe is described that can measure the magnetic field profiles of superconductors as a function of magnetic field and temperature [5]. These profiles can be used to determine both the functional form and the spatial variation of J_C. This provides crucial information for identifying the mechanisms limiting the critical current density.

For these measurements, a small ac. field is superimposed onto a much larger dc. field. This is the first flux penetration probe capable of making measurements as a function of temperature, from 2 K up to 30 K (accurate to 100 mK), which combines high ac. fields of up to 100 mT (at 19.7 Hz) with very large dc. fields of up to 17 T. The probe can be used to study short sections of superconducting cables, wires, tapes, thin films or bulk samples. Its capabilities are demonstrated by presenting variable temperature data obtained from commercial multifilamentary NbTi wire in magnetic fields up to 10 T. The data are used to calculate the critical current density and magnetic field profile of the sample as a function of field and temperature.

Section 5.2 of the chapter describes the design and construction of the flux penetration probe. This includes a discussion of the external circuitry, coil sets and thermometry.

Section 5.3 describes how the probe can be used to make flux penetration measurements on a sample as a function of field and temperature. In section 5.4 results are presented on a sample of commercial multifilamentary NbTi wire from 4.2 K to T_c in dc. fields up to 10 T. The data are used to calculate the critical current density and magnetic field profile of the sample as a function of field and temperature. Section 5.5 describes a superconducting Nb_3Sn ac. coil which has recently been built and tested. In future experiments it will extend yet further the range of ac. and dc. fields over which the probe can be used. Finally, section 5.6 summarises some of the main conclusions.

5.2 System description.

5.2.1 External circuitry.

Figure 5.1 shows the measurement and control system for the flux penetration probe. The ac. field is generated using a lock-in amplifier, LIA (Stanford Research Systems) which produces a sine wave output at 19.7 Hz. (This is a digital LIA which uses a sine wave reference signal, cf. section 3.3.1). The voltage is used to program an 8 A - 50 V bipolar operational power-supply, BOP (Kepco) which provides the current for the primary coils (P_+,P_-,P_{ex}). The current is recorded using a digital multimeter, DMM (Keithley) to measure the voltage across a 0.01 Ω standard resistor (R). The variable dc. magnetic field is produced by a 40 mm bore 15/17 T (4.2/2.2 K) superconducting magnet (Oxford Instruments), which has been calibrated using an NMR standard.

The magnetic response of the sample is recorded by using the LIA to measure the voltage induced across a set of oppositely wound secondary coils (S_+,S_-), which are located inside the primary coils. These are configured such that with no sample present the total voltage induced across them is approximately zero. A set of external coils (P_{ex}, S_{ex}) are used as a variable inductor to remove any additional out-of-balance signal that can occur when cooling the probe from room temperature to 4.2 K. (The specifications of the coil sets appear later.)

A temperature controller (Lakeshore) is used to control and record the temperature of the sample space (T) using a Carbon-Glass Resistance (CGR) thermometer. The

atmosphere is maintained at 20 torr of Helium gas using an active pressure controller (MKS), which is not shown. All external wiring for the thermometry and coil sets consists of coaxial cable and/or screened twisted pairs to reduce noise.

The measurement is computer controlled using interactive real-time graphical software (ASYST), such that all data is stored digitally. Communication is by IEEE interface except the magnet power supply which uses the RS-232 bus.

5.2.2 Top end of probe.

Figure 5.2 shows the top end of the probe. The probe consists of an outer tube (thin walled stainless steel). Inside this is a vacuum tube (tufnol). The current leads from the primary coils and the signal leads from the secondary coils lie between these two tubes and travel to the top of the probe where they connect to 10 pin connectors via a clamp (brass). This clamp seals the outer tube and holds the vacuum tube in place. The vacuum tube extends beyond the clamp to the head of the probe where it makes a fitting with an o-ring seal. During measurements, the probe is clamped to the top plate of the dc. magnet to secure the sample in the field centre and to reduce probe vibrations.

Inside the vacuum tube is an inner tube (stainless steel) which is the pumping line. It does not extend as far as the coil sets. Between the inner tube and vacuum tube is a clearance of 1 mm. It is possible to evacuate this tube through the vacuum valve using a rotary pump. The sample holder (tufnol) is attached to the inner tube. The thermometry and heater leads travel up the inner tube to two 10 pin connectors at the head of the probe. The total length of the probe is 1.9 m.

5.2.3 Bottom end of probe.

Figure 5.3 shows the bottom end of the probe. It consists of a set of primary and secondary coils suspended on an outer tube (stainless steel). The primary coil has been limited to a maximum diameter of 38 mm so that it will fit in the bore of the dc. magnet. The primary coil consists of two, coaxial, oppositely wound sections to reduce the coupling between the coil producing the ac. field and the dc. magnet [3,6].

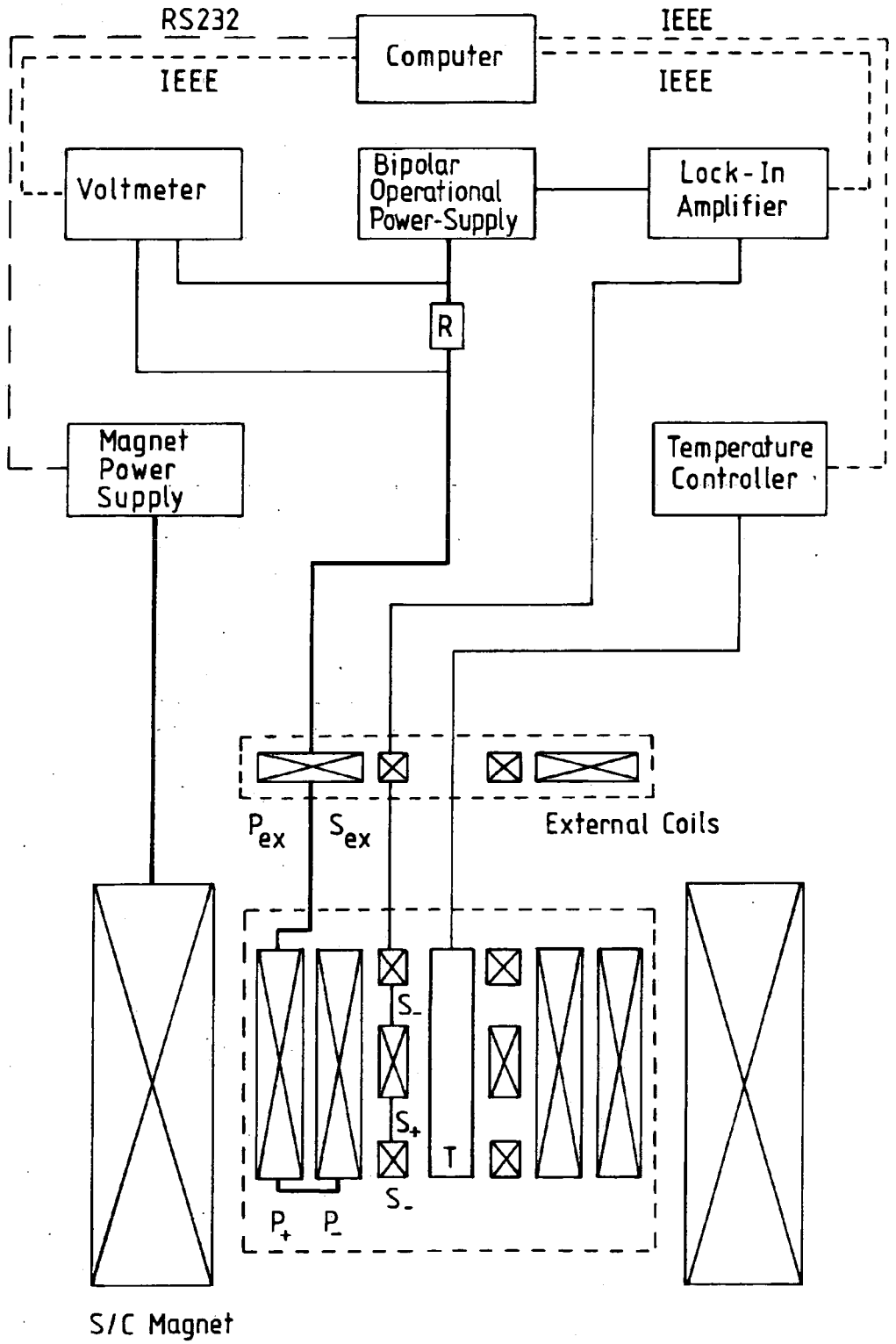

Figure 5.1 The measurement and control system for the flux penetration probe.

$P_{+/-/ex}$ - primary coils $S_{+/-/ex}$ - secondary coils

T - constant temperature environment for the superconductor.

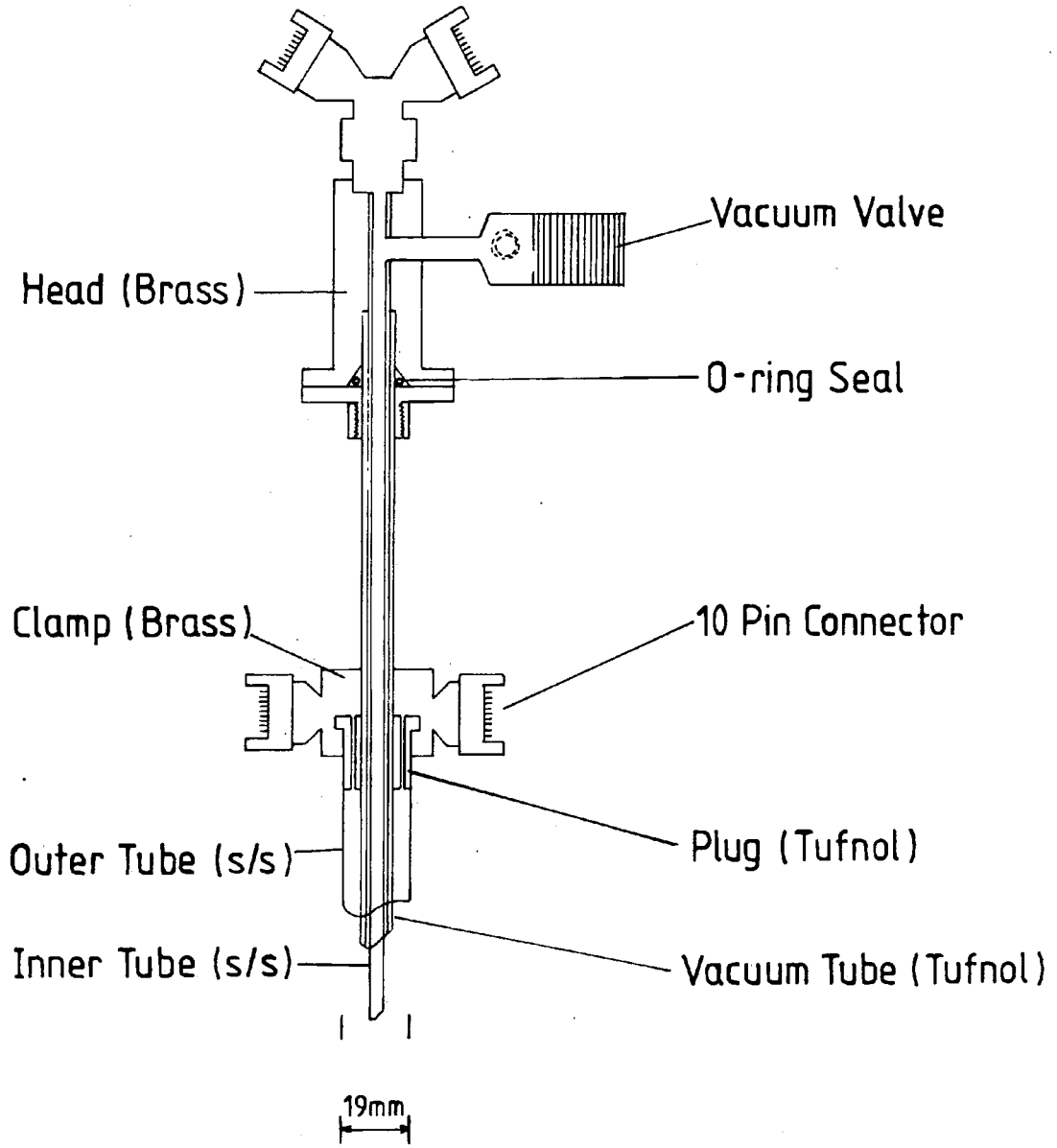

Figure 5.2 The flux penetration probe - top end.
(Drawn to scale)

After it had been wound, the two component primary coil was inserted into the bore of the superconducting dc. magnet and the coupling measured by passing an ac. current through the primary coil and measuring the voltage induced in the superconducting dc. magnet. Turns were added or removed from the outer layer of the primary coil to reduce this induced voltage. When the number of turns on each coil has been optimised and the coils are configured in the opposite sense, the coupling is 10 times less than when the coils are configured in the same sense. Reducing the coupling is essential to reduce the vibration of the probe while making measurements in large ac. fields.

It is possible to swap between one of two primary coil sets. One consists of a two-component superconducting coil made from 0.3 mm diameter, low-loss, multifilamentary NbTi wire (920304 filaments of 136 nm diameter). The coil has been impregnated with Apiezon N grease to prevent wire movement from causing the coil to quench prematurely. The maximum field the coil set can produce falls from 100 mT in zero dc. field to 0 mT at 10 T, which is the upper critical field of the superconducting wire. However at dc. fields above 7 T, probe vibrations limit the maximum ac. field at which data can be obtained to 50 mT at 8 T and 10 mT at 9 T. When measurements at 10 T and above are required, a two-component copper coil is used. This is able to produce an ac. field of 10 mT from 0 T to 17 T. The field is limited to 10 mT by the maximum current that can flow before the wire insulation begins to break down. The ac. fields produced by the probe are typically a factor of 5 greater than other purpose built systems and more than a factor of 10 larger than comparable commercial systems [7].

The superconductor sits in one of the secondary coils (S_+) which are coaxial with the primary coils. The other secondary (S_-) has been separated so that the sample is at the centre of both the ac. and dc. fields. The secondary coils (S_+ and S_-) are configured such that without a sample present, the total induced voltage across them is zero. Both the primary and secondary coils are wound on tufnol formers to reduce the background signal.

The external coils are at room temperature. These consist of a primary (P_{ex}) in series with the two-component primary coil (P_+ and P_-) and a secondary (S_{ex}) in series with S_+ and S_-. The external primary is wound using 3 mm diameter wire. (Smaller diameter

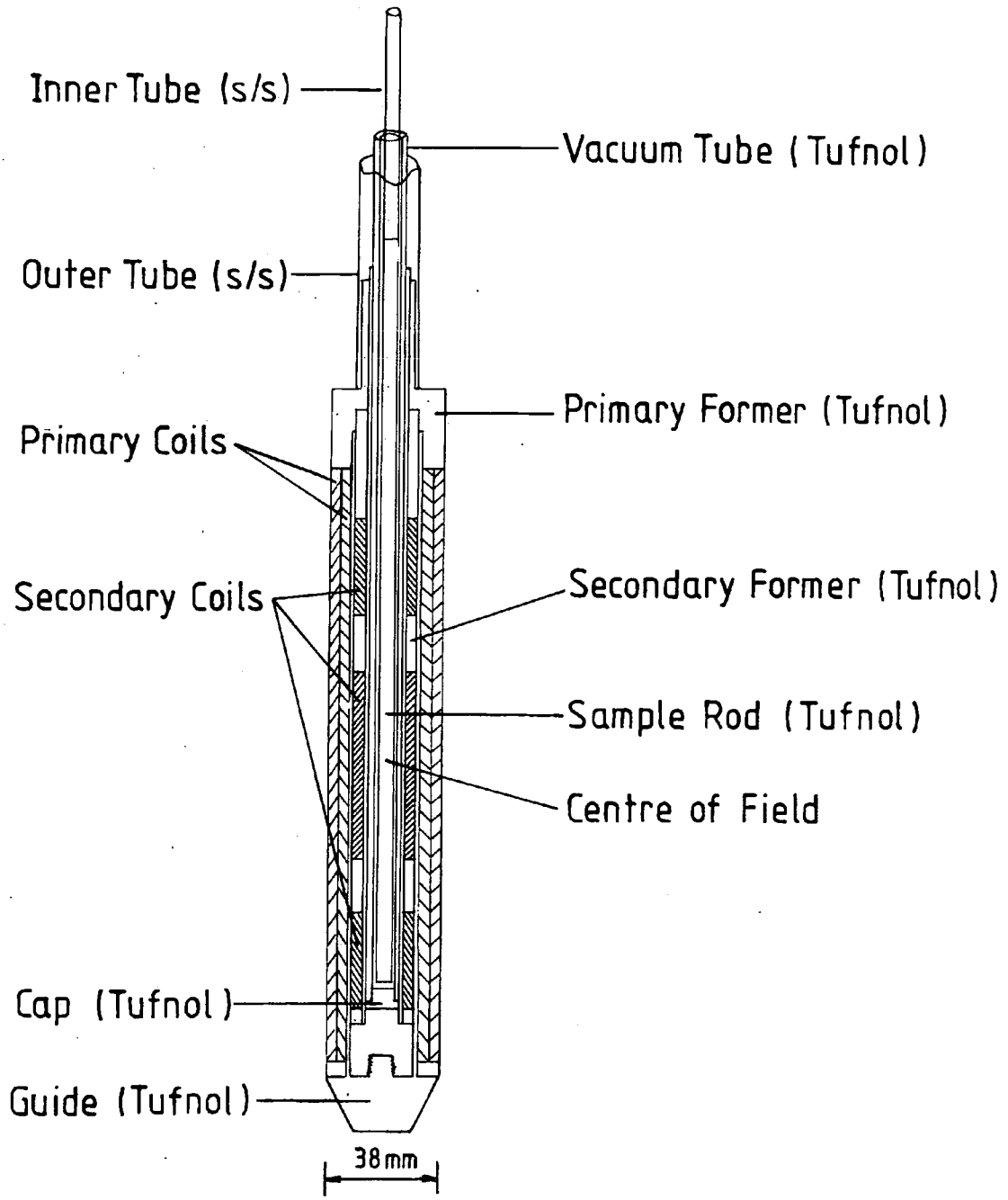

Figure 5.3 The flux penetration probe - bottom end.
(Drawn to scale)

wire leads to irreproducible results caused by thermal expansion from I^2R heating at high currents.) The external secondary has as few turns as possible, (to reduce noise). Table 5.1 shows a summary of the coil sets used in the probe.

Coil set	Material	wd (mm)	l (mm)	id (mm)	od (mm)	n
P_{ex}	Cu	3.00	100	20	100	500
P_+	Cu	0.75	215	20	30	1800
P_-	Cu	0.75	215	30	38	1400
P_+	NbTi	0.30	215	20	30	12500
P_-	NbTi	0.30	215	30	38	10000
S_{ex}	Cu	0.25	80	10	12	1250
S_+	Cu	0.25	68	12	18	3500
S_-	Cu	0.25	34	12	18	1750

Table 5.1 Summary of the coil dimensions. wd - wire diameter, cl - coil length, id - inner diameter, od - outer diameter, n - number of turns.

5.2.4 Thermometry.

Figure 5.4 shows the sample rod and thermometry. The sample sits between two commercially calibrated CGR thermometers. These have small and reproducible magnetic field induced changes in resistance [8,9]. Both thermometers have previously been calibrated as a function of magnetic field up to 15 T [10]. One of the thermometers is read by the temperature controller and used to record and control the temperature. The second thermometer is used to measure temperature gradients across the sample. (Its resistance is recorded using a constant current source (Lakeshore) and DMM (Keithley), not shown in figure 5.2.) Two cylindrically wrapped foil heaters (50Ω) are used to control the temperature. These are wired in parallel so that a potentiometer can be to vary the ratio of power to each heater. In this way it is possible to minimise the temperature gradients across the sample.

The sample, thermometers and heaters are all mounted on a tufnol rod and surrounded

by vacuum grease. This is contained in a tufnol tube where the atmosphere is controlled at 20 torr of Helium gas. Using these techniques it is possible to achieve a sample temperature accuracy of better than 100 mK from 4.2 K up to 30 K in magnetic fields up to 15 T.

5.2.5 General design considerations.

When high ac. currents flow in the primary coil, Joule heating produces cold helium gas. Some of this gas flows past the current leads via several holes in the outer tube. This gas prevents the current leads from overheating and reduces helium consumption. The thermal connections from room temperature to the liquid helium bath is primarily via tufnol or thin walled stainless steel tubing. These choices of material also reduce helium consumption while maintaining sufficient mechanical strength.

5.3 System operation.

Initially, the sample space is evacuated using a rotary pump and flushed with helium gas. This process is repeated three times. The dc. field is set to the required value and the maximum ac. field supplied by the primary coil. The superconductor is then heated into the normal state and the external coils used to set the net voltage across all of the secondary coils to zero. When properly balanced, the voltage across the secondary coils is less than 10^5 times that across just one of them. The LIA is phased using the voltage across a 0.01 Ω standard resistor in series with the primary coils. This enables measurements to be made both in-phase (lossless) and out-of-phase (loss) with the ac. field. The ac. field is then set to zero. The first temperature is set using the temperature controller and any temperature gradient across the sample minimised. When the temperature has stabilised at the required value, the primary current is ramped at 0.05 $A.s^{-1}$ (ie. the ac. field is increased) and recorded using the standard resistor and DMM. The in-phase voltage produced across the secondary coils is simultaneously recorded using the LIA. The LIA can be used to record the data at any multiple of the fundamental harmonic. A frequency of 19.7 Hz is used because it is a compromise between approaching the dc. limit and achieving a good signal to noise ratio. The ac.

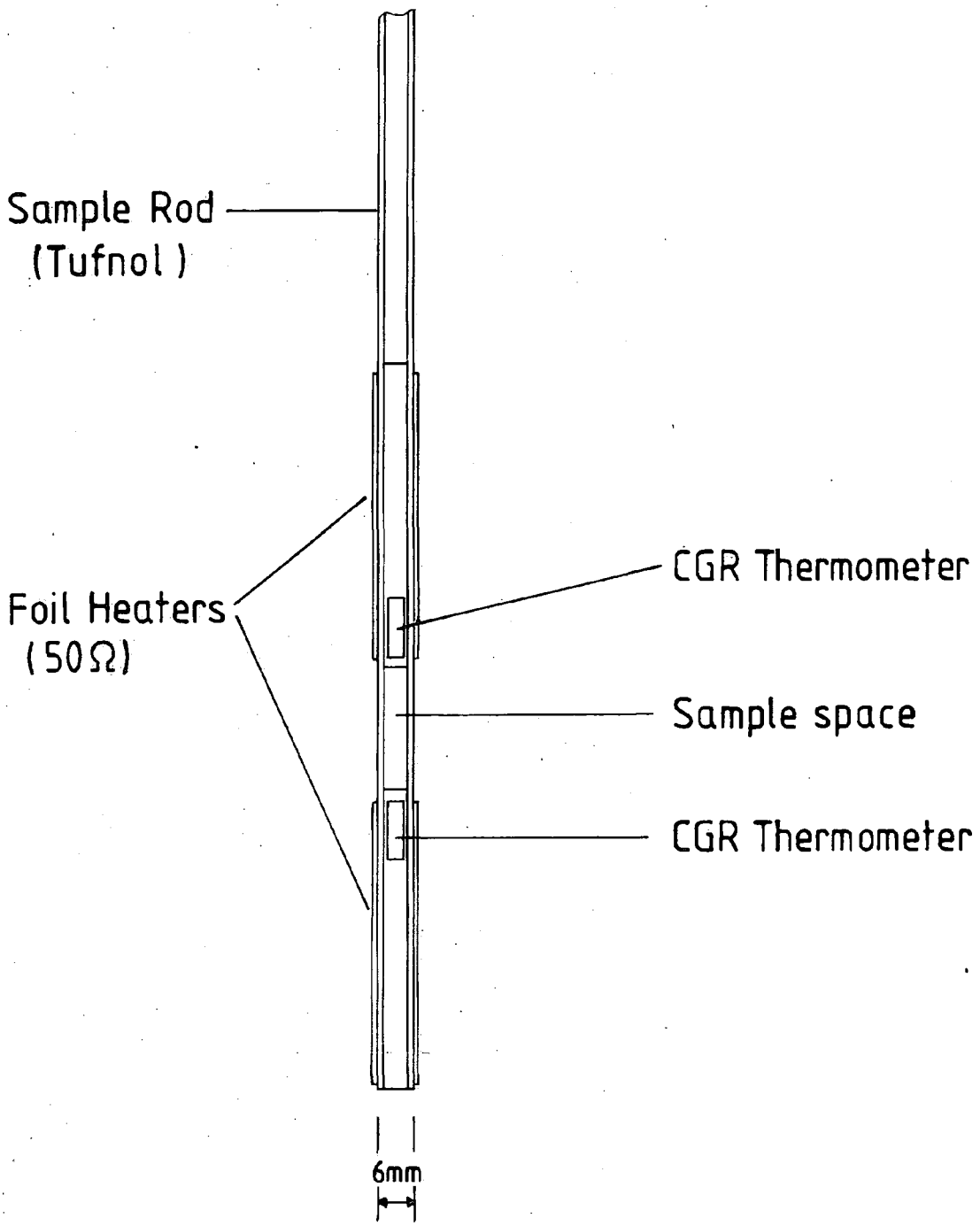

Figure 5.4 The sample holder and thermometry.
(Drawn to scale)

field is then set to zero. This is repeated for each temperature at this dc. field. After measurements have been completed for all temperatures required, the magnetic field is changed, the secondary coils re-balanced and the measurement procedure repeated. In this way a complete set of data is obtained at all temperatures and magnetic fields.

In the procedure outlined above, the secondary coils are balanced at each dc. field and subsequent measurements made as a function of temperature. This is preferable to holding the temperature fixed and making measurements as a function of magnetic field because the background signal has a large dc. field dependence, approximately 0.2 $mV.A^{-1}.T^{-1}$. This is comparable in size to the signal from the sample. The temperature dependence of the background signal is almost negligible, approximately 2 $\mu V.A^{-1}.K^{-1}$.

The probe's capabilities are demonstrated by presenting data on a commercial NbTi wire. The wire consists of 61 filaments each of diameter 28 μm. The copper matrix was removed using nitric acid and the NbTi filaments stuck together using G.E. varnish. 60 sections were cut, each 3 mm long and formed into a sample. The sample is positioned in the probe such that the ac. field is perpendicular to the axis of the NbTi filaments.

5.4 Results and discussion.

Figure 5.5 shows the magnetic moment versus ac. field as a function of dc field at 6 K. In this figure the experimentally measured quantities are included, ie. the current through the primary coil and the voltage across the secondary coils. The magnetic moment has been derived from the induced voltage using a calibration with a lead sample. A background signal, taken when $T>T_C$, has been subtracted from the data. At all temperatures there is a sharp fall in the magnetic moment to a minimum value when there is full penetration of the superconductor. After this, the magnetic moment slowly increases as the ac. field increases beyond that required for full penetration. The marked increase in magnetic moment at low temperatures and high ac. fields (below the dashed line) is attributed to eddy current heating in the copper components of the probe. The small oscillations in the traces are due to small oscillations in temperature. Only limited data can be obtained in high dc. fields due to the coupling of the ac. and dc. fields which causes the probe to vibrate.

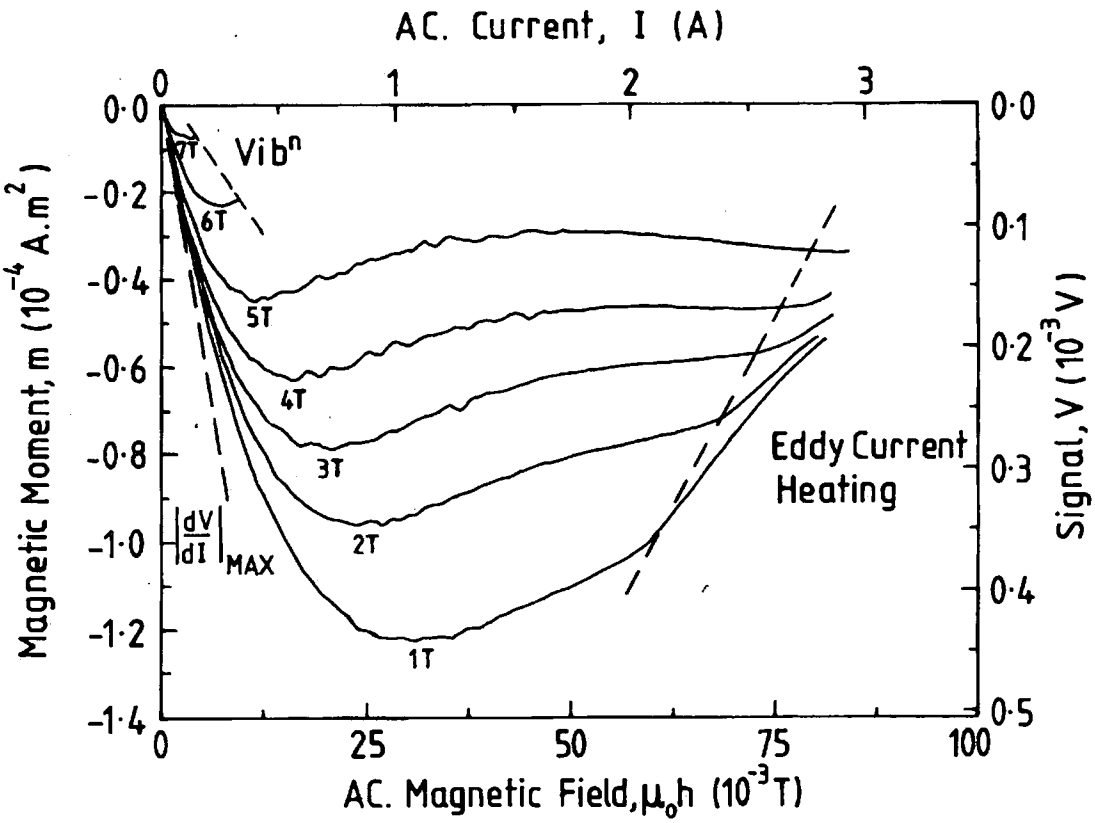

Figure 5.5 Magnetic moment versus ac. field for NbTi as a function of dc. field at 6 K. In the region below the dotted line, eddy current heating prevents effective temperature control.

From the minimum value of the magnetic moment, the coil geometry and the dimensions of the sample, it is possible to calculate the magnetisation critical current density at each magnetic field and temperature, $J_C(B,T)$, (cf. equation 3.30). Figure 5.6 shows the $J_C(B,T)$ for the NbTi sample. The uncertainty in the values of $J_C(B,T)$ is approximately 10 %, primarily due to uncertainty in the sample dimensions. The data suggests that J_C is greater than 2×10^9 A.m^{-2} at 5 T at 4.2 K which is in good agreement with the literature value [11].

By following the analysis outlined by Campbell and differentiating the data in figure 5.5, it is possible to determine the magnetic field profile inside the NbTi sample, (cf. equation 4.47). The differential is performed using the Savitsky-Golay method of simplified least squares [12]. Figure 5.7 shows the spatial variation in the magnetic field ($\mu_0 M$) in the superconductor as a function of dc. field at 6 K. The macroscopic

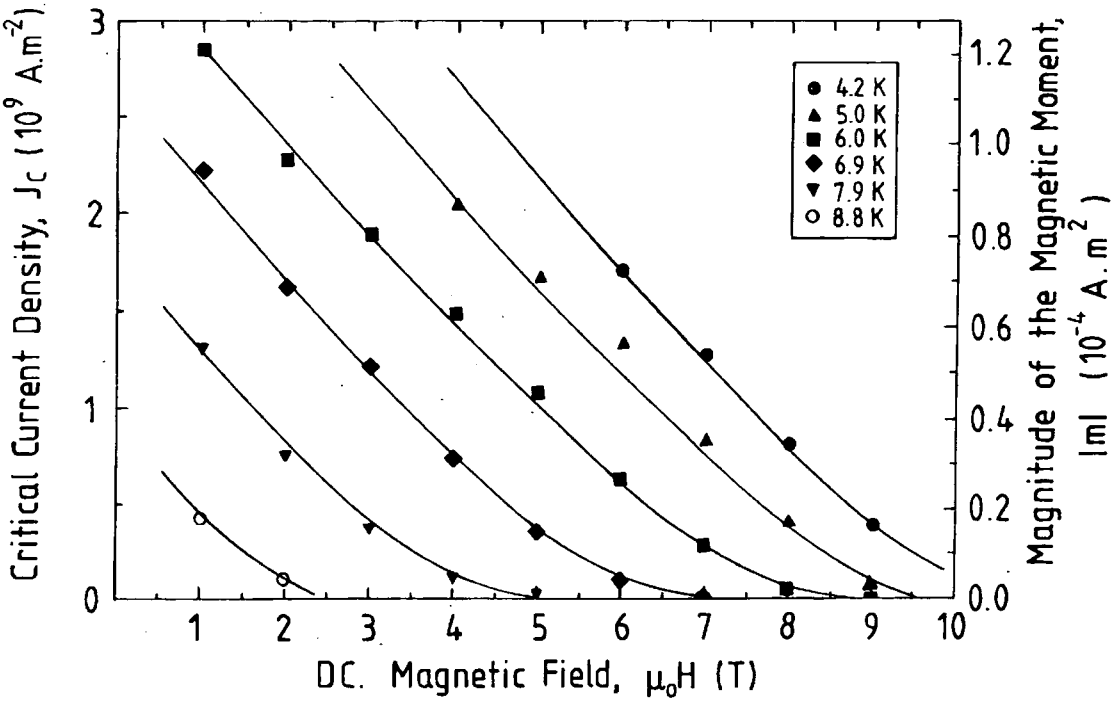

Figure 5.6 The magnetisation critical current density of NbTi as a function of field and temperature.

dimension of the sample is calculated using equation 4.48. The applied dc. field ($\mu_0 H$) and ac. field ($\mu_0 h$) can be added to the magnetic field produced by the NbTi ($\mu_0 M$) to give the net field B. This figure also shows the region of high ac. fields at low temperatures beyond which temperature control cannot be maintained due to eddy current heating. The field appears to penetrate to a distance greater than the sample radius. The analysis in chapter 4 shows that this is artifact of the applied ac. field being larger than that required for full penetration [13].

Equation 3.44 demonstrates that the gradient of the lines as a function of penetration depth gives the spatial dependence of the critical current density. It can be seen that the gradient of the lines and hence J_C is approximately constant throughout the sample. Hence surface pinning is not a significant mechanism in this material. This is expected for a bulk pinning superconductor such as NbTi, where α-Ti precipitates are considered to be responsible for pinning [14].

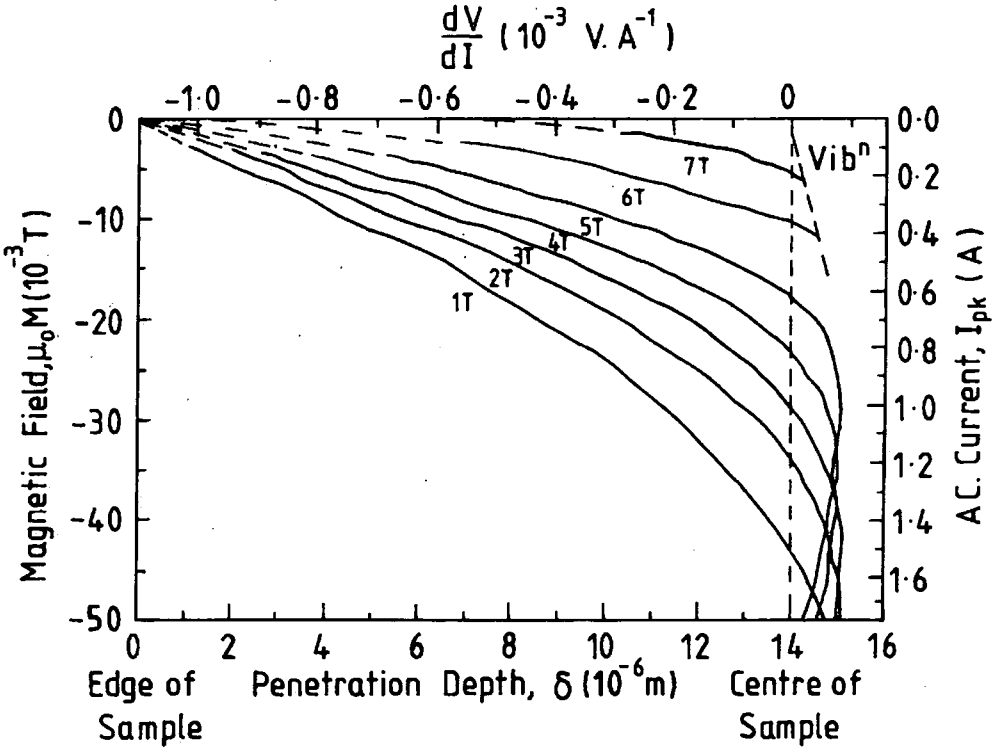

Figure 5.7 The magnetic field profile inside a NbTi sample as a function of dc. field at a temperature of 6 K. In the region below the dotted line, eddy current heating prevents effective temperature control.

5.5 The Nb_3Sn coil.

5.5.1 Coil fabrication.

Figure 5.8 shows the Nb_3Sn superconducting ac. coil [15]. The coil is made from a prototype, multifilamentary, Nb_3Sn wire fabricated at Teledyne Wah Chang Albany. It is wound on a non-magnetic, non-metallic former that consists of a silica tube with 'end-cheeks' that have been made from a machinable glass ceramic. The coil consists of two sections wound coaxially which are configured in the opposite sense to reduce the coupling with the dc. magnet. It has a diameter of 38 mm so that it will fit in the 40 mm bore of the dc. superconducting magnet. Specifications are shown in table 5.2.

After it had been wound, the Nb_3Sn ac. coil was inserted into the bore of a copper dc. magnet and the coupling measured between the coil and the magnet. Turns were added

or removed from the outer section to reduce this coupling to as close to zero as possible. When the number of turns has been optimised, and the sections are configured in the opposite sense, the coupling was 1000 times less than when they were configured in the same sense. Reducing the coupling is essential to prevent the coil from vibrating in the dc. field and to avoid causing the dc. superconducting magnet to quench.

The coil was then reacted at 650 ^{o}C for 200 hours in a nitrogen atmosphere. The Nb_3Sn wires were then soldered to the copper rings, which were connected to the current terminals by 1 mm diameter copper wires. After reaction the coil was vacuum impregnated with resin. During this procedure, the coil was placed in a mould which was sealed in a vacuum chamber. While the chamber was evacuated, heat was applied to drive off moisture and to help the outgassing process. When a good vacuum (< 0.1 torr) has been achieved, resin was admitted to the mould, which was then overpressured to 5 bar of N_2 gas to drive the resin into the windings. The resin impregnated coil was then removed from the mould and cured using the 'spit-roast' technique. This involved rotating the coil in a furnace for 50 hours, during which time the temperature was increased to 160 ^{o}C.

Unfortunately, while removing the coil from the mould, the machinable glass ceramic at the bottom end of the coil was damaged. This was replaced with tufnol. The 'spit-roast' curing ensured that the new 'end-cheek' was properly secured to the coil.

	AC_1	AC_2	Coil
Inner diameter (mm)	21	32	21
Outer diameter (mm)	32	38	38
Length of coil (mm)	216	216	216
Number of turns	1250	850	2100
Number of layers	6	4	10
Length of wire (m)	105	95	200
Wire diameter (mm)	0.8	0.8	0.8
Coil constant ($mT.A^{-1}$)	16.0	13.5	2.5

Table 5.2 The specifications of the Nb_3Sn coil. The inner section (AC_1), the outer section (AC_2) and the entire coil.

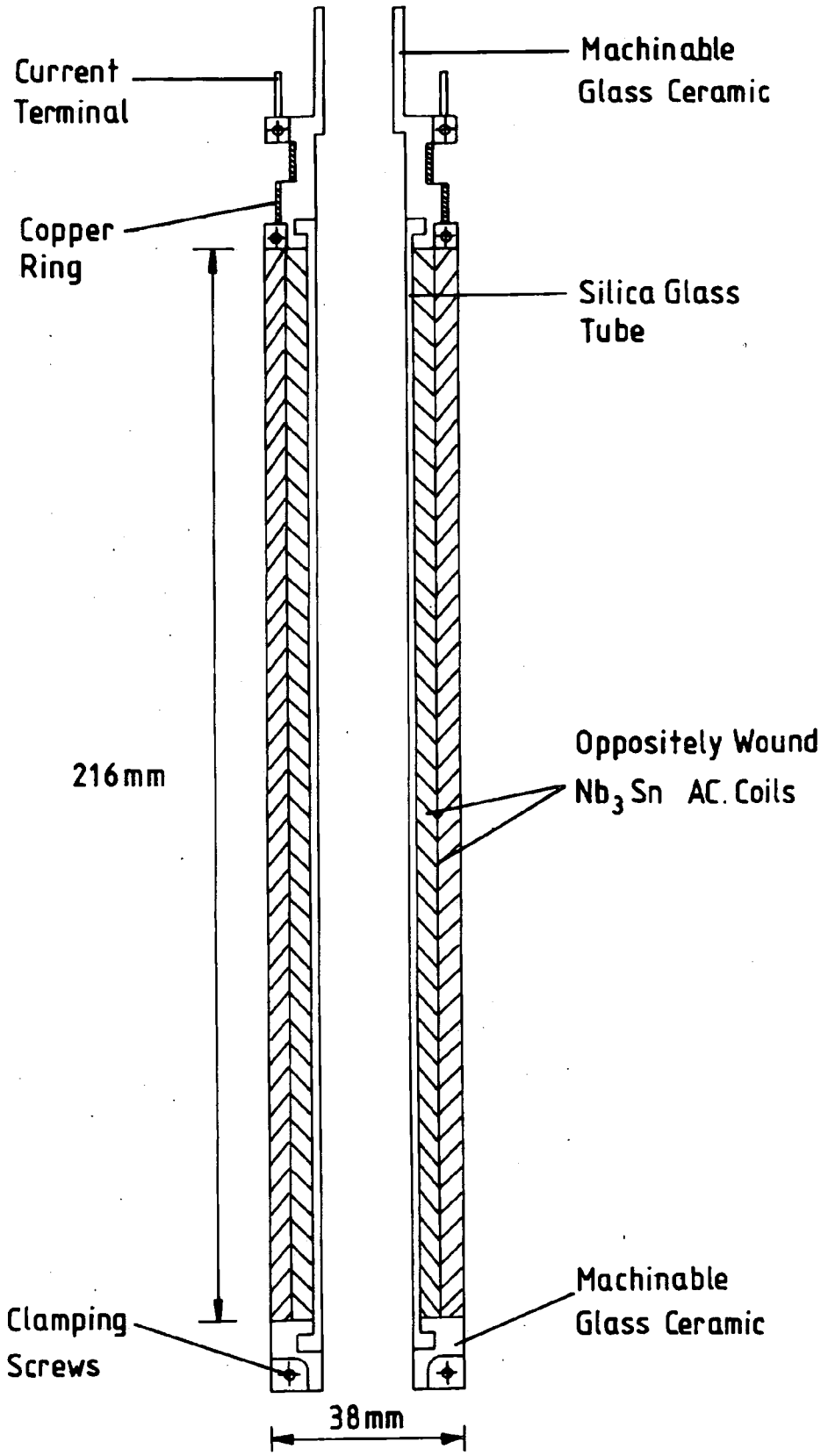

Figure 5.8 The two component, superconducting, Nb_3Sn coil wound on a non-magnetic former.

5.5.2 High field measurements.

The critical current (I_C) of the coil was measured from dc. up to 40 Hz in dc. fields up to 14 T. The current through the coil was supplies by a 500 A, 5 V power supply. The dc. values of I_C were measured using a standard resistor in series with the coil and determined when the coil quenched. Figure 5.9 shows the experimental arrangement for the ac. measurements. A differential adder was used to offset the programming voltage to the power supply to ensure that the current it supplied was always positive. The power supply is not bipolar. The large smoothing capacitors inside the dc. power supply in parallel with the inductive load of the ac. coil form an LCR circuit. This enabled very large, bipolar currents to flow through the coil. The ac. field in the Nb_3Sn coil was measured directly by a calibrated search coil. Both the magnitude and functional form of this voltage is monitored using a lock-in amplifier. The ac. fields quoted in figure 5.10 were determined when the ac. field was noticeably non-sinusoidal and are typically 10 % below the fields associated with the quench currents.

5.5.3 High field performance.

At 12 T the dc. critical current is 78 A. This is 10 % lower than the manufacturers specification of 86 A at a criterion of 1 $\mu V.m^{-1}$. This reduction in I_C increases to 17 % at 10 T. These differences may be due to several reasons. Local heating in the coil may cause the wire to quench prematurely, the wire may have been damaged during the epoxy resin impregnation or the wire may not have been fully reacted. Experience suggests that supporting the coil on a mandrel during impregnation and ensuring that the epoxy is fully keyed to the former is essential.

The ac. performance of the coil is shown in figure 5.10. As can be seen, the rms. ac. field falls off with increasing frequency but the coil is still able to produce a field of 85 mT at 20 Hz in a dc. field of 12 T. This is at least an order of magnitude better than a copper coil. NbTi compares more favourably at low fields but is unable to operate in dc. fields above 10 T, which is the upper critical field of the wire. During the ac. measurements no significant helium boil off or coil vibration were observed, even at high ac. and dc. fields. This is indicative of low coupling and low ac. losses.

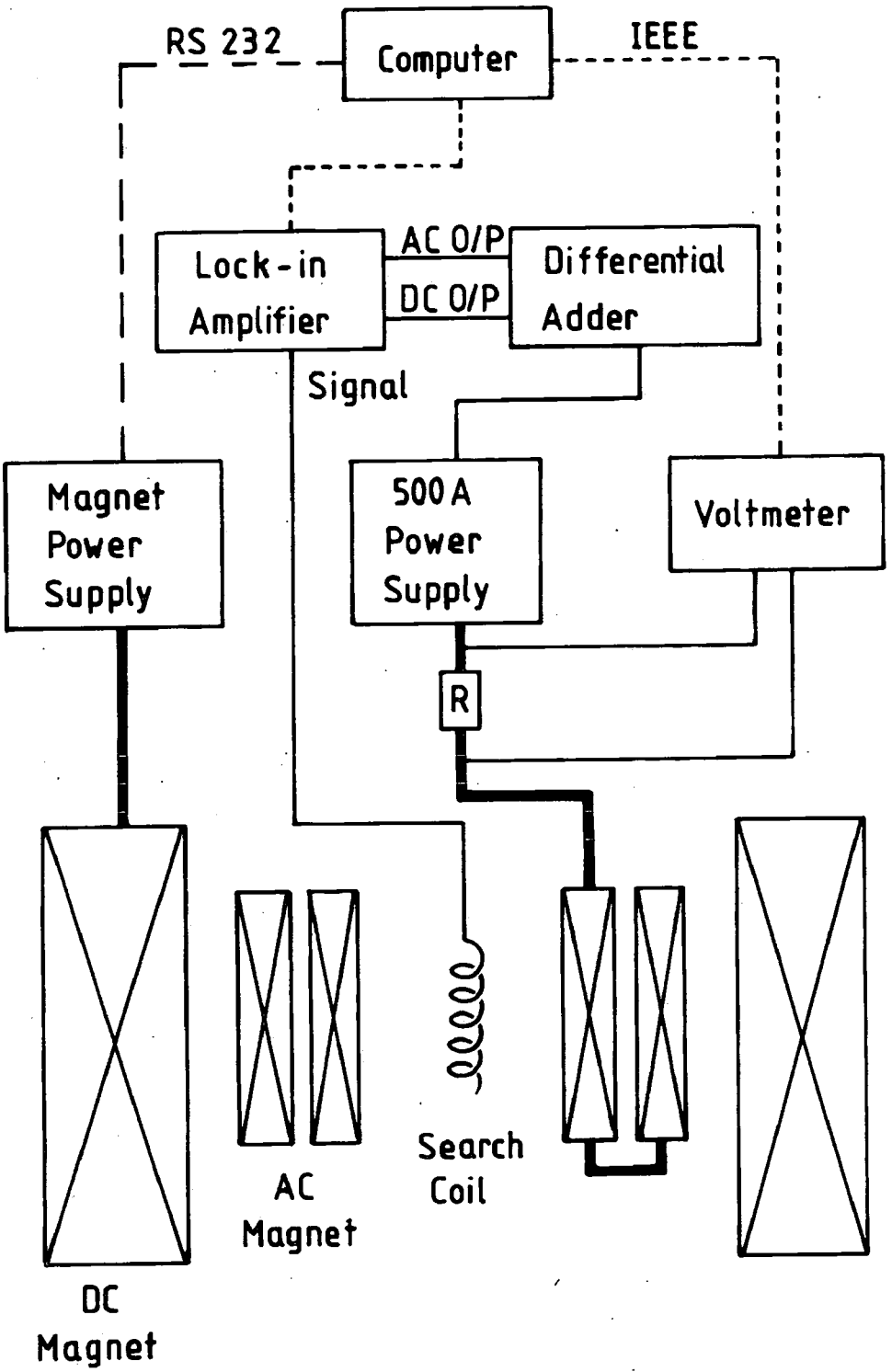

Figure 5.9 The external circuit for characterising the ac. Nb_3Sn coil.

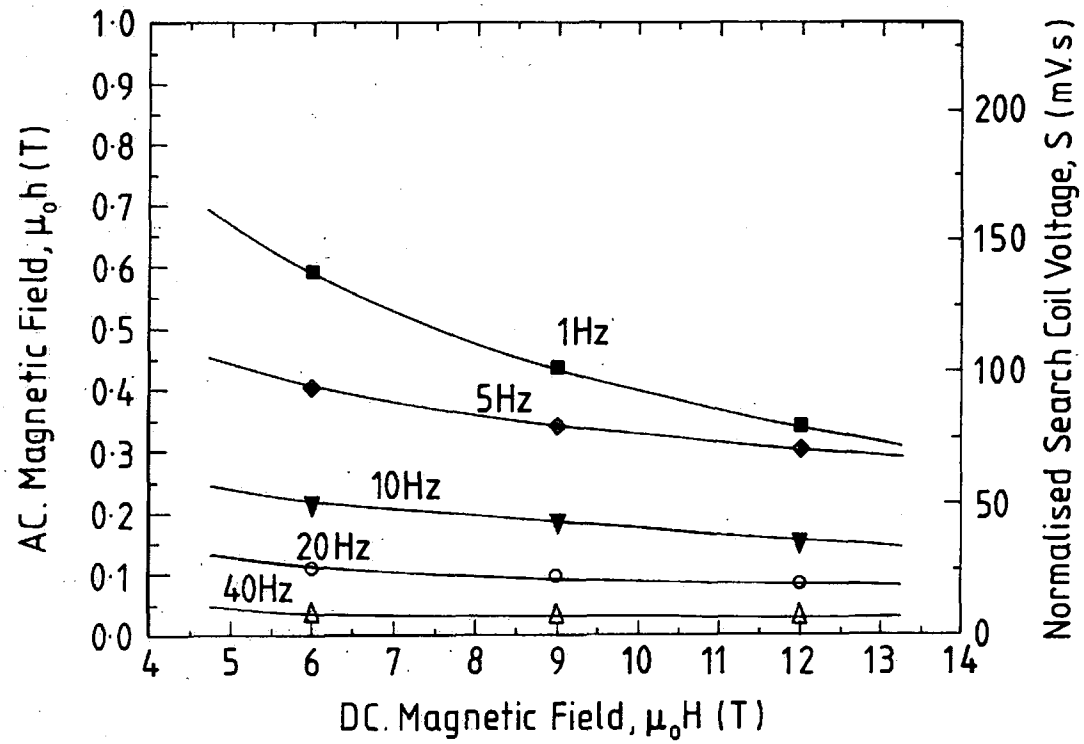

Figure 5.10 The ac. coil performance versus dc. magnetic field as a function of frequency.

5.6 Conclusion.

A probe has been designed for making flux penetration measurements on superconducting samples from 2 K to 30 K, accurate to 100 mK, in high magnetic fields up to 17 T. The probe has been used with one of two different coil sets to generate an ac. field. One is made from copper wire and can produce an ac. field of 10 mT from 0 T to 17 T. The other uses a superconducting NbTi coil, which can generate a much larger ac. field, (up to 10 times larger in zero dc. field). The capability of the probe has been demonstrated on a commercial multifilamentary NbTi wire.

The data have been analysed using Bean's critical state model to calculate the critical current density as a function of field and temperature. The value obtained compares well with the literature. Campbell's analysis has also been used to generate magnetic field profiles inside the superconducting sample. These profiles give the spatial variation of J_C from which it is possible to distinguish surface pinning from bulk pinning

and hence better determine the mechanisms that limit J_C.

A recent development has been the design and construction of an ac. superconducting Nb_3Sn coil which can produce large ac. fields in large background dc. fields. It is wound on a non-magnetic, non-metallic former to produce good field homogeneity and reduce eddy currents and ac. losses. The coil consists of two oppositely wound sections which facilitates use in high field superconducting magnets. The ac. performance of the coil falls of with increasing frequency but the coil is still able to produce an ac. field of 85 mT at 20 Hz in a dc. field of 12 T. This coil will enable flux profile measurements to be made on bulk superconducting samples with high J_C in dc. fields up to 17 T.

References.

[1] Larbalestier D C *Physics Today* **June** 74 (1991).

[2] Tozai N *Superconductor Industry* **Spring** 41 (1994).

[3] Campbell A M *J. Phys. C* **2** 1492 (1969).

[4] Rollins R W, Küpfer H and Gey W *J. Appl. Phys.* **45** (12) 5392 (1974).

[5] Ramsbottom H D and Hampshire D P *Meas. Sci. Technol.* **6** 1349 (1995).

[6] Polák M, Pitel J, Majoroš M, Kokavec J, Suchoň D, Kedrová M, Kvitkovič J, Fikis H and Kirchmayr H *IEEE Trans. on Appl. Supercond.* **5** (2) 717 (1995).

[7] Campbell A M and Blunt F J *Physica C* **172** 253 (1990).

[8] Sample H H, Brandt B L and Rubin L G *Rev. Sci. Instrum.* **53** (8) 1129 (1982).

[9] Sample H H and Rubin L G *Cryogenics* **17** 597 (1977).

[10] Ramsbottom H D, Ali S and Hampshire D P *Cryogenics* **36** (1) 61 (1995).

[11] Friend C M and Hampshire D P *Applied Superconductivity Vol. 1 Proc. European Conf. on Applied Superconductivity* 23 (1993).

[12] Savitsky A and Golay M J E *Analytical Chemistry* **36** (8) 1627 (1964).

[13] Ramsbottom H D and Hampshire D P *To be submitted to Phys. Rev. B* (1996).

[14] Stejic G, Cooley L D, Joynt R, Larbalestier D C and Takàcs S *Supercond. Sci. Technol.* **5** (S1) S176 (1992).

[15] Ramsbottom H D, Hampshire D P, Jones H and Smathers D B *Inst. Phys. Conf. Series No.* **148** *EUCAS'95* 727 (1995).

Chapter 6

Critical Current Densities, Scaling Relations and Harmonic Response of NbTi as Determined by Flux Penetration Measurements.

6.1 Introduction.

Flux penetration measurements provide a unique opportunity to study both the functional form and spatial variation of the critical current density J_C. They make it possible to quantify the inhomogeneous properties of superconducting materials and locate regions of interest. Such measurements are used to determine the inter and intragranular J_C, the role of granularity, and the relative contributions of bulk and surface pinning within a superconducting sample. An understanding of the mechanisms limiting J_C can lead to the fabrication of better materials.

This chapter contains results on a commercial, multifilamentary, superconducting NbTi wire. NbTi has been chosen because it is probably the most extensively studied and industrially important superconductor. Hence these measurements serve as a standard for assessing conductors being developed with new materials for high field applications.

Section 6.2 describes the type of wire measured and highlights experimental details. Results are presented from 4.2 K up to T_C in magnetic fields up to 10 T. The analysis of the data is shown in section 6.3. The results have been used to determine magnetic field profiles and critical current density as a function of field and temperature. These are analysed within the framework of a universal scaling law and compared with transport current data on the same sample.

Section 6.4 describes the harmonic response of the sample up to the 10^{th} harmonic, 10F. The results are compared with the theoretical predictions outlined in chapter 4. At the end of the chapter is a discussion of the results and a conclusion summarising the most important findings.

6.2 Experimental.

6.2.1 Experimental procedure.

The sample consisted of a commercial, multifilamentary, superconducting NbTi wire of 61 filaments, each 28 μm in diameter. The copper matrix was removed using nitric acid and the NbTi filaments stuck together with G.E. varnish. 60 sections were cut, each 3 mm long and formed into a sample. Flux penetration measurements were made from 4.2 K up to T_C in magnetic fields up to 10 T [1,2]. The harmonic response of the sample was also investigated. In these measurements, at each field, both the loss and lossless components of the induced voltage were recorded for the first 10 harmonics. The flux penetration measurements and harmonic analysis were investigated with the filaments both parallel (axial b) and perpendicular (transverse b) to the ac. and dc. field.

6.2.2 Experimental results.

Figures 6.1 shows the magnetic moment versus ac. field as a function of temperature for the sample in a transverse field. In this figure the experimentally determined quantities are also included. A background signal, taken when $T>T_C$, has been subtracted from the data. At all temperatures there is a sharp fall in the magnetic moment to a minimum value when there is full penetration of the sample. The marked increase in magnetic moment at the lowest temperatures and highest ac. fields is attributed to eddy current heating in the copper components of the probe.

Figures 6.2 shows the equivalent data for the sample in an axial field. At all temperatures the magnetic moment decreases as the ac. field increases. Initially the decrease is rapid but then becomes more gradual. The functional form of the data is very different from that in a transverse field or indeed from data from other superconducting materials, such as PMS. The value of $|\,dV/dI\,|_{MAX}$ in figure 6.2 is approximately half that in figure 6.1. This is consistent with the factor of 2 between c_1 in equations 4.17 and 4.19, reflecting the different demagnetisation factors arising from the two orientations. The broad features of the results in figure 6.2 were repeated in a second experiment using a similar sample, (fabricated as described in section 6.2).

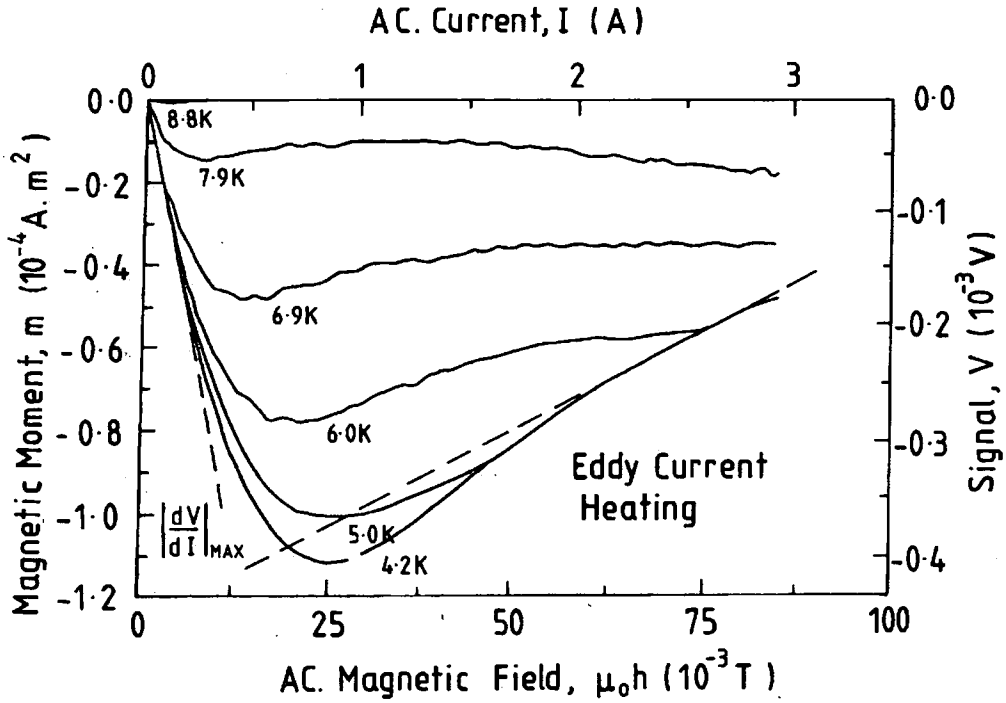

Figure 6.1 Magnetic moment versus ac. field for the NbTi sample as a function of temperature in a transverse field of 3 T.

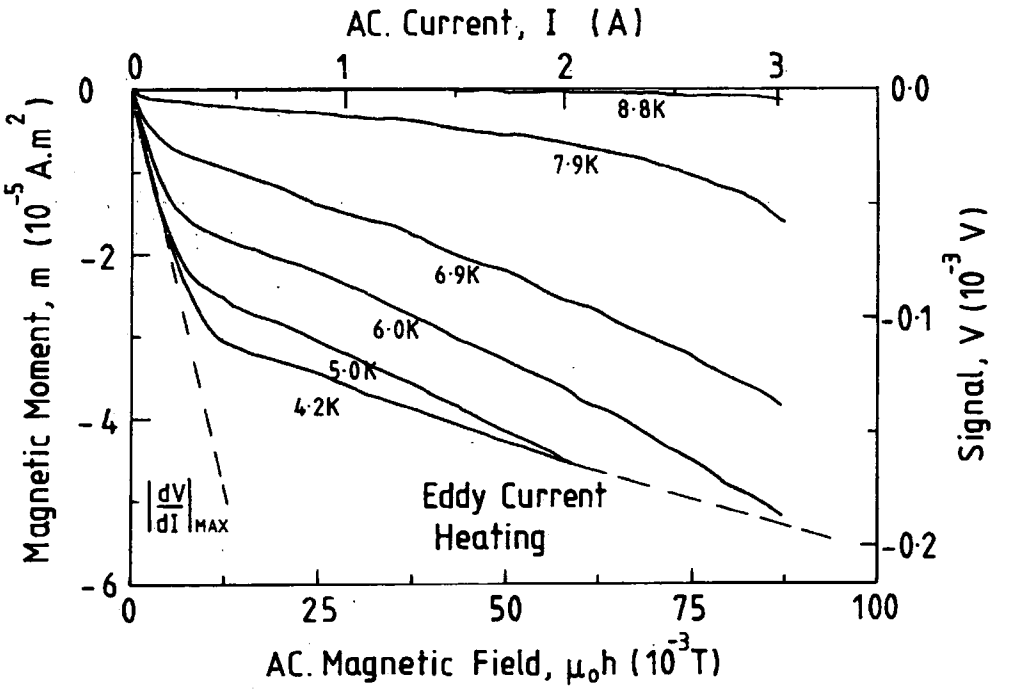

Figure 6.2 Magnetic moment versus ac. field for the NbTi sample as a function of temperature in an axial field of 3 T.

6.3 Analysis of results.

6.3.1 Magnetic field profiles.

Following the analysis outlined by Campbell [3], and using the data in figures 6.1 and 6.2, it is possible to determine magnetic field profiles inside the NbTi sample. The differential of the induced voltage with respect to the ac. field gives the penetration depth, (using equation 4.47).

Figures 6.3 and 6.4 show the spatial variation in the magnetic field ($\mu_0 M$) as a function of temperature for the sample in both a transverse and axial field. The macroscopic dimension of the sample is calculated using equation 4.48. The applied dc. field ($\mu_0 H$) and ac. field ($\mu_0 h$) can be added to the magnetic field produced by the NbTi ($\mu_0 M$) to give the net field B. The gradient of the lines ($dM/d\delta$) as a function of penetration depth gives the spatial variation of J_C, (equation 3.44).

For the sample in a transverse field, it can be seen that the gradient of the lines and hence J_C is approximately constant throughout the sample. This is expected as surface pinning is not a significant mechanism in this wire. The minimum in the magnetic moment, (in figure 6.1), corresponds to an apparent penetration of the magnetic field to a depth greater than the radius of the sample, (in figure 6.3). The fact that this is a artifact of the analysis has been shown in chapter 4 and is expected even for a bulk pinning superconductor such as NbTi [4].

For the sample in an axial field, two gradients can clearly be seen. These two gradients may be a result of two different currents flowing on two different length scales. ie. An intragranular J_C flowing with in the filaments and an intergranular J_C flowing across many filaments. This and other possible explanations are discussed in section 6.6.

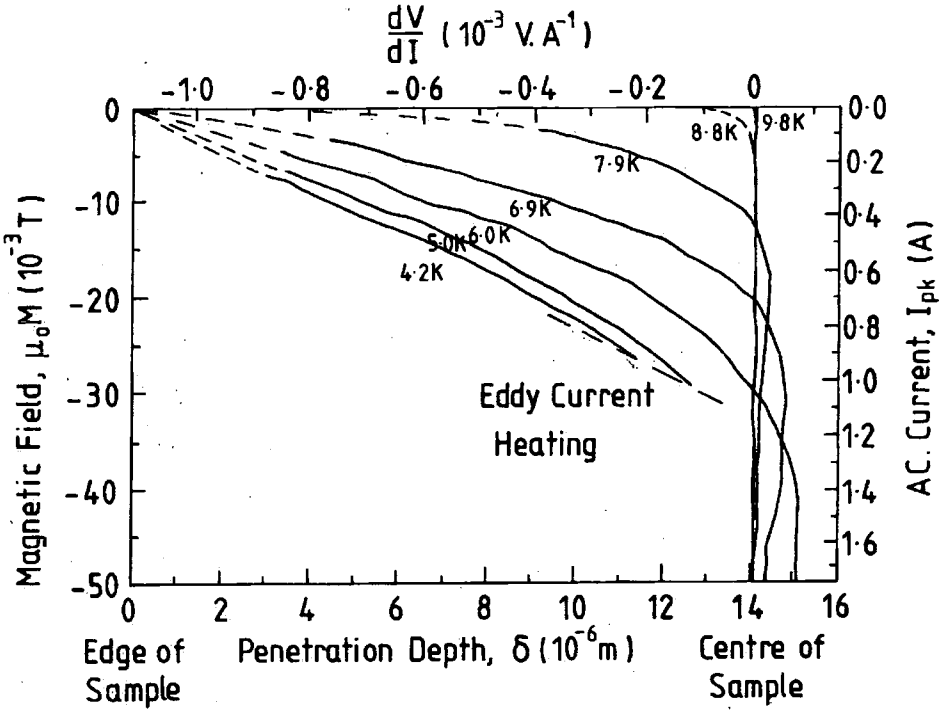

Figure 6.3 The magnetic field profile inside the NbTi sample as a function of temperature in a transverse field of 3 T.

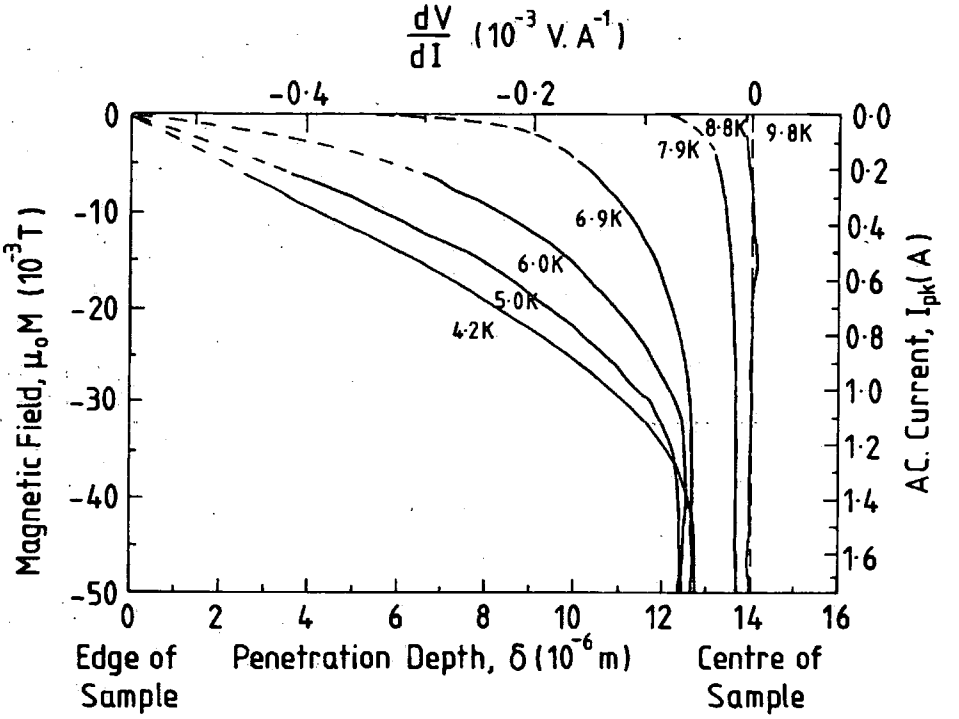

Figure 6.4 The magnetic field profile inside the NbTi sample as a function of temperature in an axial field of 3 T.

6.3.2 Critical current density.

The results obtained with the field applied perpendicular to the filaments (transverse b), are consistent with the description of a bulk pinning homogeneous superconductor, as described in chapter 4. From the minimum value of the magnetic moment, the coil geometry and the dimensions of the sample, it is possible to calculate the average critical current density at each field and temperature, (using equation 3.30). This is shown in figure 6.5. The values of J_C are accurate to within 10 %, primarily due to uncertainties in the sample dimensions.

At 6 T and 6 K, J_C is 6.2×10^8 A.m^{-2} which is in good agreement with transport current measurements on the same wire that give a value of 6.0×10^8 A.m^{-2} [5]. These values of J_C are standard for commercial NbTi wires, although higher values of have been obtained in multifilamentary NbTi by introducing artificial pinning centres to give J_C values of greater than 1×10^{10} A.m^{-2} at 1 T and 4.2 K, [6-8].

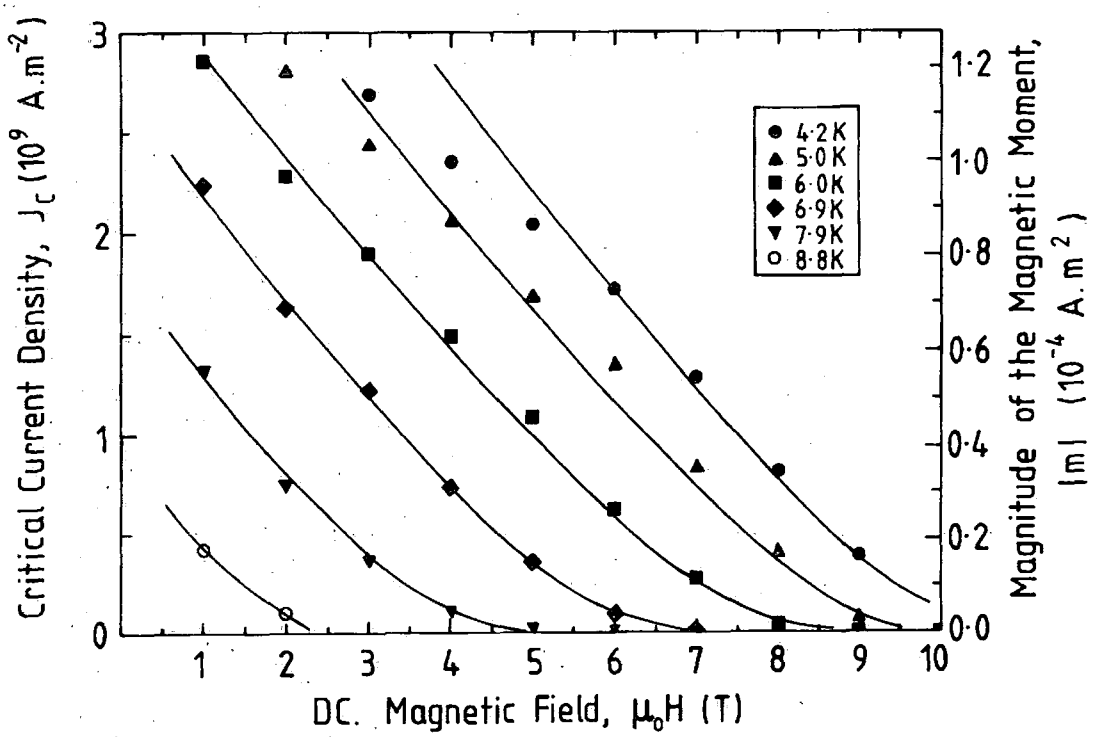

Figure 6.5 The critical current density of NbTi as a function of field and temperature.

6.3.3 Scaling relations and flux pinning.

Figure 6.6 shows the reduced volume pinning force (F_P/F_{PMAX}) versus the reduced magnetic field ($h=H/H_{C2}$) as a function of temperature. The volume pinning force is calculated using $F_P = \mu_0(J_C \times H)$ [9], while H_{C2} is taken to be the magnetic field at which the critical current density drops to zero. A single curve can be drawn through the data, consistent with Fietz-Webb scaling [10].

Alternatively, the high J_C data in figure 6.5 can be extrapolated linearly to zero. This gives an effective upper critical field ($\mu_0 H_{C2}^*$) which is about 10 % lower than that used in figure 6.6. The volume pinning force data can then be described by a scaling law of the form $F_P = \alpha(\mu_0 H_{C2})^n h(1-h)$, where $h=H/H_{C2}^*$, the index $n = 2.18 \pm 0.05$ and the constant $\alpha = (3.14 \pm 0.12) \times 10^8$ $T^{-1.18} A.m^{-2}$.

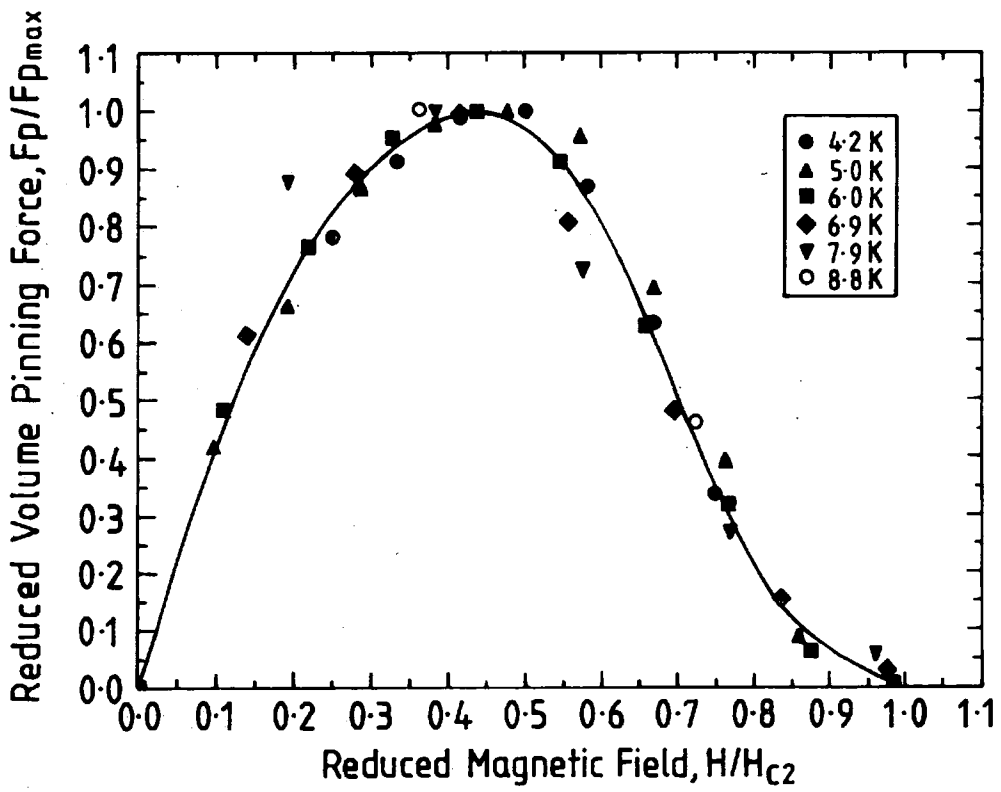

Figure 6.6 The reduced volume pinning force versus the reduced magnetic field as a function of temperature. (The curved line is a guide for the eye.)

6.4 Harmonic analysis.

Figures 6.7 and 6.8 show the harmonic response of both the lossless and loss components of the magnetic moment of NbTi in a transverse field. A background signal, taken when $T>T_C$, has been subtracted from all data. During the experiment a line filter was used to reduce noise and improve the quality of the data. The 3rd harmonic of 19.7 Hz lies close to the line frequency, (60 Hz in the USA). The filter both attenuates the signal by a factor of 0.65 and introduces a phase shift of 20°. The 3F data has been adjusted accordingly.

For the transverse field, the results are in good agreement with the theoretical predictions in chapter 4, (cf. figures 4.4-4.10). All of the even harmonics are zero, ie. less than ± 10 μV, and the odd harmonics are of the correct sign and functional form. For the lossless components (cf. figure 6.7), there is a factor of 4 between 3F and 5F in the field at which there is a minimum in the magnetic moment (b_{min}), while the magnitude of these minima (V_{min}) are similar. (Consistent with figures 4.6 and 4.10). For the loss components (figure 6.8), there is a factor of 2 in b_{min} between 3F and 5F while V_{min} are similar. (Consistent with figures 4.4 and 4.8.)

Figures 6.9 and 6.10 show the equivalent data for the sample in an axial field. As predicted, for all odd harmonics of both the loss and lossless components, the initial gradient (dV/db_m) is half that for the sample in transverse b. Again, all of the even harmonics are zero, ie. less than ± 10 μV, but the odd harmonics do not agree with the theoretical predictions in chapter 4. In particular, the 1F lossless component has a different field dependence to the higher harmonics (cf. figure 6.9). ie. As the field increases it does not reach a minimum but simply changes gradient. The higher harmonics are similar to those for a transverse field but V_{min} are an order of magnitude smaller. This is not consistent with the factor of $4/\pi$ found in chapter 4. However, in agreement with the theory, there is a factor of 3 in b_{min} between 3F and 5F while V_{min} for 3F, 5F, 7F and 9F are similar (cf. table 4.1). For the axial field, the loss components are also an order of magnitude smaller than for the transverse field, (cf. figure 6.10). Again there is a factor of 3 in b_{min} between 3F and 5F while V_{min} for 3F, 5F, 7F and 9F are similar (cf. table 4.1).

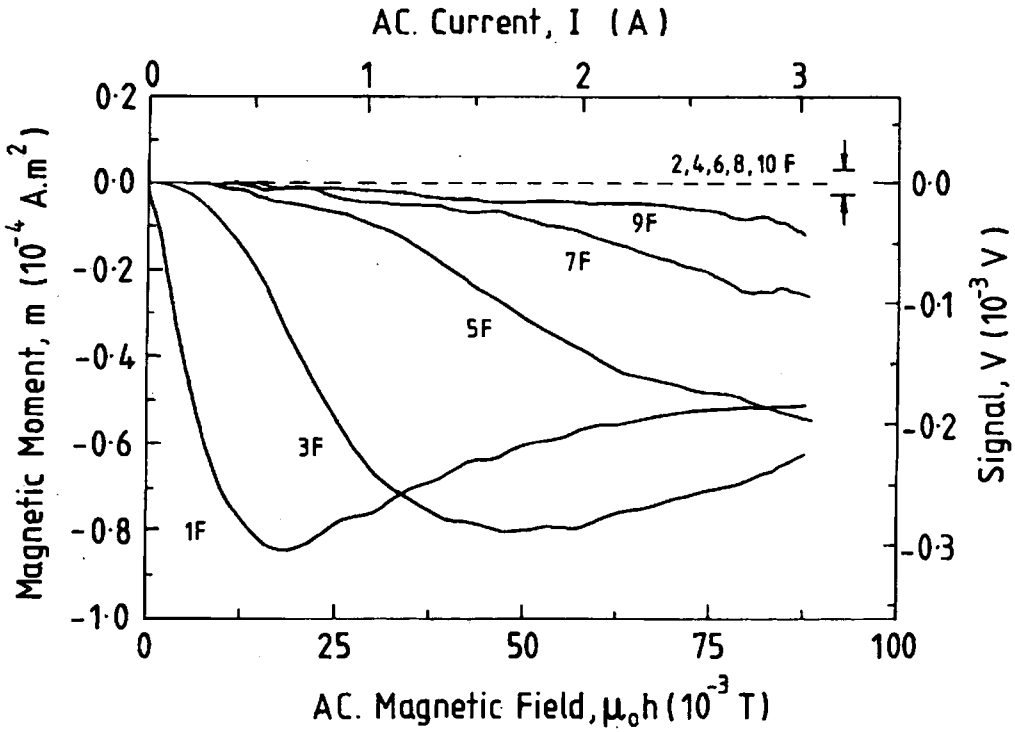

Figure 6.7 The harmonic response of the lossless component of the induced voltage for NbTi at 6 K in a transverse field of 3 T.

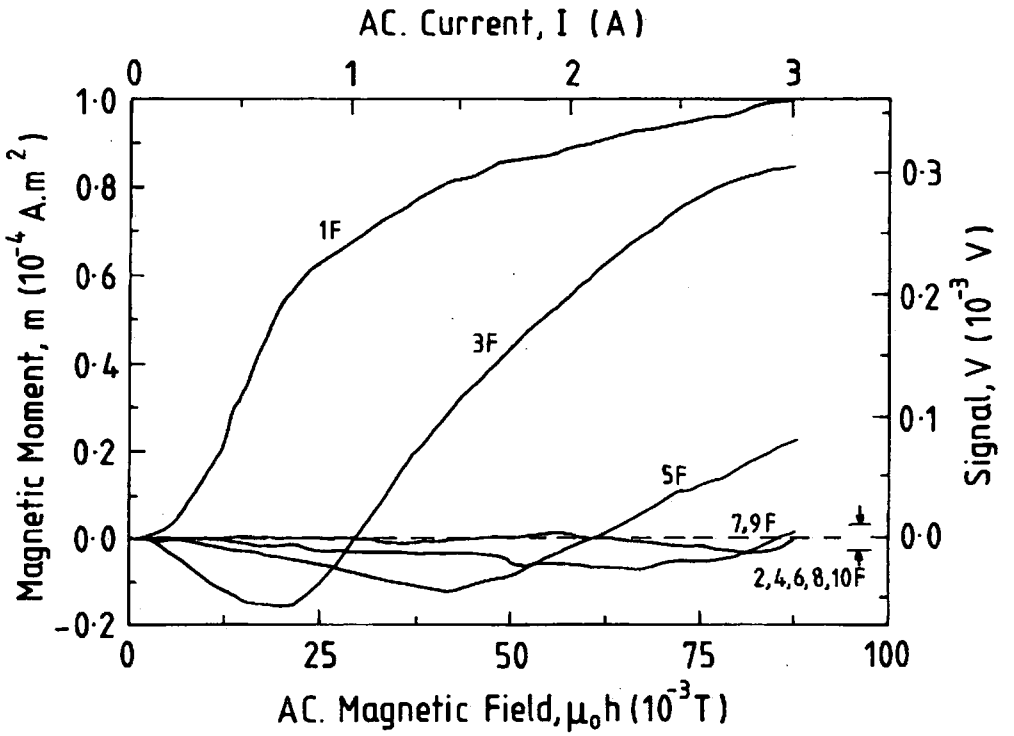

Figure 6.8 The harmonic response of the loss component of the induced voltage for NbTi at 6 K in a transverse field of 3 T.

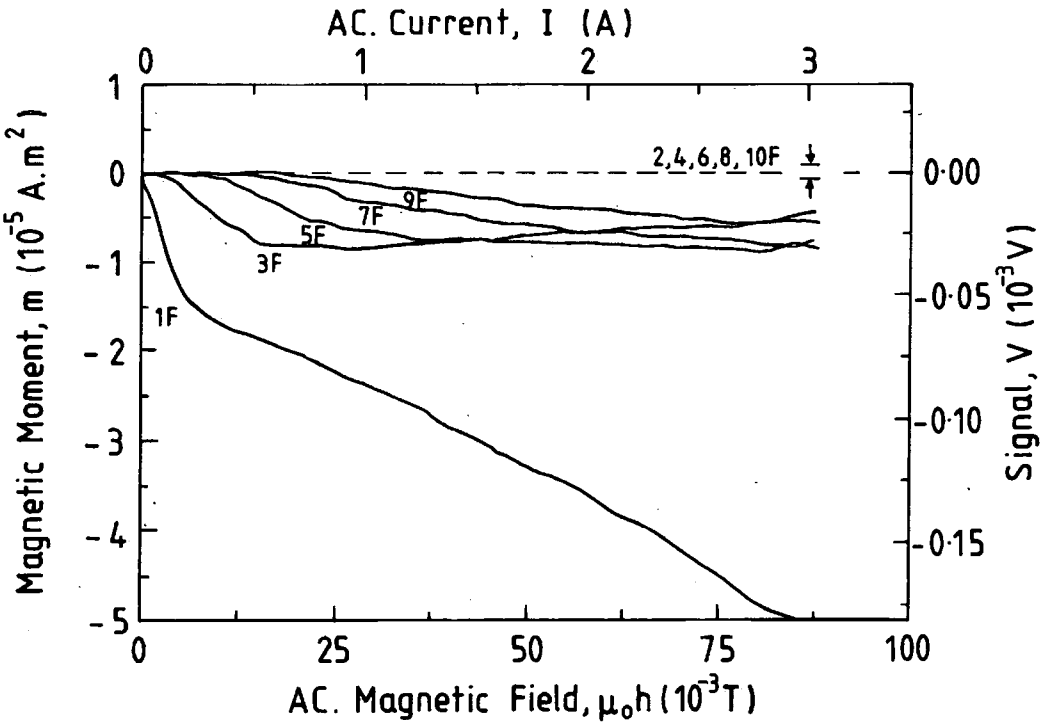

Figure 6.9 The harmonic response of the lossless component of the induced voltage for NbTi at 6 K in an axial field of 3 T.

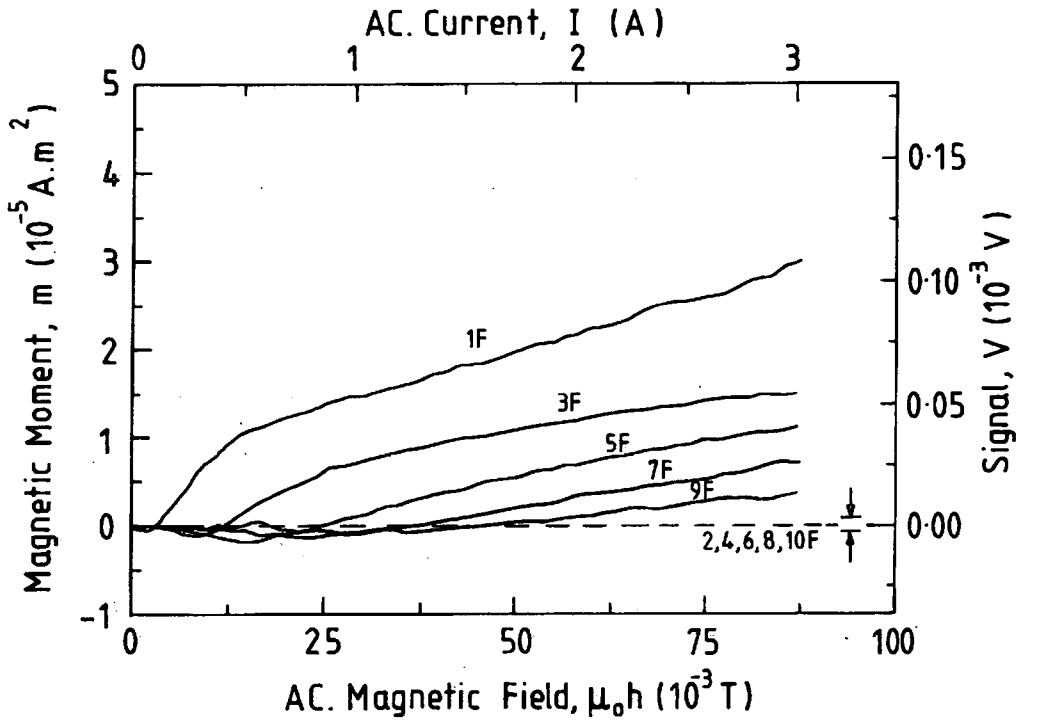

Figure 6.10 The harmonic response of the loss component of the induced voltage for NbTi at 6 K in an axial field of 3 T.

6.5 Discussion.

Several differences can be seen in the flux profiles and harmonic response of a sample in an axial field and transverse field.

For the sample in a transverse field, the flux profile is consistent with the theoretical analysis of a bulk pinning, homogenous superconductor (cf. chapter 4). The harmonic response of the sample in a transverse field is also consistent with the analysis in chapter 4 which suggests that the currents are flowing only in the filaments. This is confirmed by the values of $J_C(B,T)$ which are very similar to transport current measurements on the same sample. In this orientation, the multifilamentary NbTi sample can be considered to be a bulk pinning, homogenous superconductor.

For the sample in an axial field, two gradients can clearly be seen in the flux profile. This suggests that two J_C's are present, corresponding to the high J_C of individual filaments and the lower J_C of the entire sample. However, it is unlikely that this is the case as this granular effect would also be seen in the transverse orientation. More likely, the dramatic reduction in the magnetic moment and the unusual functional form of the 1F component can be explained by considering the construction of the sample and the Lorentz forces it experiences in an ac. field. In the axial orientation, any field gradient across the sample will cause the unconnected filaments within the 60 bundles to vibrate. This vibration will cause the filaments to quench, through frictional heating or large induced currents, thus decreasing the magnetic moment. This is unlikely to happen when the sample is in the transverse orientation for it is the entire bundle which must move. The quenching of the filaments in the axial orientation also explains the factor of 10 decrease in the magnitude of the loss components.

6.6 Conclusion.

Flux penetration measurements have been made on commercial, multifilamentary NbTi, a high J_C superconductor which exhibits strong bulk pinning. Results have been obtained with the applied field both perpendicular to the filaments (transverse b) and parallel to the filaments (axial b). The results have been used to calculate the functional form and spatial variation of J_C as a function of field and temperature. The harmonic response of the sample has also been investigated and compared to the theoretical predictions in chapter 4.

For the sample in a transverse field, the gradient of the flux profiles indicate that the spatial variation of J_C is small. As shown in chapter 4, the apparent penetration of the magnetic field to a depth greater than the sample radius is a artifact of the analysis and need not be attributed to sample granularity. At 6 T and 6 K the flux penetration measurements give a J_C of 6.2×10^8 A.m^{-2}. This is within 3.5% of transport current measurements on the same wire which give a value of 6.0×10^8 A.m^{-2}. The functional form of the volume pinning force obeys the universal Fietz-Webb scaling relation. Except at fields close to $H_{C2}(T)$, it can be described by $F_P = \alpha(\mu_0 H_{C2})^n h(1-h)$, where n = 2.18±0.05, $\alpha = (3.14\pm0.12)\times10^8$ T$^{-1.18}$A.m^{-2} and h is the reduced field. The harmonic response of the sample is consistent with the analysis of a non-granular superconductor in chapter 4. Both the flux profiles and harmonic response suggest that in this orientation the multifilamentary NbTi sample can be considered to be a bulk pinning, homogenous superconductor.

When the sample is in an axial field, the results are different. Most notably there is a dramatic reduction of the magnetic moment and the flux profiles, and harmonic response do not agree with the theoretical predictions in chapter 4. It is suggested that in this orientation, the Lorentz force on individual filaments causes them to move and quench.

References.

[1] Ramsbottom H D and Hampshire D P *Meas. Sci. Technol.* **6** 1349 (1995).

[2] Ramsbottom H D and Hampshire D P *Inst. Phys. Conf. Series No* **148** *EUCAS'95* 259 (1995).

[3] Campbell A M *J. Phys. C* **2** 1492 (1969).

[4] Ramsbottom H D and Hampshire D P *To be submitted to Phys. Rev. B* (1996).

[5] Friend C M and Hampshire D P *Applied Superconductivity Vol. 1 Proc. European Conf. on Applied Superconductivity* 23 (1993).

[6] Motowidlo L R, Zeitlin B A, Walker M S and Haldar P *Appl. Phys. Lett.* **61** (8) 991 (1992).

[7] Miura O, Inoue I, Suzuki T, Matsumoto K, Tanaka Y, Funaki K, Iwakuma M, Yamafugi K and Matsushita T *Cryogenics* **35** (3) 169 (1995).

[8] Miura O, Inoue I, Suzuki T, Matsumoto K, Tanaka Y, Funaki K, Iwakuma M, Yamafugi K and Matsushita T *Cryogenics* **35** (3) 181 (1995).

[9] Dew-Hughes D *Philos. Mag.* **30** 293 (1974).

[10] Fietz F A and Webb W W *Phys. Rev.* **178** (2) 657 (1969).

Chapter 7

Flux Penetration Measurements on unHIP'ed and HIP'ed Samples of the Chevrel Phase Superconductor $PbMo_6S_8$.

7.1 Introduction.

Since they were discovered over 20 years ago [1], Chevrel phase superconductors have been of great interest both as a potential material for new technological applications and for fundamental studies of superconductivity. With a T_C of 15 K [2] and an extremely high upper critical field of greater than 54 T at 4.2 K [3-7], $PbMo_6S_8$ (PMS) is a candidate for high field technological applications [8,9]. Equally, it has a coherence length of (2nm) [10], between that of the commercially important low temperature superconductors (5nm) and the high temperature superconductors (0.5nm) and therefore provides a model system to develop an understanding of superconductivity [11].

This chapter presents detailed variable temperature flux penetration measurements on PMS in high magnetic fields. Using a purpose-built probe [12], data were obtained from 4.2 K up to T_C in magnetic fields up to 10 T. During these measurements the magnetic field was applied parallel to the long axis of the sample. The results are used to measure the improvement in J_C achieved by fabricating PMS using a hot isostatic press (HIP). Hot isostatic pressing involves the simultaneous application of high pressure and high temperature to achieve a dramatic increase in density and improve other metallurgical properties such as homogeneity, fracture toughness and phase purity [13-17]. If the critical current density of PMS can be increased above the present state-of-the-art values by a factor of five, wires of PMS may be an essential component in the next generation of high field magnets operating above 20 T.

In section 7.2 the fabrication route for producing a HIP'ed sample of PMS is described. Results are shown which give an indication of the quality of the sample. This section also includes the results of the flux penetration measurements. In section 7.3 these results are used to investigate magnetic field profiles, critical current densities and scaling relations. At the end of the chapter is a discussion and summary.

7.2 Experimental.

7.2.1 Sample preparation and quality.

Bulk sintered PMS was prepared at ambient pressure by a two-step solid state reaction procedure. 10 g of starting material of Pb (99.9999% purity), Mo (99.95% purity, 4-8 μm grain size) and S (99.999% purity) were mixed in a glove box in the atomic ratio 1 : 6 : 8, transferred into a silica tube and sealed under vacuum. This was put into a furnace and reacted in flowing high purity argon at 450 ^{0}C for 4 hours. Then the temperature was slowly increased to 650 ^{0}C at 33 ^{0}C.hr^{-1} and held constant for 8 hours. The sample was allowed to cool to room temperature in approximately 15 minutes. Before the second reaction, the material was ground in the glove box and pressed into pellets under vacuum. It was then sealed in a silica ampoule under vacuum and reacted in flowing argon in a furnace at 1000 ^{0}C for 44 hours. Care was taken during the fabrication procedure to ensure that the PMS sample was not exposed to oxygen which degrades the superconducting properties [18-20]. The glove box maintains a controlled atmosphere such that the oxygen concentration is < 5 ppm and the moisture level is < 10 ppm. A sample with dimensions 2mm × 2mm × 6mm was cut from the as-sintered pellets for the measurements on PMS fabricated at ambient pressure (unHIP'ed sample).

The HIP'ed PMS was then fabricated as follows [21]. The sintered material was reground in the glove box and again pressed under vacuum into a pellet. The pellet was wrapped in Mo foil (99.95 %, 0.025 mm thick) and sealed under vacuum in a stainless steel tube and HIP'ed. The pressure in the HIP was increased to 1.2×10^8 N.m^{-2}. The temperature was then increased to 800 ^{0}C and the pressure increased to 2×10^8 N.m^{-2} (2000 bar). The temperature was maintained at 800 ^{0}C for 8 hours. During this period, the pressure slowly decreased from 2×10^8 N.m^{-2} to 1.3×10^8 N.m^{-2}. The HIP'ed sample was then extracted from the Mo foil and cut into dimensions 5.0mm × 2.8mm × 0.8mm for the flux penetration measurements.

The PMS samples have been characterised using ac. susceptibility, x-ray diffraction (XRD) and scanning electron microscopy (SEM). As shown in figure 7.1, ac. susceptibility measures T_C at 13.5 K ($\Delta T_C \approx 1$ K) in the HIP'ed sample, approximately

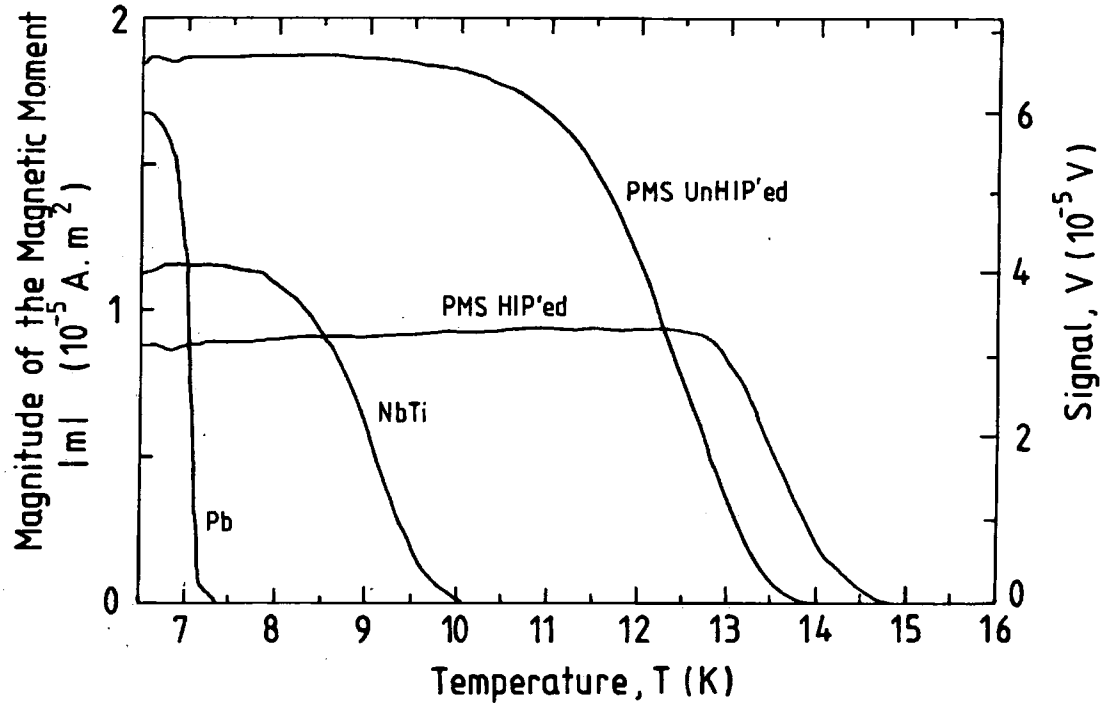

Figure 7.1 The ac. susceptibility of both unHIP'ed and HIP'ed $PbMo_6S_8$.

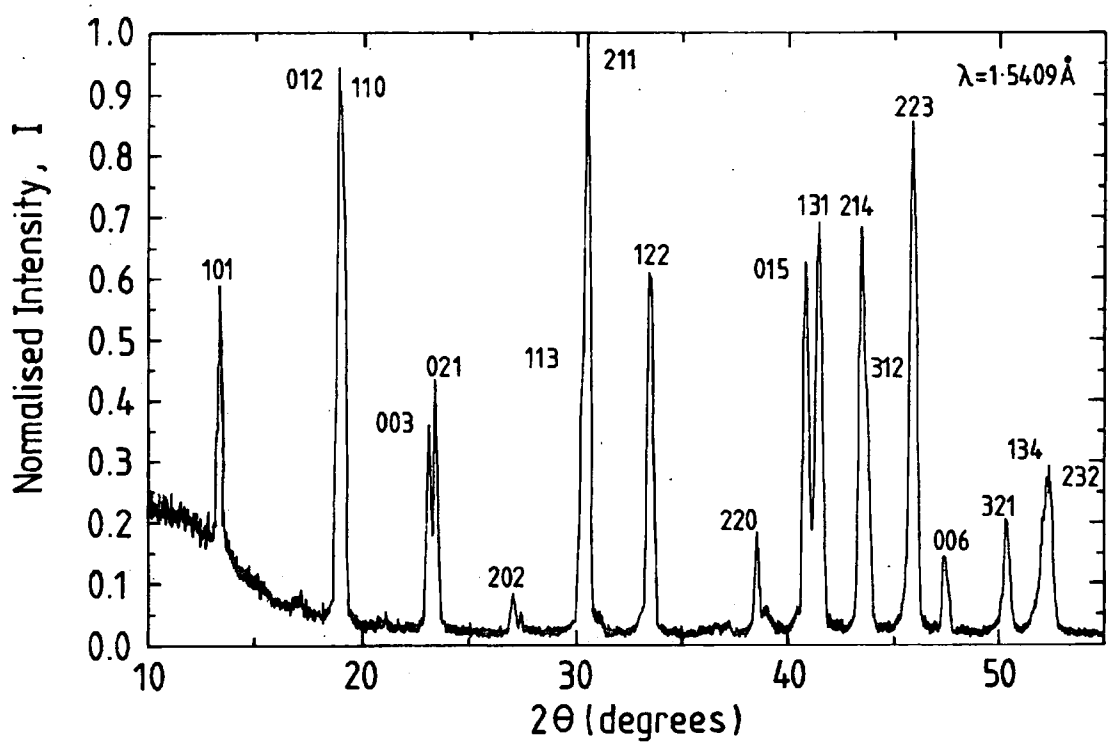

Figure 7.2 The x-ray diffraction pattern for the unHIP'ed sample of $PbMo_6S_8$.

1 K higher than that of the unHIP'ed sample, with a T_C of 12.5 K ($\Delta T_C \approx 2$ K). The increase in T_C and reduction in the transition width has also been observed by Seeber [22]. Figure 7.2 shows the XRD trace for the unHIP'ed sample. All of the major peaks can be attributed to PMS [23], which suggests that the samples are predominantly single phase. The SEM shows that the grain size is approximately 3-4 μm and demonstrates the marked increase in density, from less than 70% dense (unHIP'ed) to greater than 90% dense (HIP'ed). These results are typical of high quality PMS samples.

7.2.2 Experimental results.

Figures 7.3 and 7.4 show the magnetic moment versus the ac. field for the unHIP'ed sample as a function of temperature at both 3 T and 5 T respectively [24]. In these figures the current through the primary coil and the voltage across the secondary coils are also included. A background signal, taken when $T>T_C$, has been subtracted from the data. At both fields and at all temperatures there is a sharp fall in the magnetic moment down to a minimum value when there is full penetration of the superconductor. After this there is a slow increase in the magnetic moment as the ac. field is increased beyond that required for full penetration. The magnitude of the minimum magnetic moment for any temperature at 5 T is typically half of that found at 3 T, consistent with the expected reduction in J_C. The marked increase at high ac. fields (in figure 7.3 at 4.2, 5 and 6 K and in figure 7.4 at 4.2 K) is attributed to eddy current heating in the copper components of the probe.

Figures 7.5 and 7.6 show the equivalent data for the HIP'ed sample. The shapes of the curves are similar to those for the unHIP'ed sample but the magnitude of the magnetic moments when the sample is fully penetrated are more than an order of magnitude higher, (for equivalent fields and temperatures).

Figures 7.7 and 7.8 show the magnetic moment versus ac. field for both the unHIP'ed and a HIP'ed sample of PMS as a function of dc. field at 6 K and 11.7 K respectively. As before, the marked increase at high ac. fields is due to eddy current heating. The maximum ac. field which can be obtained is limited at high temperatures and high dc. fields, which cause the superconducting primary coil to quench.

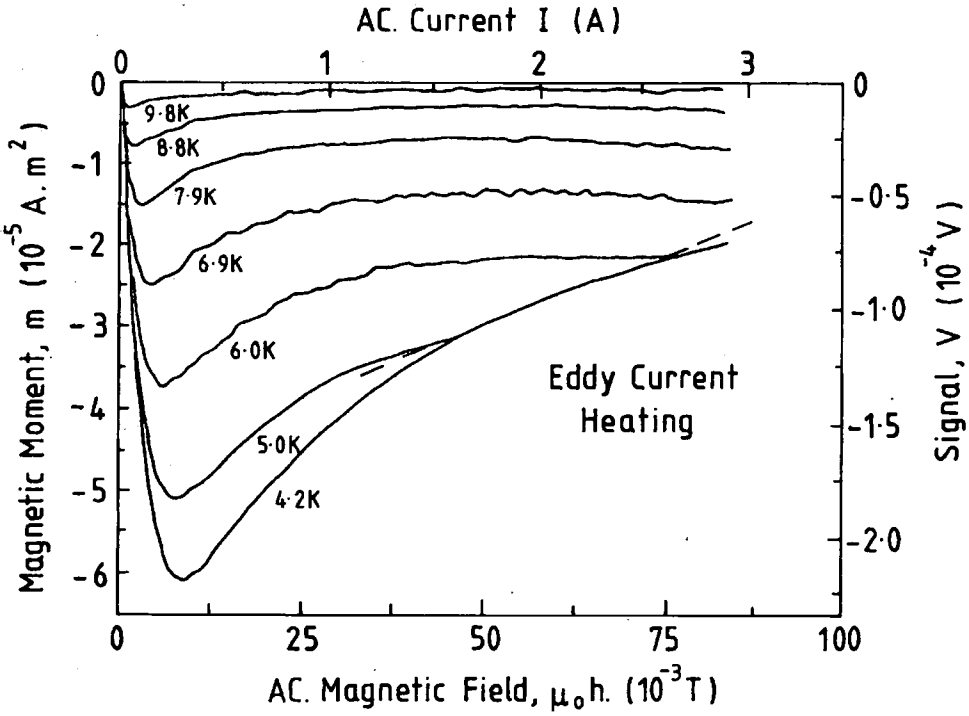

Figure 7.3 Magnetic moment versus ac. field of unHIP'ed PMS as a function of temperature at 3 T.

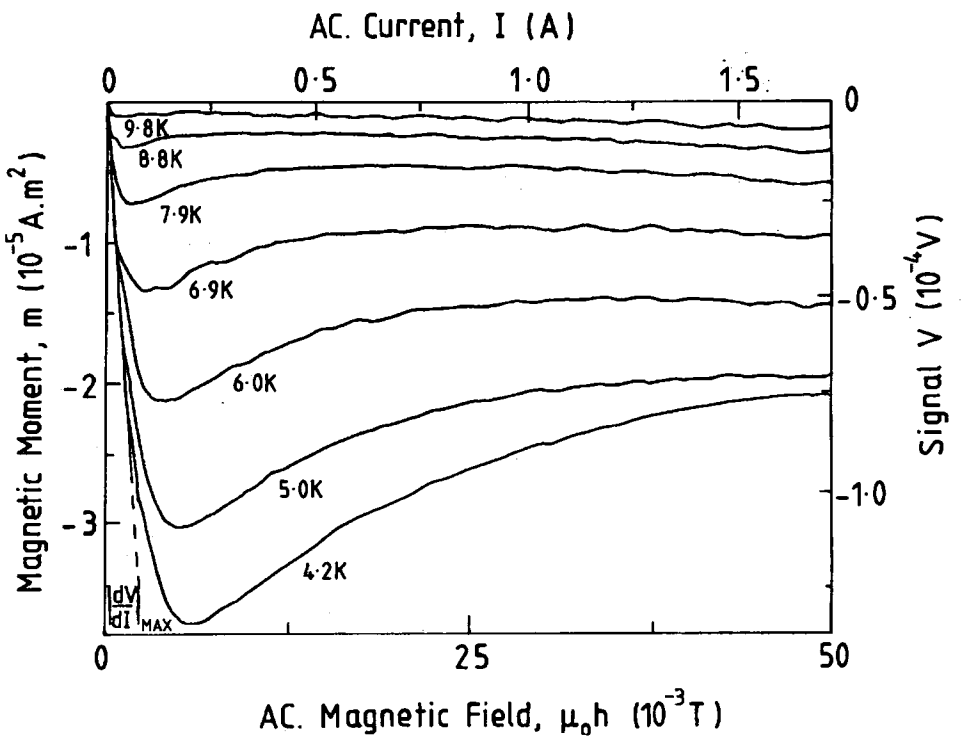

Figure 7.4 Magnetic moment versus ac. field of unHIP'ed PMS as a function of temperature at 5 T.

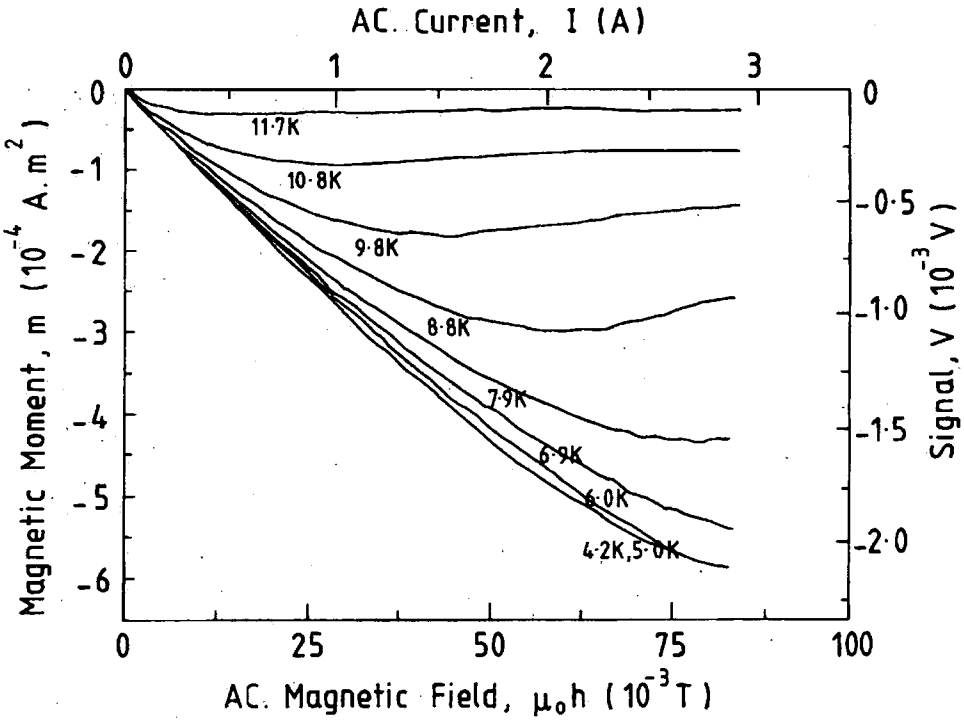

Figure 7.5 Magnetic moment versus ac. field of HIP'ed PMS as a function of temperature at 3 T.

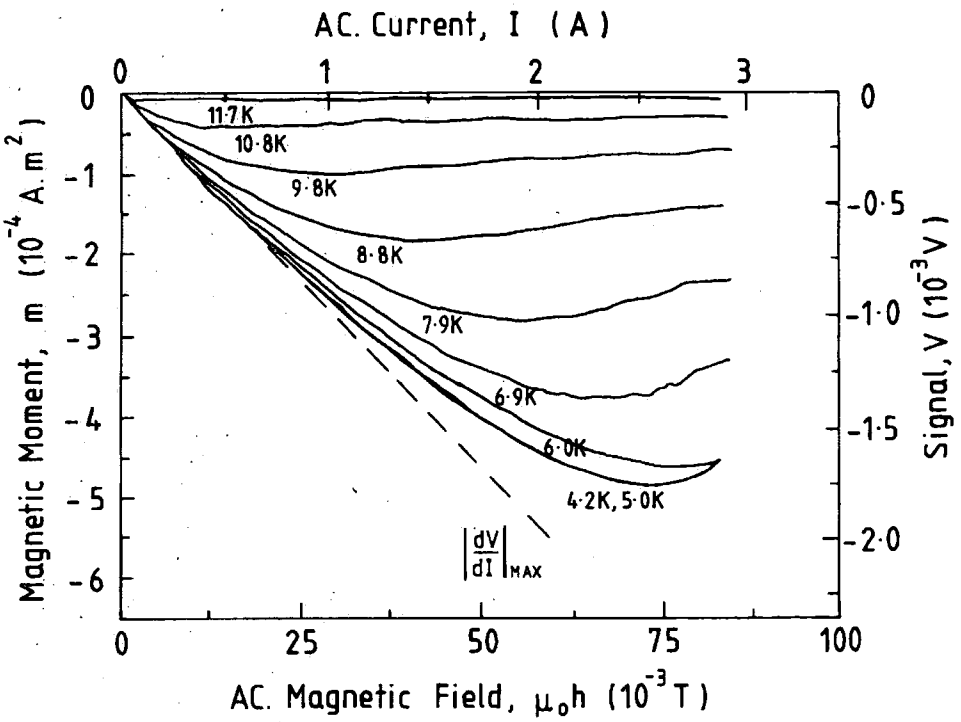

Figure 7.6 Magnetic moment versus ac. field of HIP'ed PMS as a function of temperature at 5 T.

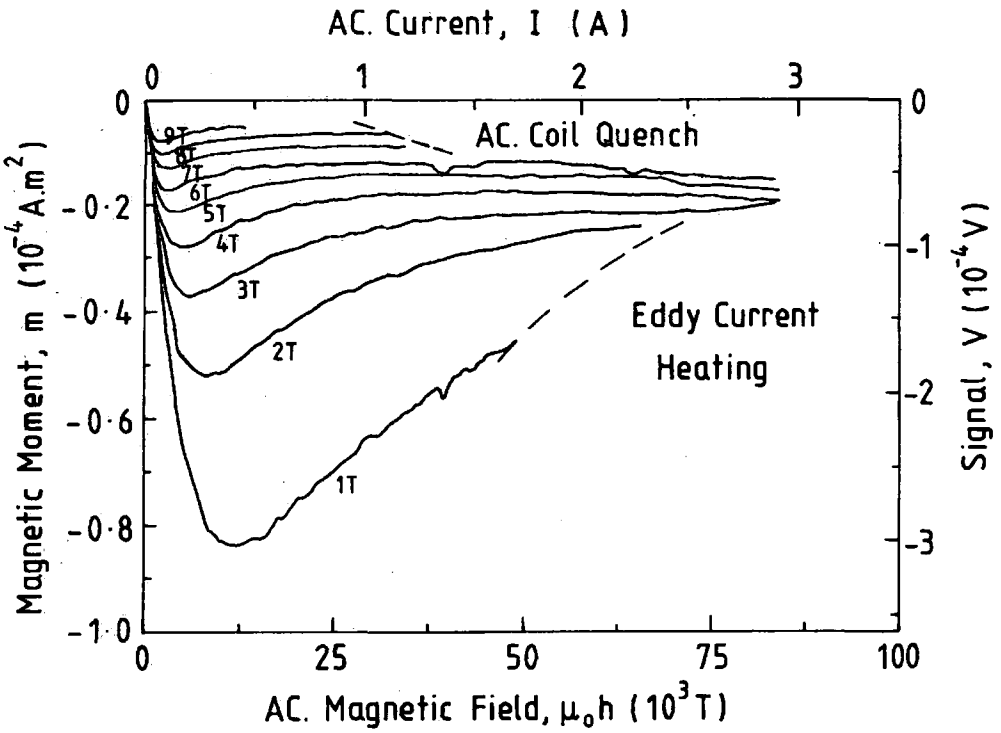

Figure 7.7 Magnetic moment versus ac. field of unHIP'ed PMS as a function of dc. field at 6 K.

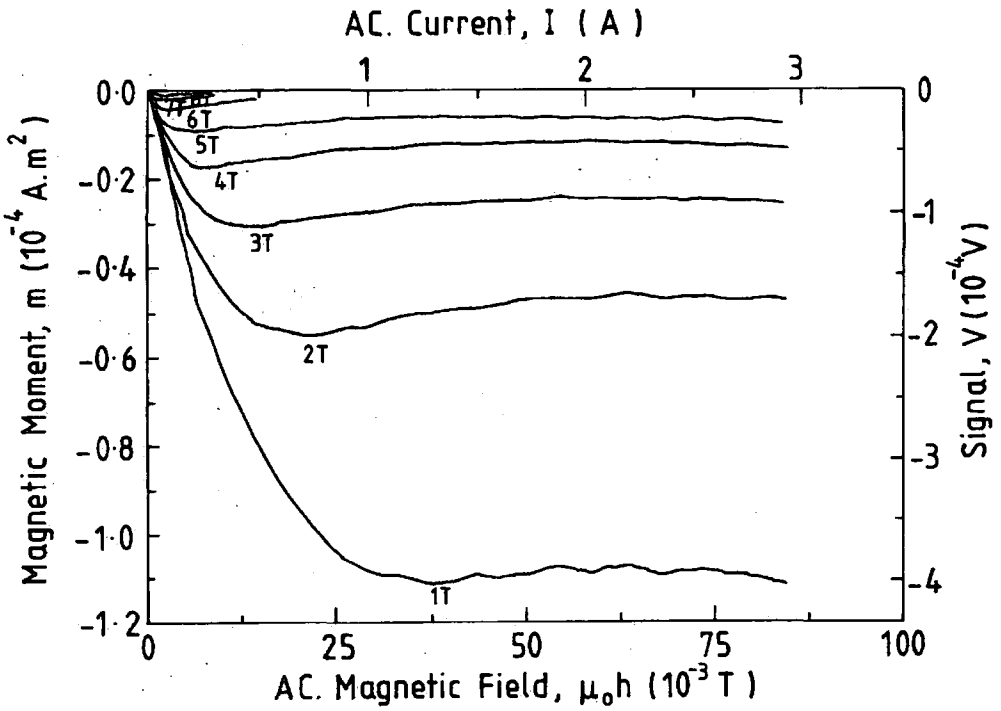

Figure 7.8 Magnetic moment versus ac. field of HIP'ed PMS as a function of dc. field at 11.7 K.

Although the experimental results for both unHIP'ed and HIP'ed PMS are quite similar, there are a few differences that are highlighted by figures 7.7 and 7.8. For the unHIP'ed sample, at low dc. fields there is a dramatic decrease in the magnitude of the magnetic moment as the ac. field is increased beyond that required to fully penetrate the sample, eg. by approximately 50% at 2 T. This effect decreases at higher dc. fields, so that by 8 T the reduction is just 15%. For the HIP'ed sample, the reduction in the magnitude of the magnetic moment as the ac. field is increased is almost constant, ie. approximately 15% for all dc. fields.

7.3 Analysis of results.

7.3.1 Magnetic field profiles.

Figures 7.9 and 7.10 show the magnetic field profiles for the unHIP'ed sample of PMS as a function of field and temperature. Figures 7.11 and 7.12 show equivalent magnetic field profiles for the HIP'ed sample of PMS. The macroscopic dimension of the sample is calculated using equation 4.48. The applied dc. field ($\mu_0 H$) and ac. field ($\mu_0 h$) can be added to the field produced by the PMS ($\mu_0 M$) to give the net field B.

7.3.2 Critical current density.

Using Bean's critical state model [25], an equivalent critical current density can be calculated from the minimum value of the magnetic moment at each field and temperature. In figures 7.13 and 7.14, the calculated J_C values are presented for the HIP'ed and unHIP'ed PMS samples. The values of J_C are accurate to within 10%, primarily due to the uncertainty in the dimensions of the samples. By comparing these two figures it can be seen that HIP'ing the PMS has increased J_C by a factor of 20, giving a value of greater than 3×10^8 A.m^{-2} at 5 T and 6 K. J_C(B,T) is of the same order as the highest values, reported by Cheggour et al [26]. They have measured the transport J_C of a HIP'ed wire to be 5.0×10^8 A.m^{-2} at 15 T and 4.2 K.

7.3.3 Scaling relations and flux pinning.

Figures 7.15 and 7.16 show Kramer plots for both the unHIP'ed and HIP'ed samples of PMS. A linear extrapolation of the data to $J_C^{1/2}(\mu_0 H)^{1/4} = 0$ gives the irreversibility field ($\mu_0 H_{irr}$) for each temperature. The volume pinning force is calculated using the equation $F_P = \mu_0(J_C \times H)$.

Figures 7.17 and 7.18 show the reduced volume pinning force (F_P/F_{PMAX}) versus the reduced magnetic field ($h=H/H_{irr}$) as a function of temperature, where H_{irr} is taken from the Kramer plots. Both sets of data can be described by $F_P = \alpha(\mu_0 H_{irr})^n h^{1/2}(1-h)^2$. The index n = 2.36±0.11 and 2.52±0.11 and the constant α = 2.00×10^5 $T^{-1.36}A.m^{-2}$ and 3.22×10^5 $T^{-1.52}A.m^{-2}$, for both the unHIP'ed and HIP'ed samples of PMS respectively. The change in α highlights the change in sample microstructure on HIP'ing. The results are in good agreement with transport data on the same samples [27].

Figure 7.19 shows the irreversibility field plotted as a function of temperature for both unHIP'ed and HIP'ed PMS. The solid squares show values of $\mu_0 H_{C2}$ for HIP'ed PMS obtained by dc. magnetisation measurements.

7.4 Discussion.

The difference between the graphs showing the magnetic moment versus ac. field as a function of dc. field for the unHIP'ed and HIP'ed samples of PMS (ie. figures 7.7 and 7.8), can be explained by considering the magnetic field dependence of J_C. The results suggest that at low dc. fields, the J_C of the unHIP'ed sample is very sensitive to changes in magnetic field. At high ac. fields, the J_C decreases and thus the magnitude of the magnetic moment is reduced to a value below that expected from the analysis of a sample with a field independent J_C (shown in chapter 4). This effect is less at high dc. fields, where the dc. field dependence of J_C dominates. For the HIP'ed sample, J_C is far less sensitive to changes in the magnetic field and can be assumed to be constant over the entire ac. field range.

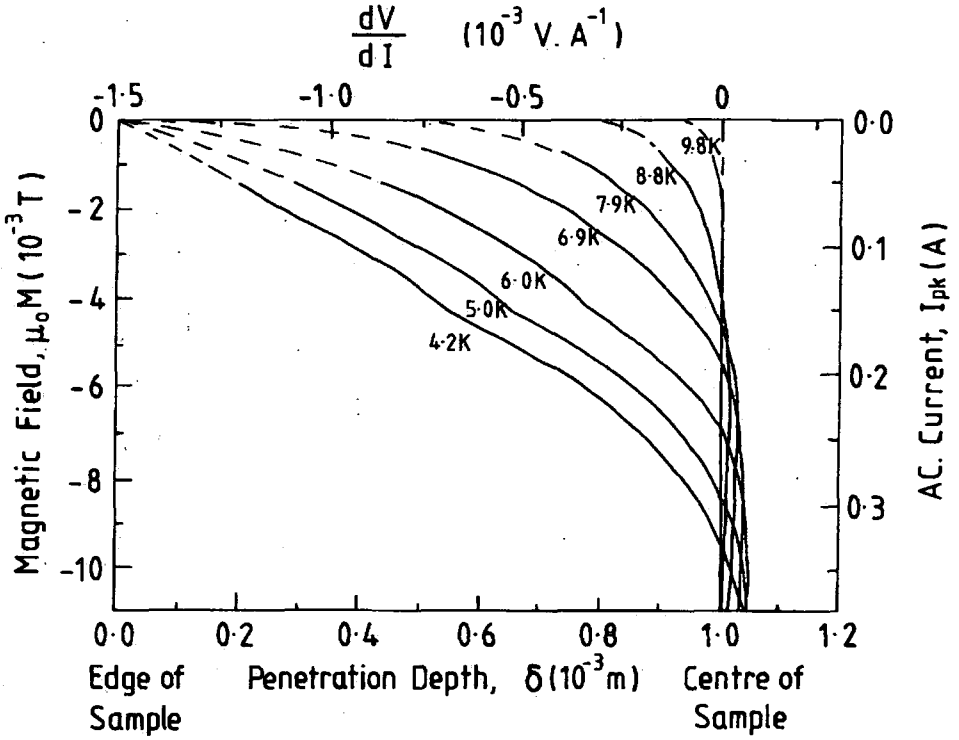

Figure 7.9 The magnetic field profile inside an unHIP'ed sample of PMS as a function of temperature at 5 T.

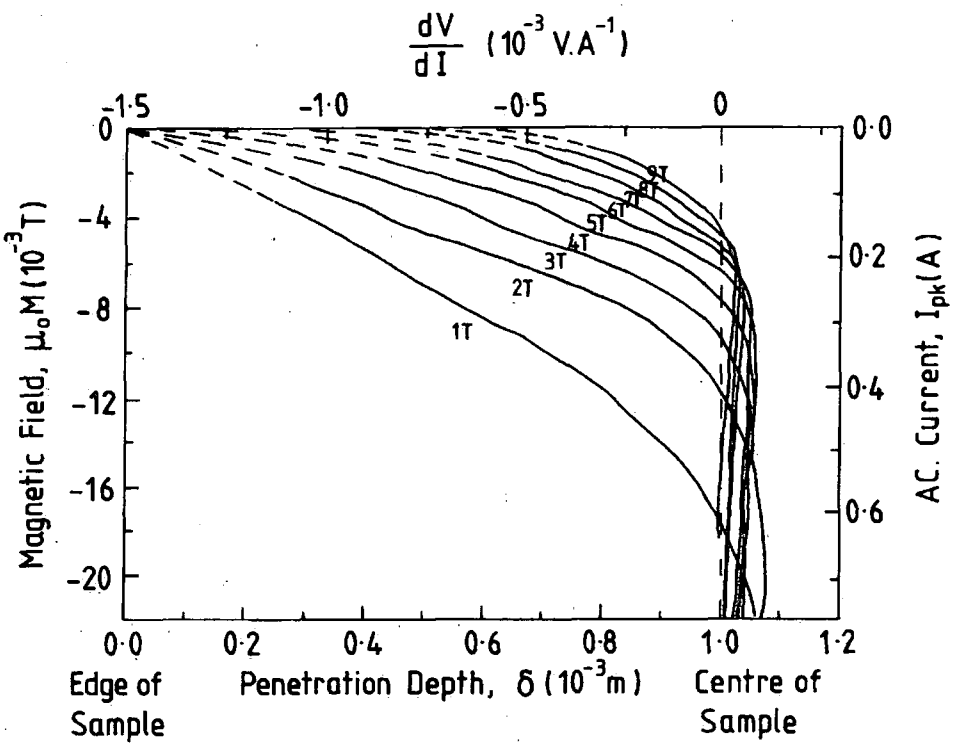

Figure 7.10 The magnetic field profile inside an unHIP'ed sample of PMS as a function of dc. field at 6 K.

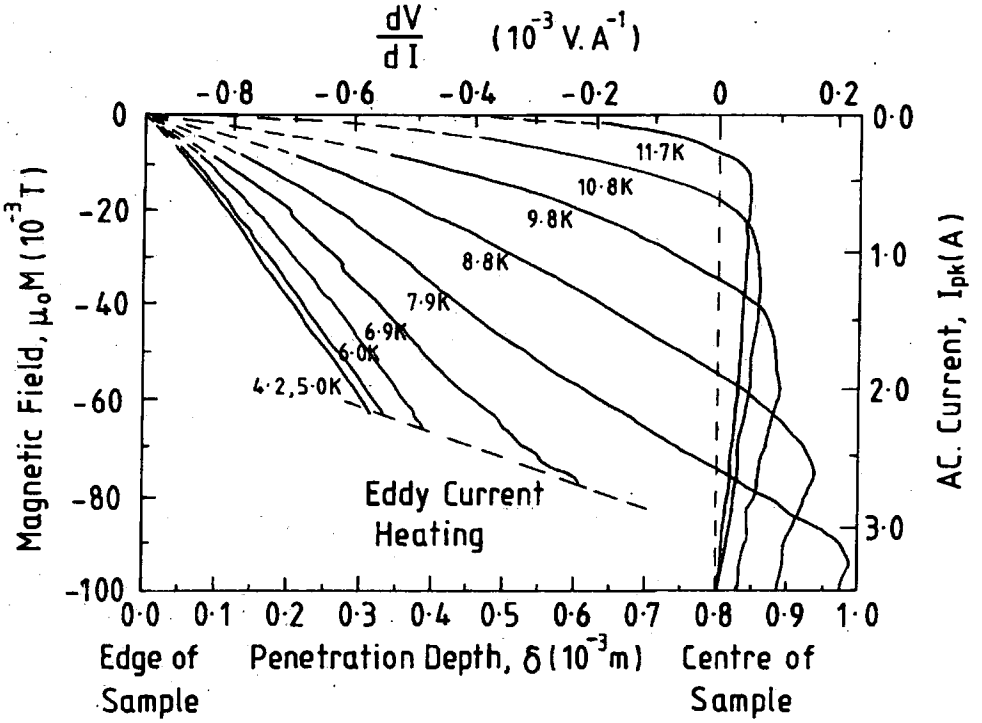

Figure 7.11 The magnetic field profile inside a HIP'ed sample of PMS as a function of temperature at 5 T.

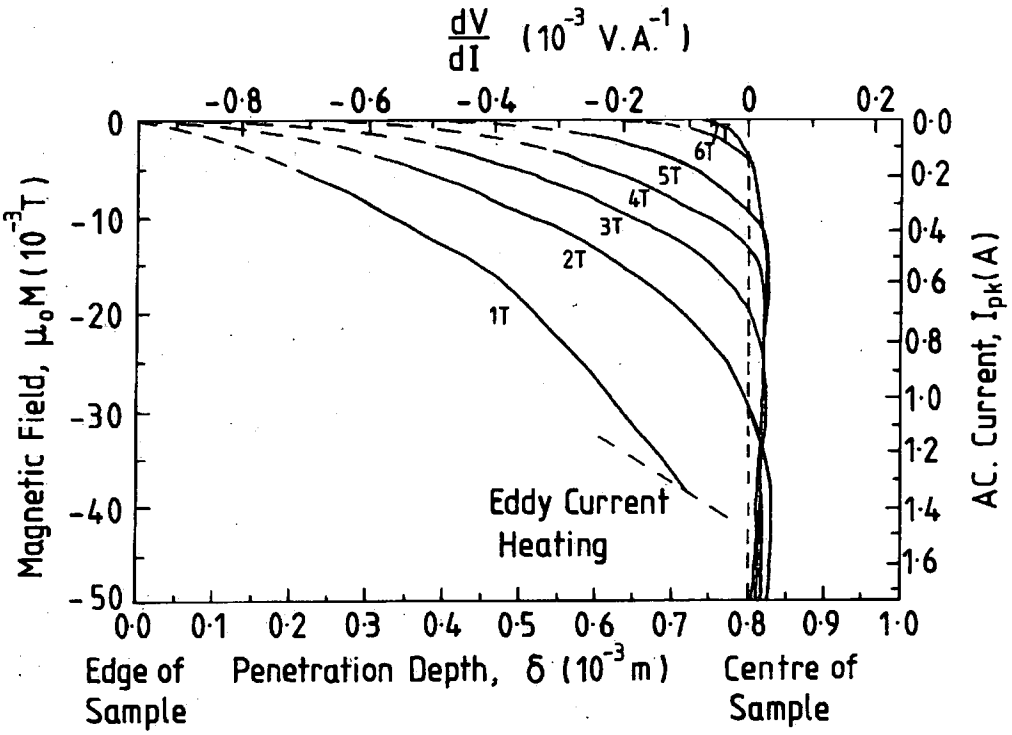

Figure 7.12 The magnetic field profile inside a HIP'ed sample of PMS as a function of dc. field at 11.7 K.

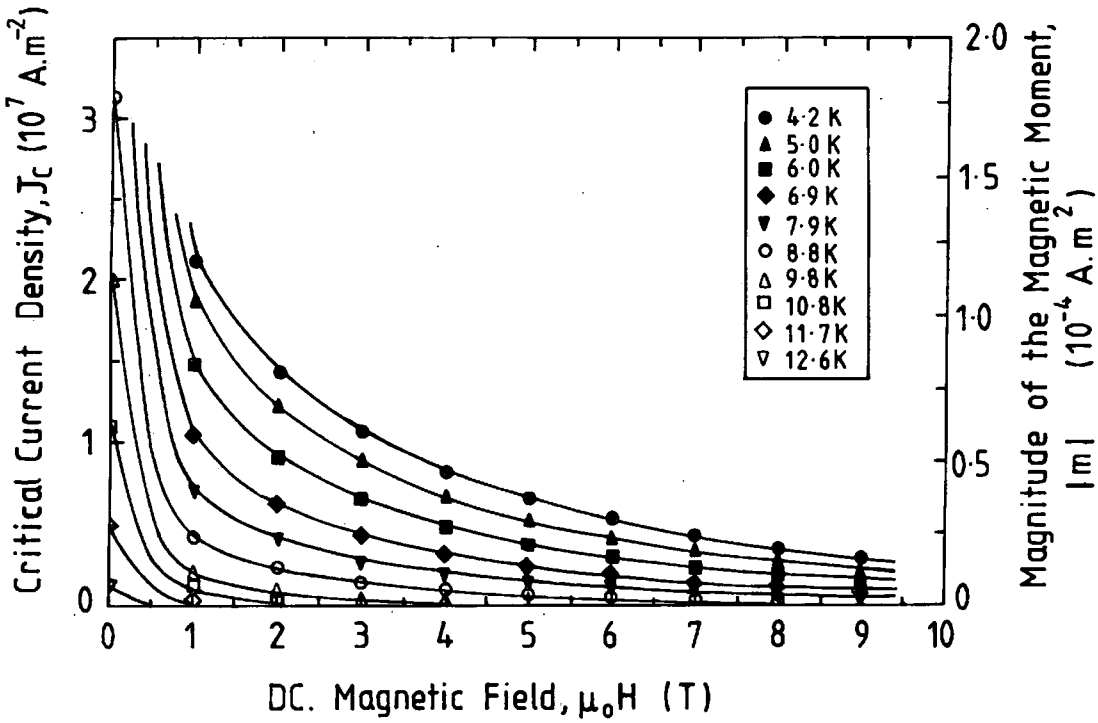

Figure 7.13 The critical current density of unHIP'ed PMS as a function of field and temperature.

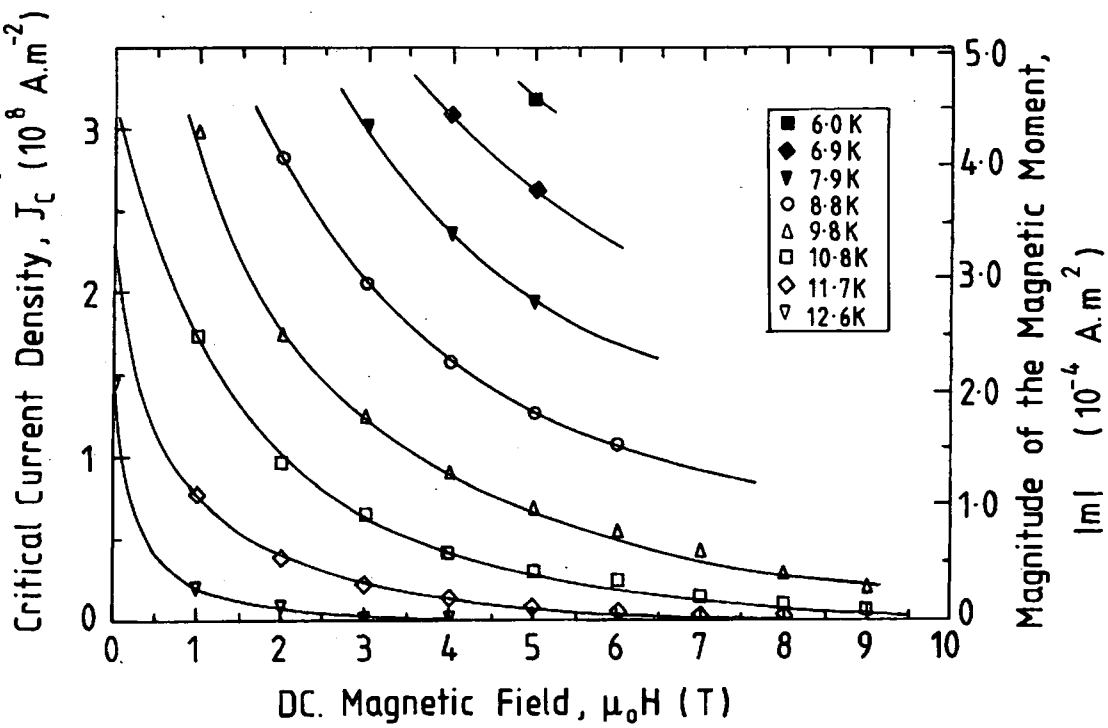

Figure 7.14 The critical current density of HIP'ed PMS as a function of field and temperature.

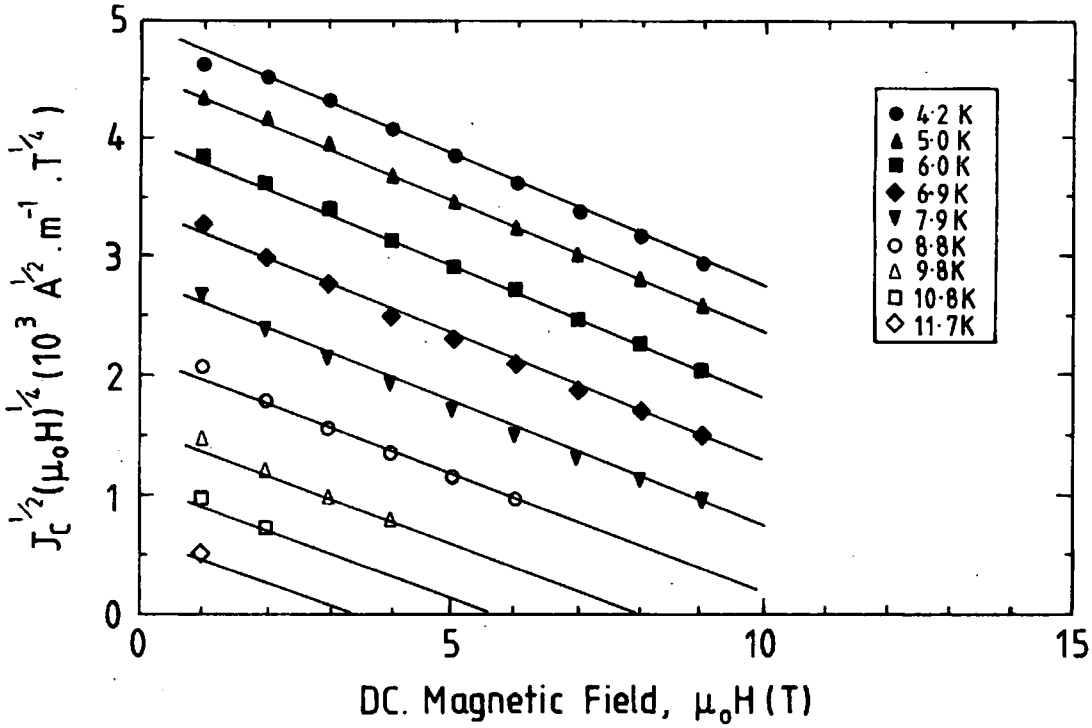

Figure 7.15 A Kramer plot for the unHIP'ed sample of PMS.

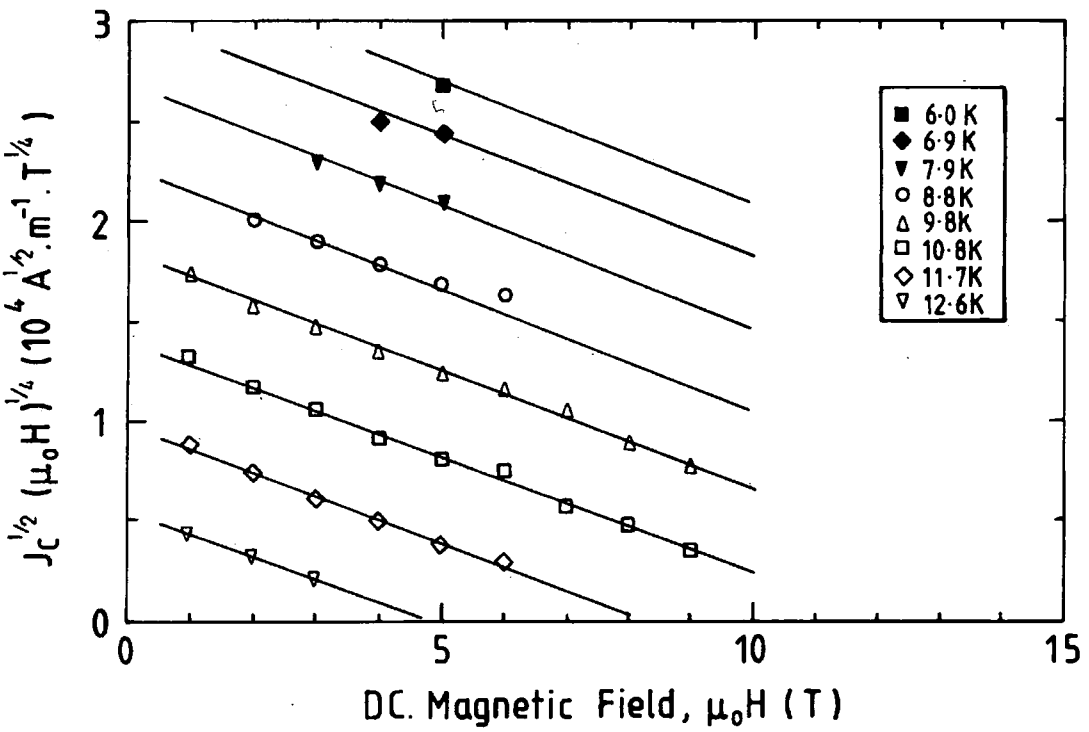

Figure 7.16 A Kramer plot for the HIP'ed sample of PMS.

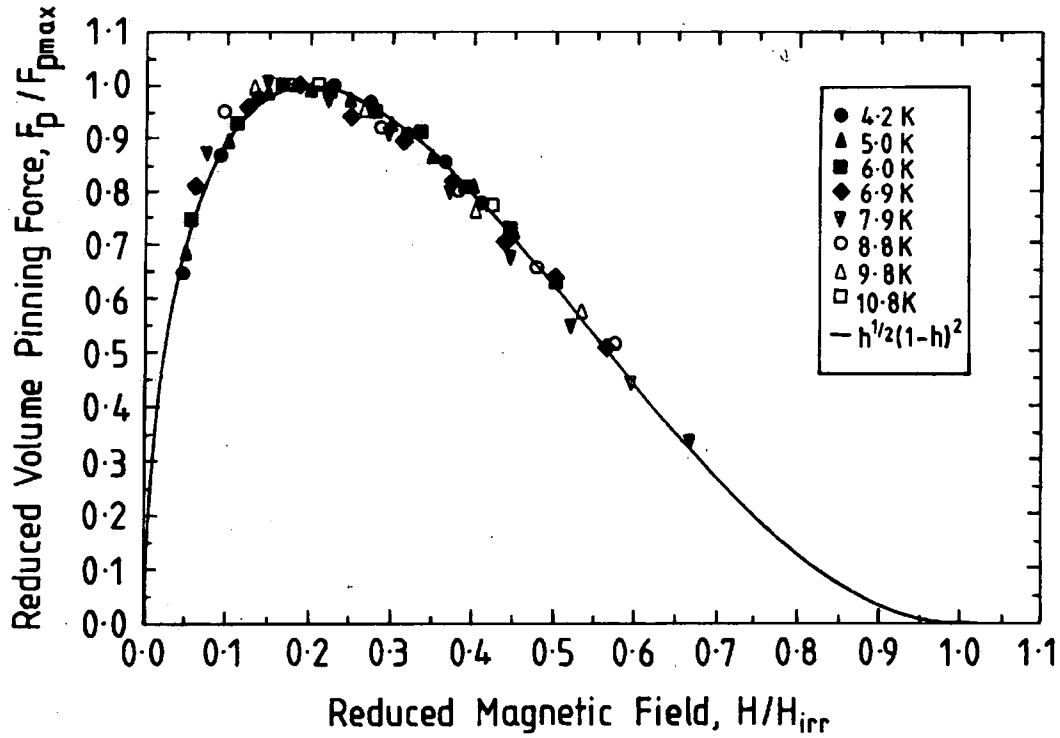

Figure 7.17 The reduced volume pinning force versus the reduced magnetic field as a function of temperature for the unHIP'ed sample of PMS.

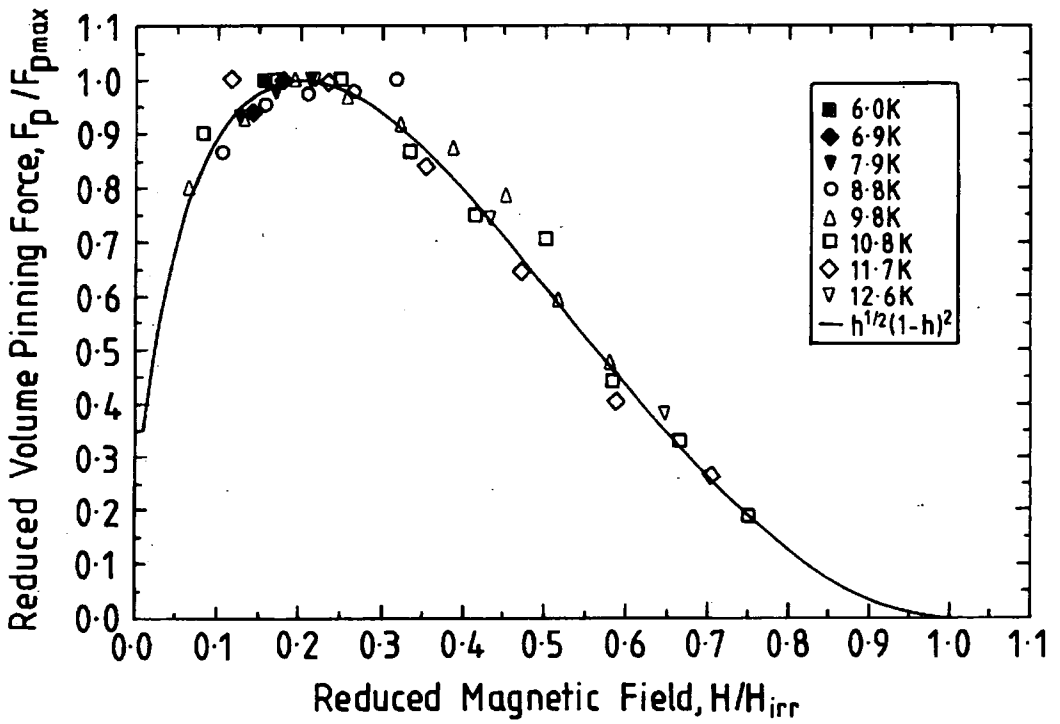

Figure 7.18 The reduced volume pinning force versus the reduced magnetic field as a function of temperature for the HIP'ed sample of PMS.

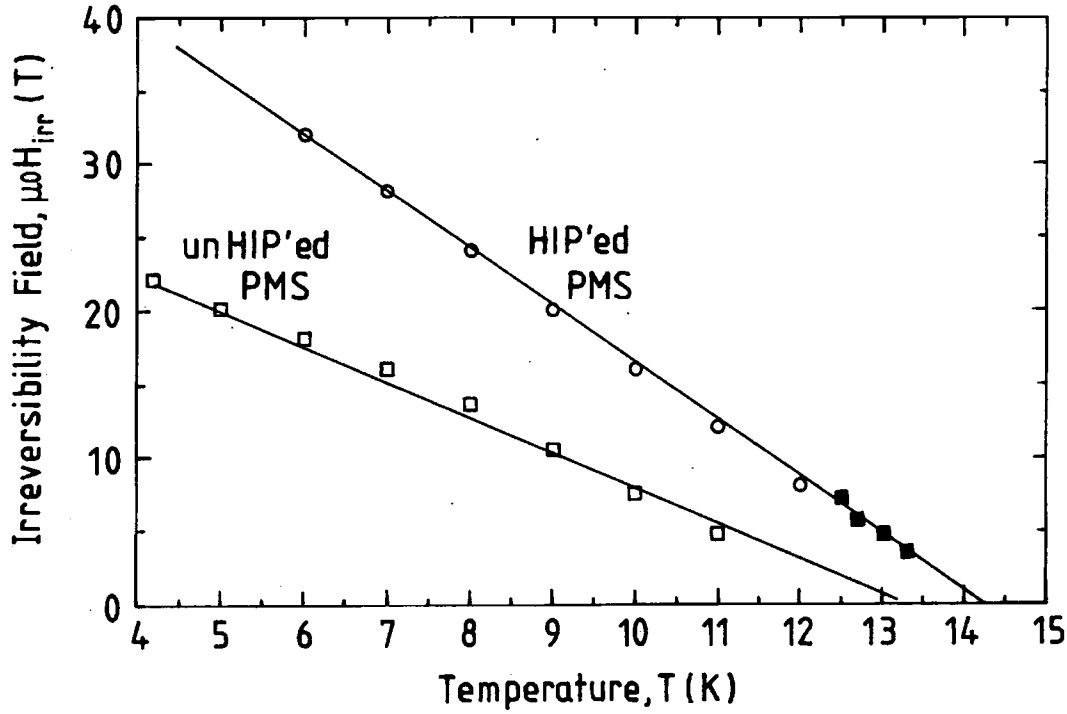

Figure 7.19 The irreversibility field of PMS as a function of temperature.
■ - values of $\mu_0 H_{C2}$ obtained from dc. magnetisation measurements.

As with fully connected NbTi, where only one type of macroscopic current is present in the sample, all the flux profile are straight lines, whose slope is proportional to J_C. The graphs show that the J_C of the HIP'ed sample is over an order of magnitude greater than that of the unHIP'ed sample. The apparent penetration of the magnetic field to a distance greater than the sample radius has been shown in chapter 4 to be an artifact of the analysis. Rossel and Fischer [28] and Karasic et al [29] have also made flux penetration measurements on PMS. In their measuring systems, the secondary coils are balanced when the sample is in the superconducting rather than the normal state and the primary coils are only able to supply an ac. field of 50 mT. Their flux profiles consist of nearly straight lines which indicates that the spatial variation of J_C is small. Cattani et al [30,31] have also found that flux profiles of PMS never show the two gradients characteristic of a granular sample, ie. a sample with both an inter and intragranular J_C. This is in agreement with our data which suggests that PMS is a bulk pinning, homogenous superconductor. When PMS is encased with a barrier such as Mo to form a wire, a steep gradient is seen in the flux profile at low δ [32]. This is caused by surface pinning at the superconducting-normal interface.

The factor of 20 increase in the J_C of the sample after HIP'ing is mainly due to the increase in density and therefore improved connectivity between the grains. Although this is partly responsible for the improvement in T_C, it may also be because fabrication at high pressure improved the homogeneity of the samples and hence the fundamental superconducting properties of the grain boundaries. Le Lay et al concluded that despite the short coherence length of PMS, the J_C of HIP'ed samples is not limited by granularity [21]. However there is evidence that in bulk PMS, the superconducting properties near to the grain boundaries are degraded [11]. Intragranular current densities of up to 5×10^9 A.m^{-2} at 4.2 K and 9 T [33,34] have been found. This demonstrates that J_C values for state-of-the-art bulk samples are by no means an intrinsic upper limit.

As seen by other authors [35-37], the volume pinning force obeys a universal scaling law of the form $F_P \propto h^{½}(1-h)^2$, where h is the reduced field. This is similar to that commonly observed in Nb_3Sn, (where grain boundaries are major pinning centres), and has led Rickel et al [38], Gupta [39] and Bonney et al [40] to propose a grain boundary pinning mechanism in PMS. Using a model assuming an optimal arrangement of pinning centres, where all flux lines are pinned [41], Rossel et al [42] have estimated the maximum possible critical current density for PMS. They found it should be above 1×10^{10} A.m^{-2} at 4.2 K and 20 T, one order of magnitude higher than the best experimental results. Low fabrication temperature reduces the grain size, increases the number of grain boundary pinning centres and improves J_C [43,44]. Karasik et al [45] have shown that the maximum value of the pinning force saturates when the grain size is less than 0.3 μm. Alternatively, Rossel and Fischer have shown that artificially introducing pinning centres by neutron irradiation and the addition of fine non-superconducting particles in hot pressed samples can increase the J_C of PMS [46].

For the HIP'ed PMS, $\mu_0H_{irr}(T)$ lies very close to $\mu_0H_{C2}(T)$ values determined from dc. magnetisation. These are in agreement with values of $\mu_0H_{C2}(T)$ obtained from specific heat measurements on the same sample [47]. This suggests that in HIP'ed PMS there are strong grain boundary pinning centres, where consistent with LTS, the pinning potential is much greater than the thermal energy. For the unHIP'ed sample, values of $\mu_0H_{irr}(T)$ are almost half those for the HIP'ed sample, due to the poor connectivity of the grains. The irreversibility line of PMS has been studied in detail by Rossel [48].

7.5 Conclusion.

A high quality HIP'ed PMS sample has been fabricated which has a T_C of 13.5 K, $\Delta T_C \approx 1$ K. Using XRD and SEM the sample has been shown to be single phase and fully densified. Using a probe capable of providing an ac. field of 100 mT, the magnetic moment of both a unHIP'ed and HIP'ed sample of PMS has been measured from 4.2 K up to T_C in magnetic fields up to 10 T. The results have been used to calculate the functional form and the spatial variation of J_C as a function of field and temperature.

The gradients of the flux profiles suggests that the spatial variation of J_C is small, indicating that both unHIP'ed and HIP'ed PMS can be considered as bulk pinning, homogenous superconductors. The J_C, scaling relations and pinning parameters of the HIP'ed sample compare well with dc. magnetisation results [49]. For both samples, the functional form of the volume pinning force obeys the universal Fietz-Webb scaling relation and can be expressed as $F_P \propto h^{1/2}(1-h)^2$, where h is the reduced field.

HIP'ing, the PMS increased the T_C by 1 K and reduced the width of the transition. The J_C increased by a factor of 20 to give a value greater than 3×10^8 A.m^{-2} at 5 T and 6 K. HIP'ing also increased $\mu_0 H_{irr}(T)$ by a factor of 2 so that for HIP'ed PMS the irreversibility line lies very close to $\mu_0 H_{C2}(T)$ values determined by dc. magnetisation measurements.

Already the J_C of PMS is large enough for the construction of wires [50-60] and small test coils have been built [61]. Recently the $J_C(B,T)$ has been increased to a level required for the practical, economic generation of high magnetic fields [26].

References.

[1] Chevrel R, Sergent S and Prigent J *J. Solid State Chem.* **3** 515 (1971).

[2] Matthias B T, Marezio M, Lorenzwit E, Cooper A S and Barz H E *Science* **175** 1465 (1972).

[3] Foner S, McNiff Jr. E J and Alexander E J *Phys. Lett.* **49A** (4) 269 (1974).

[4] Foner S, McNiff Jr. E J and Alexander E J *IEEE Trans. on Mag.* **MAG-11** (2) 155 (1975).

[5] Cattani D, Cors J, Decroux M, Seeber B and Fischer Ø *Physica C* **153-155** 461 (1988).

[6] Cors J, Cattani D, Decroux M, Stettler A and Fischer Ø *Physica B* **165** (AUG) 1521 (1990).

[7] Odermatt R, Fischer Ø, Jones H and Bongi G *J. Phys. C* **7** L13 (1974).

[8] Flükiger R, Seeber B *Europhys. News* **22** 1 (1991).

[9] Seeber B, Decroux M and Fischer Ø *Physics B* **155** 129 (1989).

[10] Rossel R NATO ASI *Relaxation in Complex Systems and Related Topics* ed. Campbell I A and Giovannella C (Plenum Press, New York) (1989).

[11] Decroux M, Selvam P, Cors J, Seeber B, Fischer Ø, Chevrel R, Rabiller P and Sergent M *IEEE Trans. on Appl. Supercond.* **3** (1) 1502 (1993).

[12] Ramsbottom H D and Hampshire D P *Meas. Sci. Technol.* **6** 1349 (1995).

[13] Atkinson H V and Rickinson B A *Hot Isostatic Processing* ed. Wood J (Adam Hilger, Bristol, UK) (1991).

[14] Arzt E, Ashby M F, Easterling K E *Metallurgical Trans.* **14A** 212 (1983).

[15] Helle A S, Easterling K E and Ashby M F *Acta Metall* **33** (12) 2163 (1985).

[16] Li W B, Ashby M F and Easterling K E *Acta Metall* **35** (12) 2831 (1987).

[17] Kaysser W A, Aslan M, Arzt E, Mitkov M and Petzow G *Powder Metallurgy* **31** (1) 63 (1988).

[18] Capone II D W, Guertin R P, Foner S, Hinks D G and Li H C *Phys. Rev. B* **29** (11) 6375 (1984).

[19] Foner S, McNiff Jr. E J and Hinks D J *Phys. Rev. B* **31** 6108 (1985).

[20] Hinks D G, Jorgensen J D and Li H C *Phys. Rev. Lett.* **51** (20) 1911 (1983).

[21] Le Lay L, Willis T C and Larbalestier D C *Appl. Phys. Lett.* **60** (6) 775 (1992).

[22] Seeber B, Erbuke L, Schroeter V, Perenboom J A A J and Grill R *IEEE Trans. on Appl. Supercond.* **5** (2) 1205 (1995).

[23] Rabiller P, Rabiller-Baudry M, Even-Boudjada S, Burel L, Chevrel R, Sergent M, Decroux M, Cours J and Maufras J L *Mat. Res. Bull.* **29** (5) 567 (1994).

[24] Ramsbottom H D, Zheng D N and Hampshire D P *IEEE Trans. on Appl. Supercond.* **5** (2) 1321 (1995).

[25] Bean C P *Rev. Mod. Phys.* **36** 31 (1964).

[26] Cheggour N, Gupta A, Decroux M, Perenboom J A A J, Langlois P, Massat H, Flükiger R and Fischer Ø *Inst. Phys. Conf. Series No.* **148** *EUCAS'95* 507 (1995).

[27] Hamid H A, Zheng D N and Hampshire D P *Inst. Phys. Conf. Series No.* **148** *EUCAS'95* 251 (1995).

[28] Rossel C, Peña O, Schmitt H and Sergent M *Physica C* **181** 363 (1991).

[29] Karasik V R, Karyaev E V, Zakasarenko V M, Rickel M O and Tsebro V I *Sov. Phys. JETP* **60** (6) 1221 (1984).

[30] Cattani D, Cors J, Decroux M, Seeber B and Fischer Ø *Helv. Phys. Acta* **63** (6) 797 (1990).

[31] Cattani D, Cors J, Decroux M and Fischer Ø *Physica B* **165** (AUG) 1409 (1990).

[32] Kajiyana K, Matsushita T, Yamafuji K, Hamasaki K and Komata T *Jap. J. of Appl. Phys.* **25** (6) 831 (1986).

[33] Gupta A, Cheggour N, Decroux M, Bouquet V, Langlois P Massat H Flükiger R and Fischer Ø *Physica C* **235-240** 2543 (1994).

[34] Cattani D *Universite Geneve PhD. Thesis* (1980).

[35] Alterovitz S A and Woollam J A *Philos. Mag. B* **38** (6) 619 (1978).

[36] Kimura Y *Phys. Stat. Sol. A* **69** K189 (1982).

[37] Karasik V R, Karyaev E V, Rickel M O and Tsebro V I *Sov. Phys. JETP* **56** (4) 881 (1982).

[38] Rikel M O, Togonidze T G and Tsebro V I *Sov. Phys. Solid State* **28** (9) 1496 (1987).

[39] Gupta A, Decroux M, Selvam P, Cattani D, Willis T C and Fischer Ø *Physica C* **234** 219 (1994).

[40] Bonney L A, Willis T C and Larbalestier D C *IEEE Trans. on Appl. Supercond.* **3** (1) 1582 (1993).

[41] Brandt E H *Phys. Lett.* **77A** (6) 484 (1980).

[42] Rossel C, Sandvold E, Sergent M, Chevrel R and Potel M *Physica C* **165** 233 (1990).

[43] Yamasaki H, Umeda M and Kosaka S *J. Appl. Phys.* **72** (3) 1180 (1992).

[44] Yamashita J, Hamasaki K, Noto K, Watanabe K and Komata I *Adv. Cryo. Eng.* **34** 669 (1988).

[45] Karasik V R, Rikel M O, Togonidze T G and Tsebro V I *Sov. Phys. Solid State* **27** (10) 1889 (1985).

[46] Rossel C and Fischer Ø *J. Phys. F* **14** 455 (1984).

[47] Ali S, Ramsbottom H D and Hampshire D P *Inst. Phys. Conf. Series No.* **148** *EUCAS'95* 583 (1995).

[48] Rossel C and Fischer Ø *J. Phys. F* **14** 473 (1984).

[49] Zheng D N, Ramsbottom H D and Hampshire D P *Phys. Rev. B* **52** (17) 12931 (1995).

[50] Chevrel R, Hirrien M, Sergent M, Couach M, Dubots P and Genevey P *Materials Letters* **7** (12) 425 (1989).

[51] Decroux M, Fischer Ø and Chevrel R *Cryogenics* **17** 291 (1977).

[52] Luhman T and Dew-Hughes D *J. Appl. Phys.* **49** (2) 936 (1978).

[53] Kubo Y, Yoshizaki K and Hashimoto Y *Synthetic Metals* **18** 851 (1987).

[54] Dubots P and Cave J *Cryogenics* **28** 661 (1988).

[55] Seeber B, Herrmann P, Schellenberg L and Zuccone J *IEEE Trans. on Mag.* **27** (2) 1108 (1991).

[56] Yamasaki H and Kimura Y *J. Appl. Phys.* **64** (2) 766 (1988).

[57] Yamasaki H *ISTEC Journal* **8** (1) 53 (1995).

[58] Yamasaki H and Kimura Y *IEEE Trans. on Mag.* **23** (2) 1756 (1987).

[59] Flükiger R *IEEE Trans. on Mag.* **24** (2) 1019 (1988).

[60] Goldacker W, Miraglia S, Hiriharan Y, Wolf T and Flükiger R *Adv. Cryo. Eng.* **34** 655 (1988).

[61] Kubo Y, Uchikawa F, Utsunomiya S, Noto K, Katagiri K and Kobayashi N *Cryogenics* **33** (9) 883 (1993).

Chapter 8

Flux Penetration Measurements and Harmonic Response of a HIP'ed Sample of Gd Doped PMS, ie. $(Pb_{0.7}Gd_{0.3})Mo_6S_8$.

8.1 Introduction.

As shown in chapter 7, Chevrel phase superconductors are well known for their relatively high T_C and very high B_{C2} values [1]. Hence they are a potential candidate for high field applications [2,3]. It has been reported that adding rare-earth elements to PMS increases both T_C and B_{C2} [4]. Gadolinium doped PMS (Gd-PMS) has the highest B_{C2} of 54 T at 4.2 K which can be extrapolated to over 60 T at 0 K. Unfortunately, critical current densities obtained so far are not high enough for practical magnet construction [5].

An unusual feature of the rare-earth doped Chevrel phase superconductors ($RE_xMo_6S_8$) is that the RE atom can in some cases be magnetic, a property usually incompatible with superconductivity. Evidence for the coexistence of superconductivity and magnetic order was first obtained from specific heat and ac. susceptibility measurements [6,7]. The internal field distribution has been investigated by magneto-optical techniques [8], neutron diffraction [9] and muon spin rotation [10]. The most important aspect of the chemistry is the occurrence of strongly bonded Mo_6S_8 octahedra with a typical nearest neighbour distance of 0.3 nm. The electronic properties have been widely studied by many authors [11,12]. Only two distinct crystallographic systems have been found to exhibit the coexistence of superconductivity and long range magnetic order. Both compounds, the Chevrel phases and the rhodium-borides are comprised of clusters of transition metal atoms and relatively isolated rare-earth ions [13].

This chapter presents results of flux penetration measurements on HIP'ed Gd-PMS from 4.2 K up to T_C in dc. magnetic fields up to 10 T. Section 8.2 describes the sample fabrication together with an outline of the experimental procedure. It also includes the results of the flux penetration measurements. In section 8.3 these results are used to investigate magnetic field profiles and J_C as a function of field and temperature in order

to evaluate whether substituting Gd improves the high field performance of PMS. It is hoped that the Gd ions may act as small normal regions which pin the flux lines, thus increasing the J_C for practical applications. The results are analysed within the framework of a universal scaling law. Section 8.4 describes the harmonic response of the sample up to the 10^{th} harmonic. The results are compared with the theoretical predictions outlined in chapter 4. At the end of the chapter is a discussion on the effect of doping PMS with Gd. The chapter concludes with a summary of the most important findings.

8.2 Experimental.

8.2.1 Sample preparation and quality.

Following phase diagram and electromagnetic studies of material with high T_C [14-16], pure elements were mixed with a nominal composition $(Pb_{0.7}Gd_{0.3})Mo_6S_8$ (Gd-PMS). In addition, a second sample of nominal composition $GdMo_6S_8$ (GMS) was fabricated.

Both samples were reacted in evacuated quartz tubes at 450 ^oC for 4 hours. This was followed by a slow temperature ramp at 33 $^oC.h^{-1}$ to 650 ^oC which was held for another 8 hours. The material was then ground, pressed into disks and reacted again in evacuated quartz tubes at 1000 ^oC for 44 hours. The Gd-PMS sample was wrapped in Mo foil and sealed under vacuum in a stainless steel tube. A HIP treatment was carried out at 2×10^8 $N.m^{-2}$ (2000 bar) and 800 ^oC for 8 hours. The sample was then extracted from the Mo foil and cut into dimensions 1.0mm × 1.0mm × 5.0mm for the flux penetration measurements. During the fabrication procedure, both samples were handled in a glove box. This maintains a controlled atmosphere such that the O_2 concentration is < 5 ppm and the moisture level is < 10 ppm.

Both samples have been characterised using ac. susceptibility and x-ray diffraction (XRD). Preliminary transmission electron microscopy (TEM) has also been completed. The XRD traces of Gd-PMS and GMS are shown in figures 8.1 and 8.2.

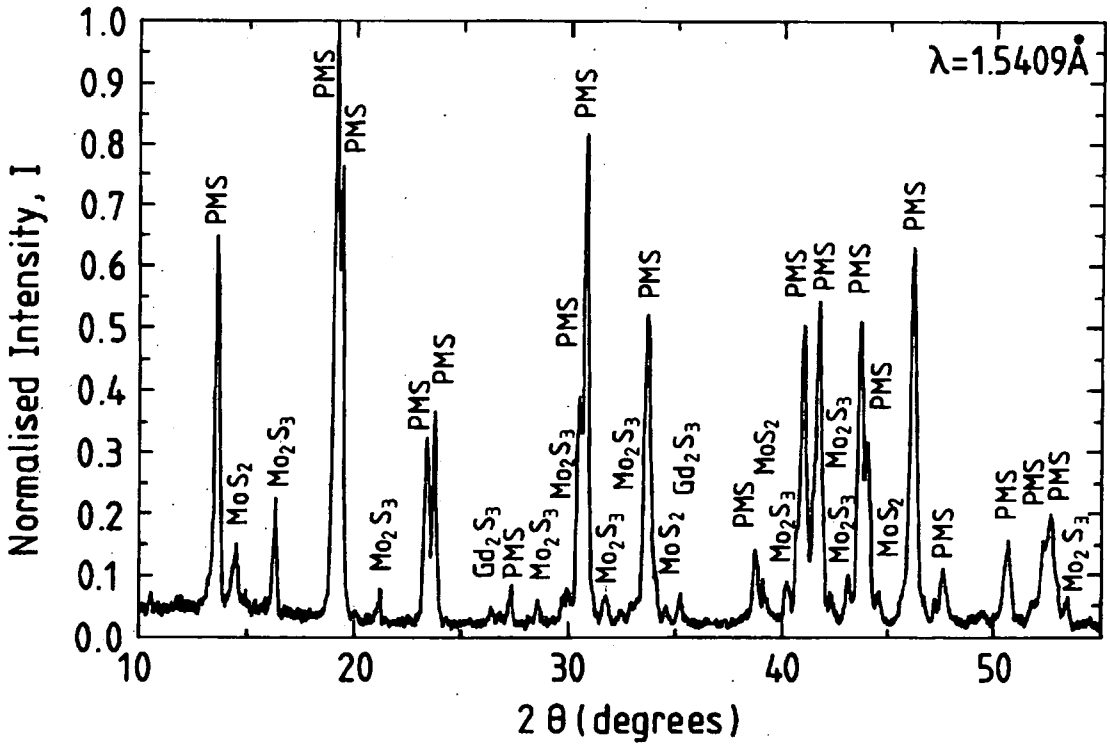

Figure 8.1 The x-ray diffraction pattern for HIP'ed Gd-PMS.

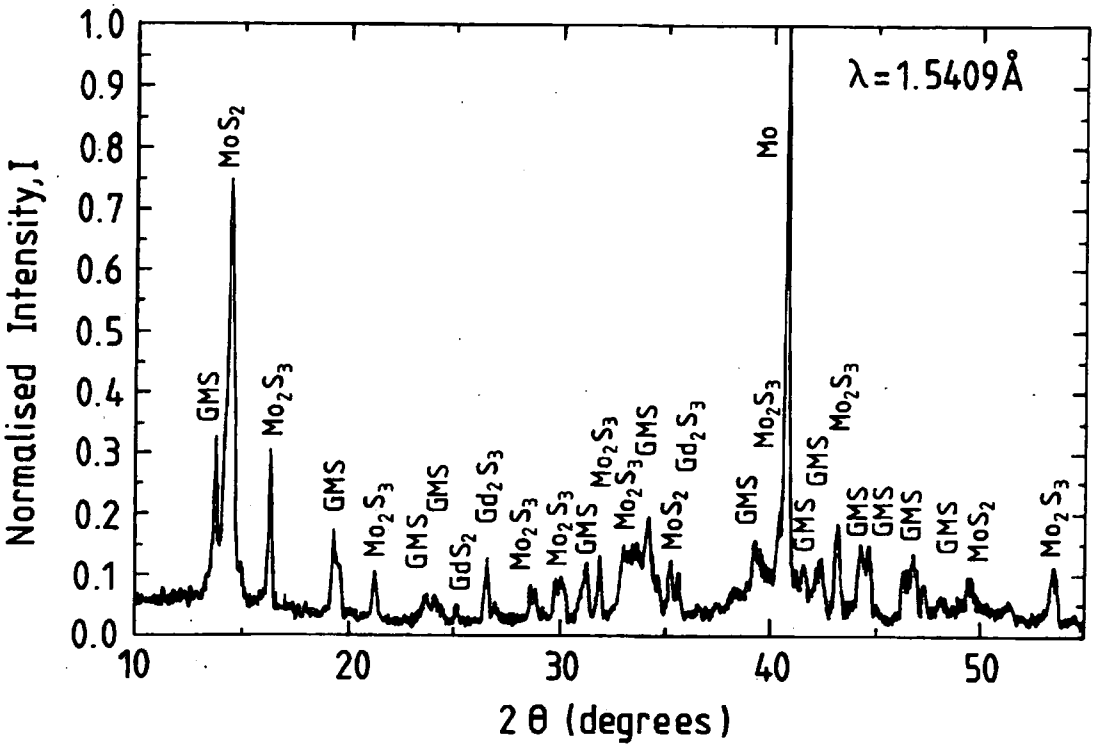

Figure 8.2 The x-ray diffraction pattern for unHIP'ed GMS.

In the Gd doped sample, most of the peaks can be identified as those for PMS, (cf. figure 7.2). The rest of the peaks are MoS_2 and Mo_2S_3 with some very small traces of Gd_2S_3. Consistent with these results, MoS_2 and Mo_2S_3 have been reported at 1000 °C [17,18] and Gd_2S_3 at 1100 °C [19]. The XRD trace of GMS shows a larger quantity of second phase material and peaks that can be associated with a Chevrel phase structure. The slight displacement of these peaks from those of PMS is due to the smaller unit cell of GMS [20]. Hence in Gd doped PMS, the compounds PMS, GMS and $(Gd_{1-x}Pb_x)Mo_6S_8$ can occur together with second phase material.

Preliminary TEM measurements show that the grain size is 0.5-1.0 μm. Unfortunately it has not yet been possible to unambiguously determine the location of the gadolinium. However, the XRD data in figure 8.1 demonstrates that some of the Gd is acting as an oxygen getter in the form of Gd_2S_3. Ac. susceptibility measures T_C at 14.5 K, approximately 1 K higher than that of an undoped sample.

8.2.2 Experimental procedure.

Using the purpose-built probe [21], flux penetration measurements were made from 4.2 K up to T_C in dc. magnetic fields up to 10 T. The harmonic response of the sample was also investigated. In these measurements, at a particular field, both the loss and lossless components of the induced voltage were recorded for the first 10 harmonics. The flux profile measurements and harmonic analysis were performed with the long axis of the sample both perpendicular (transverse b) and parallel (axial b) to the applied field.

8.2.3 Experimental results.

Figures 8.3 and 8.4 show the magnetic moment versus ac. field for Gd doped PMS as a function of temperature, in a transverse field of both 3 T and 5 T respectively. In these figures, the current through the primary coil and the voltage across the secondary coils are also included. A background signal, taken when $T>T_C$, has been subtracted from all data. At both fields and at all temperatures there is a sharp fall in the magnetic moment to a minimum value after which there is a slow increase as the ac. field is increased beyond that required for full penetration. The magnitude of the minimum

magnetic moment at any temperature at 5 T is typically 25% less than that found at 3 T. The marked increase at high ac. fields, (in figure 8.3 at 4.2 and 5 K and in figure 8.4 at 4.2 and 5 K) is attributed to eddy current heating in the copper components of the probe. Figures 8.5 and 8.6 show equivalent data for the sample in an axial field. The magnitude of the magnetic moment in an axial field is typically 25% less than in a transverse field. This compares well with section 4.3.2 where it is calculated that the magnitude of the magnetic moment in an axial field is a factor of $\pi/4$ that in a transverse field. Also, the initial gradient (dV/db_m) is twice as large in a transverse field than in an axial field and the field at which there is a minimum in the magnetic moment (b_{min}) is a factor of $2/\pi$ lower. Figures 8.7 and 8.8 show magnetic moment versus ac. field for Gd-PMS as a function of dc. field (both axial and transverse) at 7 K. The maximum ac. field which can be obtained is limited at high temperatures and high dc. fields, which cause the the superconducting primary coil to quench.

8.3 Analysis of results.

8.3.1 Magnetic field profiles.

Following the analysis outlined by Campbell [22] and using the data in figures 8.3-8.6, it is possible to determine magnetic field profiles inside the Gd-PMS sample. The differential of the induced voltage with respect to the ac. field gives the depth to which the field penetrates, (using equation 4.47). Figures 8.9-8.12 show the spatial variation in the magnetic field ($\mu_0 M$) as a function of field and temperature for both orientations. The macroscopic dimension of the sample is calculated using equation 4.48. The applied dc. field ($\mu_0 H$) and ac. field ($\mu_0 h$) can be added to the magnetic field produced by the sample ($\mu_0 M$) to give the net field B. The gradient of the lines as a function of penetration depth gives the spatial variation of J_C, (using equation 3.44). For both orientations, the gradient of the lines and hence J_C is approximately constant throughout the sample. This is expected for a bulk pinning superconductor. The minimum in magnetic moment (in figures 8.3-8.8) corresponds to an apparent penetration of the magnetic field to a depth greater than the radius of the sample (in figures 8.9-8.12). As shown in chapter 4, this is an artifact of the analysis.

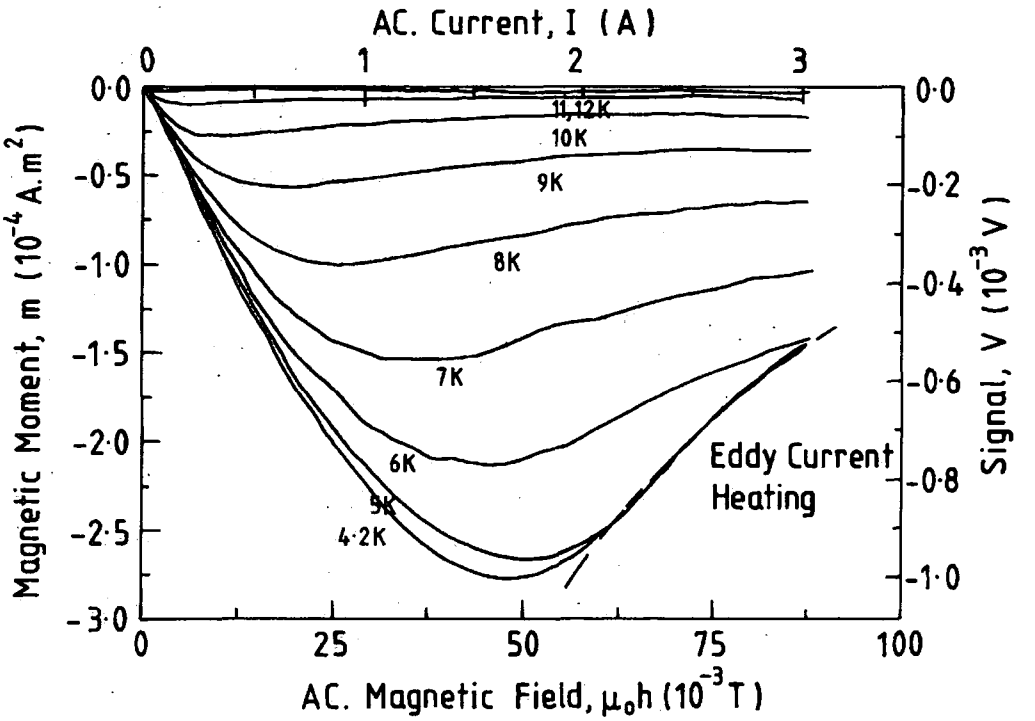

Figure 8.3 Magnetic moment versus ac. field of Gd doped PMS as a function of temperature in a transverse field of 3 T.

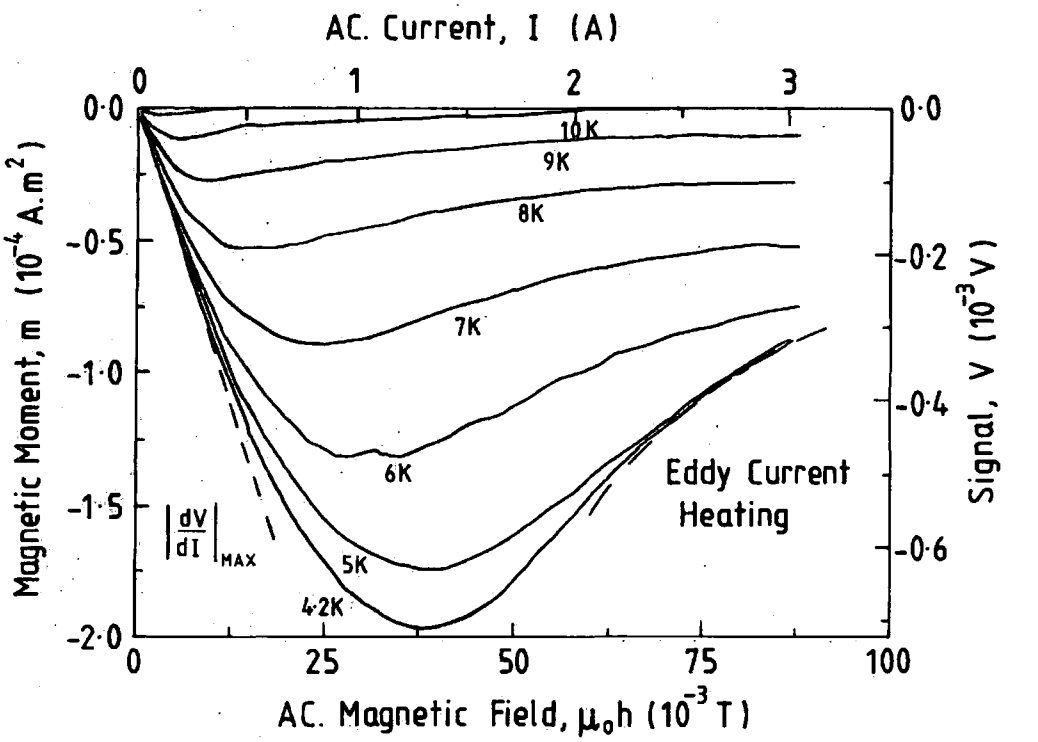

Figure 8.4 Magnetic moment versus ac. field of Gd doped PMS as a function of temperature in a transverse field of 5 T.

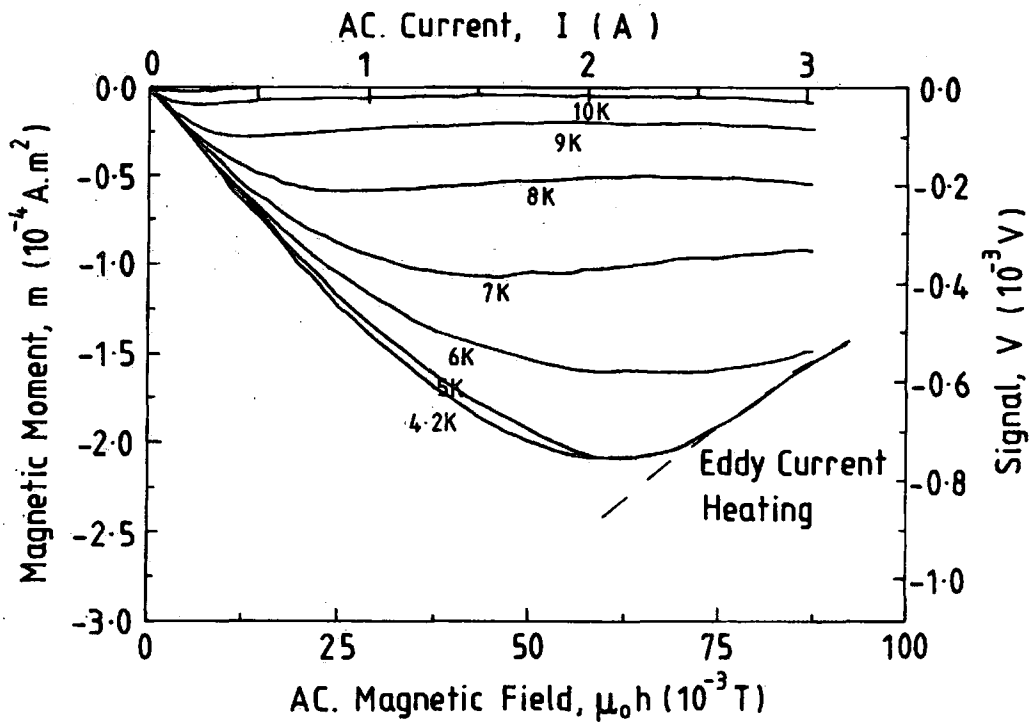

Figure 8.5 Magnetic moment versus ac. field of Gd doped PMS as a function of temperature in an axial field of 3 T.

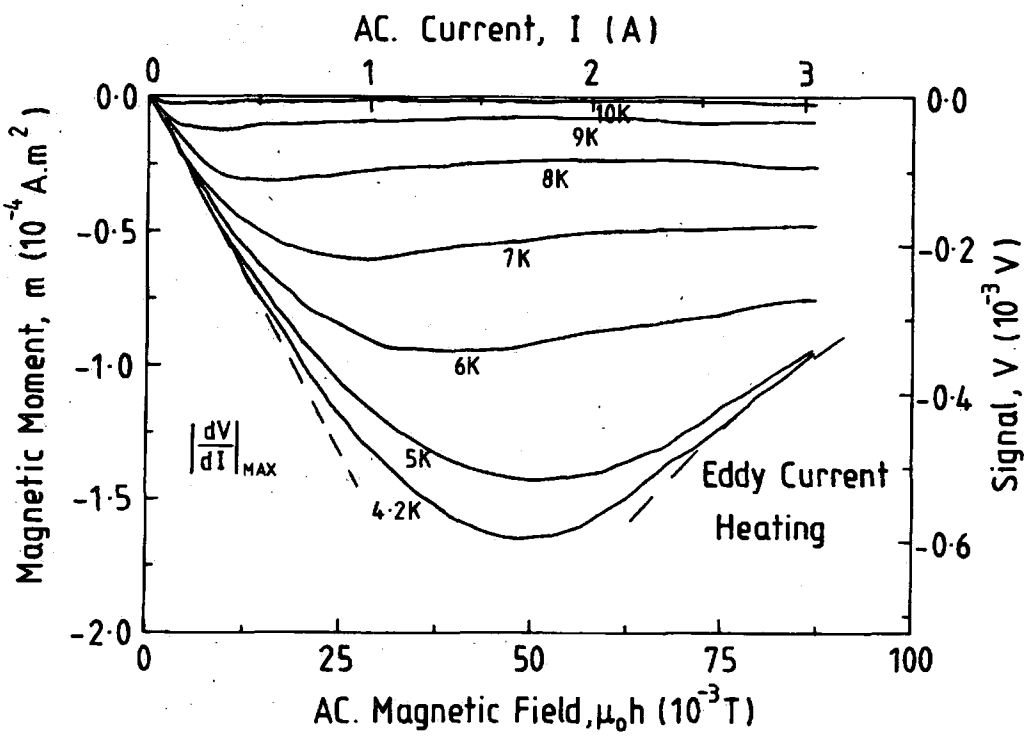

Figure 8.6 Magnetic moment versus ac. field of Gd doped PMS as a function of temperature in an axial field of 5 T.

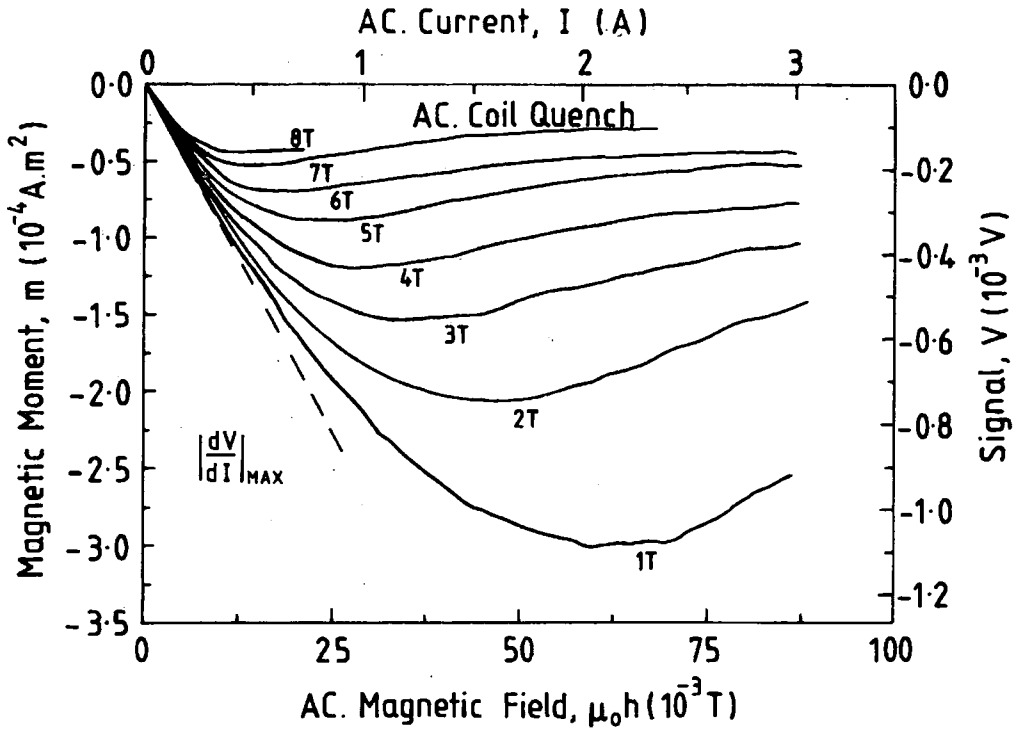

Figure 8.7 Magnetic moment versus ac. field of Gd doped PMS as a function of dc. field (transverse) at 7 K.

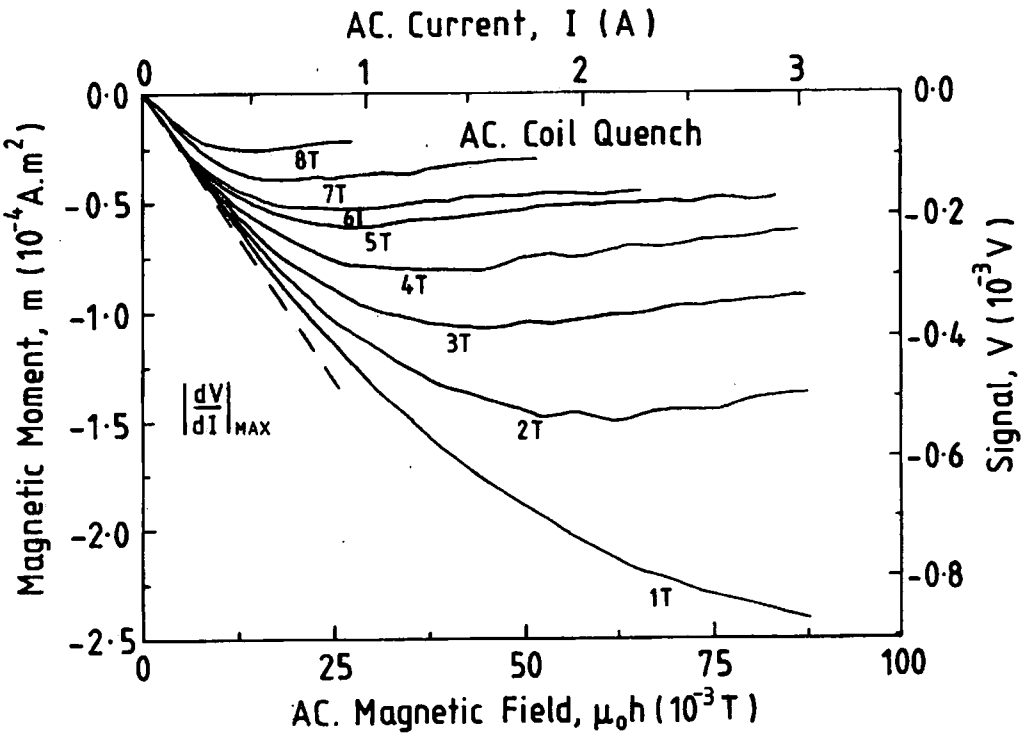

Figure 8.8 Magnetic moment versus ac. field of Gd doped PMS as a function of dc. field (axial) at 7 K.

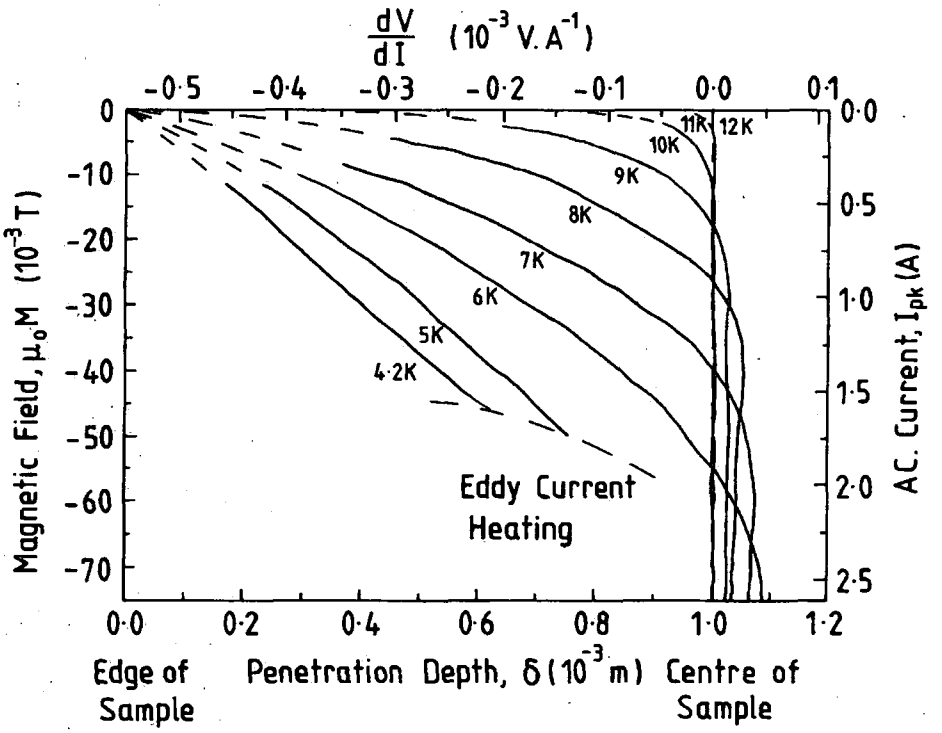

Figure 8.9 The magnetic field profile inside a Gd doped sample of PMS as a function of temperature in a transverse field of 5 T.

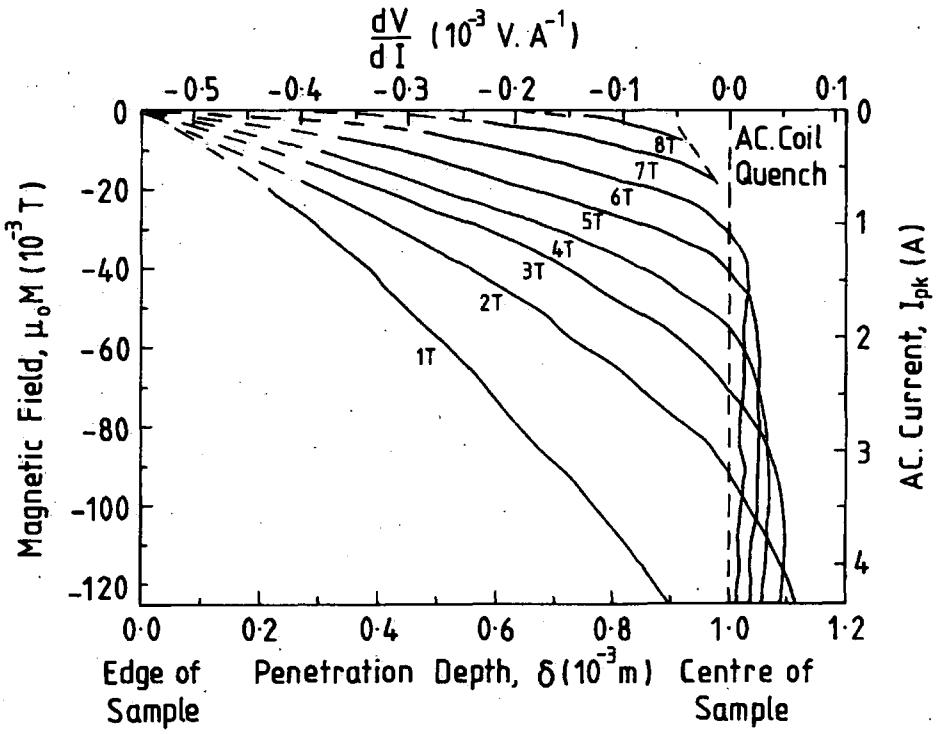

Figure 8.10 The magnetic field profile inside a Gd doped sample of PMS as a function of dc. field (transverse) at 7 K.

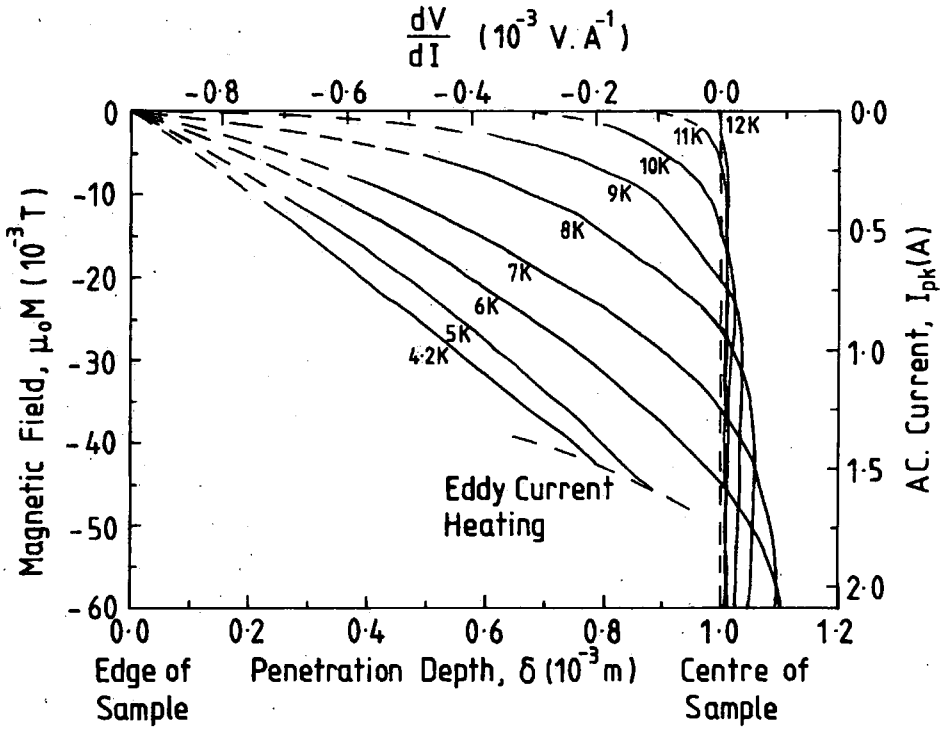

Figure 8.11 The magnetic field profile inside a Gd doped sample of PMS as a function of temperature in an axial field of 5 T.

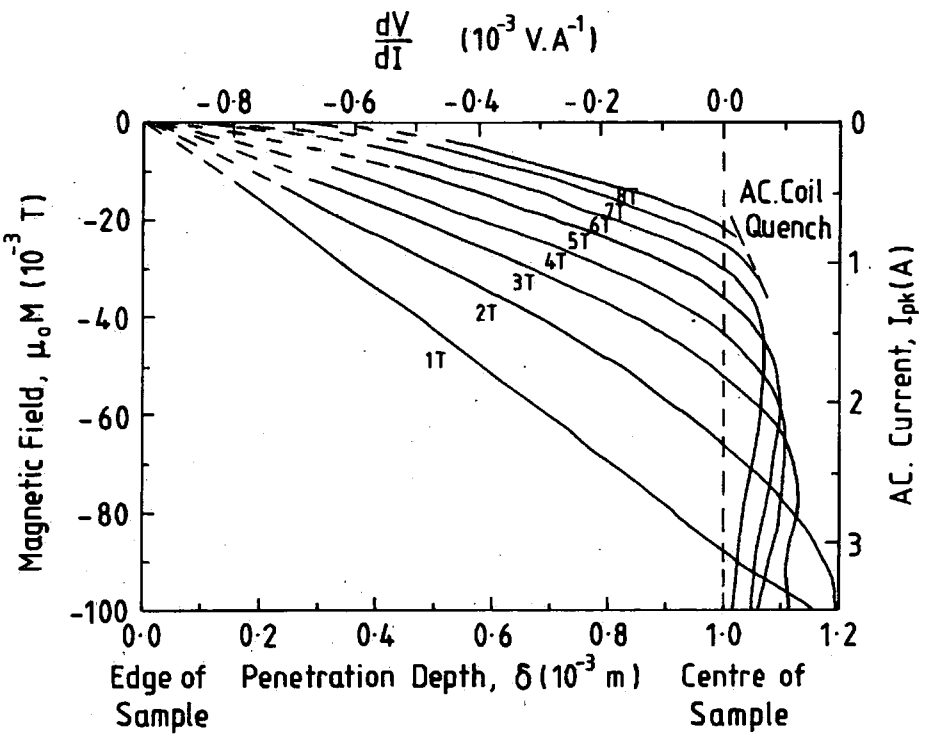

Figure 8.12 The magnetic field profile inside a Gd doped sample of PMS as a function of dc. field (axial) at 7 K.

8.3.2 Critical current density.

Using Bean's critical state model [23], an equivalent critical current density can be calculated from the minimum value of the magnetic moment at each field and temperature, (using equation 3.30). When the demagnetisation factors have been considered, the $J_C(B,T)$ graphs are very similar for both orientations. In figures 8.13 and 8.14 the calculated J_C values are presented for the Gd-PMS sample. The values of J_C are accurate to within 10%, primarily due to the uncertainty in the sample dimensions. At 5 T and 6 K the J_C is 1.6×10^8 A.m^{-2}. This is is approximately half that for the undoped PMS which gives a value of 3.0×10^8 A.m^{-2}.

8.3.3 Scaling relations and flux pinning.

Figures 8.15 and 8.16 show Kramer plots for both orientations. A linear extrapolation of the data to $J_C^{1/2}(\mu_0 H)^{1/4} = 0$ gives the irreversibility field ($\mu_0 H_{irr}$) for each temperature. The volume pinning force is calculated using $F_P = \mu_0(J_C \times H)$.

Figures 8.17 and 8.18 show the reduced volume pinning force (F_P/F_{PMAX}) versus the reduced magnetic field. ($h=H/H_{irr}$) for temperatures from 5 K to 11 K, derived from the data in figures 8.13 and 8.14. As seen by other authors [24,25], the curves obey a universal scaling law with the functional form of $F_P \propto h^{1/2}(1-h)^2$. The volume pinning force data can then be described by a scaling law of the form $F_P = \alpha(\mu_0 H_{irr})^n h^{1/2}(1-h)^2$. For the sample in a transverse field, the index $n = 2.85\pm0.05$ and the constant $\alpha = (1.45\pm0.05)\times10^5$ T$^{-1.85}$A.m^{-2}. For the sample in an axial field, the index $n = 2.79\pm0.13$ and the constant $\alpha = (1.95\pm0.15)\times10^5$ T$^{-1.79}$A.m^{-2}. The fact that the values for α and n are similar shows that both microstructural and electromagnetic properties are approximately isotropic.

Figure 8.19 shows the irreversibility field for Gd-PMS plotted as a function of temperature. The irreversibility line for a sample in both axial and transverse field is compared to that for an undoped sample. The solid squares show values of $\mu_0 H_{C2}$ for undoped PMS obtained by dc. magnetisation measurements and the open triangle shows the T_C as determined by ac. susceptibility measurements.

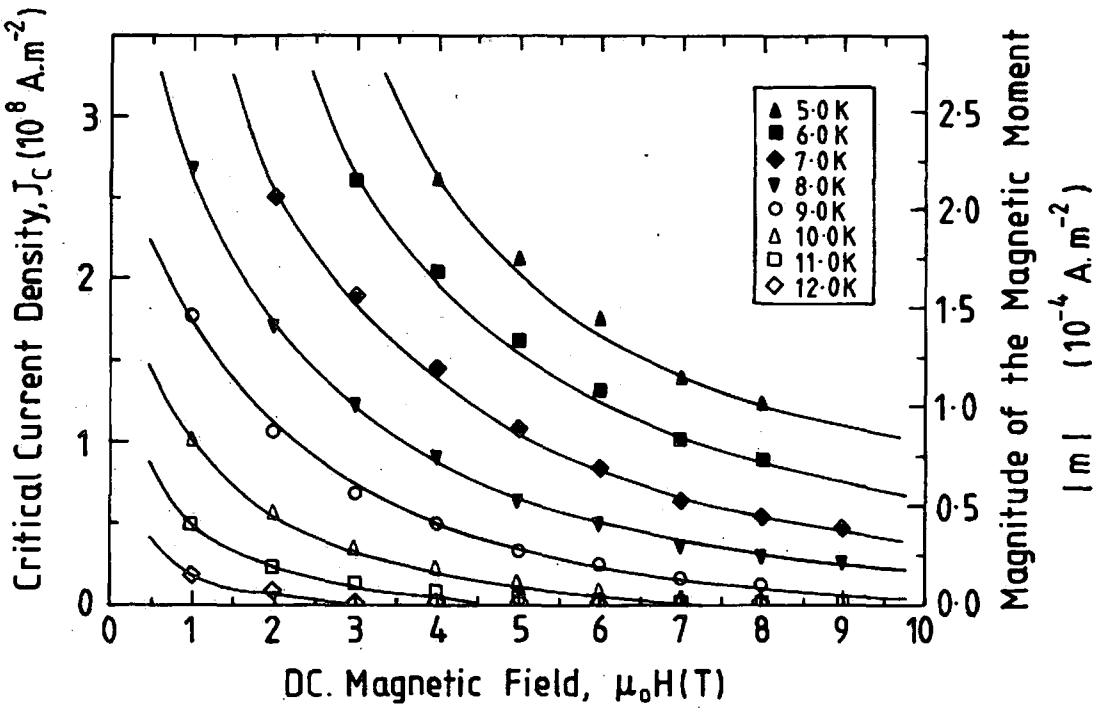

Figure 8.13 The critical current density of Gd doped PMS as a function of field and temperature, (transverse b).

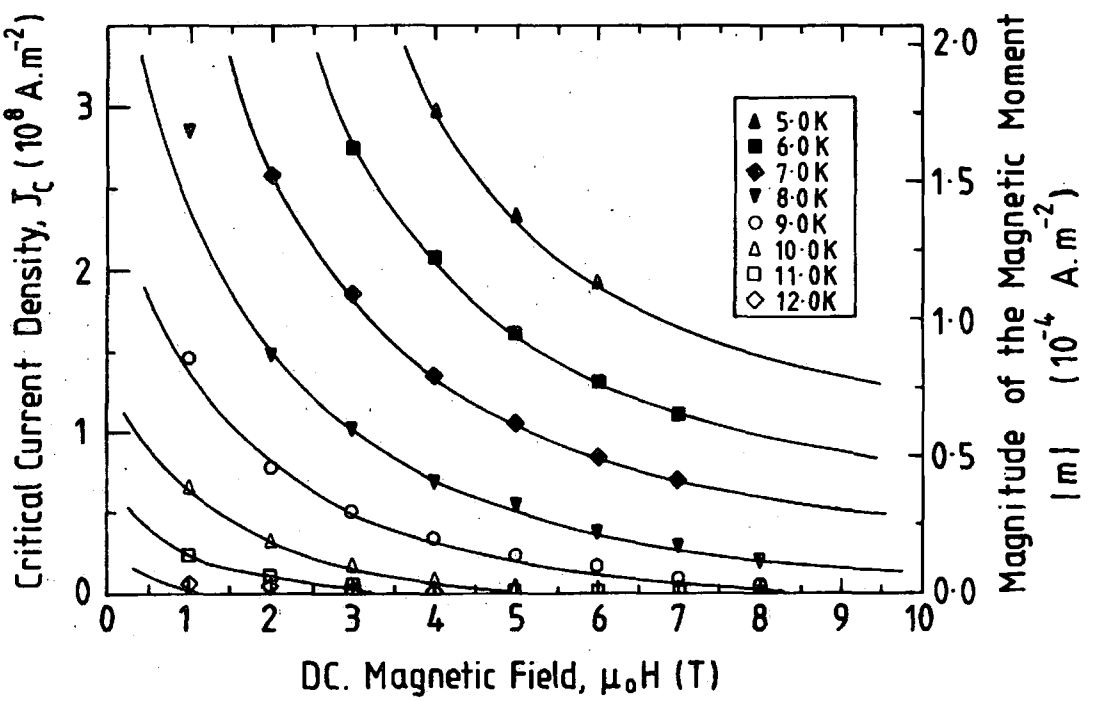

Figure 8.14 The critical current density of Gd doped PMS as a function of field and temperature, (axial b).

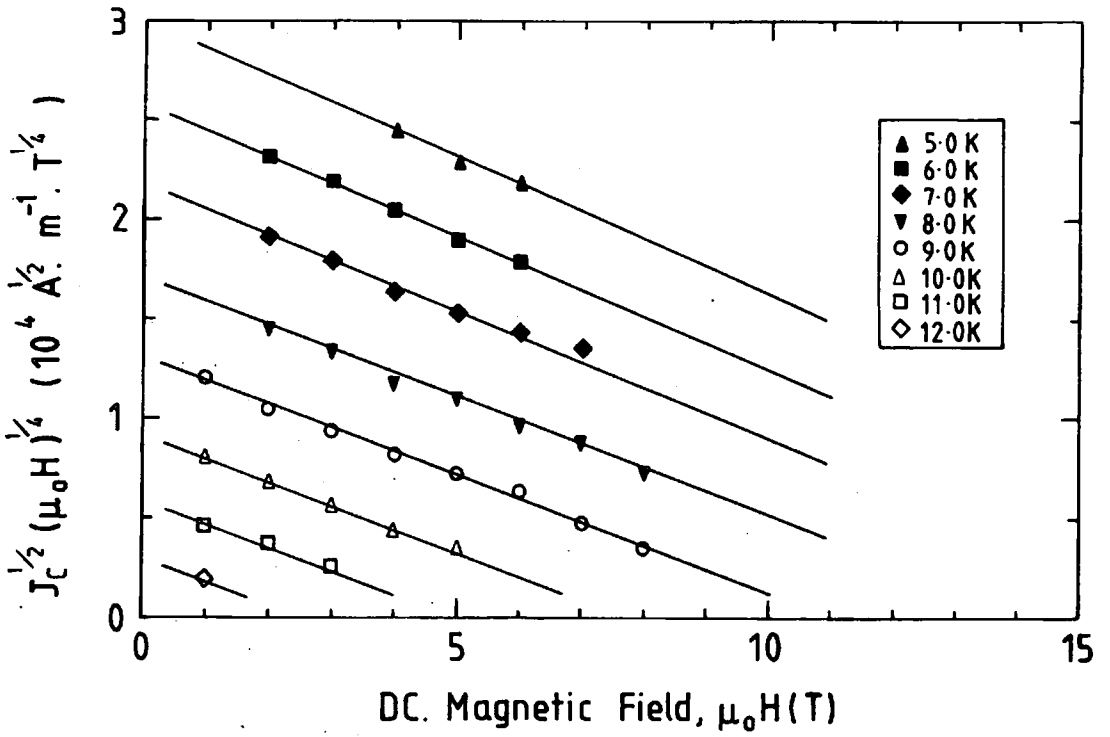

Figure 8.15 A Kramer plot for the Gd doped sample of PMS, (transverse b).

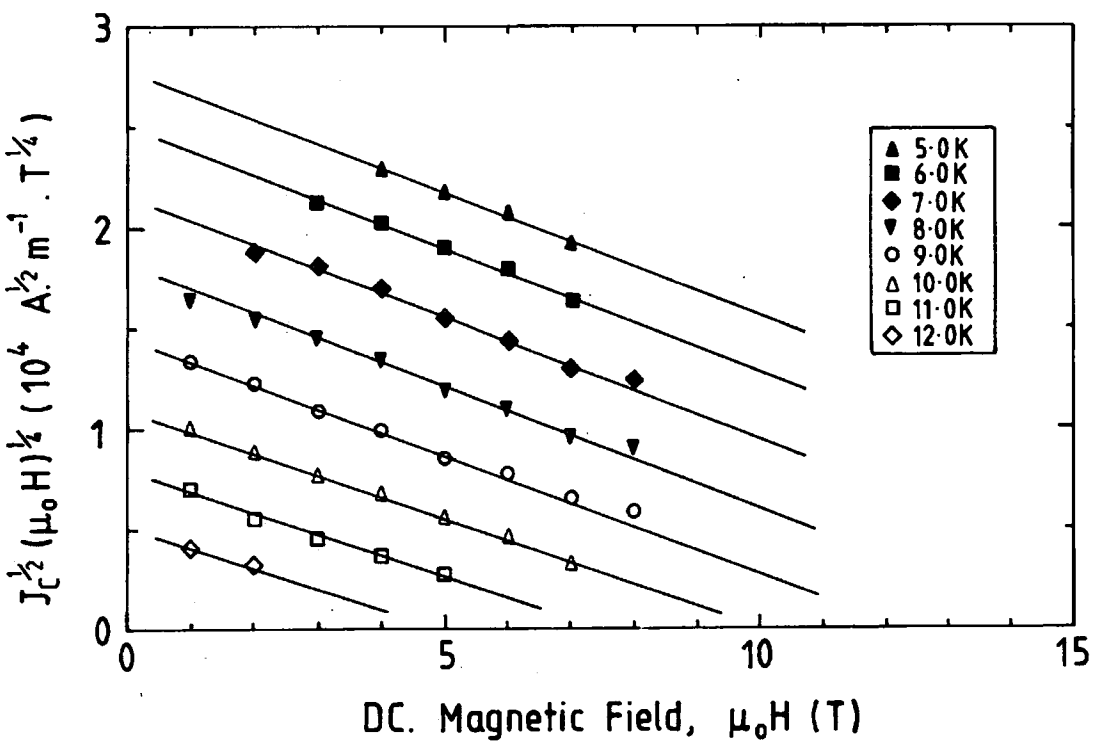

Figure 8.16 A Kramer plot for the Gd doped sample of PMS, (axial b).

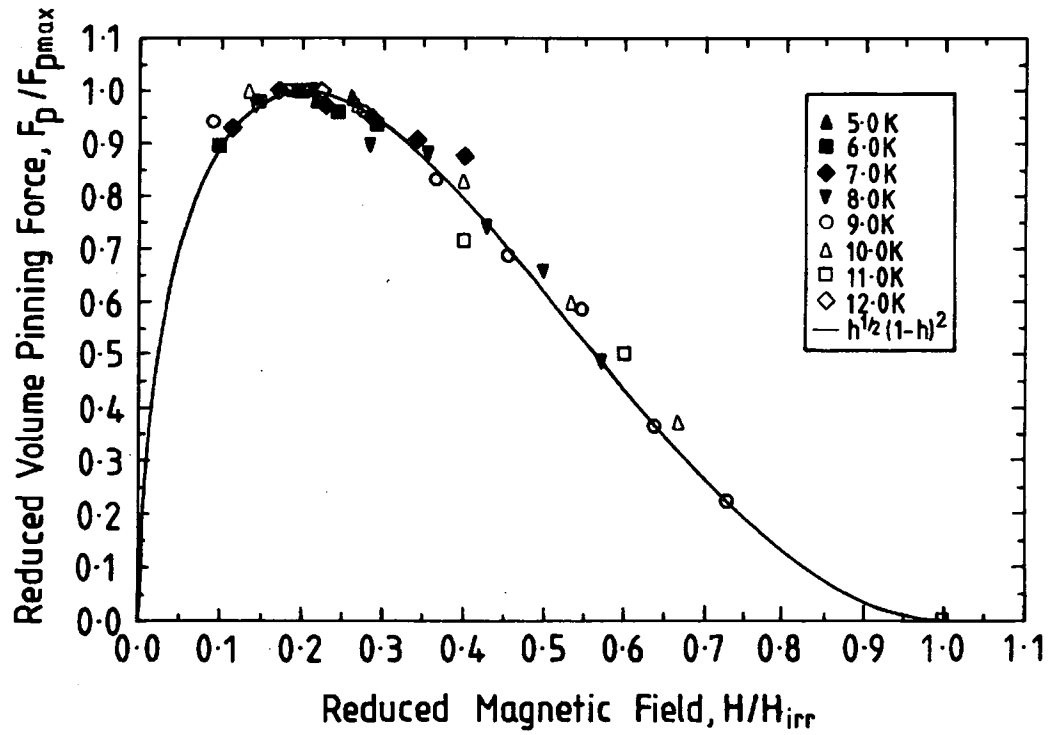

Figure 8.17 The reduced volume pinning force versus reduced magnetic field as a function of temperature for the Gd doped sample of PMS, (transverse b).

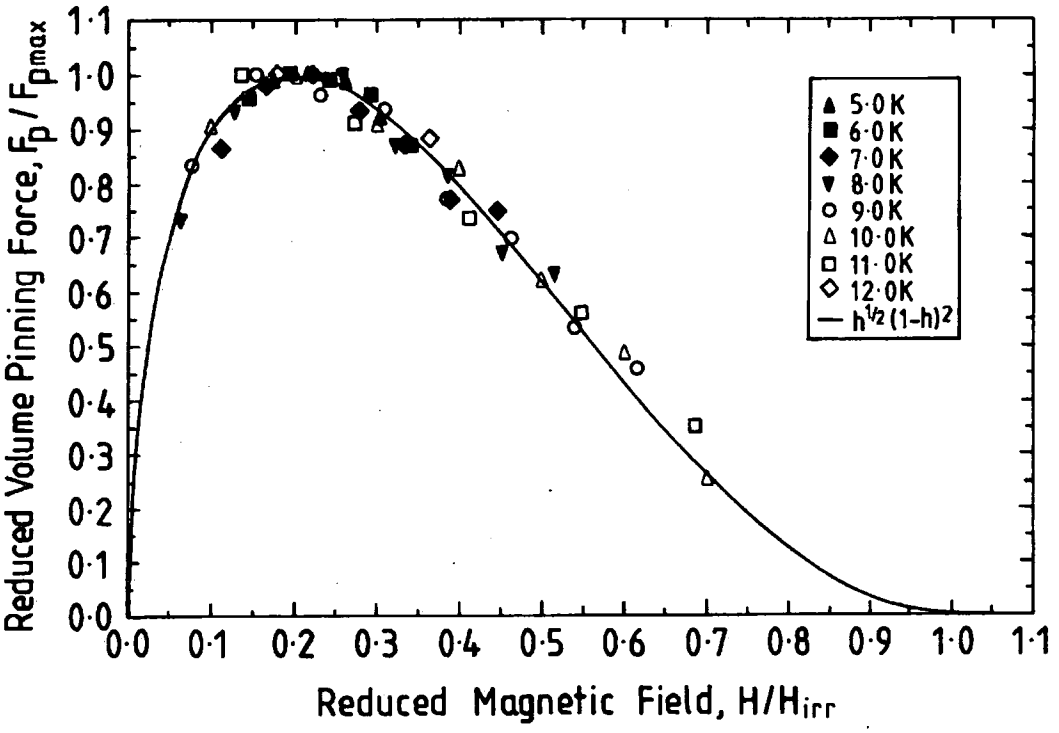

Figure 8.18 The reduced volume pinning force versus reduced magnetic field as a function of temperature for the Gd doped sample of PMS, (axial b).

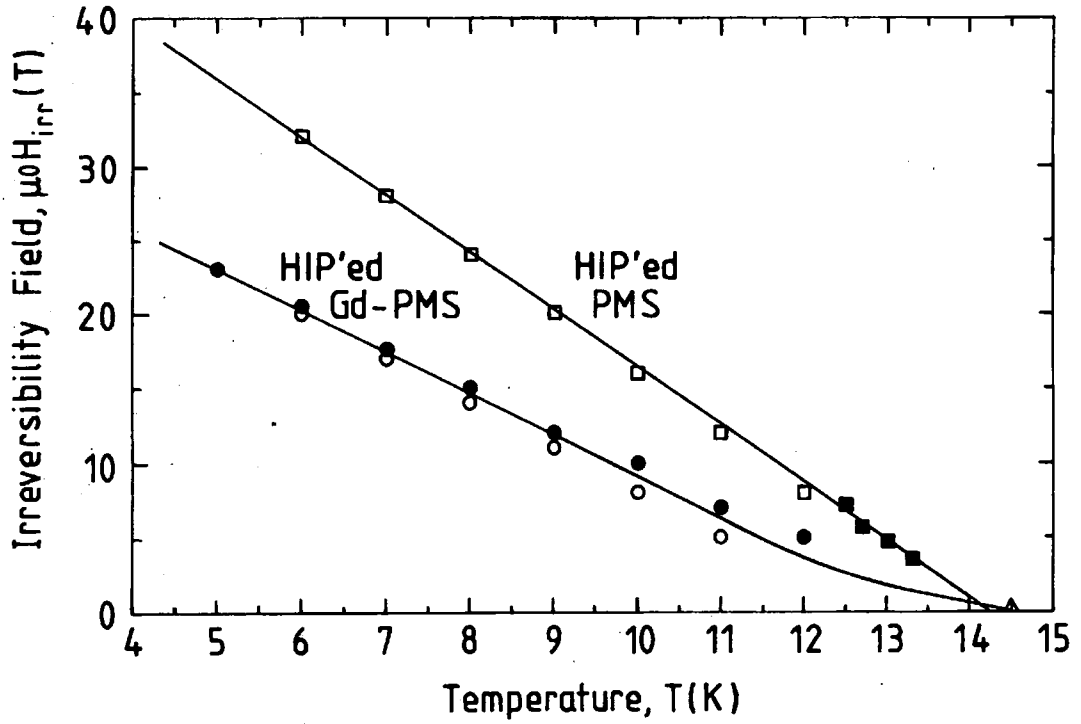

Figure 8.19 The irreversibility field of Gd-PMS in both an axial (●) and transverse (○) magnetic field compared to that of an undoped sample of PMS (□). ■ - values of $\mu_0 H_{C2}$ for PMS from dc. magnetisation measurements. △ - T_C of Gd-PMS as determined by ac. susceptibility measurements.

8.4 Harmonic analysis.

Figures 8.20 and 8.21 show the harmonic response of both the lossless and loss components of the magnetic moment of Gd-PMS in a transverse field of 3 T. A background signal, taken when $T>T_C$, has been subtracted from all data. As explained in chapter 6, the 3F data has been adjusted to compensate for the effects of the line filter. The results are in good agreement with the theoretical predictions (cf. figures 4.4-4.11). All of the even harmonics are zero, ie. less than ±10 μV and the odd harmonics are of the correct sign and functional form. For the lossless component, (cf. figure 8.20), there is a factor of 4 between 1F and 3F in the field at which there is a minimum in the magnetic moment (b_{min}) and the magnitude of these minima (V_{min}) are similar. For the loss component (cf. figure 8.21), there is a factor of 2.5 between 3F and 5F in b_{min} while V_{min} are similar, (cf. table 4.1). Figures 8.22 and 8.23 show the equivalent data for the sample in an axial field. Again there is good agreement with theoretical predictions.

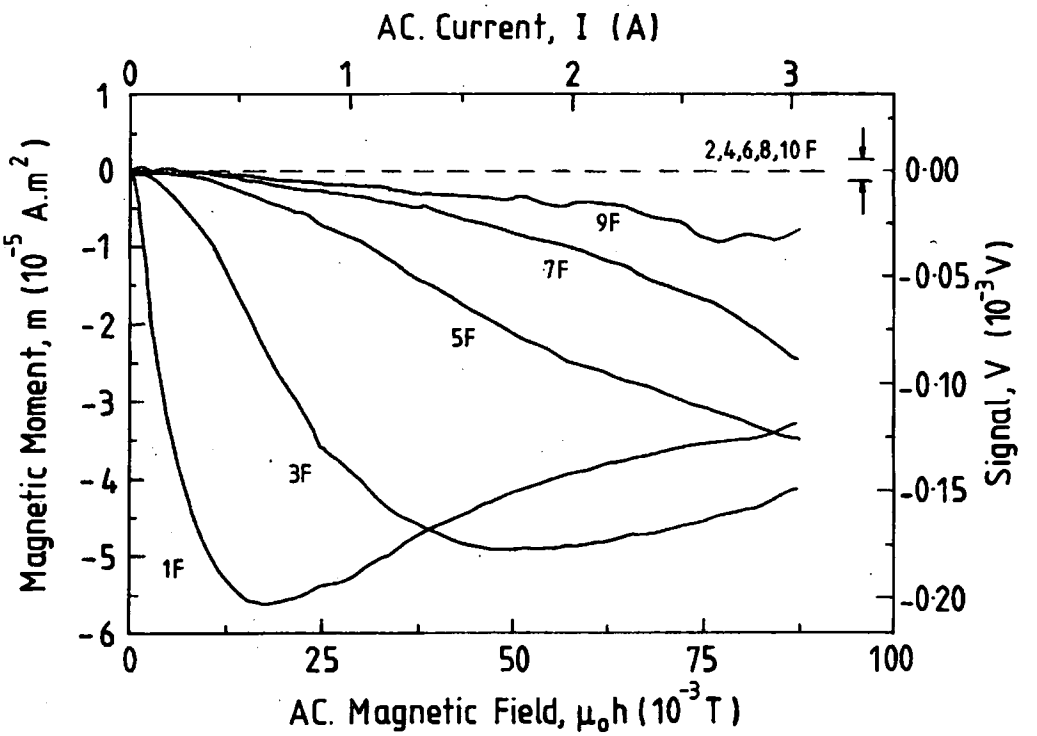

Figure 8.20 The harmonic response of the lossless components of the induced voltage for Gd-PMS at 6 K in a transverse field of 3 T.

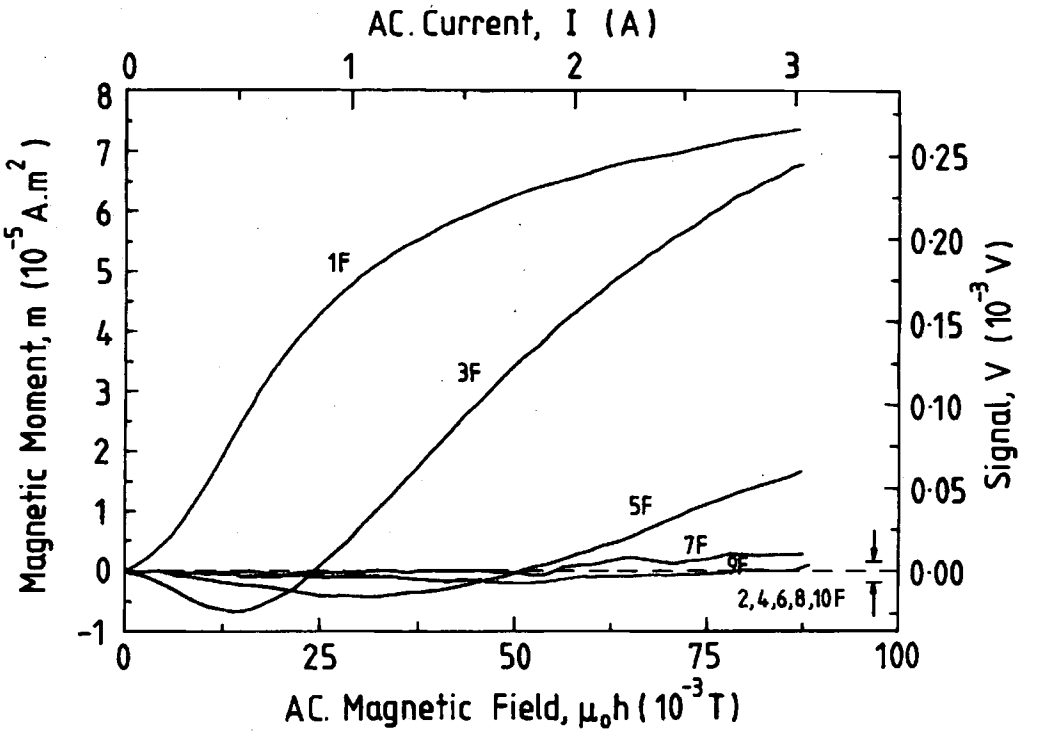

Figure 8.21 The harmonic response of the loss components of the induced voltage for Gd-PMS at 6 K in a transverse field of 3 T.

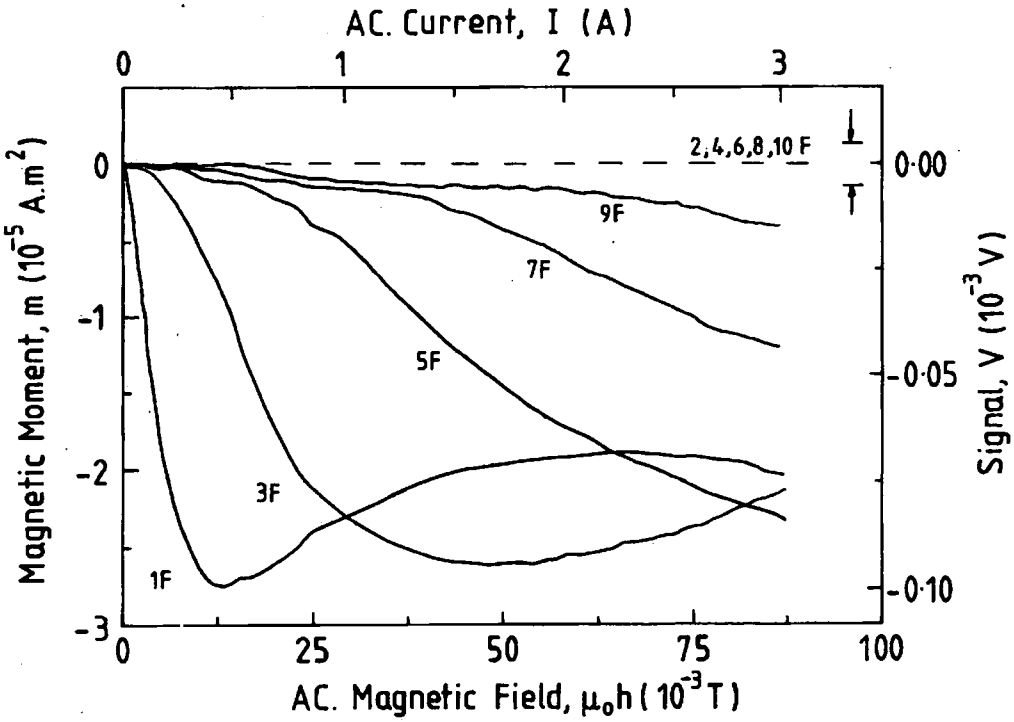

Figure 8.22 The harmonic response of the lossless components of the induced voltage for Gd-PMS at 6 K in an axial field of 3 T.

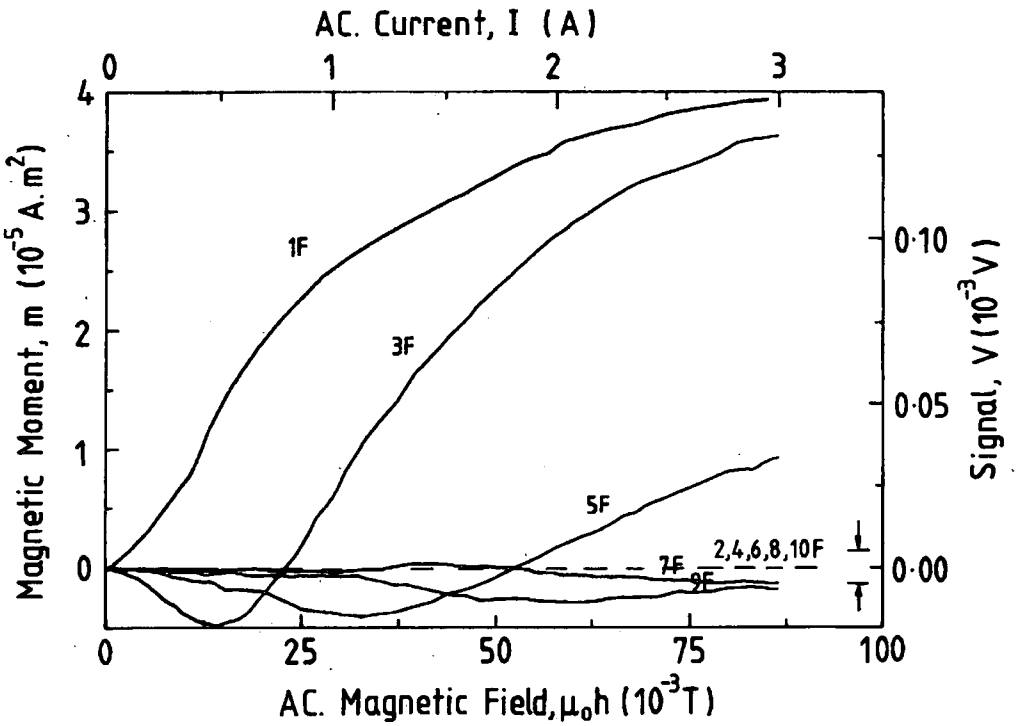

Figure 8.23 The harmonic response of the loss component of the induced voltage for Gd-PMS at 6 K in an axial field of 3 T.

8.5 Discussion.

Doping with Gd has increased the T_C of HIP'ed PMS to 14.5 K ($\Delta T_C \approx 1$ K), approximately 1 K higher than that for an undoped sample. It is thought that in low concentrations the Gd acts as an oxygen getter, thus improving the quality of the PMS. However, Sergent et al report that ac. susceptibility measurements demonstrate the presence of free Gd^{3+} ions and conclude that Gd has entered the PMS structure [20]. It is believed that in Chevrel phase compounds, the superconductivity resides in the Mo_6S_8 octahedra. By substituting onto the Pb lattice sites, the Gd may affect T_C through a change in the charge transfer to these Mo_6S_8 octahedra [26]. The effect of doping on the T_C of PMS has been studied in more detail by Zheng et al [27].

The addition of Gd significantly reduces $J_C(B,T)$ and $\mu_0 H_{irr}(T)$ by approximately 50%. The reduction in J_C may result from the presence of more second phase material, (as shown in figure 8.1). This would result in a lower J_C since the superconducting volume would be smaller than the sample volume. However, the presence of second phases should not affect $\mu_0 H_{irr}(T)$. The reduction of J_C and $\mu_0 H_{irr}$ may be explained by some of the Gd substituting onto the Pb lattice sites. When introducing magnetic ions into a superconductor, $J_C(B,T)$ and $\mu_0 H_{irr}(T)$ will in general decrease with increasing dopant concentration. This is due to the exchange scattering of the super-electrons on the magnetic ions [28]. In addition, the magnetic moments will align due to the action of the external field [29]. Fortunately, in Gd-PMS the rare-earth has a very weak exchange interaction with the super-electrons [20] and so the superconductivity is not completely destroyed. Alternatively, doping with Gd may adversely affect the properties of the grain boundaries, which are known to be responsible for the pinning.

The functional form of the volume pinning force is similar to that commonly observed in Nb_3Sn, ie. $F_P \propto h^{1/2}(1-h)^2$, where h is the reduced field. This confirms that a grain boundary pinning mechanism operates in this material. In both orientations, the harmonic response of the sample is consistent with the analysis in chapter 4. The assumption that J_C is constant over the ac. field range is good for a HIP'ed sample. The results also confirm those in chapter 7 which find HIP'ed samples to be characteristic of non-granular, bulk pinning, homogenous superconductors.

8.6 Conclusion.

A HIP'ed sample of gadolinium doped PMS has been fabricated with a T_C of 14.5 K, approximately 1 K higher than that for an undoped sample. The Gd is thought to act as an oxygen getter, thus improving the quality of the PMS. However XRD data shows that the addition of Gd also precipitates much second phase material. Preliminary TEM measurements have been unable to unambiguously determine the location of the Gd.

Flux penetration measurements have been made with the applied field both perpendicular to (transverse b) and parallel to (axial b) the long axis of the sample. The results have been used to calculate the functional form and the spatial variation of J_C as a function of field and temperature. The harmonic response of the sample has also been investigated and compared with the theoretical predictions in chapter 4.

For both orientations, the gradients of the magnetic field profiles indicate that the spatial variation in J_C is small. At 5 T and 6 K the flux penetration measurements give a J_C of 1.6×10^8 A.m^{-2}, approximately half that for undoped PMS which gives a value of 3.0×10^8 A.m^{-2}. The functional form of the volume pinning force obeys the universal Fietz-Webb scaling relation of the form $F_P \propto h^{½}(1-h)^2$, where h is the reduced field. This is very similar to that commonly observed in Nb_3Sn and confirms that J_C is still limited by a grain boundary pinning mechanism. Doping with Gd also reduces $\mu_0H_{irr}(T)$ to approximately half that for an undoped sample. The reduction of $J_C(B,T)$ and $\mu_0H_{irr}(T)$ may be explained by some of the Gd substituting onto the Pb sites in PMS. Alternatively, doping with Gd may adversely effect the properties of the grain boundaries which are known to be responsible for the pinning.

In both orientations, the harmonic response of the sample is consistent with the analysis in chapter 4. This confirms that a HIP'ed sample of Gd-PMS can be considered as a bulk pinning, homogenous superconductor.

More work is required to fully understand the interaction between the magnetic Gd ions and the superconductivity, in particular, the location of the Gd ions and why J_C and μ_0H_{irr} are reduced by the addition of Gd.

References

[1] Fischer Ø *J. Appl. Phys.* **16** 1 (1978).

[2] Odermatt R, Fischer Ø, Jones H and Bongi G *J. Phys. C* **7** L13 (1974).

[3] Chevrel R, Hirrien M and Sergent M *Polyhedron* **5** (1-2) 87 (1986).

[4] Fischer Ø, Jones H, Bongi G, Sergent M and Chevrel R *J. Phys. C* **7** L450 (1974).

[5] Seeber B, Rossel C and Fischer Ø *Ternary Superconductors* ed. Shenoy G K, Dunlap B D and Fradlin F Y 261 (Elsvier, North Holland) (1981).

[6] McCallum R W, Johnson D C, Shelton R N and Maple M B *Solid State Comms.* **29** 391 (1977).

[7] McCallum R W, Johnson D C, Shelton R N, Fertig W A and Maple M B *Solid State Comms.* **24** 501 (1977).

[8] Fumagelli P, Schoenes J, Decroux M and Fischer Ø *J. Appl. Phys.* **67** (9) 5053 (1990).

[9] Maple M B, Woolf L D, Majkrzak C F, Shirane G, Thomlinson W and Moncton D E *Phys. Lett.* **77A** (6) 487 (1980).

[10] Birrer P, Gygax F N, Hitti B, Lippett E, Schenk A, Cattani D, Cors J, Decroux M, Fischer Ø and Barth S *Physica C* **153-155** 751 (1988).

[11] Corbett J D *J. Solid State Chem.* **39** 56 (1981).

[12] Hughbanks T and Hoffmann R *J. Am. Chem. Soc.* **105** 1150 (1983).

[13] Shelton R N *J. Less-Common Metals* **94** 69 (1983).

[14] Horyn R, Peña O, Geantet C and Sergent M *Supercond. Sci. Technol.* **2** 71 (1989)

[15] Horyn R, Peña O, Wojakowski A and Sergent M *Supercond. Sci. Technol.* **7** 146 (1994).

[16] Krabbes G and Oppermann H *Crystal Research and Technol.* **16** (7) 777 (1981).

[17] Yamamoto S, Wakihara M and Taniguchi M *Mat. Res. Bull.* **20** 1493 (1985).

[18] Yamasaki H and Kimura Y *Mat. Res. Bull.* **21** 125 (1986).

[19] Sleight A W and Prewitt C T *Inorg. Chem.* **7** 2282 (1968).

[20] Sergent M, Chevrel R, Rossel C and Fischer Ø *J. Less-Common Metals* **58** 179 (1978).

[21] Ramsbottom H D and Hampshire D P *Meas. Sci. Technol.* **6** 1349 (1995).

[22] Campbell A M *J. Phys. C* **2** 1492 (1969).

[23] Bean C P *Rev. Mod. Phys.* **36** 31 (1964).

[24] Alterovitz S A and Woollam J A *Ternary Superconductors* ed. Shenoy G K, Dunlap B D and Fradin F Y 113 (Elsvier, North Holland) (1981).

[25] Woollam J A, Alterovitz S A and Luo H L *Current Topics in Physics : Superconductivity in Ternary compounds I* ed. Fischer Ø and Maple M B 143 (Springer-Verlag, New York) (1982).

[26] Varma C, Blount E, Greenside H and Ramakrishnan T *Ternary Superconductors* ed. Shenoy G K, Dunlap B D and Fradin F Y 261 (Elsvier, North Holland) (1981).

[27] Zheng D N and Hampshire D P *Inst. Phys. Conf. Series No.* **148** *EUCAS'95* 255 (1995).

[28] Fischer Ø, Decroux M, Roth S, Chevrel R and Sergent M *J. Phys. C* **8** L474 (1975).

[29] Fischer Ø, Treyvaud A, Chevrel R and Sergent M *Solid State Comms.* **17** 721 (1975).

Chapter 9
Conclusion.

9.1 Introduction.

This thesis has given a brief introduction to superconductivity and a comprehensive review of flux penetration measurements. A model has been outlined which accounts for the harmonic response of a superconductor to low frequency, high amplitude ac. fields. This was followed by a description of the design, construction and use of a probe to measure the magnetic field profiles and harmonic response of a superconductor as a function of temperature in high magnetic fields. These flux profiles give the spatial variation of J_C from which it is possible to distinguish surface pinning from bulk pinning and hence determine the mechanisms that limit J_C. Results have been obtained on a sample of multifilamentary NbTi wire, a HIP'ed and unHIP'ed sample of PMS and a Gd doped sample of PMS. These have been used to determine both the spatial variation and functional form of J_C, scaling relations and pinning laws. This final chapter summarises the main conclusions of the thesis and offers some ideas for future work.

9.2 Summary.

A critical state model has been used to calculate the magnitude and functional form of the magnetic response of a superconducting sample to an applied ac. field. A Fourier analysis is then used to generate the harmonic response of both the loss and lossless components. The analysis has been performed for both a cylinder and a slab geometry and calculated up to the 10^{th} harmonic. In flux penetration measurements, the 1^{st} harmonic of the lossless component is recorded. The overshoot in the flux profile has been shown to be due to the analysis and is not indicative of sample granularity.

A probe has been designed and built for making flux penetration measurements on superconductors from 2-30 K, accurate to 100 mK, in high magnetic fields up to 17 T. In these measurements, a small ac. field is superimposed onto a much larger dc. field. The probe can be used with one of two different ac. coils. One is made from copper wire and can produce an ac. field of 10 mT from 0 T to 17 T. The other uses a

superconducting NbTi coil, which can generate a much larger ac. field (up to 10 times larger in zero dc. field). A third coil has been made from Nb_3Sn wire. It is wound on a non-magnetic, non-metallic former to produce good field homogeneity and reduce eddy currents and ac. losses. As with the Cu and NbTi coils, it consists of two oppositely wound sections which facilitates use in high field superconducting magnets. The performance of the coil falls of with increasing frequency but it is still able to produce an ac. field of 85 mT at 20 Hz in a dc. field of 12 T. The probe can be used to study sections of superconducting cables, wires, tapes, thin films or bulk samples.

Flux penetration measurements have been made on commercial, multifilamentary NbTi, a high J_C superconductor which exhibits strong bulk pinning. Results have been obtained with the applied field both perpendicular to the filaments (transverse b) and parallel to the filaments (axial b). These have been analysed using Bean's critical state model to calculate $J_C(B,T)$. Campbell's analysis has been used to generate the magnetic field profiles inside the sample. For the sample in a transverse field, the gradient of the magnetic field profiles indicate that the spatial variation of J_C is small. The magnetic field profiles also provide experimental confirmation of an overshoot for a non-granular superconductor. At 6 T and 6 K the flux penetration measurements give a J_C of 6.2×10^8 $A.m^{-2}$. This is within 3.5% of transport critical current measurements on the same wire which give a value of 6.0×10^8 $A.m^{-2}$. The functional form of the volume pinning force obeys the universal Fietz-Webb scaling relation of the form $F_P \propto h(1-h)$ where h is the reduced field H/H_{C2}. The harmonic response of the sample has also been investigated. The results are consistent with the theoretical analysis of a non-granular superconductor. Both the magnetic field profiles and harmonic response suggest that in this orientation, the multifilamentary NbTi can be considered to be a bulk pinning, homogenous superconductor. When the sample is in an axial field, the results are different. Most noticeably there is a dramatic reduction in the magnetic moments and the magnetic field profiles and harmonic response do not agree with the theoretical predictions. In this orientation, the Lorentz force on individual filaments caused them to move and quench.

A high quality, hot isostatically pressed (HIP'ed) PMS sample has been fabricated which has a T_C of 13.5 K, (ΔT_C = 1 K). Using XRD and SEM the sample has been shown to be single phase and fully densified. HIP'ing the PMS increased the T_C by 1 K and

reduced the width of the transition. The magnetic moment of both HIP'ed and unHIP'ed samples of PMS has been measured from 4.2 K up to T_C in magnetic field up to 10 T. The results have been used to calculate the functional form and the spatial variation of J_C as a function of field and temperature. The gradients of the flux profiles suggest that the spatial variation of J_C is small, indicating that PMS is a bulk pinning superconductor. On HIP'ing $J_C(B,T)$ increases by a factor of 20 to greater than 3.0×10^8 A.m^{-2} at 5 T and 6 K. The functional form of the volume pinning force obeys the universal Fietz-Webb scaling relation of the form $F_p \propto h^{½}(1-h)^2$, where $h=H/H_{irr}$. HIP'ing also increases $\mu_0 H_{irr}(T)$ by a factor of 2 so that the irreversibility line for HIP'ed PMS lies close to $\mu_0 H_{C2}(T)$ values determined by dc. magnetisation. The J_C, scaling relations and pinning parameters are also in agreement with dc. magnetisation results on the same sample.

A HIP'ed sample of Gd doped PMS has been fabricated with a T_C of 14.5 K, approximately 1 K higher than that for an undoped sample. It is thought that the Gd acts as an oxygen getter and improves the quality of the PMS. However, XRD shows that the addition of Gd also precipitates much second phase material, such as Mo_2S_3, MoS_2 and Gd_2S_3. Flux penetration measurements have been made with the applied field both perpendicular to (transverse b) and parallel to (axial b) the long axis of the sample. The results have been used to calculate the functional form and the spatial variation of J_C as a function of field and temperature. For both orientations, the gradients of the flux profiles suggests that the spatial variation of J_C is small. At 5 T and 6 K the J_C is 1.6×10^8 A.m^{-2}, approximately half that for undoped PMS which gives a value of 3.0×10^8 A.m^{-2}. The functional form of the volume pinning force obeys the universal Fietz-Webb scaling relation of the form $F_p \propto h^{½}(1-h)^2$, where $h=H/H_{irr}$. This is similar to that observed in Nb_3Sn and confirms that J_C is still limited by grain boundary pinning. Doping with Gd also reduces $\mu_0 H_{irr}(T)$ to approximately half that for an undoped sample. The reduction of $J_C(B,T)$ and $\mu_0 H_{irr}(T)$ may be explained by some of the Gd substituting onto the Pb sites in PMS. Alternatively, doping with Gd may adversely effect the properties of the grain boundaries which are known to be responsible for the pinning. The harmonic response of the sample has also been investigated and compared with the theoretical predictions. In both orientations, the results are consistent with the analysis of a non-granular sample. This confirms that a HIP'ed sample of Gd-PMS can be considered as a bulk pinning, homogenous superconductor.

9.3 Future work.

A recent development has been the design and construction of an ac. superconducting Nb_3Sn coil which can produce large ac. fields in large background dc. fields. It will extend the range of fields and temperatures over which flux penetration measurements can be made. (At present limited by the NbTi coil quenching at high dc. fields and high temperatures.) In the future, the Nb_3Sn coil will ensure that the flux penetration probe remains state-of-the-art and enable flux penetration measurements to be made on samples with high J_C's in dc. fields up to 17 T.

Further work is necessary for the complete interpretation of the experimental observations in this thesis and for the development of a better understanding of the magnetic field profiles of real superconducting samples. Flux penetration measurements should be made on superconducting samples with spatially separated regions having different J_C's, to see if two gradients can be seen in the flux profile. For example, the flux profile of PMS wire may show evidence of surface pinning at the superconductor-normal interface. With further analysis of the magnetic field profiles and harmonic response it may also be possible to find an unambiguous signature of granularity.

Future work should focus on the effort to increase the J_C of PMS. This could involve the optimisation of the HIP'ing and heat treatments in order to decrease the grain size, attempts to produce an essentially single crystal PMS sample and further investigations on doping with rare-earth metals. (In particular, neutron diffraction measurements and transmission electron microscopy should be performed in order to determine the location of the magnetic ions.) In this way it may be possible to increase J_C to the level required for the practical and economic generation of high dc. magnetic fields. Even then, more work is necessary to achieve high J_C and both thermal and mechanical stability over long lengths.

Combining flux penetration measurements with techniques such as dc. magnetisation, transport J_C and specific heat, together with materials characterisation by XRD, SEM and TEM, is crucial for a thorough understanding of Chevrel phase superconductors.

Appendices.

Appendix 1 Publications.

[1] Flux penetration measurements on superconductors.
Ramsbottom H D and Hampshire D P.
Submitted for publication in Phys. Rev. Lett. (1996).

[2] Flux penetration and harmonic generation measurements on superconductors in high magnetic fields.
Ramsbottom H D and Hampshire D P.
Submitted for publication in Phys. Rev. B. (1996).

[3] The response of a new ceramic-oxynitride (cernox) resistance temperature sensor in high magnetic fields.
Ramsbottom H D, Ali S and Hampshire D P.
Cryogenics **36** (1) 61-63 (1996).

[4] Critical current densities, scaling relations and flux pinning in NbTi determined by flux penetration measurements.
Ramsbottom H D and Hampshire D P.
Inst. Phys. Conf. Series No. **148** *EUCAS'95* 259-262 (1995).

[5] An ac. superconducting Nb_3Sn coil for use in high magnetic fields.
Ramsbottom H D, Hampshire D P, Jones H and Smathers D B.
Inst. Phys. Conf. Series No. **148** *EUCAS'95* 727-730 (1995).

[6] Specific heat of $PbMo_6S_8$ and $(Pb_{0.7}Gd_{0.3})Mo_6S_8$ superconductors in high magnetic fields.
Ali S, Ramsbottom H D and Hampshire D P.
Inst. Phys. Conf. Series No. **148** *EUCAS'95* 583-586 (1995).

[7] Reversible and irreversible magnetisation of the Chevrel phase superconductor $PbMo_6S_8$.
Zheng D N, Ramsbottom H D and Hampshire D P.
Phys. Rev. B. **52** (17) 12931-12938 (1995).

[8] A probe for measuring magnetic field profiles inside superconductors from 4.2 K up to T_C in high magnetic fields.
Ramsbottom H D and Hampshire D P.
Meas. Sci. Technol. **6** 1349-1355 (1995).

[9] Ac magnetisation measurements on hot isostatically pressed bulk $PbMo_6S_8$ from 4.2 Kelvin up to T_C in high magnetic fields.
Ramsbottom H D, Zheng D N and Hampshire D P.
IEEE Trans. on Appl. Supercond. **5** (2) 1321-1324 (1995).

Appendix 2 Courses and Conferences.

December	1995	University of Liverpool	CMMP 95.
August	1995	Eger, Hungary	International workshop on HTSC
July	1995	University of Edinburgh	EUCAS 95.
December	1994	University of Warwick	CMMP 94.
November	1994	IRC in Superconductivity	Engineering aspects of HTSC.
November	1994	Institute of Physics	Magnetic measurements on HTSC.
October	1994	Boston, USA	ASC 94.
May	1994	IOP, London	Strongly correlated systems.
March	1994	University of Durham	SERC graduate school.
December	1993	University of Leeds	CMMP 93.
June	1993	University of Durham	Mechanical workshop course.
January	1993	IRC in Superconductivity	Winterschool on Superconductivity.
November	1992	University of Birmingham	Cryogenic techniques.
November	1992	University of York	Vacuum technology.

Appendix 3 Computer programs.

All of the measurements are computer controlled using interactive, real-time graphical software ASYST v.4 (Keithley), such that all data are stored digitally. Communication is via IEEE interface except for the dc. magnet power supply that uses the RS 232 bus. The default ASYST system has been modified. System overlays, file sharing, graphics and memory information are saved in two files called ***HARRY.COM*** and ***HARRY.OVL***. A program called ***NEW.Q*** is saved as part of the system. This automatically loads a file called ***DEVICES.PRO***. This file contains the IEEE address settings, initialisation sequences, serial polling and setup routines for all of the electronic apparatus.

A3.1 General programs.

Several other programs have been written. These can be divided into three groups.

i. Those used for thermometry calibration and temperature control. These include ***RUNCGIF.HAZ*** which can be used to calibrate a carbon-glass thermometer as a function of dc. field, ***PID.HAZ***, which can be used to find the correct PID parameters for a particular cryogenic system and ***CURVE.HAZ*** which can be used to enter a calibration curve into a Lakeshore temperature controller.

ii. Several programs have been written to control the various power supplies. These include ***BOPAC.HAZ*** which ramps the BOP in ac. mode using the LIA, ***BOPDC.HAZ*** which ramps the BOP in dc. mode, ***OPSU.HAZ*** which controls the 15/17 T dc. magnet and ***DEMAG.HAZ*** which demagnetises the 15/17 T magnet.

iii. The last set of programs are more mathematical. ***RUNSGALL.HAZ*** is able to perform Savitsky-Golay differential filtering of the data produced by the flux penetration program. This analysis is required to obtain magnetic field profiles. Another program ***COIL.HAZ*** is able to calculate the magnetic characteristics of magnetic coils of various dimensions.

A3.2 Ac. susceptibility measurements.

This program is capable of making ac. susceptibility measurements at various dc. fields. For each field, the temperature is ramped and χ' and χ'' recorded. All data is saved in a LOTUS 123 file. The program ***RUNSSUC.HAZ*** load all of the files required. These include the files ***TCON.VAR*** and ***TCONZFCG.HAZ*** which contain the zero-field calibrations for the two carbon-glass thermometers. All program variables are saved in the file ***ACSUSC.VAR***. The rest of the program is split into 5 files. Table A1 lists the programming blocks in each file and figure A1 shows the control sequence in which they are executed.

ACSUSC1	*ACSUSC2*	*ACSUSC3*	*ACSUSC4*	*ACSUSCGO*
left	title	go2words	labels	setup
bottom	alterations	sensitivity	plotscreen	go1
pol	choicent	phasing	time	go2
poll	choicepc	balancing	dataplot1	go3
polll	tcontrol	timing	dataplot2	go
response	temprange	chkspeedsuper	dataplot3	
reply	temprate	chkspeednorm	dataplot4	
nimput	temprecap	stopDC	dataplot5	
look	totalrecap	stopAC	takedata	
setupA	tconvert	stopHeat	saveit	
setupB		setDCfield	totalrecall1	
setupC		setACfield	totalrecall2	
setupD		PID	finish	
setupE		tempwords	totalfinish	
switch		setpoint		
sleeping		3pointcheck		
wake		checkstable		
		settemp		

Table A1 The various blocks for the ac. susceptibility program.

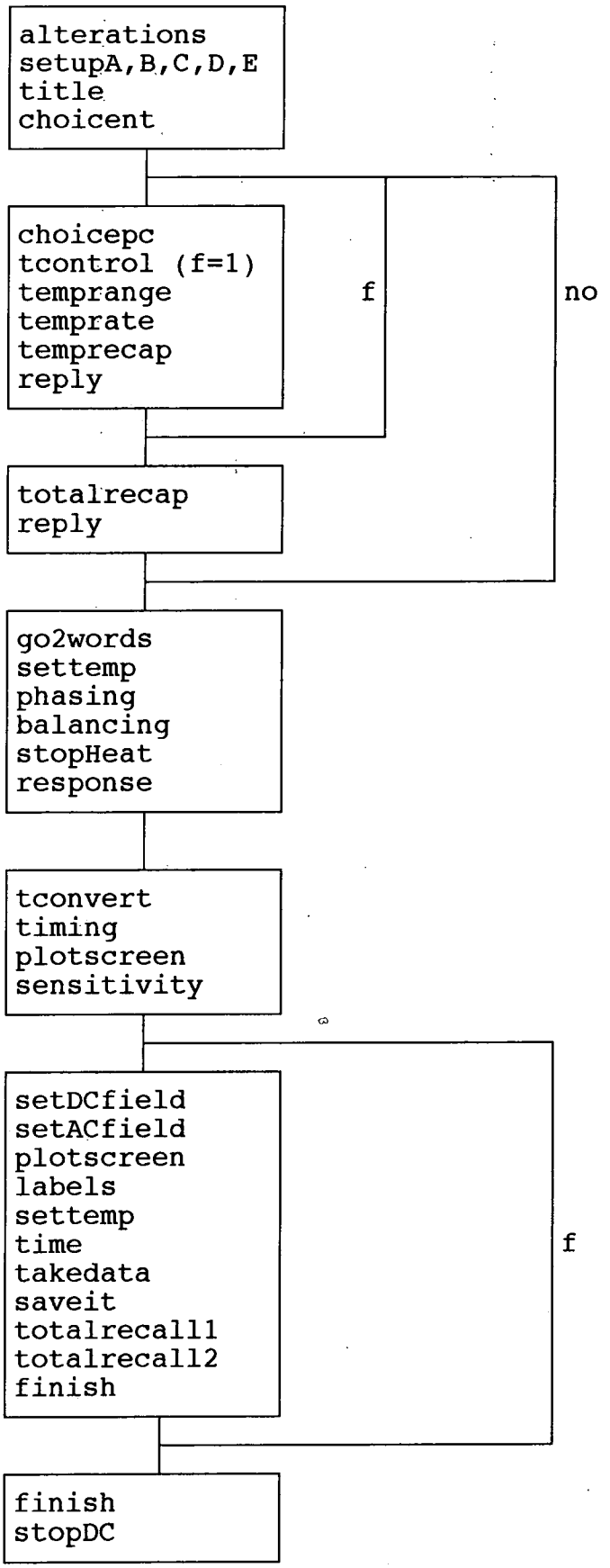

Figure A1 The control sequence for the ac. susceptibility program.

A3.3 Flux penetration measurements.

This program is capable of making flux penetration measurements as a function of field and temperature. For each field and ac. field is ramped and χ' and χ'' recorded. After measurements have been completed for all temperatures, the field is changed and the measurement repeated. In this way a complete set of data is obtained at all fields and temperatures. The data for each dc. field is saved in a separate LOTUS 123 file. The file ***RUNMAGN.HAZ*** load all of the relevant files. These include ***TCON.VAR***, ***TCONZFCG.HAZ*** and ***TCONBTCG.HAZ***, which contain the zero-field and in-field calibrations for the two carbon-glass thermometers. All other variables are saved in the file ***ACMAGN.VAR***. The rest of the program is in 5 files. Table A2 shows the various programming blocks and figures A2 and A3 show the control sequence.

ACMAGN1	*ACMAGN2*	*ACMAGN3*	*ACMAGN4*	*ACMAGNGO*
pol	title	normalisation	labels	setup
poll	alterations	phasing	plotscreen	go1
polll	choicefile	sensitivity	time	go2
response	choicepc	rerunmsg	dataplot1	gofield
reply	recap	balancing	dataplot2	go3
nimput	checkfield	chkspeedsuper	dataplot3	go12
ab	checktemp	chkspeednorm	dataplot4	go13
look	choicefield	demag	dataplot5	go23
switchON	choicetemp	stopDC	takedata	go123
switchOFF	recapfield	stopAC	saveit	
setupA	recaptemp	stopHeat	totalrecall1	
setupB	totalrecap	chkstop	totalrecall2	
setupC		setfield	finish	
setupD		PID	totalfinish	
setupE		checkstable		
		settemp		

Table A2 The various blocks for the flux penetration program.

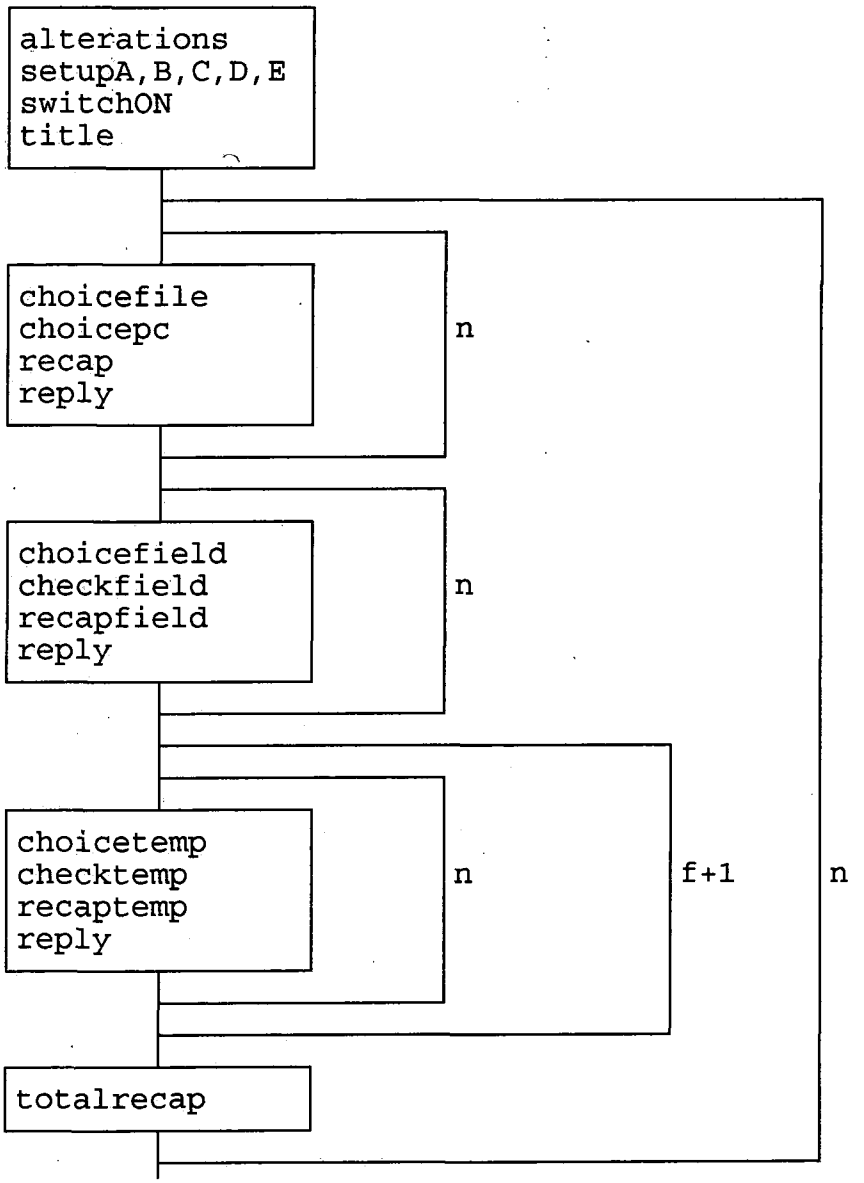

Figure A2 The control sequence for the flux penetration program (user inputs).

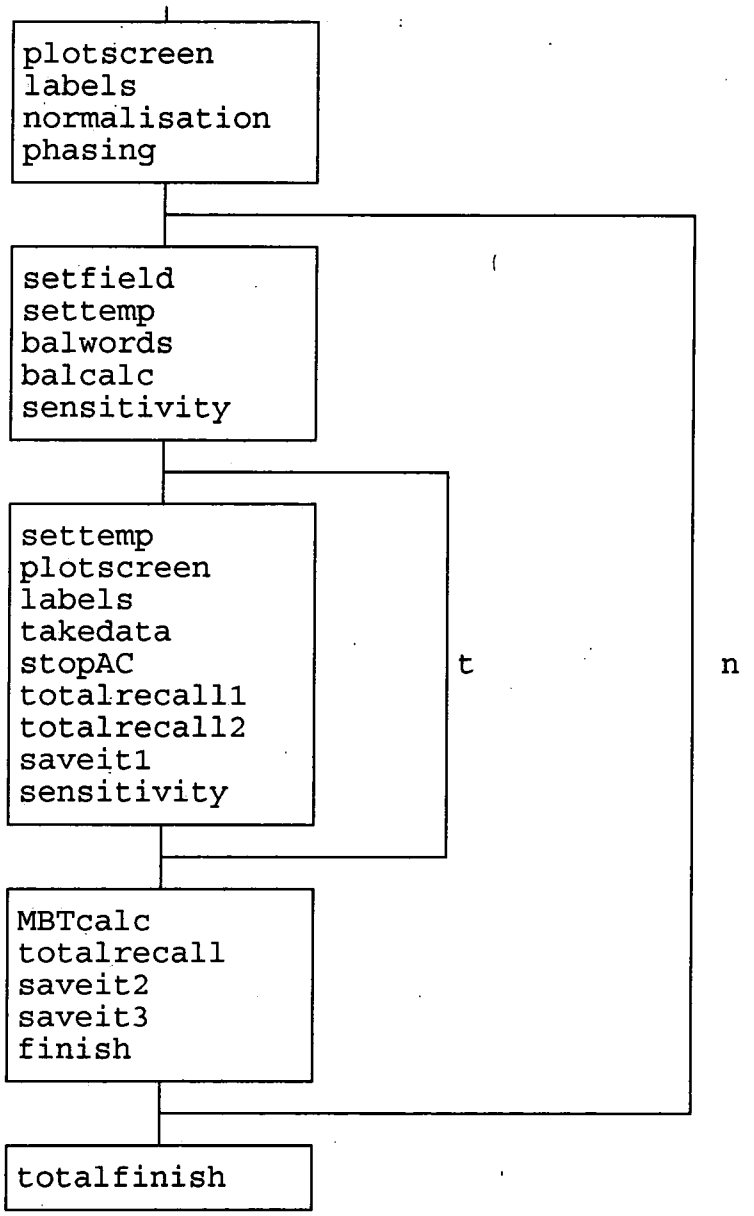

Figure A3 The control sequence for the flux penetration program (data acquisition).